

Hydrodynamics of the Atomic Force Microscope

A thesis submitted to
the University of Nottingham
for the Degree of Doctor of Philosophy

by

Richard J. Clarke

September, 2005

Acknowledgments

This work was conducted principally under the supervision of Prof. Oliver Jensen, to whom I owe a great debt of thanks, as I do to co-supervisors Dr. Phil Williams ¹, Prof. John Billingham and Dr. Steve Cox ². My thanks also to Anita Pearson ¹, for her help and expertise in obtaining the experimental data presented in chapter 6.

This work was funded by EPSRC grant GR/R88991/01 *Assessing Molecular Forces*, some of which has been submitted for publication, specifically the two-dimensional study in chapter 2 (Clarke et al. 2005a) and its extensions into three-dimensions in chapter 3 (Clarke et al. 2005b).

¹Laboratory of Biophysics and Surface Analysis, School of Pharmacy, University of Nottingham

²Present address: Department of Applied Mathematics, University of Adelaide, Australia

Contents

1	Introduction	1
1.1	AFM in the biosciences	3
1.1.1	Principles of atomic force microscopy	3
1.1.2	AFM imaging	5
1.1.3	AFM force spectroscopy	8
1.1.4	Calibration	12
1.2	Unsteady linearized flow	16
1.2.1	Fluid–solid interfaces	18
1.2.2	Steady flow	21
1.2.3	Unsteady linearized flow	28
1.2.4	Oscillatory flow	31
1.3	Objectives and structure of thesis	35
2	Flows generated by an infinite-length circular cylinder	37
2.1	Numerical treatment	38
2.2	Asymptotic treatment	39
2.2.1	Viscous wall interactions: $\Delta \ll \gamma^{-1}$	40
2.2.2	Inviscid wall interactions: $\Delta \gg \gamma^{-1}$	43
2.2.3	Viscous/inertial wall interactions: $\Delta\gamma = O(1)$	46
2.3	Results	50
2.3.1	Streamlines	50
2.3.2	Drag	53

2.4	Discussion	54
3	Flows generated by a finite-length circular cylinder	57
3.1	Numerical treatment	61
3.2	Asymptotic treatment	62
3.3	Results	65
3.3.1	Screening of three-dimensional effects	65
3.3.2	Modified resistive-force-theory	68
3.3.3	Drag	69
3.3.4	Tilt	72
3.4	Discussion	74
4	Flows generated by a thin rectangular plate	79
4.1	Two-dimensional boundary-integral formulation	81
4.1.1	High-frequency limit	82
4.1.2	Numerical treatment	83
4.2	Two-dimensional thin-plate formulation	84
4.2.1	High-frequency limit	85
4.2.2	Lubrication limit	86
4.3	Three-dimensional thin-plate formulation	87
4.3.1	Numerical scheme	88
4.3.2	Lubrication limit	89
4.4	Results	92
4.4.1	Two-dimensional finite-thickness plate	92
4.4.2	Two-dimensional thin-plate theory	97
4.4.3	Three-dimensional thin-plate theory	99
4.4.4	Three-dimensional lubrication theory	103
4.5	Discussion	105
5	Damped dynamics of a sinusoidally-driven cantilever	109
5.1	One-dimensional beams	110

5.1.1	Two-dimensional hydrodynamics	111
5.1.2	Slender-body-theory hydrodynamics	112
5.1.3	Modified resistive-force-theory	114
5.2	Two-dimensional plates	114
5.2.1	Lubrication hydrodynamics	116
5.2.2	Thin-plate hydrodynamics	120
5.3	Results	122
5.3.1	Elastic beams	122
5.3.2	Elastic plates	124
5.4	Discussion	128
6	Damped dynamics of a thermally-driven cantilever	133
6.1	Equipartition of energy approach	134
6.2	Fluctuations in the canonical ensemble	135
6.2.1	Microscopic equilibrium fluctuations	137
6.2.2	Thermal spectra	139
6.3	Fluctuating beams	141
6.3.1	Two-dimensional drag	142
6.3.2	USBT hydrodynamics	144
6.3.3	Experimental setup	145
6.4	Results	145
6.4.1	Theory	145
6.4.2	Experiment	150
6.5	Discussion	154
7	Conclusions	160
7.1	Hydrodynamic theory	161
7.1.1	Wall effects	161
7.1.2	Finite-length effects	163
7.1.3	Tilt	164
7.2	AFM implications	165

7.2.1	TM-AFM	165
7.2.2	Thermal spectra	166
7.3	Extensions	167
7.3.1	Non-linear effects	167
7.3.2	Slip	168
7.3.3	Cantilever considerations	169
7.3.4	Sample considerations	169
7.3.5	AFM Experiments	170
A	Effects of slip	171
A.1	Two-dimensional circular cantilever	171
A.2	Rectangular cantilever in the lubrication limit	172
B	Two-dimensional inviscid flow for a cylinder above a wall	175
C	Unsteady two-dimensional image Stokeslets	177
C.1	Leading-order flow	177
C.2	Quasi-steady limit	180
D	Two-dimensional inviscid flow for a cylinder touching a wall	182
E	Unsteady slender-body-theory integrals	184
E.1	Distribution-independent integrals	184
E.2	Distribution-dependent integrals	185

Abstract

With a proven ability to uncover fundamental biological processes, the atomic force microscope (AFM) represents one of the most valuable and versatile tools available to the biophysical sciences. We study the unsteady small-scale flows generated within the AFM by its sensing probe (a long thin cantilever), which have received relatively little attention to date, yet which are increasingly relevant in an age of microdevices.

The early parts of this thesis investigate some canonical two-dimensional flows driven by oscillations of an infinite-length rigid cantilever. These prove amenable to analysis and enable us to investigate many of the important physical phenomena and compile a comprehensive collection of asymptotic expressions for the drag. The corresponding results lay out the influence of a nearby wall, geometry and oscillation frequency. The limitations of a two-dimensional approach are then explored through the development of a novel unsteady slender-body theory (USBT) for finite-length cylinders, an asymptotic treatment of which offers corrections to traditional resistive-force-theory (RFT) methods by accounting for geometric factors and flow inertia. These ideas are then extended to the study of thin rectangular plates. Two key parameters are identified which promote two-dimensionality in the flow, namely the frequency of oscillation and the proximity of a nearby boundary. We then examine flexible cylinders and plates by coupling the hydrodynamics to linearized elastic beam and plate equations, which simulate the hydrodynamically-damped high-speed deformable motion of the AFM's cantilever, when driven either externally or by Brownian motion. In the later case, we adopt an approach which offers notable improvements over the most advanced method currently available to the AFM community.

Chapter 1

Introduction

Since its conception by Binnig et al. (1986), the atomic force microscope (AFM) has revolutionised the biosciences. The AFM belongs to a group of techniques collectively termed scanning-probe microscopy, so-named because their central capabilities lie in the use of a sensing probe. Figure 1.1 displays one particular model of an AFM manufactured by Digital Instruments. A variety of techniques now fall under scanning-probe microscopy, all of which can trace their origins back to the original scanning-probe microscope (SPM), the scanning-tunnelling microscope (STM, Binnig et al. 1982); scanning near-field optical microscopy (SNOM), which uses a optic fibre to investigate a sample using the photon tunnel effect (Durig et al. 1986); scanning magnetic microscopy, which measures the magnetic interaction between the sample and a magnetised probe (Saenz et al. 1987); scanning ion conductance microscopy (SICM), which uses the flow-rate of ions from an electrolyte-filled pipette (Hansma et al. 1989) and scanning electrochemical microscopy (SECM), which measures the current of an electrode immersed in electro-active solution to judge both electrode-sample distance and sample conductivity (Bard et al. 1991). Over the years, however, the AFM has maintained its status as one of the most popular and versatile members of the SPM family.

Now established as a standard and widely available commercial tool for probing the structure and chemistry of biological samples, the AFM itself continues to evolve. Al-



FIGURE 1.1: A Digital Instruments Nanoscope IIIa Scanning Probe Microscope.

though use of the AFM is not exclusive to the biosciences, having established important roles in the physical sciences alongside other techniques such as electron microscopy (EM) and STM, its invaluable contribution to the biosciences lies in its ability to operate in fluid; this presents the opportunity to study the biology of samples in their native environment. The study of samples in a fluid environment brings its own set of challenges, yet these hydrodynamic challenges are not unique to the AFM. A host of new microelectromechanical systems (MEMS) are also capable of producing the types of small-scale high-speed flows which are encountered in the AFM. Traditionally, studies into microscopic bodies moving in fluid have focused on the relatively low-speed flows generated by micro-organism propulsion. The advent of the AFM and other microtechnologies places demands on us for a better understanding of high-velocity flow regimes.

In § 1.1 we introduce the AFM and discuss its chief applications, in particular sample imaging (§ 1.1.2) and force spectroscopy (§ 1.1.3), together with a review of calibration methods (§ 1.1.4) which are vital to obtaining accurate force measurements. In § 1.2 we present the formulation appropriate for describing the flow generated by the rapid motion of microscopic bodies and outline key results for slow movement (§ 1.2.2), some

general findings for time-dependent flows (§ 1.2.3) following by some results pertaining specifically to oscillatory motion (§ 1.2.4). The objectives and structure of the remaining thesis will be laid out in § 1.3.

1.1 AFM in the biosciences

1.1.1 Principles of atomic force microscopy

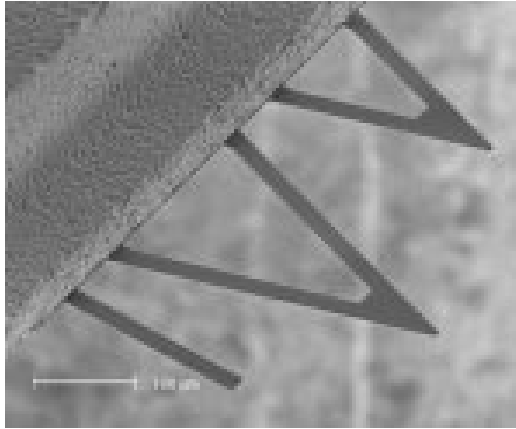


FIGURE 1.2: AFM cantilevers are predominantly diving-board or V-shaped and usually made from silicon nitride which can be gold-coated to improve reflectivity.

In the case of the AFM, the probe used to investigate a sample is a microcantilever, often etched out of silicon nitride (Si_3N_4), which has a density and Young's modulus of about 2gcm^{-3} and $2 \times 10^{12}\text{gcm}^{-1}\text{s}^{-2}$, respectively. This microcantilever is suspended above a substrate (usually cleaved mica, which is virtually an atomically flat surface), usually at an angle of 10–15 degrees. The substrate is mounted on a platform which can be moved vertically as well as in the horizontal plane. Specimens are then immobilised onto the mica in a variety of ways, including the use of Van der Waals forces, hydration effects or hydrophobicity, all of which work by producing a net attraction of the specimen to the surface.

Cantilever dimensions vary, but are typically $100\mu\text{m}$, $10\mu\text{m}$ and $1\mu\text{m}$, in length, width and thickness respectively, and are shaped as diving-boards or are V-shaped (see

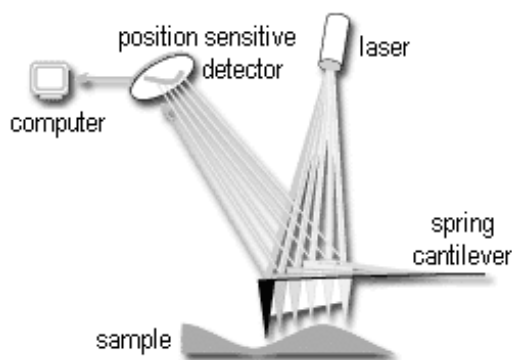


FIGURE 1.3: Interactions with the sample cause the AFM cantilever to deflect, which is measured by reflecting laser light off the cantilever's top surface. This reflected light is detected by photo-diodes and fed to processing software.

figure 1.2). Conventionally, V-shaped cantilevers are considered more resistant to lateral forces, although a theoretical study has recently cast doubt on this preconception (Sader 2003). The cantilever can be moved, with a displacement sensitivity of 0.01nm, via piezo-crystals attached to its supported end, which expand in reaction to an electric current and a sharp tip at the cantilever's end provides high measurement resolution (in colloidal probe experiments this tip is replaced by a particle, approximately $10\mu\text{m}$ in radius).

Specimens are analysed through their interactions with the cantilever tip, as it is brought close. Any interactions cause the cantilever to bend and so. In order to make precise measurements, it is necessary to accurately determine these deflections. Most modern AFM's achieve this by focusing a laser beam onto the back of the cantilever. Silicon nitride has a reflectivity of only about 13% and so the cantilever is often coated with gold to improve its reflective properties. The reflected beam is collected by a 4×4 array of photoreceptors, as illustrated in figure 1.3, which determine both the deflection of the cantilever at its tip-end and the degree to which it has twisted about its axis.

AFM experiments can be conducted in air, yet this has its disadvantages. Measurements can be distorted by capillary forces, produced by the formation of a meniscus between the tip and specimen. Also, in the case of biological specimens, gaseous surroundings do not always represent the desired physiological conditions. Therefore bi-

ological samples are usually immersed in a fluid, which typically has the viscosity of water ($0.01\text{cm}^2\text{s}^{-1}$). The fluid may be contained by an O-ring (which can leak if the cantilever–substrate separation exceeds around $50\mu\text{m}$, Maeda and Senden 2000). Operating in liquids, however, brings its own set of challenges. AFM liquid experiments are exposed to thermal-noise contamination, arising from thermally-excited solvent molecules bombarding the AFM cantilever. As a result, in the absence of any externally applied driving force, the cantilever still fluctuates (albeit with nanometre-scale amplitudes at room temperature). Furthermore, any motion of the cantilever through the fluid environment is met with hydrodynamic resistance, which can significantly affect AFM readings. The nature of this hydrodynamic effect depends greatly upon the way in which the AFM is used, so let us briefly review the principal experimental techniques.

1.1.2 AFM imaging

The AFM built its early reputation in the biosciences on its imaging capabilities. Although the pioneering membrane investigations of Worcester et al. (1988) were received with scepticism, the work on imaging DNA in air by Bustamante et al. (1992) firmly established the AFM's potential as a powerful tool in the study of biological structures. In its original form, when the AFM scanned a specimen, contact between the cantilever and the sample was maintained throughout the scan. This method created an image by measuring the twisting and bending of the cantilever as it rode the peaks and troughs of the sample's surface, much like a phonograph needle. However, full-contact modes can damage soft biological samples and so, to overcome this flaw, Hansma et al. (1994) developed tapping-mode (TM-AFM). In TM-AFM the cantilever is excited to oscillate close to its resonant frequency (10 – 600 kHz), with amplitudes ranging up to 20nm. This results in only intermittent contact between the cantilever and the sample, which minimises the chances of damage to the specimen.

The catalogue of biological samples investigated using the AFM is now extensive. AFM imaging of DNA, conducted in a physiological fluid environment (Lyubchenko et al. 1993), can now capture enzyme degradation of DNA (see figure 1.4), observe RNA transcription and probe the damage caused to chromosomes by exposure to ra-

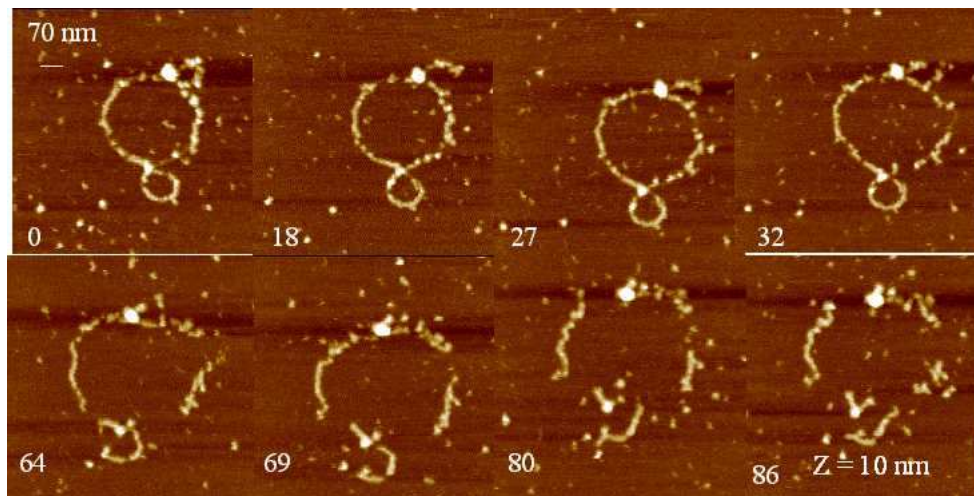


FIGURE 1.4: AFM snapshots of the degradation of DNA-G4 complexes by the enzyme DNase I, imaged in deionised water (Laboratory of Biophysics and Surface Analysis, University of Nottingham).

diation. Since Worcester et al. (1988), the study of membranes has become an active area of research, with particular interest in the complex behaviour of lipid-bilayers (Hui et al. 1995), insertion of molecules into a membrane and the mechanical properties of the membrane itself. Membrane proteins have also been the subject of much work, in part due to the stability and limited degrees of freedom imposed upon the protein by the membrane (for an example, see Heymann et al. 1997). The study of non-membrane proteins includes the muscle fibres actin and myosin, which have also been imaged by Weisenhorn et al. (1990), Hallet et al. (1995). The AFM also offers tantalising opportunities to visualise cells in their native environment, as well as intracellular structures such as synaptic vesicles and the cytoskeleton. The difficulties associated with cell experiments mean that it is common practice to couple AFM imaging to a second technique, such as optical microscopy (Vesenka et al. 1995), to minimise the risk of falsely identifying structures. All the areas of biological investigation covered above are detailed more completely in a recent review article by Santos and Castanho (2004).

One consequence of hydrodynamic damping during sample imaging is its effect on the responsiveness of the cantilever. This, in turn, places a limit upon the rate at

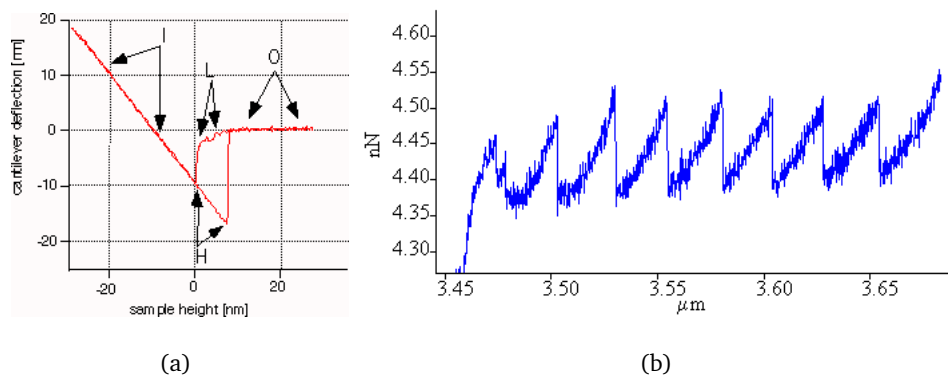


FIGURE 1.5: (a) force-distance curve for single molecular interaction (<http://www.chemsoc.org/exemplarchem/entries/kscott/afm.htm>), (b) force-distance plot showing unfolding of multiple immunoglobulin domains in the muscle protein titin (<http://www.biophysik.uni-bremen.de/radmacher/elasticity.html>).

which samples can be scanned. Furthermore, fluid effects reduce the sharpness of the cantilever's response, decreasing the so-called Q-factor of the measurement (Butt et al. 1993). A theoretical model for the effect of fluid damping in TM-AFM was proposed by Chen et al. (1994), who modelled the cantilever as a damped one-dimensional oscillator with loading equal to the steady hydrodynamic drag on a sphere. The predictions from this simple model illustrated a decrease in Q-factor with an increase in fluid viscosity. However, the assumption that fluid inertia can be neglected is dubious for TM-AFM, where the cantilever oscillates with considerable frequency. Unsteadiness in the AFM's flow was taken into account by Kirstein et al. (1998), who modelled the cantilever as an infinitely-long circular cylinder. By substituting the calculated drag coefficients into the elasticity equation for a simple beam, the damped resonant frequencies of the cantilever were found as a function of the resonant frequency in vacuo. Once these quantities had been found by fitting the oscillator model to experimental data in air, this approach was successfully able to predict the resonant frequency of the cantilever in water.

1.1.3 AFM force spectroscopy

The field of AFM force measurement is an area which holds huge promise, having the potential to profoundly increase our understanding of biology by exposing the fundamental processes by which molecular bonds form and proteins are stabilized.

It works by lowering the cantilever tip towards a sample until the strength of the tip-sample attraction overcomes the cantilever stiffness, causing the tip to jump into contact with the specimen. The cantilever is then raised at approximately $1\mu\text{ms}^{-1}$ whilst the tip is still attached to the sample by intermolecular forces, thereby causing the cantilever to bend. Application of Hooke's law then converts this deflection into a force and a force-distance curve can be generated for the interaction. An annotated example of such a curve is shown in figure 1.5(a). The cantilever approaches the substrate (O), until it comes sufficiently close that attractive forces cause it to jump into contact with the sample (L) and any further decrease in separation during contact produces in a linear change in the deflection (I). The cantilever is then retracted until the intermolecular bond breaks, with a noticeable hysteresis between the attachment and detachment distances (H). The strength of the intermolecular bond is directly proportional to detachment distance, via the spring constant. Using this technique, early force spectroscopy examined ligand-receptor bonds (Florin et al. 1994) and the affinity between strands of DNA (Lee et al. 1994), measured down to an accuracy of a few pico-Newtons.

When the sample has a complex spatial structure, such as a folded protein, the molecule may alter its configuration under an applied load resulting in the type of force curve shown in figure 1.5(b). Here the muscle protein titin is being unfolded and the distance between each peak in the force curve gives the length of one (unfolded) immunoglobulin domain in the protein and the height of each peak corresponds to the force required to unfold it. Interest in protein unfolding has remained high since the celebrated work of Rief et al. (1997) on the muscle protein titin (see Janovjak et al. 2004 and references therein). By understanding the unfolding process of proteins, the hope is to understand the folded structures which dictate so much of a protein's biological function. Developments in this area include analysing the unfolding process as a function of retraction

speed (Strunz et al. 1999), in so-called dynamic-force spectroscopy (DFS). Using sophisticated analysis, DFS offers insights into the potential barriers overcome during the unfolding process and the rate at which these barriers can naturally be crossed (specific details can be found in a review article by Evans 2001). These potential barriers are often referred to as the energy landscape of the folding process. The extent to which this energy landscape can be explored is currently restricted by limitations on cantilever retraction speeds. With pulling speeds much above $10\mu\text{ms}^{-1}$ the fluid drag on the cantilever becomes comparable with the strength of the molecular forces being measured. For this reason, there is considerable interest in quantifying the hydrodynamic effects at work in these experiments.

Vinogradova et al. (2001) exploited the close proximity between cantilever and sample during force measurements to approximate fluid effects using lubrication theory. This quasi-steady lubricating flow was combined with the three-dimensional elastic behaviour of the cantilever to give a coupled system for flow pressure and cantilever deflection. This was then solved numerically using finite-element analysis (FEA). In the limiting case of a narrow cantilever, the system becomes amenable to analysis. It was shown that, in contrast to the case of a concentrated point-force applied at the end of the cantilever, a distributed hydrodynamic loading over the length of the cantilever results in deflections which are highly sensitive to the angle of inclination. This study gives an indication of when it is appropriate to consider tip-sample-dominated hydrodynamics or when the cantilever is sufficiently close (i.e. when the tip/colloidal-probe distance is sufficiently small) that hydrodynamic loading along its entire length becomes an issue. Applying this work to force measurements, Vinogradova and Yakubov (2003) approximated the drag on a cantilever fitted with a colloidal probe ($10\mu\text{m}$ sphere), at moderate cantilever-sample distances, by adding a wall-independent term to the lubrication drag which is fitted to experimental data. The deflection caused by this hydrodynamic loading was combined with that due to a point loading at the tip under lubrication forces, representing tip-sample interactions. This study also examined the validity of the no-slip condition in colloidal-probe experiments (see § 1.2.1). Close to a substrate Craig and Neto (2001) suggested that the drag on a cantilever loaded

with a colloidal probe is estimated well by the classical result for the drag on a sphere approaching a rigid wall (Brenner 1961). This drag, together with measurements of cantilever deflection on approach, were used to find a value for the cantilever spring constant through Hooke's law. A similar approach was offered by Notley et al. (2003), who oscillated the substrate in close proximity to the colloidal particle at amplitudes of up to 10nm and frequencies less than 1kHz. A relationship between fluid viscosity, frequency of oscillation, amplitude of response and spring constant, derived by Israelachvili (1986a) for thin fluid films, was then called upon.

By gathering force-curves from many points on a sample's surface, a map of tip-surface interactions can be created. An early version of this technique was implemented by Burnham et al. (1990), who used a tungsten-tipped cantilever to differentiate between two compounds with differing chemistries. By functionalising the cantilever tip with chemically active compounds, the force-mapping technique continued to find application in the analysis of sample chemistry. A review by Green et al. (2002) covers some recent chemical-force microscopy (CFM) investigations into the chemical functionality of compounds, including the work of Werts et al. (1997) on real-time scanning of chemical reactions. The mapping of specific biomolecular interactions came with the work done by Ludwig et al. (1997) who investigated antibody-antigen complexes, using a tip functionalised with biotin scanned over a streptavidin-patterned substrate. There is now an industry of research which uses antibody-modified tips to map antigen-coated surfaces (Green et al. 2002 gives a more comprehensive survey). Other biological studies include the mapping of a mixed group of blood cells (Grandbois et al. 2000) and identifying complementary DNA (Mazzola et al. 1999).

The long sampling-time and large data-storage-capacity problems encountered when generating a force-distance curve at each sampling point were addressed by Frisbie et al. (1994) who, instead, measured the frictional force experienced by the tip as the cantilever scans whilst in contact with the surface. This friction-force mode of force sensing has the advantage of speed, minimising experimental error derived from effects such as sample drift, but has the potential to damage samples. As in imaging techniques, the resolution to this problem is to use intermittent contact to keep spec-

imen damage down to a minimum. For this reason, TM-AFM has also found a role in force measurement experiments. Moreover, analysis of the difference in oscillation phase between the tip and the driven end of the cantilever provides information about the adhesive and viscoelastic properties of the sample (Winkler et al. 1996), the wetting properties of the sample (Gil et al. 2000) and the sample's surface charge (Czajkowsky et al. 1998). For example, Radmacher et al. (1994) used tip adhesion to survey the viscoelastic qualities of the enzyme lysozyme.

One of the major problems for techniques which set out to probe dynamic sample properties, however, is the fact that tip-sample interactions are often non-linear. Despite the ability of TM-AFM to tap with amplitudes of 1nm, the displacement remains large enough on the molecular scale that a linear sample response cannot be guaranteed, which is a prerequisite for determining properties such as local compliance. Both thermal and mechanical (electrical) noise are traditionally an obstacle to further amplitude reduction, with manufacturers producing smaller cantilevers which are less susceptible to such effects both in force spectroscopy (Viani et al. 1999) and imaging (Walters et al. 1996). If properly understood, however, these effects offer a means by which cantilevers can be driven with amplitudes of just 0.1nm.

In their theoretical analysis of the thermal spectrum, Roters and Johannsmann (1996) introduced a δ -correlated (white-noise) forcing term into the damped harmonic oscillator equation, where the damping coefficient is considered to be steady. This results in a Langevin equation (Reichl 1987) to describe the stochastic behaviour of the cantilever tip. Solving this equation gives a power spectrum in the form of a Lorentzian ($f(x) \propto 1/(a^2 + (x - b)^2)$ where a and b are constants) which depends upon the damping coefficient, the spring constant and the mass of the cantilever. Values for these quantities are then found by fitting the Lorentzian to experimental data in the absence of any tip-sample interactions. On bringing the tip close to both hard (glass) and soft (polymer brush) surfaces, the resonant peaks were seen to flatten, more so in the case of a soft surface. Lorentzians were fitted to these flattened peaks, with the corresponding adjustments in the fitting-parameters acting as an empirical measure of viscous and elastic coupling in the system.

In order to convert the cantilever deflection measured in experiments into a force requires knowledge of the cantilever spring constant, which usually must be found through calibration methods.

1.1.4 Calibration

Cantilever manufacturers are often unable to provide a precise value for the spring constant, which is central to the use of Hooke's law when converting cantilever deflection into a force. Furthermore, factors such as temperature dependence, structural defects and gold coating change the cantilever's elastic properties from any manufacturer estimates. Consequently, calibration is central to force measurement experiments. A traditional method of Cleveland et al. (1993) involves attaching small masses to the cantilever and recording the change in its resonant frequency. Unfortunately, the resulting spring constant can depend upon the location of the masses along the cantilever and, moreover, this process can also render the cantilever unusable for subsequent experiments.

By examining the elasticity equation which governs cantilever behaviour, efforts have been made theoretically to predict the spring constant. Noting that AFM cantilevers are generally much longer than they are wide, Sader and White (1993) assumed that the leading-order deflection in vacuum involves only transverse bending, with twisting motion appearing as a second-order correction, which is realistic when the cantilever is thin. This resulted in cantilever dynamics governed by the one-dimensional Euler-Bernoulli beam equation at leading order. The spring constant was then given as the strength of the force over the deflection at the point of application (Hooke's law). The three-dimensional elastic plate equations were also considered (again in vacuum), using FEA computations, for both rectangular and V-shaped cantilevers. A FEA computation, taking account of the full three-dimensional geometry of both rectangular and V-shaped cantilevers, was also conducted with the findings casting doubt on the validity of modelling a V-shaped cantilever as two beams (Albrecht et al. 1990). In later work, Sader et al. (1995) provided an expression connecting cantilever the spring constant with its mass and resonant frequency in vacuum. The constant of proportionality con-

necting these quantities was computed numerically, for both rectangular and V-shaped cantilevers, by solving the full elasticity equation, without damping, again using FEA. Estimates for spring constants using this approach showed good agreement with values obtained using the method of Cleveland et al. (1993). The results also demonstrate the effect on the spring constant of positioning calibration masses at different distances from the cantilever tip, which also has implications for colloidal probe experiments (see above). Nonetheless, a drawback of this approach is that it requires knowledge of cantilever mass and resonant frequency in vacuum. Results were also presented which predict the change in resonant frequency due to gold-coating, which appear to agree well with experimental data.

The calibration methods above, which arrive at the spring constant by purely theoretical means, are often hampered in practice by a lack of information about the cantilever's material properties. Combining experimental and theoretical analyses can lead to greater robustness in predictions. Such a calibration method, which enjoys widespread popularity, uses thermal fluctuations of the cantilever. Theoretical analysis of these fluctuations began with the work of Hutter and Bechhoefer (1993), who modelled the cantilever tip as a sphere undergoing harmonic oscillations with average energy given by $\frac{1}{2} k_B \mathcal{T}$ (k_B Boltzmann's constant, \mathcal{T} is temperature), in accordance with the equipartition theorem for a tip in thermal equilibrium. This approach provides an expression for the spring constant in terms of the temperature and the root-mean-square (rms) displacement of the tip, both of which are experimentally measurable quantities. By considering only the tip, however, this model fails to account for the full elastic behaviour of the cantilever itself. This deficiency was addressed by Butt and Jaschke (1995), in the absence of any fluid damping, by expressing the deflection of a rectangular cantilever's as a superposition of all undamped modes. Each undamped mode receives $\frac{1}{2} k_B \mathcal{T}$ by equipartition of energy, which was equated to the total (bending and kinetic) energy for that particular vibrational mode. In doing so, a revised expression for the spring constant was obtained for each mode in terms of the temperature, the eigenfrequency of that mode and mean deflection at the tip, or its derivative. This modal analysis was repeated by Stark et al. (2001) for V-shaped cantilevers, although

the complex geometry meant that eigenmodes had to be computed using FEA.

All of the models mentioned so far neglect hydrodynamic damping. However, from an AFM perspective it is important to take into account the influence of the fluid environment. Functionalising the tip in biological experiments changes the effective spring constant of the cantilever. Calibration must therefore be conducted within the liquid environment, to prevent drying out of the tip, which would again alter the effective spring constant. Elmer and Dreier (1997) modelled a rectangular cantilever as an elastic beam (i.e. one-dimensional deflections only). The cantilever experienced an added mass due to the presence of the fluid, but viscous effects were neglected. A relationship between the resonant frequencies in fluid and vacuum was derived. Consideration of viscous effects came with the work of Sader (1998), who approximated the drag on a thin rectangular cantilever by that exerted on an infinite-length circular cylinder in unbounded fluid, which permits the use of the classical result of Stokes (1851). This is justified for a long, thin cantilever provided that the mode of oscillation is not too high (recent work by Maali et al. (2005) highlights problems with two-dimensional flow models after the fourth harmonic, which they attribute to the non-negligible axial flows). Thermally-excited transverse deflections were written as a sum of all undamped (in vacuo) modes, each weighted according to the effects of fluid damping. The eigenmode amplitudes were once more determined by equipartition of energy. In the limit of small dissipative effects e.g. in gas, the harmonic peaks became distinct and Sader (1998) showed that the thermal spectra can be reduced down to an expression which describes the behaviour of a damped-harmonic oscillator, where there exists a relationship between the experimentally-measurable Q-factor (peak sharpness), fundamental resonant frequency in vacuum, plan-view dimensions (length and width) and the spring constant (Sader 1999).

Strictly speaking, however, some of the $\frac{1}{2}k_B\mathcal{T}$ of thermal energy given exclusively to each cantilever mode by Sader (1998) should go into moving the fluid (Hinch 1975). Furthermore, the analysis made an assumption that the thermal noise was frequency independent, which is untrue when the hydrodynamic drag is unsteady. Time-dependent hydrodynamic drag depends upon the earlier dynamics and this in turn leads to mem-

ory in the Brownian forcing, which is no longer δ -correlated (i.e. it has a frequency-dependent, rather than constant, power spectrum). Despite these issues, Chon et al. (2000) demonstrated that the model of Sader (1998) performs well against experimental data in both air and water. Comparisons were made using the full viscous model, a simple harmonic-oscillator (SHO) model and an approach which takes the immersing fluid to be inviscid. The viscous model was seen to perform well, as was the SHO model when dissipative effects were not too strong but, by contrast, the inviscid model performed poorly. Paul and Cross (2004) offered an alternative approach, however, using the fluctuation-dissipation theorem (Reichl 1987), although no direct comparison was made with the results of Sader (1998). The linear response of a cantilever, after a uniformly applied small force is turned off, was simulated using a computational fluid dynamics (CFD) package, which simultaneously solved for the flow and the dynamics of the cantilever. The sophistication of this package allowed cantilevers with complex geometries, as well as an array of multiple cantilevers, to be investigated. The thermal spectrum of the cantilever's tip was determined by substituting the change in its average position, on removal of the force, into the fluctuation-dissipation theorem. In a companion paper to Sader (1998), Green and Sader (2002) considered torsional oscillations of a thermally driven cantilever which can be coupled to earlier work on transverse oscillations (through the linearity of the governing equations) to describe a clamped thermally-excited cantilever undergoing both transverse and rotational motion. This work finds application in lateral-force experiments where the cantilever is twisted at high frequencies, for example in the study of in-plane surface acoustic wave phenomena. Recognising the need to understand the effect of a nearby boundary, recent follow-up work by Green and Sader (2005)¹ has examined the flow generated by two-dimensional cantilevers oscillating near a wall, using boundary element methods (BEM), considering both translational and torsional oscillations.

¹Some of the issues and methods used in this work were studied in parallel work by Clarke et al. (2005a)

1.2 Unsteady linearized flow

The preceding discussion outlined the influence of hydrodynamics in the AFM. With much still to do in quantifying these effects, we now focus on the pertinent hydrodynamic theory.

In the majority of imaging and force measurement techniques the liquid (of density ρ , viscosity μ and kinematic viscosity $\nu = \mu/\rho$) used within the AFM is incompressible and Newtonian. Let us assume the AFM contains a cantilever with length $2L$, width $2R$ and thickness $2D$, whose tip is deflected with maximum amplitude \mathcal{A} during measurements. The flow is governed by Navier-Stokes equations and by scaling lengths on an appropriate lengthscale \mathcal{L} , velocities and time on typical AFM operating parameters V and \mathcal{T} we are able to assess the relative importance of fluid inertia and viscosity by inspecting the non-dimensional version of these equations

$$\text{St} \frac{\partial \mathbf{U}}{\partial t} + \text{Re} (\mathbf{U} \cdot \nabla \mathbf{U}) = \nabla \cdot \boldsymbol{\sigma}, \quad \nabla \cdot \mathbf{U} = \mathbf{0}, \quad (1.1a)$$

$$\boldsymbol{\sigma} = -IP + \nabla \mathbf{U} + \nabla \mathbf{U}^T. \quad (1.1b)$$

Here \mathbf{U} the fluid velocity, $\boldsymbol{\sigma}$ is the stress tensor (superscript T denotes transpose) and P is the pressure (scaled on $\mu V/\mathcal{L}$). The dimensionless parameters $\text{St} \equiv \mathcal{L}^2 \rho/\mathcal{T} \mu$ and $\text{Re} \equiv V \mathcal{L} \rho/\mu$ are the Strouhal and Reynolds numbers, respectively. When the AFM cantilever operates at a distance \mathcal{H} from a sample surface, it proves useful to define another dimensionless parameter

$$\Delta \equiv \mathcal{H}/L, \quad (1.2)$$

which measures the separation distance between the wall and the cantilever relative to cantilever length.

Table 1.1 provides typical values for these parameters under the various AFM techniques. During dynamic-force (DFS) and tapping-mode (TM-AFM) spectroscopy the dominant length scale \mathcal{L} is the small cantilever–substrate separation distance (about $1\mu\text{m}$), whilst amplitudes \mathcal{A} are in the order of 10nm , much smaller than the cantilever's thickness. During calibration, amplitudes are smaller still, about 0.1nm , since they arise from thermal excitation. The dominant length scale here is the cantilever's length

	\mathcal{L} (cm)	\mathcal{A} (cm)	$1/T$ (s ⁻¹)	V (cm s ⁻¹)	Re	Δ	St
DFS	$\mathcal{H} = 10^{-4}$	10^{-6}	10^2	10^{-4}	10^{-8}	0.01	10^{-4}
TM-AFM	$\mathcal{H} = 10^{-4}$	10^{-6}	10^5	10^{-1}	10^{-3}	0.01	0.1
Calibration	$L = \mathcal{H} = 10^{-2}$	10^{-8}	10^4	10^{-4}	10^{-4}	1	100

TABLE 1.1: Typical operating parameters encountered during dynamic-force spectroscopy (DFS), tapping-mode AFM (TM-AFM) and calibration in water ($\mu/\rho = 10^{-2}\text{cm}^2\text{s}^{-1}$), for a cantilever with width $R = 10^{-3}\text{cm}$, length $L = 10^{-2}\text{cm}$ and thickness $\mathcal{D} = 10^{-4}\text{cm}$ (Santos and Castanho 2004, Chon et al. 2000, Rief et al. 1997).

($O(100\mu\text{m})$). In TM-AFM and calibration the timescale \mathcal{T} is determined by the oscillation frequency, whereas in DFS it is decided by the duration of retraction.

The Reynolds number is seen to be small for all techniques, which allow us to neglect the nonlinear convective term in (1.1), leaving us with the unsteady Stokes equation for linearized viscous flow

$$\text{St} \frac{\partial \mathbf{U}}{\partial t} = -\nabla P + \nabla^2 \mathbf{U}, \quad \nabla \cdot \mathbf{U} = 0. \quad (1.3)$$

For the purposes of describing AFM hydrodynamics, we are especially interested in unsteady linearized flows generated by the motion of bodies and in particular the hydrodynamic drag (scaled on $\mu V \mathcal{L}$), which is defined by

$$\mathbf{D} \equiv \int_{\mathcal{S}} \boldsymbol{\sigma} \cdot \mathbf{n} \, dA, \quad (1.4)$$

i.e. the integral over the body's surface \mathcal{S} of the normal stress component. Since analytic solutions of (1.3) are obtainable for only the most basic body shapes, many workers have also sought to find principles for approximating quantities such as drag from knowledge of behaviour in simpler flows (c.f. Basset forces and Faxen relations in § 1.2.2).

In most cases we shall assume no-slip and no-penetration boundary conditions

$$\mathbf{U}|_{\mathcal{S}} = \mathbf{V}, \quad (1.5)$$

where \mathbf{V} is the velocity of the solid surface \mathcal{S} . However, under certain circumstances (1.5) is inappropriate, as we discuss below.

1.2.1 Fluid–solid interfaces

The no-slip condition was a contentious issue in the early development of fluid mechanics. However, experimental observations appeared to confirm its validity over a vast array of differing situations. Over time, of course, situations arose where the no-slip condition was manifestly incorrect, for example in the study of moving contact-lines, where the no-slip condition leads to a non-integrable stress singularity (Huh and Scriven 1971). The need for more sophisticated boundary conditions when the fluid is non-Newtonian is also well-established (Schowalter 1988).

A popular way of modelling slip uses the Navier-slip condition

$$(\mathbf{U} \cdot \mathbf{t}_k - \mathbf{V} \cdot \mathbf{t}_k)|_S = \mathcal{L}_s (\mathbf{t}_k \cdot \boldsymbol{\sigma} \cdot \mathbf{n})|_S, \quad k = 1, 2 \quad (1.6a)$$

$$\mathbf{U} \cdot \mathbf{n}|_S = \mathbf{V} \cdot \mathbf{n}|_S, \quad (1.6b)$$

(\mathbf{t}_k and \mathbf{n} are the orthogonal unit tangents and normal to S respectively) where \mathcal{L}_s is the slip-length, scaled on the dominant length scale. We should note, however, that there is experimental support for the existence of a non-linear slip–shear relationship (Zhu and Granick 2001), perhaps due to the presence of surface nanobubbles (see below).

With the growing importance of microfluidics, driven by the arrival of micro-devices such as MEMS and the AFM, efforts are being made to evaluate \mathcal{L}_s to a high level of precision. Indirect methods infer the slip from macroscopic flow properties; for example, the flow rate through a channel due to an applied pressure drop (Choi et al. 2003) is a function of slip length. A variation on this idea involves measuring the slip-dependent lubrication forces acting on a body which translates or oscillates near a surface. Force measurements can be made with the surface force apparatus (SFA), where slip lengths of $1\mu\text{m}$ have been recorded for mica coated with a hydrophobic compound (Zhu and Granick 2001) (compared with the no-slip results for untreated mica (Israelachvili 1986b)). Alternatively, several investigations have used the AFM equipped with colloidal-probe at the tip, which have recorded $\text{O}(10\text{nm})$ slip for saline solution over polystyrene (Vinogradova and Yakubov 2003) or glass (Bonaccorso et al. 2002), sucrose solution over silica coated with gold and thiols (Craig et al. 2001, Neto et al.

2003) or silicon (Bonaccorso et al. 2003), propanol over glass (Sun et al. 2002), water over mica/silica (Henry et al. 2004) and various hydrocarbons over treated borosilicate (Cho et al. 2004).

Direct measurements of slip can be made using particle image velocimetry (PIV), which records the change to the velocity field, resulting from finite slip, using small particles as tracers. With this method, slip lengths of up to 50nm were measured for water flowing over glass (Joseph and Tabeling 2005). Other direct methods include fluorescence recovery after photobleaching (FRAP), where focussing a laser on fluorescent probes strips them of their fluorescence and subsequent monitoring of the overall fluorescence then reveals the velocity field. The way in which the probes are illuminated takes advantage of the refractive properties of light travelling from a dense material (e.g. glass coverslip) into a less dense medium (e.g. sample fluid). When the incident angle is larger than a critical value, total internal reflection is possible and light propagates through the fluid parallel to the surface, as evanescent waves. The purpose of generating these evanescent waves is that their depth can be controlled very precisely, thereby reducing the background noise due to reflection off out-of-focus particles and allowing for very localized flowfield measurements. Pit et al. (2000) recorded slip lengths of 175nm for hexadecane over sapphire using this technique. For an entirely different direct approach which uses nuclear magnetic resonance (NMR) see Britton and Callaghan (1997).

Experimental findings all point towards several major factors which determine slip over a solid surface. A rough surface resists fluid motion and an experimental value for no-slip roughness was found to be 6nm (Zhu and Granick 2002). Richardson (1973) showed that roughness can lead to an effective no-slip condition for the bulk flow even when the boundary condition on the scale of the roughness is perfect slip, by recognising that small surface features can exert resistances over relatively large distances. There is speculation as to whether a critical shear rate exists for slip to occur, although Baudry et al. (2001) and others have reported slip over a broad range of flow rates.

The wetting properties of a surface are widely accepted as crucial in determining the slip lengths on a solid surface. Thermodynamic considerations can yield slip-length

predictions, with Tolstoi (1952) predicting zero slip when there is perfect wetting. A different approach uses the fluctuation–dissipation theorem (see § 6), which predicts zero slip for perfect wetting once the surface roughness exceeds the molecular size by a few percent (Bocquet and Barrat 1994). Cottin-Bizonne et al. (2004) have suggested that roughness can cause dewetting between surface aberrations.

A different mechanism for slip was proposed by Vinogradova (1999), who proposed that shear induces vapour bubbles to coalesce and eventually cover the surface, so that the liquid flows over a cushion of gas rather than the solid itself. Experimental support for this hypothesis comes from experiments which showed that slip depends upon the type of gas which saturates a liquid (Granick et al. 2003). In contrast to the perfect-wetting scenario (Richardson 1973), Cottin-Bizonne et al. (2003) suggest that, for partial wetting, rough features can enhance slip by acting as surface nucleation sites for vapour bubbles. Several experimental observations of nanobubbles have been reported recently, including those of Ishida et al. (2000) using the AFM. A theoretical effective slip (slip as inferred indirectly by observation of a macroscopic measurable, rather than by molecular considerations) due to the presence of nanobubbles in a microchannel is computed by Lauga and Stone (2003), who consider a heterogeneously patterned slip/no-slip surface. Understanding the stability of these nanobubbles, however, is an ongoing issue. An increase in roughness could be due to surface contamination and this is offered as an explanation for the noticeable slip during low-shear observed by Cottin-Bizonne et al. (2005) using a highly-sensitive dynamic SFA. These results were in disagreement with the no-slip observations of Zhu and Granick (2001), who conducted a similar experiment but with a surface densely contaminated with platinum nanoparticles. Furthermore, unlike Pit et al. (2000), Cottin-Bizonne et al. (2005) found no slip when the liquid was wetting. This is indicative of the problems preventing a definitive cataloguing of liquid–surface dynamics: seemingly very similar experiments report markedly different results.

In gases the slip length is related to the Knudsen number Kn which is the ratio of the mean-free-path to the dominant flow dimensions. For most practical surfaces, the molecular mean-free-path is comparable in magnitude to the slip-length (Gad-El-Hak

2001) and $\mathcal{L}_s \approx \text{Kn}$. Therefore for an AFM cantilever in air, when operating far from the wall, we estimate Kn to be approximately 0.014 (based on cantilever half-width). Although there is no consensus on an exact figure, no-slip is expected to fail when $\text{Kn} \gtrsim 0.01$ (Roy et al. 2003).

Evidence of finite slip is also confirmed by (computationally very demanding) non-continuum simulations. Molecular dynamics (MD) simulations calculate individual trajectories for a large number ($O(10^4)$) of particles which obey Newton's laws of motion, where the interaction potentials between particles can take a variety of forms (e.g. Lennard–Jones potential). Simulations have shown how the properties of the wall (Thompson and Troian 1997), the liquid density (Koplik et al. 1989) and liquid–solid interactions (Barrat and Bocquet 1999) can all influence slip, though these computations are unable to reproduce experimentally-realizable shear rates due to limitations on the distances and time intervals that are feasible to simulate. Direct simulation Monte Carlo (DSMC) offers an alternative to MD computations and has shown that for a low-density gas ($\text{Kn} \gtrsim 0.1$), the flow model given by (1.3, 1.5) loses its validity not only through high values of slip but also through discrete molecular effects (Gallis and Torczynski 2004). A continuum approach is still possible for $\text{Kn} \lesssim 10$ by replacing Navier–Stokes with the Burnett equation (Agarwal et al. 2001), which is obtained from the Chapman–Enskog expansion of the Boltzmann equations. Beyond $\text{Kn} = 10$, however, discrete simulations are the only option.

All of these investigations therefore point to the fact that, on a sufficiently small scale, the no-slip condition must be interpreted with considerable caution under some circumstances. Foss et al. (2005) covers many the issues described here in more detail.

1.2.2 Steady flow

By and large, research into linearized viscous flow has concentrated on the quasi-steady limit ($\text{St} \ll 1$) where flow is dominated by viscous effects. The work done in this area is far too extensive to be included here as a discussion in its own right, although it contains some directly relevant results and techniques that we shall draw attention to below.

A fundamental issue with the Stokes flow generated by the motion of a body is its singular behaviour at large distances. For body translation, this is most evident in two-dimensions where it is referred to as Stokes' paradox. Here the velocity field exhibits logarithmic growth at infinity. The three-dimensional analogy, Whitehead's paradox, although less marked (flow velocities decay at infinity) nevertheless presents difficulties. For rotational motion the equivalent problem is known as Jeffery's paradox. Oseen (1910) had the first success in tackling these paradoxes by accounting for convective forces (in a linear fashion) in the far field, which was later improved upon through the matched asymptotic analysis of Proudman and Pearson (1957).

For bodies of arbitrary shape, an important general result was derived by Brenner (1964). Using the Lorentz reciprocal theorem (Lorentz 1907)

$$\nabla \cdot [\mu' \mathbf{u}' \cdot \boldsymbol{\sigma} - \mu \mathbf{u} \cdot \boldsymbol{\sigma}'] = 0 \quad (1.7)$$

(where \mathbf{u}' , \mathbf{u} are two independent flows) it was shown that the drag on a body held in an arbitrary flow is related to the traction on the same body under rigid-body motion in quiescent fluid. This relation between incident velocity and force represents one version of the generalised Faxen relations, after Faxen (1924) who found that the force on a sphere of radius a is $6\pi\mu a$ times the average unperturbed surface velocity. Karrila (1988) has since derived an inverse relation which expresses the traction field for rigid body motion from knowledge of the drag in arbitrary flow.

The linearity of (1.3) implies the existence of Green functions (i.e. solutions under δ -function forcing), which in the context of viscous-flow are usually referred to as Stokeslets. From these, further higher-order singularities can be derived. Hasimoto and Sano (1980) compiled a table of the most commonly used fundamental singularities (as well as describing the existence of quasi-steady eddy structures, important for the generation of micro-organism feeding currents (Liron and Blake 1981), as shall be discussed in more detail shortly). These Stokeslets will prove hugely important to our work, not least of all because they yield a boundary-integral flow representation, early examples of which include the works of Williams (1966a) and Youngren and Acrivos (1975). Under this formulation Stokeslets are distributed over all flow

surfaces, except for those upon which the boundary conditions are automatically satisfied by the Stokeslet; a judicious choice of Stokeslets can therefore drastically reduce computational overheads, e.g. when implementing numerical techniques such as boundary-element methods (BEM). In the event of a long and thin body geometry, the boundary-integral representation can be replaced by a distribution of singularities along the body's axis and this approximation is referred to as slender-body theory (see below). Singularity methods extend this idea to a more general class of body shape, by finding an internal distribution of Stokeslets and higher-order singularities which approximately satisfies the surface boundary conditions. An example of this technique is provided by Chwang and Yao-Tsu Wu (1974), who consider the rotational motion of a prolate axisymmetric body using a distribution of singular torques, called rotlets.

Slender bodies

Boundary-integral methods allow the flow generated by the motion of a body to be represented by a surface distribution of singularities (as discussed above). When the body is long and thin, slender-body theory (SBT) offers a further simplification, allowing the flow to be approximated by a one-dimensional distribution of singularities (typically Stokeslets and dipoles) along the body axis (Hancock 1953).

SBT for quasi-steady flow has enjoyed particular success in the study of micro-organism motility in fluid (Brennen and Winet 1977). Early theoretical work utilised resistive-force theory (RFT), a simplification of SBT which yields a local relationship between velocity and force over each segment of the slender body (Gray and Hancock 1955). Although simple, the predictions of RFT applied to modelling simple waves in a flagellum proved remarkably successful in describing the propulsion of sea-urchin spermatozoa. Encouraged by this achievement, Brokaw (1965) used RFT to investigate non-sinusoidal flagella waves, as well as modelling multiple spermatozoa. This was followed by RFT work on helical waves (Chwang and Wu 1971) and very large amplitude waves (Silvestre and Holwill 1972). In their study of sea-urchin spermatozoa, Gray and Hancock (1955) chose resistance coefficients which had a tangential to normal ratio of 0.5. Lighthill (1975) found a relationship between the segment length and the

wavelength of flagellar undulations, resulting in a revised normal–tangent ratio of 0.7. Confusingly, this revised ratio seemed to perform worse against observations of spermatozoa, until it was realised that the presence of the nearby microscopic glass slide was influencing the measurements. The ability of a local boundary to effect micro-organism swimming is now a well-recorded phenomenon, with experimental data (Frymier et al. 1995) clearly demonstrating that bacteria adopt circular trajectories when swimming near a solid surface, which numerical simulations have reproduced, incorporating hydrodynamic wall-effects (Magariyama et al. 2005).

Unfortunately RFT is limited by the difficulty of accounting for the motion of neighbouring sections of the body; the long-range character of quasi-steady flow means that RFT captures only the dominant terms in an asymptotic expansion in powers of $\ln(1/\epsilon)^{-1}$, where $\epsilon \ll 1$ is the body's aspect ratio. Early asymptotic attempts to determine the flow generated by the entire slender body were made by Hancock (1953), yet real understanding and progress came with matched asymptotic analysis; local flows near a segment of a body were matched to a global flow which exploited the slender geometry. The original formulations, developed for rigid axisymmetric bodies with straight (Tillett 1970) and curved axes (Cox 1970, 1971) were later improved by Geer (1976), who derived a uniform asymptotic expression for the flow. Non-axisymmetric rigid bodies (Batchelor 1970) and bodies that could twist and dilate (Keller and Sol 1976) also received attention. However, a particular weakness of SBT is the logarithmic nature of the expansion. Strategies for improving the accuracy of SBT to obtain algebraic accuracy in ϵ include the use of higher-order singularities in the governing integral equation (Johnson 1980). More recent developments in SBT include the incorporation of convective inertial effects (Khayat and Cox 1989, Chadwick 2002).

A slender-body approach for modelling for the swimming motion of a micro-organism with a spherical head and a flagellum was laid out in a series of papers by Higdon (1979a,b,c). Quasi-steady image Stokeslets, designed automatically to satisfy no-slip and no-penetration on the spherical body (see below), were distributed along the flagellum. In the first instance, planar waves were prescribed along the flagellum, later replaced by more realistic helical waves. The overall translation and rotation of the

organism was accounted for by placing a Stokeslet, dipole and rotlet, of unknown strengths, inside the cell body. The strength of these singularities, together with the Stokeslet distribution along the flagellum, were then found by imposing zero net force and net torque conditions. Moreover, by adding a wall and utilising image Stokeslets, it was shown how the development of a toroidal eddy in the flow offers insights into the way in which certain organisms (e.g. flagellate protozoa, such as choanoflagellates) use their flagella to generate feeding currents, once their body is tethered to a solid surface. This subject was revived some time later by Orme et al. (2003), who considered feeding currents generated by helical flagellar waves (not dealt with by Higdon 1979a in connection with feeding currents). Results focused on flow patterns and showed favourable qualitative agreement with the experimental findings of Pettitt (2001). The importance of the cell-body shape on micro-organism mobility was examined by Phan-Thien et al. (1987) who, using a three-dimensional boundary-integral formulation, showed that cell bodies most suited to swimming efficiently have a flattened ellipsoidal shape.

An alternative method by which micro-organisms can propel themselves (e.g. *opalina*) or generate feeding currents (e.g. *vorticella*) involves the beating action of a dense covering of cilia. These hair-like cilia (which are about $10-50\mu\text{m}$ in length and $0.5\mu\text{m}$ in diameter and attached to a nearby surface) beat at frequencies up to 50Hz in metachronal waves (i.e. waves of in-phase beating). This is in contrast to flagellar bundles, which are seen to synchronise their motions. The elongated shape of cilia again make slender-body a natural modelling choice, as shown by Blake (1972) who studied beating waves which move in the direction of the effective stroke (symplectic) and against it (antiplectic). For a single cilium the flow was found to have a two-layer structure. The upper layer only feels a mean flow produced by the fast effective (forward) stroke of a cilium, whereas the lower layer experiences a comparable oscillatory flow generated by the both the effective and (slower) recovery strokes. An array of cilia was modelled by averaging the cumulative influence of each cilium over time and the area over which the cilia are attached. The sheet of fluid which was found to migrate over the beating cilia is central to such physiological processes as transport of mucus in the airways, where it is believed that penetration of the cilia from the periciliary fluid into the mu-

cus layer is essential for effective transport. Further theoretical work in muco-ciliary transport mechanisms includes a SBT study into the effect of cilia penetrating through a fluid–fluid interface (Blake 1984). SBT continues to contribute to biophysics, in studies of flexible biopolymers such as actin (Wiggins et al. 1998) and the coiling of protein filaments during DNA transcription (Wolgemuth et al. 2000).

Another field to profit from slender-body theory is the study of rods falling in fluids, where differences between axial and transverse drag coefficients leads to the lateral drift observed when a rigid rod sediments (Taylor 1969). Linearity and irreversibility of Stokes flow means that the orientation of a rod remains constant during sedimentation in an unbounded fluid. In practice, however, the long-range character of Stokes flow means that the influence of container walls can affect the rod's angle of orientation. Drag coefficients were obtained using a slender-body treatment of the flow due to both horizontally and vertically orientated rods translating with prescribed velocity near a single wall or midway between two parallel walls. Initially this was done for the case where the distance to the wall was much greater than the rod length (De Mestre 1973) and then later for arbitrary separations (Katz et al. 1975). The no-slip and no-penetration conditions were satisfied on both walls simultaneously, using a technique developed by Faxen (1923) for describing the motion of a sphere between walls, rather than by using the method of successive images. In experiments it was found that, for non-horizontal or non-vertical inclination angles, a constant orientation was not maintained during falling motion, as the rod was seen to rotate as well as drift. De Mestre and Russel (1975) treated these rotations theoretically, by looking at rods falling axially and transversely towards horizontal and vertical plane wall. For axial fall parallel to the wall the no-torque condition was seen to lead the rotation of the leading edge away from the wall observed in the experiments of De Mestre (1973). These results are also supported by the experimental work of Trahan and Hussey (1985). Russel et al. (1977) examined the general case of a rod released at an arbitrary angle and allowed to sediment under the influence of gravity, with rotational and translational velocities determined through force balance and no-torque considerations in the slender-body equations. It was seen that lateral drift caused the rod to come into contact with a

vertical wall, where the initial inclination angle determined whether the leading end rotates away from the wall (glancing action) or whether the trailing end rotates (reversing action).

Wall effects

The nature of AFM experiments means that the cantilever usually operates in close proximity to a sample and, therefore, cantilever-generated flow will be influenced by nearby surfaces. Some of the AFM literature discussed above takes account of this fact, in particular drawing upon the result due to Brenner (1962), who solved the quasi-steady flow generated by a sphere translating normally to a plane wall in bispherical coordinates. This investigation was extended by Williams (1966a), who analysed the boundary-integral formulation for the flow produced when a body of arbitrary shape moves near a wall at distances much greater than the body geometry, obtaining approximate force-velocity relationships. Other investigations into quasi-steady wall-effects includes the work of Jeffrey and Onishi (1981) who, using bipolar coordinates, solved the analogous problem in two dimensions, as well as considering rotations. For more complex bodies, singularity-based methods can be adapted to account for the presence of a wall using the method of images. Numerous quasi-steady image systems have been discovered since Lorentz (1896) first calculated the image of a three-dimensional Stokeslet in a plane wall using the reciprocal theorem. Blake (1971), using Fourier transforms, showed that this image system can be neatly expressed by a second Stokeslet, a dipole and a stresslet (a force-doublet). Examples of common image systems include a Stokeslet outside a sphere (Oseen 1927), a rotlet above a plane wall (Blake and Chwang 1974), a Stokeslet inside a cylinder or between parallel planes (Liron and Mochon 1976), a higher-order singularity (Blake 1979) inside an infinite cylinder and a ring of Stokeslets between parallel planes (Liron and Blake 1981). (Some of these compact representations were used in the aforementioned applications of slender-body theory.) A finite number of image singularities, appropriately located, can be used to describe flows of considerable geometric complexity, for example the Stokes flow generated by moving one cylinder inside another (Finn and Cox 2001).

When the distance between the body and the boundary is small, the flow becomes amenable to asymptotic analysis. For the case of infinitely thin plates, of arbitrary shape, in squeezing motion (Kim et al. 2001b) or sliding motion (Kim et al. 2001a) above a plane wall, the flow is determined by matching an inner lubrication region to a quasi-steady outer flow driven by point sources on the wall; the flow around the plate rim which connects these regions is found using complex-variable methods, conformally mapping the flow domain into the upper-half plane.

Despite its ability to accurately determine a huge range of fluid dynamical phenomena there are, naturally, limits on the scope of quasi-steady flow's applicability. Feng and Joseph (1995) provide a nice account of some of the well-documented failings of the quasi-steady predictions, before considering some novel cases (rotation of an ellipsoid in shear flow, sedimentation of multiple cylinders) where flow inertia cannot be ignored. We shall expand on and extend some of these themes below.

1.2.3 Unsteady linearized flow

When a quasi-steady flow is generated by a body which starts from rest, there is a period of unsteady transient behaviour before steady flow is attained. This could be of importance in AFM force measurement experiments, where an initially stationary cantilever generates a flow over a short period of time.

Numerous workers have addressed the problem of the unsteady drag on an isolated body following Stokes' (1851) treatment of a cylinder and sphere oscillating at small amplitude (see Rosenhead 1963). Basset (1888) realised that, by taking an inverse Fourier transform of the oscillatory motion, the general time-dependent drag on a sphere may be decomposed into the steady (Stokes) drag, an added-mass term and a term which is dependent upon the history of the flow, often called the Basset force. A similar decomposition was found for the torque on the sphere due to rotational motion, but only for times much less than the diffusive time-scale (based on sphere radius). This was improved upon by Feuillebois and Lasek (1977) who considered the impulsive (e.g. δ -function in time) rotation of a sphere of radius a using a Laplace transform and were able to write the torque as the steady Stokes couple plus Basset forces for all time. These

history-terms were seen to become $O(\text{Re})$ (i.e. comparable in size to the neglected convective forces) in $O(a/U)$ times (where U is a typical translational velocity). This is in contrast to translational motion, where the Basset forces become this small only over $O(\text{Re}^{-1}a/U)$ times. In further studies, Hocquart and Hinch (1983) found the decay rate of the flow after an impulsive force or couple applied to a centrally-symmetric body.

Lawrence and Weinbaum (1986, 1988) demonstrated that the simple drag decomposition found by Basset (1888) does not carry over to axially translating spheroids, for which the body's non-spherical geometry produces a complicated fourth drag component. Despite its complexity, a good approximation could be made to this additional drag component by taking a suitable linear combination of the Basset force and the first inertial correction to the steady Stokes drag. Although this *ad hoc* approximation was developed from results for axially oscillating spheroids, its applicability has been shown to be quite general. Pozrikidis (1989a) used singularity methods to demonstrate its success in approximating the drag on a transversely oscillating spheroid and Loewenberg (1993) showed that the Lawrence and Weinbaum (1988) prescription could also reliably approximate the drag on an axially or transversely oscillating cylinder, provided that it has moderate aspect ratio.

Smith (1987) examined the evolution of a flow created by impulsively introducing a singularity into the flow for times $t > 0$ (i.e. with the singularity strength given by a Heaviside step function in time) and considered the realisation of a steady state through the act of diffusion alone. The impulsive Stokeslets and rotlets exhibited large-time singularities as a consequence of Stokes' paradox (large-distance singularity) because of the similarity structure of diffusive flow. This time-dependent paradox, like its quasi-steady counterpart, can be resolved by including Oseen-convective terms or, alternatively, by considering the two-dimensional body as a limit of a three-dimensional geometry (Smith 1991). Gavze (1990) conducted further formal work in this area by considering the force on an accelerating body of arbitrary shape, where they report the appearance of an extra drag term when the forcing is changed from impulsive to continuous in time. In addition, they derive some general results regarding the symmetry of resistance tensors for pure translational or rotational motion and investigate how these

tensors couple under combined translation and rotation.

When Avudainayagam and Geetha (1995) studied the linear flow produced by an instantaneously introduced point-force (i.e. strength given by a δ -function in time), this time-dependent Stokes' paradox was not observed when the fluid was initially at rest but re-emerged if a quasi-steady Stokeslet was prescribed as the initial condition. A time-distribution of these instantaneous Stokeslets, together with inviscid singularities, was used to describe arbitrary motion of a cylinder starting from rest. This was solved analytically for one special case, producing a flow with bounded velocity at infinity. A Faxen relation was also derived for arbitrary translations of the circular cylinder in terms of an integral equation.

Bounding the flow with an infinite plane wall also eradicates Stokes' paradox and provides the opportunity to observe flow reversal on the wall. The introduction of a Stokeslet results in shear layers on the wall which expand into the initially irrotational bulk flow. The Stokeslet also causes immediate reversal of the flow from the wall, in contrast to the impulsive rotlet where there is a delay before the onset of reversal (Smith 1987). Although flow reversal is a feature of quasi-steady flow for a rotlet placed above a plane wall (Ranger 1980), it is seen that reversal due to the presence of a Stokeslet is a purely transient phenomenon which decays at large times. Eddy structures formed by flow reversal have also been noted for quasi-steady flows generated by a rotlet in the presence of various other types of boundary. These include a rotlet inside a cylinder (Wannier 1950), a rotlet outside a cylinder (Dorrepaal et al. 1984) and a rotlet between parallel plates (Hackborn 1980). The development of the reversed flow structures from transient beginnings was examined by (Smith 1993). For example, the rotlet inside a cylinder stimulates flow reversal at all distances from the cylinder wall, however at distances less than some critical value these reversals were found to be transitory, decaying at large time. The value of this critical value agreed with the prediction of Wannier (1950) for the formation of a quasi-steady eddy structure.

One specific type of unsteady flow of particular interest in the study of AFM hydrodynamics is that generated by the oscillatory motion of a body and we discuss this in more detail next.

1.2.4 Oscillatory flow

AFM cantilevers in imaging or thermally-driven modes generate oscillatory flows (of frequency ω) and under these circumstances we seek solutions to (1.3) of the form $\mathbf{U}(\mathbf{x}, t) = \text{Re}(\mathbf{u}(\mathbf{x})e^{i\omega t})$, $P(\mathbf{x}, t) = \text{Re}(p(\mathbf{x})e^{i\omega t})$, and choose to scale length on cantilever length L , yielding

$$i\gamma^2 \mathbf{u} = -\nabla p + \nabla^2 \mathbf{u}, \quad \nabla \cdot \mathbf{u} = 0, \quad (1.8)$$

where

$$\gamma = L\sqrt{\rho\omega/\mu}. \quad (1.9)$$

Unsteady inertial forces confine the diffusion of vorticity away from any solid surfaces to a distance of $O(\mathcal{L})$, where $\mathcal{L} = \sqrt{\mu/\rho\omega}$.

Mathematically equivalent to oscillatory Stokes flow, Brinkman's equation is a model for flow in porous media that is valid at low solid volume fraction (Durlinsky and Brady 1987), with \mathcal{L} now interpreted as the Brinkman screening length. This similarity in mathematical structure means that the motion of bodies in a Brinkman medium also have relevance to flows generated by small-amplitude oscillations.

Rotational oscillations

One of the earliest works on rotational oscillatory flow is detailed in Lamb (1932) (pp.642–644) and is concerned with the flow produced in the fluid between two spheres when the inner sphere executes rotational oscillations, which is expressed in terms of spherical harmonics. Other geometries were considered by Kanwal (1955a), who used the Stokes streamfunction to solve the flow due to rotational oscillations of an infinite cylinder, as well as a prolate or oblate spheroid (with a thin disk as a limiting case). Hocquart (1976) calculated the Basset force for the torque experienced by a rotating ellipsoid.

Much research into the flow produced by rotationally oscillating disks has been stimulated by the rotatory oscillating disk viscometer, which measures fluid viscosity via the torque exerted on a disk undergoing rotational oscillations. In the low-frequency

limit, Kanwal (1970) derived the torque on an infinitely-thin disk using results from elasticity theory, whilst Landau and Lifshitz (1959) solved the high-frequency case. An approach to modelling both rotational and translational motions of disks using dual-integral techniques was taken by Zhang and Stone (1998), adapting the quasi-steady formulation of Davis (1993b). The drag was found to consist of Stokes and Basset components alone. Feng et al. (1998a) treated the mathematically equivalent problem of a disk moving in a Brinkman medium.

The above studies consider a disk of infinitesimal thickness, however viscometers have disks with finite depth. In addition to providing a general review of rotatory oscillatory flows, Tekasakul et al. (1998) laid out a boundary-integral formulation for finding the torque on slowly oscillating axi-symmetric bodies, including a finite-thickness disk. An alternative viscometer consists of an oscillating wire grid and this has received theoretical treatment from Davis (1993a).

Singularity methods also provide a means by which oscillatory rotational flow can be analysed, with Shatz (2004) approximating the flow generated by rotations of oblate and prolate spheroids by distributing rotlets along the focal length.

Translational oscillations

The investigations of Kanwal (1955a) not only considered rotational oscillations of axi-symmetric bodies, but also their longitudinal oscillations. In two dimensions, Kanwal (1955b) used elliptic coordinates to express the flow produced by an infinitely thin plate oscillating in unbounded fluid as an infinite series of Matthieu functions.

An alternative approach to the flow produced by an infinite plate was presented by Tuck (1969), who proposed a boundary-integral expression for two-dimensional oscillatory flow in terms of the flow's pressure and streamfunction. This formulation has the advantage that it can describe plates of finite thickness and arbitrary cross section. The BEM computations showed that the drag exerted on the plate bears remarkable similarity to that experienced by a circular cylinder of equivalent width and this was exploited by Sader (1998) in his estimation of the drag on a rectangular AFM cantilever. In earlier work, Williams (1966b) expressed oscillatory viscous flow in boundary-integral

form and obtained the leading-order inertial correction to the quasi-steady drag on an arbitrary accelerating body, qualifying a previously derived expression due to Kanwal (1964) (although the latter had considered the case where both inertial and convective inertia were equally important).

Three-dimensional free-space oscillatory Stokeslets were computed by Pozrikidis (1989a) and used in a singularity method approximation to the flow generated by axial and transverse oscillations of a prolate spheroid. In subsequent work, these Stokeslets were used in boundary-integral expressions for the oscillatory three-dimensional flow (Pozrikidis 1989b), which exploited Lorentz's reciprocal relation (1.7), with \mathbf{u}' as the flow generated by the presence of an oscillatory Stokeslet and \mathbf{u} as the flow generated by the motion of the body. The same approach works in two-dimensions (Avudainayagam and Geetha 1998) using the oscillatory Stokeslets calculated by Avudainayagam and Geetha (1993). The three-dimensional formulation was used to compute the flow generated by oscillating spheroids, dumbbells and biconcave disks (Pozrikidis 1989b), as well as the axial (Loewenberg 1994b) and transverse (Loewenberg 1994a) oscillations of a finite-length cylinder. One of the main features of these results is the appearance of viscous eddies on the surface of the bodies, which eventually detach and dissipate in the bulk flow. At low frequencies of oscillation Smith (1995) analysed this flow reversal in some detail, examining the structure of the transition between two steady flows which occurs when a body changes direction. An asymptotically distinct outer region was discovered at $O(\gamma^{-1/2})$ distances from the body, which sees the body as a three-dimensional Stokeslet, whilst the local flow is quasi-steady except during a change in direction. These regions were matched asymptotically, to describe slow oscillatory flow past any axisymmetric body. In separate analysis, general conditions were obtained for separation of flow on the surface of an axisymmetric body placed in streaming flow.

In two-dimensions, such considerations provide an alternative perspective into the paradoxes of Stokes and Jeffery (see above). Traditionally these paradoxes are resolved by recognising the importance of convective forces in the far field. For slow oscillatory flow ($\gamma \ll 1$), however, Smith (1997) chose to make unsteady inertia dominant over

convection in the far field. In this regime, slowly oscillating flow past a circular cylinder generates eddies which detach into the local flow. These eddies dissipate only in an asymptotic region which lies at $O(\gamma^{-1/2})$ distances from the body, with this transition taking place over an $O((\ln \gamma)^{-1})$ timeframe. The Jeffery paradox was investigated by considering a rotlet outside of a cylinder (Dorrepaal et al. 1984). The outer flow here is more complex, having two distinct outer flows at $O(\gamma^{-1/2})$ and $O((\ln \gamma)^{-1})$ distances. The inner flow is once again quasi-steady for most of the time and a locally generated eddy again collapses in the far-field; however, in this case the process can take longer than an oscillation cycle.

Wall effects

Few studies of oscillatory flows have accounted for the presence of nearby walls. Chu and Kim (2002) determined the oscillatory two-dimensional flow around a semi-infinite plate above a wall by conformally mapping the geometry to the upper-half plane and then solving numerically using finite-differences. In separate work, they extended the dual-integral-equation method of Zhang and Stone (1998) to describe a disk undergoing rotational and translation motions above a plane wall (Chu and Kim 2004). Several other examples can be found in the literature on Brinkman flow. Kim and Russel (1985) examined the flow due to two spheres in a Brinkman medium using the method of reflections and a boundary collocation technique. Feng et al. (1998b) computed the flow due to a translating sphere in the presence of a plane wall, employing a boundary-integral technique that exploits symmetry but requires the solution of integral equations on all solid boundaries. Broday (2002) used a boundary-integral method to determine the drag on a spherical bead near a planar interface between two Brinkman media, while Sugihara-Seki (2004) used a finite-element method to compute the motion of a sphere in a cylindrical tube. The motion of a two-dimensional body in a Brinkman medium near a rigid boundary does not appear to have been studied in any detail.

For oscillatory flows, image methods are less straightforward. As shown by Pozrikidis (1989a) in three dimensions and Chu and Kim (2001) in two dimensions, to satisfy no-slip and no-penetration conditions on a wall, an oscillatory Stokeslet must be sup-

plemented with an image system reflected in the wall plus a distribution of singularities along the wall.

Steady streaming

The linearized momentum equation (1.3) describes the leading-order flow in the limit in which the amplitude of oscillation is small compared to the body diameter. At higher orders, nonlinearities associated with convective inertia lead to steady streaming effects, which produces irreversible migration of fluid particles over time. This phenomenon was reported by Faraday (1831) during his work on vibrating plates and later by Schlichting (1932), who also conducted a theoretical study using boundary-layer theory. Some theoretical work had been done in this area by Rayleigh (1884) but outside the framework of boundary-layer theory. When the viscous length scale is small, the Reynolds stresses in the Stokes layer produce a streaming flow which persists outside of this shear layer. A streaming Reynolds number R_s can be defined for this mean flow which characterizes its behaviour outside of the boundary layer. When $R_s \gg 1$ a secondary-boundary layer forms (Stuart 1966), where migrating fluid particles can collide forming jet-like flow along the axis of oscillation (see Van Dyke 1982). Riley (1967) showed that $R_s \ll 1$ and $R_s = O(1)$ characterize quasi-steady and fully non-linear steady outer flows, respectively. Riley (2001) has compiled a comprehensive review of steady streaming, including streaming in inviscid flows with a free surface and acoustic streaming, where there is apparent slip on the length scale of the boundary-layer thickness.

1.3 Objectives and structure of thesis

The study of biological specimens using the AFM is hampered by the presence of fluid effects, especially in high-speed regimes (e.g. TM-AFM and during calibration). The nature of AFM measurements mean that the sample is often in close proximity to the fast moving components and this increases the influence of hydrodynamic effects still further. We therefore set out to develop techniques which allow us to compute or

approximate these small-scale high-speed flows which are confined by the presence of a nearby boundary; we believe this will find relevance not only with the AFM, but also with respect to a much wider class of micro-devices (e.g. MEMS). Results will seek to quantify the effects on the drag of varying the flow speed and geometry, looking for situations where the simple approaches work well. (Although surface slip discussed in § 1.2.1 is not a major focus of this study, we do briefly consider its effects in Appendix A, for a couple of simple two-dimensional geometries. Also, while recognising that steady streaming is of great theoretical interest, we do not include it in this study.) Then, by coupling the fluid dynamics to solid-body mechanics, we simulate cantilever behaviour and make comparisons with actual experimental results.

As we progress, the flow models shall advance towards more realistic AFM cantilever geometries, starting in chapter 2 with the very general problem of the two-dimensional flow generated by an infinite-length circular cylinder oscillating above a plane wall. Three-dimensional effects are then included in chapter 3, where we consider the flow generated by a finite-length circular-cylinder oscillating above a plane wall, using a novel unsteady slender-body flow approximation. We then extend the hydrodynamics in chapter 4 to flows which are generated by both infinite and finite-length plates with a rectangular cross-sections. Determining the dynamics of a viscously-damped cantilever requires an understanding of the solid-body mechanics and so in chapter 5 we incorporate the hydrodynamics into models describing the elastic behaviour of beams and plates driven sinusoidally. As we have seen, there is much interest in determining the behaviour of thermally-driven cantilevers and this forms the focus of chapter 6, where we compare our theoretical model to experimental data. We draw some overall conclusions and outline possible extensions to this work in chapter 7.

Chapter 2

Flows generated by an infinite-length circular cylinder

We begin by considering an infinitely long cantilever, circular in cross section, which oscillates above a flat, rigid substrate. This simple geometry will provide some early insights into wall effects and form useful validation when dealing with more sophisticated cantilever shapes.

Specifically, we consider the two-dimensional unsteady flow generated by small-amplitude vertical oscillatory motion of a cylinder, whose surface is denoted by S and which has a circular cross-section of radius R , aligned parallel to an infinite rigid horizontal wall. In Cartesian coordinates (x_2, x_3) , the wall lies at $x_3 = 0$ and the centre of the cylinder lies at $(0, \mathcal{H})$ (see figure 2.1*a*). The cylinder oscillates normal to the wall with frequency ω , with an amplitude of oscillation \mathcal{A} , where $\mathcal{A} \ll R$. The two-dimensionality of the geometry means that the focus here is on $\epsilon\gamma = R\sqrt{\rho\omega/\mu}$, $\Delta/\epsilon = (\mathcal{H} - R)/R$. Rescaling lengths on R rather than L recasts (1.8) into the form

$$i(\epsilon\gamma)^2 \mathbf{u} = -\nabla p' + \nabla^2 \mathbf{u}, \quad \nabla \cdot \mathbf{u} = 0, \quad (2.1a)$$

where $p' = \epsilon p$ is the pressure rescaled on $R/\mu V$.

This must be solved subject to no-slip and no-penetration boundary conditions

$$\mathbf{u}|_S = \hat{\mathbf{x}}_3, \quad \mathbf{u}(x_2, 0) = \mathbf{0} \text{ for } -\infty < x_2 < \infty, \quad \mathbf{u} \rightarrow \mathbf{0} \text{ as } |\mathbf{x}| \rightarrow \infty. \quad (2.1b)$$

$(\epsilon\gamma)^{-1}$ is a measure of the distance over which vorticity diffuses during an oscillation relative to the cylinder's diameter. The dimensionless separation parameter, $\Delta/\epsilon = (\mathcal{H} - R)/R$ now measures the minimum distance between S and the wall in terms of the cylinder's radius (see figure 2.1a). We also define a streamfunction ψ by $\mathbf{u} = (\psi_{x_3}, -\psi_{x_2})$, where subscripts x_2 and x_3 denote derivatives. Taking the curl of (2.1a) yields

$$i(\epsilon\gamma)^2 \nabla^2 \psi = \nabla^4 \psi, \quad (2.2a)$$

$$\psi(x_2, 0) = 0, \quad \psi_{x_3}(x_2, 0) = 0, \quad \psi_{x_2}|_S = -1, \quad \psi_{x_3}|_S = 0, \quad \psi \rightarrow 0 \text{ as } |\mathbf{x}| \rightarrow \infty. \quad (2.2b)$$

Symmetry of the flow about $x_2 = 0$ means that we need consider the flow only in the quadrant $x_2 \geq 0, x_3 \geq 0$.

In §2.1 we describe the numerical scheme use to compute the flow generated by a two-dimensional circular cylinder near a wall, followed in §2.2 by numerous asymptotic results used to validate and extend the numerics. The results in §2.3 concentrate on how the vertical component of drag per unit length D_3 (refer to (1.4) where lengths are scaled on R) is influenced by (Δ/ϵ) and $\epsilon\gamma$, with the findings discussed in §2.4. The effect of slip (see §1.2.1) on the drag for an unbounded fluid are presented in Appendix A.1.

2.1 Numerical treatment

When the cylinder is circular, the geometry of the flow lends itself to cylindrical bipolar coordinates (ξ', η') , defined by (Jeffery 1921)

$$x_2 = -\frac{c \sin \xi'}{\cosh \eta' - \cos \xi'}, \quad x_3 = \frac{c \sinh \eta'}{\cosh \eta' - \cos \xi'}, \quad c = \sqrt{(\Delta/\epsilon)((\Delta/\epsilon) + 2)}. \quad (2.3)$$

In this coordinate system, the flow domain in $x_2 \geq 0$ maps to the rectangle $-\pi \leq \xi' \leq 0, 0 \leq \eta' \leq \eta_1 \equiv \cosh^{-1}(1 + (\Delta/\epsilon))$ (see figure 2.1b). However, we gain this finite

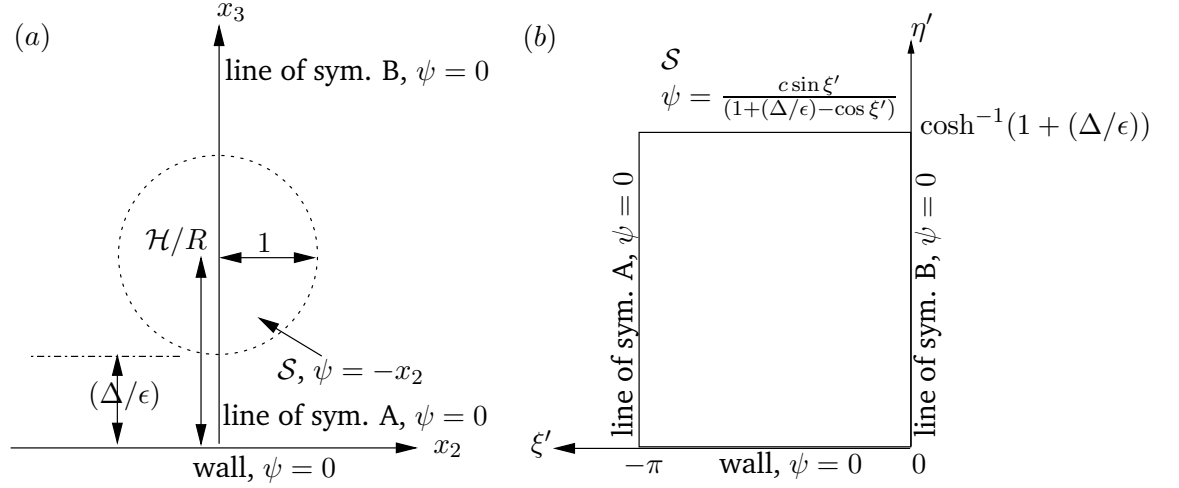


FIGURE 2.1: Geometry of the flow domain for a circular cylinder above a wall (non-dimensional units) in (a) Cartesian coordinates and (b) bipolars (2.3).

rectilinear geometry at the cost of losing separability in our governing equation (2.2a), which becomes

$$i(\epsilon\gamma)^2 c^2 \nabla^2 \psi = \nabla^2 \left((\cosh \eta' - \cos \xi')^2 \nabla^2 \psi \right). \quad (2.4)$$

We discretize (2.4) using a finite-difference scheme on a uniform mesh and solve the resulting linear system of equations by Gaussian elimination. Following Jeffery (1921) we choose to work with $(\cosh \eta' - \cos \xi')\psi/c$ rather than with ψ itself, as this results in a simpler form for the operator and the boundary conditions. As $\epsilon\gamma$ is increased the demand for mesh points also increases, to resolve the boundary layers that arise on the cylinder and wall. We obtained solutions for $\epsilon\gamma \leq 30$ on a 200×200 mesh, with convergence verified on a 350×350 mesh and validation provided by comparison with asymptotic results derived in §2.2.

2.2 Asymptotic treatment

Figure 2.2 charts the distinct asymptotic regions (I–VI) of $(\epsilon\gamma, (\Delta/\epsilon))$ -parameter space for a two-dimensional circular cylinder. In §2.2.1 we treat the case where the distance that vorticity diffuses over one oscillation is much greater than the wall–cylinder separa-

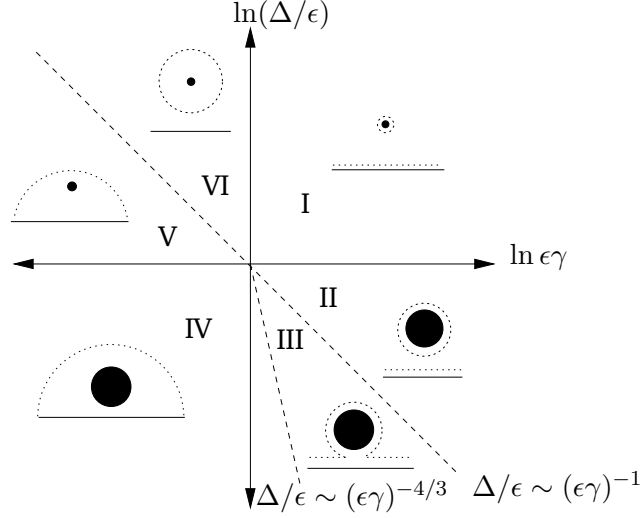


FIGURE 2.2: Asymptotic regions of $(\epsilon\gamma, (\Delta/\epsilon))$ -parameter space for a circular cylinder. A sketch inside each region shows the physical picture, with dotted lines indicating the distance over which vorticity diffuses during one oscillation.

tion ($(\Delta/\epsilon) \ll (\epsilon\gamma)^{-1}$) and wall effects are controlled by viscosity. In §2.2.2 the converse situation is investigated ($(\Delta/\epsilon) \gg (\epsilon\gamma)^{-1}$), where inviscid wall interactions dominate. Finally §2.2.3 describes the transition between these two states ($\Delta\gamma = O(1)$). In the following we denote the boundaries between regions (IV and V, say) as IV/V.

2.2.1 Viscous wall interactions: $\Delta \ll \gamma^{-1}$

Small separations: Region IV, $(\Delta/\epsilon) \ll \min(1, (\epsilon\gamma)^{-4/3})$

When the cylinder is close to the wall (region IV) we can model the flow in the gap between these two surfaces using lubrication theory, approximating the surface of the cylinder with the parabola $x_3 = (\Delta/\epsilon) + (x_2^2/2)$. Rescaling using

$$\begin{aligned} x_3 &= (\Delta/\epsilon) \check{x}_3, \quad x_2 = (\Delta/\epsilon)^{1/2} \check{x}_2, \\ u_2 &= (\Delta/\epsilon)^{-1/2} \check{u}_2, \quad u_3 = \check{u}_3, \quad p = (\Delta/\epsilon)^{-2} \check{p}, \quad \psi = (\Delta/\epsilon)^{-3/2} \check{\psi}, \end{aligned} \quad (2.5)$$

the governing equations for the streamfunction become at leading order

$$\check{\psi}_{\check{x}_3\check{x}_3\check{x}_3} = \check{p}_{\check{x}_2}, \quad \check{p}_{\check{x}_3} = 0, \quad (2.6a)$$

$$\check{\psi}_{\check{x}_2}(\check{x}_2, 0) = 0, \quad \check{\psi}_{\check{x}_3}(\check{x}_2, 0) = 0, \quad \check{\psi}_{\check{x}_2}(\check{x}_2, 1 + \check{x}_2^2/2) = -1, \quad \check{\psi}_{\check{x}_3}(\check{x}_2, 1 + \check{x}_2^2/2) = 0, \quad (2.6b)$$

which yields

$$\check{\psi} = -\frac{2\check{x}_2\check{x}_3^3}{(1 + \frac{1}{2}\check{x}_2^2)^3} + \frac{3\check{x}_2\check{x}_3^2}{(1 + \frac{1}{2}\check{x}_2^2)^2}, \quad \check{p} = -\frac{24}{(2 + \check{x}_2^2)^2}, \quad (2.7)$$

so that

$$D_3 = 3\sqrt{2}\pi(\Delta/\epsilon)^{-3/2} + O((\Delta/\epsilon)^{-1/2}), \quad (2.8)$$

in agreement with Jeffrey and Onishi (1981). The flow outside the gap provides an $O(1)$ drag contribution when $\epsilon\gamma \lesssim 1$. For $1 \ll \epsilon\gamma \ll (\Delta/\epsilon)^{-3/4}$, the leading-order drag outside the lubrication region is $O((\epsilon\gamma)^2)$ but remains sub-dominant to (2.8). We discuss the case in which these contributions become comparable in §2.2.3 below.

Moderate separations: Region IV/V, $(\Delta/\epsilon) = O(1)$, $\epsilon\gamma \ll 1$

When $\epsilon\gamma \ll 1$ and $(\Delta/\epsilon) = O(1)$, (2.1a) reduces to the steady Stokes equations

$$\mathbf{0} = -\nabla p' + \nabla^2 \mathbf{u}, \quad \nabla \cdot \mathbf{u} = 0, \quad (2.9)$$

subject to (2.1b). The steady Stokes' problem of a circular cylinder translating perpendicularly to a horizontal wall was solved as a finite series in bipolar coordinates (2.3) by Jeffrey and Onishi (1981). A more compact form of the solution may be obtained using complex-variable techniques, such as adopted by Finn and Cox (2001), who determined the quasi-steady flow generated by one circular cylinder translating inside another. From their closed-form solution, we take the limit in which the radius of the outer cylinder tends to infinity and recover a solution which reveals the singularity structure of the flow:

$$\psi = \beta_1 \left(\frac{x_2}{2} \ln \frac{r_+}{r_-} - \frac{2cx_2(x_3 + c)}{r_+} + \frac{2c^2x_2}{r_+} \right) + \beta_2 \left(\frac{x_2}{2} \ln \frac{r_-}{r_+} + \frac{2cx_2(x_3 - c)}{r_-} + \frac{2c^2x_2}{r_-} \right), \quad (2.10)$$

where $r_+ = x_2^2 + (x_3 + c)^2$, $r_- = x_2^2 + (x_3 - c)^2$, c is given by (2.3c) and

$$\beta_1 = \frac{c + (\Delta/\epsilon) + 1}{c - (\Delta/\epsilon) - 1} \beta_2, \quad \beta_2 = (c - (\Delta/\epsilon) - 1) \left(2c + (1 + (\Delta/\epsilon)) \ln \left(\frac{1 + (\Delta/\epsilon) - c}{1 + (\Delta/\epsilon) + c} \right) \right)^{-1}. \quad (2.11)$$

Defining

$$\mathbf{M} = \begin{pmatrix} 1 & 0 \\ 0 & -1 \end{pmatrix}, \quad (2.12)$$

(2.10) can be interpreted as a superposition of (i) two Stokeslets within the cylinder at $(0, c)$ of strengths $-\beta_1 \hat{x}_3$ and $\beta_2 \hat{x}_3$, (ii) two image Stokeslets at $(0, -c)$ of strengths $\beta_1 \hat{x}_3$ and $-\beta_2 \hat{x}_3$, (iii) a stresslet at $(0, -c)$ of strength $-c\beta_1 \mathbf{M}$, (iv) a stresslet at $(0, c)$ of strength $c\beta_2 \mathbf{M}$ and (v) dipoles at $(0, -c)$ and $(0, c)$ of strengths $c^2\beta_1 \hat{x}_3$ and $c^2\beta_2 \hat{x}_3$ respectively. This description of the flow in terms of these singularities immediately gives the leading-order drag on the body to be

$$D_3 = (\beta_2 - \beta_1) = -8\pi(1 + (\Delta/\epsilon)) \left(2c + (1 + (\Delta/\epsilon)) \ln \left(\frac{1 + (\Delta/\epsilon) - c}{1 + (\Delta/\epsilon) + c} \right) \right)^{-1}, \quad (2.13)$$

which is the net strength of the Stokeslets inside the cylinder. For $(\Delta/\epsilon) \ll 1$, (2.13) reduces to (2.8). It is instructive to obtain the large- (Δ/ϵ) limit of (2.13) using an independent argument, as follows.

Large separations: Region V, $1 \ll \Delta \ll \gamma^{-1}$

Even though in region V the wall–cylinder separation distance is large, the cylinder oscillates so slowly that vorticity diffuses a distance much greater than the distance to the wall during an oscillation. Thus we expect the cylinder to generate an $O(\ln(\Delta/\epsilon))$ flow at the wall. An image flow of similar magnitude must be present to allow the boundary conditions at the wall to be satisfied. This is determined as follows. Setting $\mathbf{x} = (\Delta/\epsilon)\check{\mathbf{x}}$, $p = (\Delta/\epsilon)^{-1}\check{p}$, $\psi = (\Delta/\epsilon)\check{\psi}$ and $D_3 = (\Delta/\epsilon)^{-1}\check{D}_3$ gives the following form for (2.1a):

$$-\check{\nabla} \check{p} + \check{\nabla}^2 \mathbf{u} = O((\Delta\gamma)^2), \quad \check{\nabla} \cdot \mathbf{u} = 0. \quad (2.14)$$

Since $\Delta\gamma \ll 1$ in region V, we have a quasi-steady flow at leading-order. Suppose a point force is located at $\check{x} = (0, 1)$ of unknown strength $4\pi A$, orientated perpendicular to the wall, on which no-slip and no-penetration are satisfied. Liron and Blake (1981) give the streamfunction for the resulting flow as

$$\check{\psi} = A \left(\check{x}_2 \ln \sqrt{\frac{\check{x}_2^2 + (\check{x}_3 - 1)^2}{\check{x}_2^2 + (\check{x}_3 + 1)^2}} + \frac{2\check{x}_2(\check{x}_3 + 1)}{\check{x}_2^2 + (\check{x}_3 + 1)^2} - \frac{2\check{x}_2}{\check{x}_2^2 + (\check{x}_3 + 1)^2} \right). \quad (2.15)$$

We can identify the singularity structure of (2.15) as comprising Stokeslets of non-dimensional strength $4\pi A\hat{x}_3$ at $(0, 1)$ and $(0, -1)$, a dipole of strength $-4\pi A\hat{x}_3$ at $(0, -1)$ and a stresslet of strength $4\pi AM$ at $(0, -1)$. We now modify (2.15) to produce a flow that satisfies no-slip and no-penetration at the cylinder's surface. The flow near the cylinder is assumed to be a superposition of a Stokeslet, uniform flow and dipole of the form

$$\psi = Bx_2 \ln \sqrt{x_2^2 + (x_3 - 1 - (\Delta/\epsilon))^2} + Cx_2 + Ex_2/(x_2^2 + (x_3 - 1 - (\Delta/\epsilon))^2); \quad (2.16)$$

the boundary conditions on the cylinder surface are satisfied by choosing $C = -1 - B/2$ and $E = B/2$. Using the requirement that the outer flow (2.15) evaluated near the cylinder matches the inner flow (2.16) evaluated far from the cylinder, asymptotic matching shows that

$$B = (\ln(\Delta/\epsilon))^{-1} + (\ln(\Delta/\epsilon))^{-2}(1 - \ln 2) + O((\ln(\Delta/\epsilon))^{-3}), \quad A = (\Delta/\epsilon)B. \quad (2.17)$$

Thus the drag is given by the strength of the Stokeslet inside the cylinder

$$D_3 = \frac{4\pi}{\ln(\Delta/\epsilon)} + \frac{4\pi(1 - \ln 2)}{(\ln(\Delta/\epsilon))^2} + O\left(\frac{1}{(\ln(\Delta/\epsilon))^3}\right), \quad (2.18)$$

in agreement with (2.13) for $(\Delta/\epsilon) \gg 1$. We shall exploit this constructive method again in §2.2.3 below.

2.2.2 Inviscid wall interactions: $\Delta \gg \gamma^{-1}$

Large separations: Regions VI & I, $(\Delta/\epsilon) \gg \max(1, (\epsilon\gamma)^{-1})$

On the region VI/I boundary ($(\Delta/\epsilon) \gg 1$, $\epsilon\gamma = O(1)$) the flow is largely inviscid. The flow must satisfy no-penetration at the wall and (far from the cylinder) can be described

by a dipole at the centre of the cylinder together with its image dipole in the wall. The flow produced by the image dipole is very weak at the cylinder, with velocity of order $(\Delta/\epsilon)^{-2}$, and so the drag is approximately that exerted on an oscillating cylinder in unbounded fluid (Stokes 1851):

$$D_3 = i\pi(\epsilon\gamma)^2 \left(1 + \frac{4K_1(\sqrt{i}\epsilon\gamma)}{\sqrt{i}\epsilon\gamma K_0(\sqrt{i}\epsilon\gamma)} \right) \quad (2.19)$$

subject to an $O(\epsilon^3\gamma^2/\Delta)$ error, due to the generation of a cylinder surface pressure of this size from the image dipole (see Appendix A for the effect of slip on this drag result).

Taking the limit $\epsilon\gamma \ll 1$ in (2.19), we obtain the drag in region VI ($\epsilon\gamma \ll 1$)

$$D_3 = -\frac{4\pi}{\ln \epsilon\gamma} + \frac{4\pi c_0}{(\ln \epsilon\gamma)^2} - \frac{4\pi c_0^2}{(\ln \epsilon\gamma)^3} + \frac{4\pi c_0^3}{(\ln \epsilon\gamma)^4} + O\left(\frac{1}{(\ln \epsilon\gamma)^5}\right), \quad c_0 = \left(\frac{i\pi}{4} + \epsilon_0 - \ln 2\right), \quad (2.20)$$

where $\epsilon_0 \approx 0.57721$ is Euler's constant. When $\epsilon\gamma \gg 1$, (2.19) gives the leading-order drag in region I

$$D_3 = i\pi(\epsilon\gamma)^2 + 4\pi\sqrt{i}\epsilon\gamma + 3\pi + O((\epsilon\gamma)^{-1}), \quad (2.21)$$

provided that $(\Delta/\epsilon) \gg \epsilon\gamma$. When this is the case, the wall-cylinder interaction does not feature in the $O(\epsilon\gamma)$ secondary flow and so the drag is successfully approximated by that exerted on a circular cylinder oscillating in an unbounded fluid. However, if $(\Delta/\epsilon) \ll \epsilon\gamma$ then the secondary $O(\epsilon\gamma)$ flow is described by a collection of inviscid singularities located at the centre of the cylinder, together with their images in the wall. Rather than determine these directly, we use the Fourier-series method outlined below.

Moderate and small separations: Regions I & II, $\epsilon\gamma \gg \max(1, (\Delta/\epsilon)^{-1})$

On the region I/II boundary ($(\Delta/\epsilon) = O(1)$, $\epsilon\gamma \gg 1$) we write

$$p' = (\epsilon\gamma)^2 p^{(0)} + \epsilon\gamma p^{(1)} + \dots, \quad \mathbf{u} = \mathbf{u}^{(0)} + (\epsilon\gamma)^{-1} \mathbf{u}^{(1)} + \dots, \quad (2.22)$$

and (2.1a) implies that

$$i\mathbf{u}^{(0)} = -\nabla p^{(0)}, \quad i\mathbf{u}^{(1)} = -\nabla p^{(1)}, \quad (2.23)$$

where $\mathbf{u}^{(0)}(x_2, 0) = \mathbf{0}$ and $\mathbf{u}^{(0)}|_{\mathcal{S}} = \hat{x}_3$. Thus the primary and secondary flows are both inviscid with viscous effects restricted to thin boundary layers on the solid surfaces. Furthermore, the boundary layers that match to \mathbf{u}_0 determine the boundary conditions for $\mathbf{u}^{(1)}$. The secondary inviscid flow provides an $O(\epsilon\gamma)$ drag contribution, commensurate with that from the boundary layers, which requires its retention.

A Fourier-series solution for the leading-order inviscid flow may be found by mapping the infinite Cartesian flow domain into a finite rectangular domain using bipolar coordinates (2.3) (see Appendix B), giving

$$\psi^{(0)} = 2c \sum_{n=1}^{\infty} e_n \sinh(n\eta') \sin(n\xi'), \quad e_n = \frac{e^{-n\eta_1}}{\sinh(n\eta_1)}, \quad (2.24)$$

where $\eta_1 = \cosh^{-1}(1 + (\Delta/\epsilon))$, from which we determine the slip velocities u_c^s on the cylinder and u_w^s on the wall. Using (2.23a) and (2.24) it is straightforward to show that the pressure is given by

$$p^{(0)} = 2ic \sum_{n=1}^{\infty} e_n \cosh(n\eta') \cos(n\xi'), \quad (2.25)$$

from which the leading-order $O((\epsilon\gamma)^2)$ drag may be determined.

Writing $x_3 = (\epsilon\gamma)^{-1}\tilde{x}_3$, we find the usual Stokes boundary layer on the wall in the form

$$u(x_2, \tilde{x}_3) = u_w^s(x_2) \left(1 - e^{-\sqrt{i}\tilde{x}_3}\right) + O((\epsilon\gamma)^{-1}). \quad (2.26)$$

By transforming into polar coordinates with origin at the cylinder centre

$$x_2 = r \cos \theta, \quad x_3 = 1 + (\Delta/\epsilon) + r \sin \theta \quad (2.27)$$

and rescaling radial distances $r = 1 + (\epsilon\gamma)^{-1}\tilde{r}$, we find a Stokes boundary layer on the cylinder surface

$$u_\theta(\tilde{r}, \theta) = u_c^s(\theta) - (u_c^s(\theta) - \cos \theta) e^{-\sqrt{i}\tilde{r}} + O((\epsilon\gamma)^{-1}), \quad (2.28)$$

where u_θ is the azimuthal component of velocity. The normal boundary-layer velocities drive the secondary $O(\epsilon\gamma)$ inviscid outer flow, imposing upon it the following boundary conditions

$$\psi^{(1)}(1, \theta) = i^{-1/2} (-\cos \theta + u_c^s(\theta)), \quad \psi^{(1)}(x_2, 0) = -i^{-1/2} u_w^s(x_2), \quad (2.29)$$

which correspond to conditions at $\eta' = 0$ and $\eta' = \eta_1$ in bipolar space.

By expressing the boundary conditions (2.29) as a Fourier sine series in bipolar coordinates (see Appendix B), we can write the secondary inviscid flow as

$$\psi^{(1)} = \sum_{n=1}^{\infty} (a_n \cosh n\eta' + b_n \sinh n\eta') \sin n\xi', \quad (2.30)$$

where

$$a_n = \frac{1}{\sqrt{i}} \left[(n-1)e_{n-1} + (n+1)e_{n+1} - 2ne_n \right], \quad (2.31a)$$

$$b_n = \frac{1}{\sqrt{i}} \left[2(n d_n + c) e_n - (d_n - c)(n-1)e_{n-1} - (d_n + c)(n+1)e_{n+1} \right], \quad (2.31b)$$

with $d_n = (2 + (\Delta/\epsilon)) / \tanh n\eta_1$ and c given by (2.3c). The secondary pressure is then

$$p^{(1)} = i \sum_{n=1}^{\infty} (a_n \sinh n\eta' + b_n \cosh n\eta') \cos n\xi', \quad (2.32)$$

which, when combined with (2.25) and (2.28) and converted to polar coordinates, gives the drag

$$D_3 = -(\epsilon\gamma)^2 \int_0^{2\pi} p^{(0)}(\theta) \sin \theta \, d\theta - \epsilon\gamma \int_0^{2\pi} \left(p^{(1)}(\theta) \sin \theta - \sqrt{i} (u_c^s(\theta) - \cos \theta) \cos \theta \right) d\theta, \quad (2.33)$$

where $p^{(0)}$, $p^{(1)}$ and u_c^s are given by (2.25), (2.32) and (B.5a), respectively. We show in §2.3 below how (2.33) matches to (2.21) for sufficiently large (Δ/ϵ) . The small- (Δ/ϵ) limit of (2.33) is discussed in §2.2.3 below.

2.2.3 Viscous/inertial wall interactions: $\Delta\gamma = O(1)$

We now consider situations in which the interaction between the particle and the wall is mediated by both viscous and unsteady inertial effects. This occurs primarily when the parameter $\tau \equiv \Delta\gamma = O(1)$.

Large separations: Region V/VI, $(\Delta/\epsilon) \sim (\epsilon\gamma)^{-1} \gg 1$

Between regions V and VI, the lengthscale for viscous diffusion is comparable to the separation between the cylinder and the wall. As in §2.2.1, we find the flow by se-

quential construction, first introducing an oscillating two-dimensional Stokeslet (Avudainayagam and Geetha 1993), of unknown strength C , combined with a dipole,

$$\psi = C \left(-\frac{1}{r} \left(1 + \frac{2K_1(\sqrt{i\epsilon\gamma})}{\sqrt{i\epsilon\gamma}K_0(\sqrt{i\epsilon\gamma})} \right) + \frac{2K_1(\sqrt{i\epsilon\gamma}r)}{\sqrt{i\epsilon\gamma}K_0(\sqrt{i\epsilon\gamma})} \right) \cos \theta, \quad (2.34)$$

where (r, θ) are polar coordinates centred on the cylinder. As these singular solutions induce non-zero flow at the wall, we must also add their image system (see Appendix C.1)

$$\begin{aligned} \psi_I = C \int_0^\infty \left[-A_1 \left((k+q)e^{-k(x_3+2(\Delta/\epsilon))} - 2ke^{-q(x_3+(\Delta/\epsilon))-(\Delta/\epsilon)k} \right) \right. \\ \left. - \frac{A_2}{i(\epsilon\gamma)^2} \left(\frac{k}{q}(k+q)e^{-q(x_3+2(\Delta/\epsilon))} - 2ke^{-k(x_3+(\Delta/\epsilon))-(\Delta/\epsilon)q} \right) \right] \frac{\sin kx_2}{(k-q)} dk, \end{aligned} \quad (2.35)$$

where $q = \sqrt{i(\epsilon\gamma)^2 + k^2}$, $A_1 = 1 + 2K_1(\sqrt{i\epsilon\gamma})/\sqrt{i\epsilon\gamma}K_0(\sqrt{i\epsilon\gamma})$ and $A_2 = 2/K_0(\sqrt{i\epsilon\gamma})$. At leading order, the image system generates a uniform flow near the cylinder, as can be seen by asymptotically evaluating the integrals in (2.35) to give $\psi_I = Cx_2(\Delta/\epsilon)^{-2}I(\tau, \epsilon\gamma) + O((\Delta/\epsilon)^{-1})$, where

$$\begin{aligned} I(\tau, \epsilon\gamma) = \int_0^\infty \left[-A_1 \left(\frac{u(u+q_2)e^{-2u}}{(u-q_2)} \right) - \frac{A_2}{i(\epsilon\gamma)^2} \frac{u^2(u+q_2)e^{-2q_2}}{q_2(u-q_2)} \right. \\ \left. + 2 \left(A_1 + \frac{A_2}{i(\epsilon\gamma)^2} \right) \frac{u^2 e^{-(u+q_2)}}{(u-q_2)} \right] du \end{aligned} \quad (2.36)$$

and $q_2 = \sqrt{u^2 + \tau^2}$. Consequently, the flow local to the cylinder is given by

$$\psi = C \left(-\frac{1}{r} \left(1 + \frac{2K_1(\sqrt{i\epsilon\gamma})}{\sqrt{i\epsilon\gamma}K_0(\sqrt{i\epsilon\gamma})} \right) + \frac{2K_1(\sqrt{i\epsilon\gamma}r)}{\sqrt{i\epsilon\gamma}K_0(\sqrt{i\epsilon\gamma})} + \frac{I(\tau, \epsilon\gamma)r}{(\Delta/\epsilon)^2} \right) \cos \theta + O((\Delta/\epsilon)^{-1}). \quad (2.37)$$

We can satisfy $\psi = -r \cos \theta$ on \mathcal{S} by setting $C = (1 - (\Delta/\epsilon)^{-2}I(\tau, \epsilon\gamma))^{-1}$. Only the Stokeslet exerts drag on the cylinder and thus the drag is

$$\begin{aligned} D_3 = i\pi C(\epsilon\gamma)^2 \left(1 + \frac{4K_1(\sqrt{i\epsilon\gamma})}{\sqrt{i\epsilon\gamma}K_0(\sqrt{i\epsilon\gamma})} \right) \approx \\ \left(1 - \frac{I(\tau, \epsilon\gamma)}{(\Delta/\epsilon)^2} \right)^{-1} \left(\frac{4\pi}{\ln 2 - \ln(\sqrt{i\epsilon\gamma}) - \epsilon_0} + O((\epsilon\gamma)^2) \right), \end{aligned} \quad (2.38)$$

where, as in §2.2.2, ϵ_0 is Euler's constant. In the limit $\tau \ll 1$ we are able to evaluate the integral $I(\tau, \epsilon\gamma)$ asymptotically, to obtain (see Appendix C.2)

$$D_3 = \frac{4\pi}{(\ln(\Delta/\epsilon) + \ln 2 - 1 - \tau^2/4)} + O((\epsilon\gamma)^2 (\ln(\Delta/\epsilon))^{-1}, ((\Delta/\epsilon)^2 \ln \epsilon\gamma)^{-1}, (\epsilon\gamma)^4), \quad (2.39)$$

with $\tau^2/4$ giving the first inertial correction to the quasi-steady result (2.18) for region V. Conversely, in the limit $\tau \gg 1$, since $I/(\Delta/\epsilon)^2 \propto (\tau^2 \ln \tau)^{-1}$ we see that (2.38) reduces to the region-VI limit (2.19).

Small separations: Region III, $(\epsilon\gamma)^{-4/3} \lesssim (\Delta/\epsilon) \lesssim (\epsilon\gamma)^{-1} \ll 1$

A second interaction between viscous, inertial and wall effects occurs in region III. The boundaries of this region are defined as follows. For $(\Delta/\epsilon) \sim (\epsilon\gamma)^{-1} \ll 1$ (the II/III boundary), the Stokes layers on the cylinder and wall are comparable in thickness to the wall-cylinder spacing. Thus the inner lubrication flow has a mixed viscous-inertial structure over a horizontal length scale $(\Delta/\epsilon)^{1/2}$. However, the drag remains dominated by the $O((\epsilon\gamma)^2)$ inviscid contribution from the outer flow. As (Δ/ϵ) is reduced, the lubrication region develops a nested structure, with a viscous region of width $(\Delta/\epsilon)^{1/2}$ (contributing an $O((\Delta/\epsilon)^{-3/2})$ drag, see (2.8)) lying within a viscous/inertial region of width $(\epsilon\gamma)^{-1/2}$. Once $(\Delta/\epsilon) = O((\epsilon\gamma)^{-4/3})$, the drag from the viscous region becomes comparable with the leading-order inertial drag in the outer region; this defines the III/IV boundary. For $(\Delta/\epsilon) \ll (\epsilon\gamma)^{-4/3}$, we enter region IV and (2.8) dominates.

We derive here an expression connecting the behaviour in regions II and IV. It is sufficient to work along the region II/III boundary, since the nested boundary layer structure in region III is captured implicitly. Along this boundary, we anticipate drag contributions at $O((\epsilon\gamma)^2)$ (inviscid outer), $O((\epsilon\gamma)^{3/2})$ (viscous/inviscid inner) and $O(\epsilon\gamma)$ (viscous outer). Thus both inner and outer regions are needed for a reliable estimate of the drag.

The inviscid flow is found by conformally mapping the outer flow domain, in which the cylinder appears to be in contact with the wall, to an infinite strip, where Fourier

transform methods yield the following streamfunction for the flow (see Appendix D)

$$\psi = 4\pi \int_0^\infty \left(\frac{e^{-2\pi k}}{\sinh 2\pi k} \right) \sinh(2\pi k \eta'') \sin(2\pi k \xi'') dk. \quad (2.40)$$

In the lubrication region, (2.5) yields the following governing equations

$$\check{\psi}_{x_3 x_3 x_3} - i\tau^2 \check{\psi}_{x_3} = \check{p}_{\check{x}_2}, \quad \check{p}_{\check{x}_3} = 0, \quad (2.41a)$$

up to an $O(\Delta/\epsilon)$ correction, subject to the boundary conditions (2.6b), which are satisfied by

$$\check{\psi} = A(\check{x}_2) e^{\sqrt{i}\tau \check{x}_3} + B(\check{x}_2) e^{-\sqrt{i}\tau \check{x}_3} + (\sqrt{i}\tau)^{-2} C(\check{x}_2) \check{x}_3 + (\sqrt{i}\tau)^{-2} E(\check{x}_2). \quad (2.42a)$$

Defining $\kappa = \sqrt{i}\tau (1 + \check{x}_2^2/2)$, the coefficients in (2.42a) are

$$\begin{aligned} A(\check{x}_2) &= \frac{1}{2} \left(\frac{\check{x}_2 (1 - e^{-\kappa})}{\kappa \sinh \tau - 2 \cosh \kappa + 2} \right), & B(\check{x}_2) &= \frac{1}{2} \left(\frac{\check{x}_2 (1 - e^{\kappa})}{\kappa \sinh \kappa - 2 \cosh \kappa + 2} \right), \\ C(\check{x}_2) &= \frac{-(\sqrt{i}\tau)^3 \check{x}_2 \sinh \kappa}{\kappa \sinh \kappa - 2 \cosh \kappa + 2}, & E(\check{x}_2) &= \frac{-(\sqrt{i}\tau)^2 \check{x}_2 (1 - \cosh \kappa)}{\kappa \sinh \kappa - 2 \cosh \kappa + 2}. \end{aligned} \quad (2.42b)$$

For $\tau \ll 1$ with $\check{x}_2 = O(1)$, (2.42) reduces to (2.7).

The leading-order drag in both the inner and outer flows comes from the pressure, whose gradient we now express as a composite expansion. Adding the outer p_θ^O and inner p_θ^I expressions for the pressure gradient, and subtracting off their common expression p_θ^C in the intermediate region between inner and outer, we arrive at the following uniformly valid expression for the pressure gradient on \mathcal{S}

$$p_\theta = (\Delta/\epsilon)^{-2} (p_\theta^I + \tau^2 p_\theta^O - \tau^2 p_\theta^C), \quad (2.43a)$$

where

$$p_\theta^I = (\sqrt{i}\Delta\gamma)^3 \Theta \sinh \alpha (\alpha \sinh \alpha - 2 \cosh \alpha + 2)^{-1}, \quad \alpha = (\sqrt{i}\Delta\gamma) (1 + \Theta^2/2), \quad (2.43b)$$

$$p_\theta^O = 8i\pi^2 \int_0^\infty \left(\frac{k e^{-2\pi k}}{\tanh 2\pi k} \right) \frac{\sin(2\pi k \cos \theta (1 + \sin \theta)^{-1})}{(1 + \sin \theta)} dk, \quad (2.43c)$$

$$p_\theta^C = 2i (\theta + \pi/2)^{-1}, \quad (2.43d)$$

with $\Theta = (\Delta/\epsilon)^{-1/2} (\theta + \pi/2)$. We numerically integrate p_θ for the pressure, which is then used to determine the drag

$$D_3 = 2 \int_0^\pi \left(\int_0^\beta p_\theta \, d\theta \right) \sin \beta \, d\beta. \quad (2.44)$$

We have not included the cylinder boundary layers and secondary inviscid flows in the outer flow, but (2.44) successfully connects the leading-order drag in region II with that in region IV, as demonstrated numerically in §2.3.2 below.

2.3 Results

We now present numerical results for circular cylinders. In §2.3.2 we compare calculations for the drag on a circular cylinder using the scheme outlined in §2.1 with the asymptotic predictions developed in §2.2 in limiting cases.

2.3.1 Streamlines

Figure 2.3 shows two sets of streamlines for a circular cylinder at unit distance from the horizontal wall $x_3 = 0$, each showing the instantaneous behaviour at three distinct times in the oscillation cycle for $(\epsilon\gamma)^2 = 1$ (panels *a-c*) and $(\epsilon\gamma)^2 = 10$ (panels *d-f*). At both frequencies we see that there is an up-down asymmetry in the streamlines induced by the presence of the wall. However, this asymmetry is less pronounced for $(\epsilon\gamma)^2 = 10$, indicating that, as viscous effects become confined to boundary surfaces, wall effects diminish elsewhere in the flow. At $t = 0$ the cylinder passes through its zero-displacement position; as the cylinder changes direction at $t = \pi/2$, closed streamlines are shed from the cylinder's surface. Such flow reversal has been noted in other studies of oscillating bodies (Pozrikidis 1989b; Loewenberg 1994b) in the absence of external boundaries. In the presence of a nearby wall we observe reversal on this external boundary which, at $(\epsilon\gamma)^2 = 10$, occurs fractionally earlier than the reversal on the body's surface.

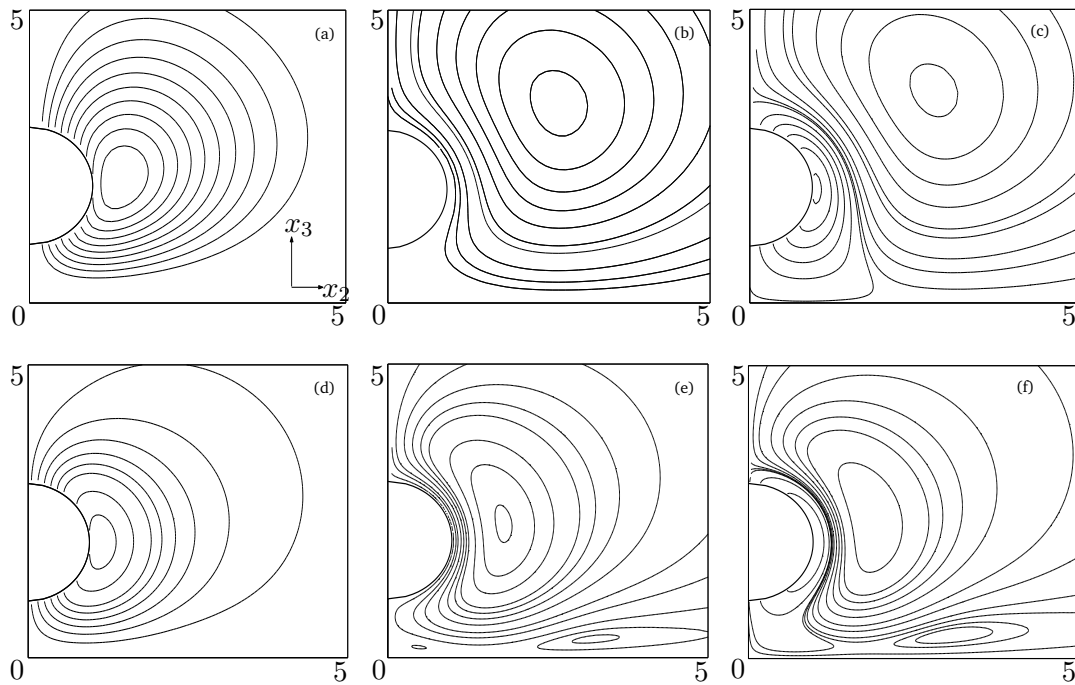


FIGURE 2.3: Streamlines for a circular cylinder when $(\Delta/\epsilon) = 1$ at (a) $t = 0$, (b) $t = \pi/2$, (c) $t = \pi/2 + 0.1$ when $(\epsilon\gamma)^2 = 1$ and at the same times for $(\epsilon\gamma)^2 = 10$, (d, e and f respectively). The wall is located along the x_2 -axis.

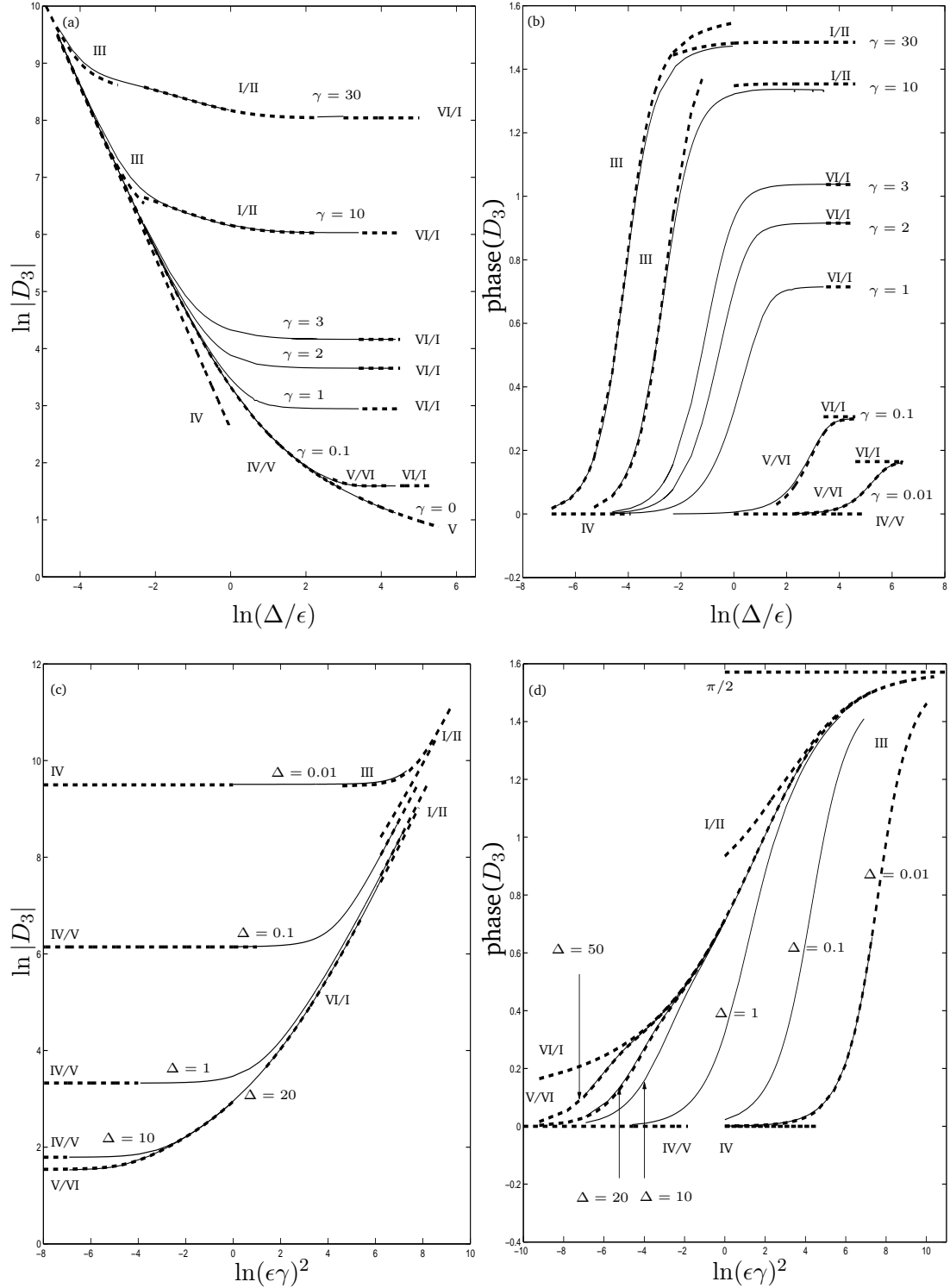


FIGURE 2.4: Modulus (a) and phase (b) of the drag when $(\epsilon\gamma)^2 = 0, 0.1, 1, 2, 3, 10, 30$ plotted over a range of (Δ/ϵ) , together with modulus (c) and phase (d) of the drag when $(\Delta/\epsilon) = 0.01, 0.1, 1, 10, 20$ and 50 , plotted over a range of $(\epsilon\gamma)$. Thin solid lines correspond to numerical computations, whilst asymptotic results for regions I/II (2.33), III (2.44), IV (2.8), IV/V (2.13), V (2.18), V/VI (2.38) and VI/I (2.19) (covering both I & VI) are shown with thicker dashed lines.

2.3.2 Drag

Figure 2.4 presents numerical drag computations for a infinite-length circular cylinder alongside the corresponding asymptotic limits, highlighting the trends in drag as (Δ/ϵ) and $(\epsilon\gamma)$ are varied. For fixed $(\epsilon\gamma)$ (figure 2.4*a, b*), a decrease in (Δ/ϵ) produces a monotonic increase in the drag's modulus and a monotonic decrease in its phase. This change is seen to be a function of $(\epsilon\gamma)$, occurring at lower values of (Δ/ϵ) as $(\epsilon\gamma)$ is increased. The results for fixed (Δ/ϵ) (figure 2.4*c, d*) show that drag's modulus increases and becomes less sensitive to separation distance at larger $(\epsilon\gamma)$. The phase tends towards the inviscid limit of $\pi/2$ as $(\epsilon\gamma)$ is increased, but with the rate of convergence slower at small (Δ/ϵ) .

An important feature of these results is the comprehensive coverage of parameter space provided by the asymptotics, with good continuity between these limits. Thus we are able to make a circuit of parameter space and use the asymptotics to explain the dominant features which contribute to the drag. In figure 2.4(*a, b*) we see that, at sufficiently small separations, steady lubrication theory (region IV, (2.8)) approximates the drag well even at high frequencies. However, as the separation is increased the behaviour of the drag depends upon the frequency. At low frequencies the lubrication approximation to the drag is maintained until the separation increases to roughly one tenth of the cylinder radius, at which point the finite dimensions of the cylinder need to be taken into account. A geometrically more advanced quasi-steady estimate when $(\Delta/\epsilon) = O(1)$ (IV/V, (2.13)) and the steady Stokeslet image system, valid for $(\Delta/\epsilon) \gg 1$ (V, (2.18)), work well until the separation becomes comparable with the viscous length $(\epsilon\gamma)^{-1}$, at which point it breaks down due to the importance of unsteadiness on these length scales. However, here we are able to turn to the unsteady Stokeslet image system (V/VI, (2.38)) which provides accurate estimates for the drag right up to the unsteady unbounded limit (VI/I, (2.19)). Conversely, at high frequencies, steady lubrication theory quickly fails and we require the merged boundary-layer model to describe the transition to inertia-dominated flow (III, (2.44)). This takes us to the limit of inviscid flow, with viscous effects restricted to thin boundary layers on the solid surfaces (I/II, (2.33)). In this limit, even at $O(1)$ separations the presence of the wall is seen to

exert little influence upon the drag, illustrating the weaker nature of the inviscid wall interactions in the high-frequency regime.

An alternative perspective is offered by figure 2.4(*c, d*), which shows how the modulus and phase of the drag both increase monotonically with frequency at fixed separation. At sufficiently large frequencies an inviscid flow plus boundary layers (I/II) provides a good drag estimate, capturing the increase in the drag's modulus at small separations due to the inviscid wall interaction. However, in the small separation limit, as the frequency is reduced, the boundary-layer model rapidly fails and the merged boundary-layer model (III) describes the transition to quasi-steady lubrication flow (IV). At large separations the boundary-layer approximation persists for longer, yet provides a drag which is already estimated well by the unbounded fluid limit (VI/I). As the frequency is decreased still further the distance over which vorticity diffuses grows until becoming comparable with the large wall–cylinder separation, resulting initially in a wall interaction which is governed by unsteady viscous flow and finally in an interaction governed by steady viscous flow; the unsteady Stokeslet image system (V/VI) is seen to capture this transition.

2.4 Discussion

We have examined the influence of a nearby rigid wall on the drag experienced by a two-dimensional oscillating cylinder as a function of the dimensionless oscillation frequency $(\epsilon\gamma)^2$ and the separation distance (Δ/ϵ) . Drag predictions have been obtained numerically, using a finite-difference method accompanied by extensive asymptotic results spanning all extremes of $(\epsilon\gamma, \Delta/\epsilon)$ -parameter space. A summary of our leading-order asymptotic drag expressions for circular cylinders (in dimensional form) has been compiled in Table 2.1.

Our results demonstrate the boundaries in parameter space across which wall effects have a significant leading-order influence on the drag. At low frequencies ($(\epsilon\gamma) \ll 1$), wall effects are important for $(\Delta/\epsilon) = O((\epsilon\gamma)^{-1})$, indicating that wall interactions are significant even at large separation distances (as expected from Stokes' paradox). As

Region	D_3^*
IV	$3\sqrt{2}\pi\mu V(\Delta/\epsilon)^{-3/2}$
IV / V	$\frac{-8\pi\mu V(1 + (\Delta/\epsilon))}{\left(2\sqrt{(\Delta/\epsilon)((\Delta/\epsilon) + 2)} + (1 + (\Delta/\epsilon)) \ln \left(\frac{1 + (\Delta/\epsilon) - \sqrt{(\Delta/\epsilon)((\Delta/\epsilon) + 2)}}{1 + (\Delta/\epsilon) + \sqrt{(\Delta/\epsilon)((\Delta/\epsilon) + 2)}}\right)\right)}$
V	$\frac{4\pi\mu V}{\ln(\Delta/\epsilon)} + \frac{4\pi\mu V(1 - \ln 2)}{(\ln(\Delta/\epsilon))^2}$
V / VI	$\mu V \left(1 - \frac{I((\Delta/\epsilon), R\sqrt{\omega\rho/\mu})}{(\Delta/\epsilon)^2}\right)^{-1} \left(\frac{4\pi}{\ln 2 - \ln(R\sqrt{i\omega\rho/\mu}) - \epsilon_0}\right)$
VI	$-\frac{4\pi\mu V}{\ln R\sqrt{\omega\rho/\mu}} + \frac{4\pi(i\pi/4 + \epsilon_0 - \ln 2)\mu V}{(\ln R\sqrt{\omega\rho/\mu})^2}$
VI / I	$\frac{i\pi R^2\omega\rho V}{\mu} \left(1 + \frac{4K_1(R\sqrt{i\omega\rho/\mu})}{R\sqrt{i\omega\rho/\mu}K_0(R\sqrt{i\omega\rho/\mu})}\right)$
I	$i\pi R^2\omega\rho V/\mu + 4\pi V R\sqrt{i\omega\rho/\mu}$
I / II	See (2.33)
III	See (2.44)

TABLE 2.1: Summary of the leading-order drag (lengths scaled on R) $\text{Re}(D_3^* e^{i\omega t})$ experienced by a circular cylinder of radius R oscillating in a fluid of viscosity μ with frequency ω normally to a wall, with its centre a height \mathcal{H} above the wall. Here $(\Delta/\epsilon) = (\mathcal{H} - R)/R$, $\epsilon_0 \approx 0.57721$ and I is given by (2.36). Regions of parameter space are as shown in figure 2.2.

(Δ/ϵ) is reduced from an initially large value, we demonstrated how wall effects have their first nontrivial impact when $(\Delta/\epsilon) \sim (\epsilon\gamma)^{-1}$ by using the image system of an unsteady Stokeslet to determine the drag on a circular cylinder. This image system is distributed along the wall, thus appearing as an integral in the expression for the drag (2.38). For $(\Delta/\epsilon) = o((\epsilon\gamma)^{-1})$ the flow is dominated by quasi-steady viscous effects: the magnitude of the drag rises rapidly (figures 2.4a, b) until being dominated by viscous lubrication forces as $(\Delta/\epsilon) \rightarrow 0$. At high frequencies $((\epsilon\gamma) \gg 1)$, when viscous effects

are typically confined to thin Stokes layers, the wall has negligible effect on the drag until the separation is very small. For circular cylinders, for $(\Delta/\epsilon) \sim (\epsilon\gamma)^{-1}$, there is the first nontrivial change in the structure of the flow when the Stokes layers on the cylinder and wall overlap. However it is not until $(\Delta/\epsilon) \sim (\epsilon\gamma)^{-4/3}$ that the leading-order drag depends explicitly on (Δ/ϵ) . For sufficiently small (Δ/ϵ) , the quasi-steady lubrication drag dominates that from the outer oscillatory flow.

A key aspect of any experimental system is three-dimensionality, and we should be concerned that our assumption of two-dimensional flow may be unrealistic. Certainly a finite-length circular cylinder, possibly tilted relative to the wall, is capable of generating three-dimensional flows and we shall address this issue next (chapter 3). Also, since AFM cantilevers are rarely circular in practice, later work will examine cantilevers with more typical rectangular cross sections (chapter 4). We shall also treat flexible cantilevers in chapters 5 and 6.

Chapter 3

Flows generated by a finite-length circular cylinder

Although two-dimensional models can capture many important aspects of the flow physics, they are nonetheless limited in their ability faithfully to represent the true hydrodynamics of an AFM cantilever. The ends of the cantilever, which have the potential to influence the overall flow, are neglected, as are any axial flows generated due to non-horizontal orientations. We exploit the elongated geometry of an AFM cantilever and use slender-body theory to approximate the flow.

Let us consider a rigid circular cylinder, of length $2L$ and radius R , that is tilted at an angle α to the horizontal and which oscillates in a plane either vertically or normal to its axis. The cylinder's axis lies a minimum distance \mathcal{H} above a plane horizontal wall (see figure 3.1). The plate's velocity is $\text{Re}(V e^{i\omega t})$, where $V = \mathcal{A}\omega$, ω is the driving frequency and $\mathcal{A} \ll R$ is the amplitude of oscillation. At small amplitudes, rescaling lengths on L , velocities on V and the pressure on $\mu V/L$, the flow is governed by the linearized Navier–Stokes equations (1.8)

$$i\gamma^2 \mathbf{u} = -\nabla p + \nabla^2 \mathbf{u}, \quad \nabla \cdot \mathbf{u} = 0, \quad (3.1a)$$

recalling that $\gamma = L\sqrt{\omega\rho/\mu}$. This must be solved subject to the following boundary

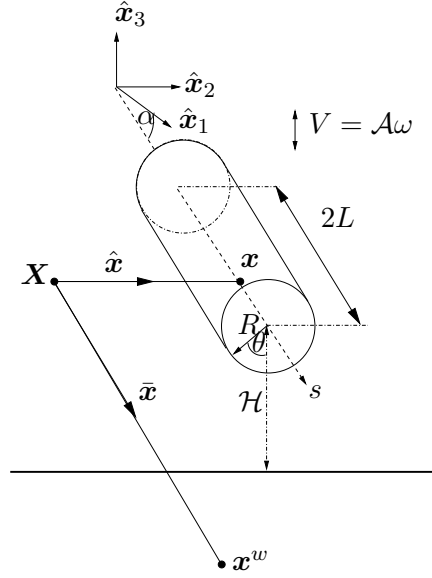


FIGURE 3.1: A cylinder with length $2L$ oscillates either vertically or normal to its axis with frequency ω and amplitude \mathcal{A} above a plane wall ($x_3 = 0$). The cylinder axis lies a minimum distance \mathcal{H} from the wall.

conditions, expressed in Cartesian coordinates (x_1, x_2, x_3)

$$\mathbf{u} \cdot \mathbf{d} = \mathbf{d}, \quad \mathbf{u}(x_1, x_2, 0) = \mathbf{0}, \quad \mathbf{u} \rightarrow \mathbf{0} \text{ as } |\mathbf{x}| \rightarrow \infty \text{ for } x_3 \geq 0. \quad (3.1b)$$

Because the boundary conditions are linearized we may take the cylinder surface \mathcal{S} to be fixed. When the cylinder oscillates normal to its axis $\mathbf{d} = \hat{\mathbf{n}} \equiv (\sin \alpha, 0, \cos \alpha)$ and for vertical motion $\mathbf{d} = \hat{\mathbf{x}}_3 \equiv (0, 0, 1)$. The wall lies along $x_3 = 0$. The problem is characterized by three dimensionless geometric parameters, the minimum wall-cylinder separation $\Delta = (\mathcal{H} - R)/L$, the aspect ratio $\epsilon = R/L \ll 1$ and the tilt angle α . \mathcal{S} is then parameterized using dimensionless cylindrical polar coordinates (s, ϵ, θ) as

$$\mathbf{x} = (s \cos \alpha + \epsilon \sin \theta \sin \alpha) \hat{\mathbf{x}}_1 + \epsilon \cos \theta \hat{\mathbf{x}}_2 + (\Delta - s \sin \alpha - \epsilon \sin \theta \cos \alpha) \hat{\mathbf{x}}_3 \quad (3.2)$$

for $\mathbf{x} \in \mathcal{S}$ and where $-1 \leq s \leq 1$ is a coordinate along the cylinder axis. We seek the leading-order flow in the limit $\epsilon \rightarrow 0$ with γ , Δ and α fixed.

In a slender-body formulation, the velocity at a point \mathbf{X} in the flow may be approx-

imated by the integral (c.f. Blake 1974)

$$u_i(\mathbf{X}) = \frac{1}{8\pi} \int_{-1}^1 [S_{ij}^w(\mathbf{x}, \mathbf{X}; \gamma, \Delta) f_j(\mathbf{x}; \gamma, \Delta) + 2d_k Q_{ik}(\hat{\mathbf{x}})] ds, \quad (3.3)$$

where $\mathbf{x}(s)$ lies on the cylinder axis and $\hat{\mathbf{x}} = \mathbf{x} - \mathbf{X}$. S_{ij}^w and Q_{ik} are the three-dimensional oscillatory Stokeslet (accounting for the presence of the wall) and free-space potential dipole, respectively, and $\mathbf{f}(\mathbf{x}; \gamma, \Delta)$ is an unknown Stokeslet distribution (scaled on μV). Letting $\mathbf{X} \in \mathcal{S}$, where \mathbf{u} is prescribed, yields a first-kind integral equation for the Stokeslet distribution. The drag (1.4) due to this singularity distribution is given by Pozrikidis (1989a) to be $\mathbf{D} = \int_{-1}^1 \mathbf{f}(s) ds - i\gamma^2 \int_{V_p} \mathbf{u} dV$, where V_p is the volume of the body and \mathbf{u} is an internal flow which satisfies the surface boundary conditions (3.1b).

The free-space dipole and oscillatory Stokeslet are (Pozrikidis 1989a)

$$S_{ij}(\hat{\mathbf{x}}; \gamma) = A(\hat{r}; \gamma) \frac{\delta_{ij}}{\hat{r}} + B(\hat{r}; \gamma) \frac{\hat{x}_i \hat{x}_j}{\hat{r}^3}, \quad (3.4a)$$

$$Q_{ij}(\hat{\mathbf{x}}) = -\frac{\delta_{ij}}{\hat{r}^3} + 3\frac{\hat{x}_i \hat{x}_j}{\hat{r}^5}, \quad (3.4b)$$

respectively, where $\hat{r} = |\hat{\mathbf{x}}|$ and

$$A(\hat{r}; \gamma) = 2e^{-\sqrt{i}\gamma\hat{r}} \left(1 + \frac{1}{\sqrt{i}\gamma\hat{r}} - \frac{i}{\gamma^2\hat{r}^2} \right) + \frac{2i}{\gamma^2\hat{r}^2}, \quad (3.4c)$$

$$B(\hat{r}; \gamma) = -2e^{-\sqrt{i}\gamma\hat{r}} \left(1 + \frac{3}{\sqrt{i}\gamma\hat{r}} - \frac{3i}{\gamma^2\hat{r}^2} \right) - \frac{6i}{\gamma^2\hat{r}^2}. \quad (3.4d)$$

For $\gamma \ll 1$, we recover the quasi-steady Stokeslet

$$S_{ij} = \frac{\delta_{ij}}{\hat{r}} + \frac{\hat{x}_i \hat{x}_j}{\hat{r}^3} + O(\gamma). \quad (3.5)$$

Pozrikidis (1989a) has also determined the three-dimensional oscillating Stokeslet which satisfies no-slip and no-penetration on a plane wall at $x_3 = 0$

$$S_{ij}^w(\mathbf{x}, \mathbf{X}; \gamma, \Delta) = S_{ij}(\hat{\mathbf{x}}; \gamma) - S_{ij}(\bar{\mathbf{x}}; \gamma) + \Lambda_{ij}(\mathbf{x}, \mathbf{X}; \gamma, \Delta), \quad (3.6)$$

where $\bar{\mathbf{x}} = \mathbf{x}^w - \mathbf{X}$ and \mathbf{x}^w is the image of \mathbf{x} in the plane $x_3 = 0$ (figure 3.1). The wall-interaction tensor Λ_{ij} involves integrals over the wall,

$$2\pi\gamma^4 \Lambda_{i3}(\mathbf{x}, \mathbf{X}; \gamma, \Delta) = (\delta_{i3}\partial_k\partial_k - \partial_i\partial_3) \Sigma_1(\mathbf{x}, \mathbf{X}; \gamma), \quad (3.7a)$$

$$2\pi\gamma^4 \Lambda_{ij}(\mathbf{x}, \mathbf{X}; \gamma, \Delta) = \partial_j [\partial_i \Sigma_2(\mathbf{x}, \mathbf{X}; \gamma) + (\delta_{i3}\partial_k\partial_k - \partial_i\partial_3) \Sigma_3(\mathbf{x}, \mathbf{X}; \gamma)] \quad (3.7b)$$

where $\partial_k \equiv \partial/\partial x_k$, for $i, k = 1, \dots, 3$ (sum over k) and $j = 1, 2$ with

$$\Sigma_1(\mathbf{x}, \mathbf{X}; \gamma) = \int_0^\infty b(a+b) \left[\left(1 - e^{(a-b)X_3}\right) e^{-ax_3} + \left(1 - e^{(b-a)X_3}\right) e^{-bx_3} \right] J_0(b\rho) db, \quad (3.7c)$$

$$\Sigma_2(\mathbf{x}, \mathbf{X}; \gamma) = \int_0^\infty a(a+b) \left(1 - e^{(b-a)X_3}\right) e^{-bx_3} J_0(b\rho) db, \quad (3.7d)$$

$$\Sigma_3(\mathbf{x}, \mathbf{X}; \gamma) = \int_0^\infty (a+b) \left(1 - e^{(a-b)X_3}\right) e^{-ax_3} J_0(b\rho) db \quad (3.7e)$$

where $a^2 = b^2 + i\gamma^2$, $\rho = \sqrt{\hat{x}_1^2 + \hat{x}_2^2}$ and J_0 is a Bessel function of the first kind. Substituting (3.6) into (3.3) yields our unsteady slender-body theory (USBT) description of the flow.

The coefficients d_k in (3.3) must be chosen to reflect the fact that the prescribed motion at $\mathbf{X} \in \mathcal{S}$ should depend only upon $\mathbf{X} \cdot \mathbf{t}$, where $\mathbf{t} = (\cos \alpha, 0, -\sin \alpha)$ is the unit vector along the cylinder's axis. In other words, any θ -dependence (see figure 3.1) about the axis due to the Stokeslets must be cancelled out (to leading order in ϵ) by the dipoles. By expressing a surface point using polar coordinates (3.2), θ -dependence arises from the presence of $\epsilon \cos \theta$, $\epsilon \sin \theta$ terms in the dipole, Stokeslet and image Stokeslet numerators (3.4a–c) and (3.7c–e). However as long as $\Delta \gg \epsilon$ the θ -dependent terms in the image Stokeslets (3.6, 3.7) are negligible. Furthermore, since the θ -dependence about an axial point is a local phenomenon, $f_j(s)$ can be approximated by its value at that axial point. A local analysis for quasi-steady Stokeslets (3.5) and dipoles (Hancock 1953, Higdon 1979b) shows that their respective θ -dependence can be cancelled out by setting

$$2d_k = a_{kj} f_j, \text{ where } a_{kj} \equiv -\frac{1}{2}\epsilon^2 (\delta_{kj} - t_k t_j) \quad (3.8)$$

(up to an error which is algebraically small in ϵ). Since this analysis is local about a given axial point, where the oscillatory Stokeslet reduces to (3.5), (3.8) also proves suitable for an unsteady formulation.

In addition to the constraint $\Delta \gg \epsilon$, there is also an upper bound to the frequencies which can be explored using (3.3). This can be seen by recalling that boundary-integral methods offer an exact representation of the flow through a surface distribution of Stokeslets. Under these circumstances \hat{r} measures the distance from a point in the flow

to a surface point \mathbf{X} . This differs in value from the distance to the axis point with coordinate $s = \mathbf{X} \cdot \mathbf{t}$ (see figure 3.1) by only an $O(\epsilon)$ amount. Therefore we can expand the surface oscillatory Stokeslets (3.4–3.6) about the cylinder axis, resulting in an axial distribution of Stokeslets at leading-order plus higher-order singularities at $O(\max(\epsilon, \gamma\epsilon))$. We expect $O(\gamma\epsilon)$ errors due to the neglect of the remaining higher-order singularities (see (3.4)). Their contribution will be negligible, leaving the flow well-described by (3.3), provided that $\gamma \ll \epsilon^{-1}$, i.e. when viscous boundary-layers are much thicker than the cylinder radius. This also ensures that the dipoles operate effectively via (3.8) and that the drag can be approximated by an integral of the Stokeslet distribution alone, $\mathbf{D} = \int_{-1}^1 \mathbf{f}(s) ds$.

3.1 Numerical treatment

We solve (3.3) numerically by discretizing the cylinder axis $-1 \leq s \leq 1$ into N equally-sized elements consisting of the closed intervals $s_m = [(2(m-1)/N) - 1, (2m/N) - 1]$ with mid-point \mathbf{x}_m ($m = 1, \dots, N$), and assume that each component of the Stokeslet distribution and prescribed velocity is uniform across each element. We then define

$$\mathbf{F} = (f_1(\mathbf{x}_1), f_2(\mathbf{x}_1), f_3(\mathbf{x}_1), \dots, f_1(\mathbf{x}_N), f_2(\mathbf{x}_N), f_3(\mathbf{x}_N)), \quad (3.9a)$$

$$\mathbf{V} = (u_1(\mathbf{X}_1), u_2(\mathbf{X}_1), u_3(\mathbf{X}_1), \dots, u_1(\mathbf{X}_N), u_2(\mathbf{X}_N), u_3(\mathbf{X}_N)), \quad (3.9b)$$

where \mathbf{X}_m is a surface point that satisfies $\mathbf{X}_m \cdot \mathbf{t} = \mathbf{x}_m \cdot \mathbf{t}$. Equation (3.3) then produces the linear system ($\alpha', \beta = 1 \dots 3N$)

$$V_{\alpha'} = G_{\alpha'\beta} F_{\beta}, \quad G_{\alpha'\beta} = \frac{1}{8\pi} \int_{s_m} [S_{ij}^{vw}(\mathbf{x}_M, \mathbf{X}_M; \gamma, \Delta) + a_{kj} Q_{ik}(\hat{\mathbf{x}}_M)] ds, \quad (3.10)$$

($\hat{\mathbf{x}}_M = \mathbf{x}_M - \mathbf{X}_M$) where $1 \leq i, j \leq 3$ and $1 \leq m, M \leq N$ are given through $\alpha' = 3k' + i$, $\beta = 3k'' + j$ and $\alpha' = 3(M-1) + h'$, $\beta = 3(m-1) + h''$ (for $0 \leq k', k'' \leq N-1$ and $1 \leq h', h'' \leq 3$). Determining $G_{\alpha'\beta}$ involves evaluating the integrals which contain image Stokeslets S_{ij}^{vw} that are computed by taking $\Sigma_i(\mathbf{x}, \mathbf{X}; \gamma)$ derivatives (3.7c–e) as specified by (3.7a, b) and then numerically integrating over b . The system (3.10) is then solved by Gaussian elimination for the unknown distribution vector \mathbf{F} using $N = 60$ axial elements, with convergence verified using $N = 100$.

3.2 Asymptotic treatment

We can also solve (3.3) using techniques which have proved effective in the quasi-steady case (Batchelor 1970, Blake 1974). This approach exploits the existence of an approximately local relationship between the force and velocity at any point along the body axis. The USBT formulation (3.3), on the other hand, takes account of non-local effects arising from the body's extended geometry, as well as the influence of flow inertia. An iterative process can be derived which extracts resistive-force theory (RFT) and its unsteady non-local corrections from (3.3).

To this end, we take a frame of reference where the cylinder lies horizontally and the wall is tilted, accounted for by the Stokeslet image system. In a cylindrical polar coordinate system (s, r, θ) orientated along the cylinder axis (see figure 3.1), surface points (ξ, ϵ, θ) and axial points are given by

$$\mathbf{X} = \xi \hat{\mathbf{x}}_1 - \epsilon \sin \theta \hat{\mathbf{x}}_2 + (\Delta - \cos \theta) \hat{\mathbf{x}}_3, \quad \mathbf{x} = s \hat{\mathbf{x}}_1 + \Delta \hat{\mathbf{x}}_3, \quad (3.11a)$$

respectively, with image $\mathbf{x}^w = s \hat{\mathbf{x}}_1 - \Delta \hat{\mathbf{x}}_3$. Hence (for $-1 \leq \xi \leq 1$, $-1 \leq s \leq 1$)

$$\hat{\mathbf{x}} = (s - \xi) \hat{\mathbf{x}}_1 + \epsilon \sin \theta \hat{\mathbf{x}}_2 + \epsilon \cos \theta \hat{\mathbf{x}}_3, \quad (3.11b)$$

$$\bar{\mathbf{x}} = (s - \xi) \hat{\mathbf{x}}_1 + \epsilon \sin \theta \hat{\mathbf{x}}_2 - (2\Delta - \epsilon \cos \theta) \hat{\mathbf{x}}_3. \quad (3.11c)$$

Anticipating a local relationship between force and velocity, we rewrite (3.3–3.7) as

$$8\pi u_i(\xi) = I_{ij}(\xi; \gamma) f_j(\xi; \gamma, \Delta) + T_i(\xi, \mathbf{f}; \gamma) + W_i(\xi, \mathbf{f}; \gamma, \Delta), \quad (3.12a)$$

where

$$I_{ij}(\xi; \gamma) \equiv \int_{-1}^1 (S_{ij}(\hat{\mathbf{x}}; \gamma) + a_{kj} Q_{ik}(\hat{\mathbf{x}})) \, ds, \quad (3.12b)$$

$$T_i(\xi, \mathbf{f}; \gamma) \equiv \int_{-1}^1 (S_{ij}(\hat{\mathbf{x}}; \gamma) + a_{kj} Q_{ik}(\hat{\mathbf{x}})) (f_j(s) - f_j(\xi)) \, ds, \quad (3.12c)$$

$$W_i(\xi, \mathbf{f}; \gamma, \Delta) \equiv \int_{-1}^1 (\Lambda_{ij}(\mathbf{x}, \mathbf{X}; \gamma, \Delta) - S_{ij}(\bar{\mathbf{x}}; \gamma, \Delta)) f_j(s) \, ds. \quad (3.12d)$$

S_{ij} , Λ_{ij} are given in (3.4) and (3.7), respectively. The basis of RFT comes from the fact that the integrands in (3.12) take their largest values close to ξ and their integrated

contributions (provided ξ is not too close to ± 1) are

$$\begin{aligned} \int_{\xi-\delta}^{\xi+\delta} S_{ij}(\hat{\mathbf{x}}; \gamma) \, ds &= O(\ln \epsilon), & \int_{\xi+\delta}^1 a_{kj} Q_{ik}(\hat{\mathbf{x}}) \, ds &= O(\epsilon^2), \\ \int_{\xi+\delta}^1 S_{ij}(\hat{\mathbf{x}}; \gamma) \, ds &= O(1), & \int_{\xi-\delta}^{\xi+\delta} a_{kj} Q_{ik}(\hat{\mathbf{x}}) \, ds &= O(1), \end{aligned} \quad (3.13)$$

($\epsilon \ll \delta \ll 1$) when $i = j$ and similarly for the $(-1, \xi - \delta)$ intervals. The off-diagonal contributions $i \neq j$ are at most $O(\epsilon)$. Although the Stokeslet integral over $[\xi - \delta, \xi + \delta]$ is $O(\ln \epsilon)$, the θ -dependent terms make only an $O(1)$ contribution and can therefore be cancelled by the $O(1)$ dipole contributions, thus leaving I_{ij} independent of θ to leading order in ϵ .

Over $O(\delta)$ intervals about ξ , $f_j(s; \gamma, \Delta) - f_j(\xi; \gamma, \Delta) = O(\delta)$ and so from (3.13) the T_i will not exhibit any significant θ dependence and will make at most an $O(1)$ contribution via the outer intervals. This is sub-dominant to the $O(\ln \epsilon)$ terms in I_{ij} , which therefore controls the local velocity–force relationship. As W_i terms depend upon the cylinder–wall distance these too will be sub-dominant to I_{ij} and are θ -independent provided $\Delta \gg \epsilon$. Detailed calculations (see Appendix E) reveal

$$8\pi u_i(\xi) = q_i^{-1} f_i(\xi; \gamma, \Delta) (-2 \ln \epsilon + H_i(\xi; \gamma)) + \mathcal{T}_i(\xi, f_i; \gamma) + W_i(\xi, \mathbf{f}; \gamma, \Delta) \quad (3.14)$$

(no sum over i , with $q_i \equiv \frac{1}{2}(1 + \delta_{i2} + \delta_{i3})$ and subject to $O(\epsilon \ln \epsilon)$ errors) where

$$\begin{aligned} H_i(\xi; \gamma) \equiv n_i \left[\frac{e^{-\sqrt{i}\gamma(1-\xi)}}{\sqrt{i}\gamma(1-\xi)} + \frac{e^{-\sqrt{i}\gamma(1+\xi)}}{\sqrt{i}\gamma(1+\xi)} - \frac{i(e^{-\sqrt{i}\gamma(1-\xi)} - 1)}{\gamma^2(1-\xi)^2} - \frac{i(e^{-\sqrt{i}\gamma(1+\xi)} - 1)}{\gamma^2(1+\xi)^2} \right] \\ - \text{Ei}(\sqrt{i}\gamma(1-\xi)) - \text{Ei}(\sqrt{i}\gamma(1+\xi)) - 2\epsilon_0 - 2 \ln \sqrt{i}\gamma + \ln 4, \end{aligned} \quad (3.15)$$

with $n_i \equiv (2\delta_{i1} - 1)$, $\epsilon_0 \approx 0.5772$ (Euler's constant) and $\text{Ei}(z) \equiv \int_1^\infty t^{-1} e^{-tz} \, dt$ is the exponential integral. Also

$$\begin{aligned} \mathcal{T}_i(\xi, f_i; \gamma) \equiv 2(1 - \delta_{i1}) \int_{-1}^1 \frac{e^{-\sqrt{i}\gamma|s-\xi|}}{|s-\xi|} (f_i(s; \gamma, \Delta) - f_i(\xi; \gamma, \Delta)) \, ds \\ + 2(1 - 3\delta_{i1}) \int_{-1}^1 \left(\frac{e^{-\sqrt{i}\gamma|s-\xi|}}{\sqrt{i}\gamma|s-\xi|^2} - \frac{i(e^{-\sqrt{i}\gamma|s-\xi|} - 1)}{\gamma^2|s-\xi|^3} \right) (f_i(s; \gamma, \Delta) - f_i(\xi; \gamma, \Delta)) \, ds \end{aligned} \quad (3.16)$$

(no sum over i) with the second integral defined in the Cauchy-principal-value sense. The dominant term in I_{ij} in (3.14) is $O(\ln \epsilon)$ and so by expanding \mathbf{f} in powers of $1/\ln \epsilon$ as

$$\mathbf{f}(\xi; \gamma, \Delta) = (\ln \epsilon)^{-1} \mathbf{f}^{(0)}(\xi) + (\ln \epsilon)^{-2} \mathbf{f}^{(1)}(\xi; \gamma, \Delta) + \dots, \quad (3.17a)$$

the leading-order quasi-steady RFT solution

$$f_i^{(0)}(\xi) = -4\pi q_i u_i(\xi) \quad (3.17b)$$

has the first correction

$$f_i^{(1)}(\xi; \gamma, \Delta) = -2\pi q_i [H_i(\xi; \gamma)u_i(\xi) + q_i \mathcal{T}_i(\xi, u_i(\xi); \gamma) + q_i W_i(\xi, \mathbf{v}; \gamma, \Delta)], \quad (3.17c)$$

(no sum over i in (3.17b, c)) with $\mathbf{v} = (u_1/2, u_2, u_3)$, where we have substituted u_i for f_i in \mathcal{T}_i using (3.17b). This captures: (i) the nonlocal force–velocity relationship through integrals over the entire body axis which appear in \mathcal{T}_i and W_i , (ii) flow inertia through γ -dependence in H_i, \mathcal{T}_i and W_i and (iii) a non-diagonal resistance matrix accounting for wall effects via W_i . However, \mathcal{T}_i depends on differences in u_i and so, for prescribed uniform velocity, $\mathcal{T}_i = 0$. Thus, far from the wall, where $|W_i| \ll 1$, (3.17c) provides a local velocity–force relationship but, unlike traditional RFT, this relationship varies with axial position s and frequency γ . The ability of this local relationship to capture finite-length effects can be further explored by examining the limiting behaviour of H_i close to the cylinder ends. For $\epsilon \ll 1 - \xi \ll 1$, (3.15) takes the limiting form $H_i(\xi; \gamma) = \ln(\sqrt{i}\gamma(1 - \xi)) + O(1)$, (likewise for $\xi \rightarrow -1$); thus γ controls the magnitude of the logarithmic singularities at the cylinder ends. Higher-order terms (for $i > 1$) can be determined through

$$2f_i^{(k)} = H_i(\xi; \gamma)f_i^{(k-1)} + q_i \mathcal{T}_i(\xi, f_i^{(k-1)}; \gamma) + q_i W_i(\xi, \mathbf{f}^{(k-1)}; \gamma, \Delta) \quad (3.18)$$

(no summation over i). In the quasi-steady limit ($\gamma \ll 1$)

$$H_1(\xi; \gamma) = \ln(1 - \xi^2) - 1 + \ln 4 + O(\gamma), \quad H_2(\xi; \gamma) = H_1(\xi; \gamma) + 2, \quad (3.19a)$$

and hence

$$u_i(\xi) = \frac{(1 + \delta_{i1})}{4\pi} (\ln(2/\epsilon) + \frac{1}{2} \ln(1 - \xi^2) - \frac{1}{2} + \delta_{i2} + \delta_{i3}) f_i(\xi; \gamma, \Delta) + \frac{\delta_{ij}(1 + \delta_{i1})}{8\pi} \int_{-1}^1 \frac{(f_j(s; \gamma, \Delta) - f_j(\xi; \gamma, \Delta))}{|s - \xi|} ds + \frac{1}{8\pi} W_i(\xi, \mathbf{f}; \gamma, \Delta), \quad (3.19b)$$

(again, no summation over i) subject to an $O(\gamma)$ correction, in agreement with Blake (1974).

When oscillations are high frequency ($1 \ll \gamma \ll \epsilon^{-1}$), the $\exp(-\sqrt{i}\gamma\hat{r})$ (viscous) contributions to the oscillatory Stokeslet (3.4b,c) are exponentially small except within $O(\gamma^{-1})$ distances of the singularity ($\epsilon \ll \gamma^{-1} \ll 1$)

$$\int_{\xi - \mathcal{U}\gamma^{-1}}^{\xi + \mathcal{U}\gamma^{-1}} S_{ij}(\hat{\mathbf{x}}; \gamma) ds = O(\ln \epsilon), \quad \int_{\xi + \mathcal{U}\gamma^{-1}}^1 S_{ij}(\hat{\mathbf{x}}; \gamma) ds = O(1) \quad (3.20)$$

($\mathcal{U} = O(1)$). Hence the T_i terms in (3.12) are algebraically small in γ^{-1} , leading (assuming the wall is sufficiently distant) to a local force–velocity relationship

$$8\pi u_i(\xi) = f_i(\xi; \gamma)(1 + \delta_{i1})(-2 \ln \epsilon + H_i(\xi; \gamma)) + O(\gamma^{-1} \ln \epsilon, \gamma\epsilon) \quad (3.21)$$

(no sum over i). As will be demonstrated in § 3.3, (3.21) captures end-effects in the Stokeslet profile without the need for the iteration scheme (3.17, 3.18), which converges slowly in the large- γ limit.

3.3 Results

We now use unsteady slender-body theory (USBT) to examine (in § 3.3.1) finite-length effects as a function of oscillation frequency γ and wall separation distance Δ when the tilt angle α is 0. We then inspect Stokeslet distributions (§ 3.3.2) to judge the accuracy of modified RFT against USBT computations. Drag curves are presented in § 3.3.3, computed for a range of γ and Δ ; § 3.3.4 examines the influence of tilting the cantilever as the wall is approached.

3.3.1 Screening of three-dimensional effects

The role of end effects as the frequency and separation distance are changed is explored in figures 3.2 and 3.3, where computations highlight the Δ and γ -dependence of the

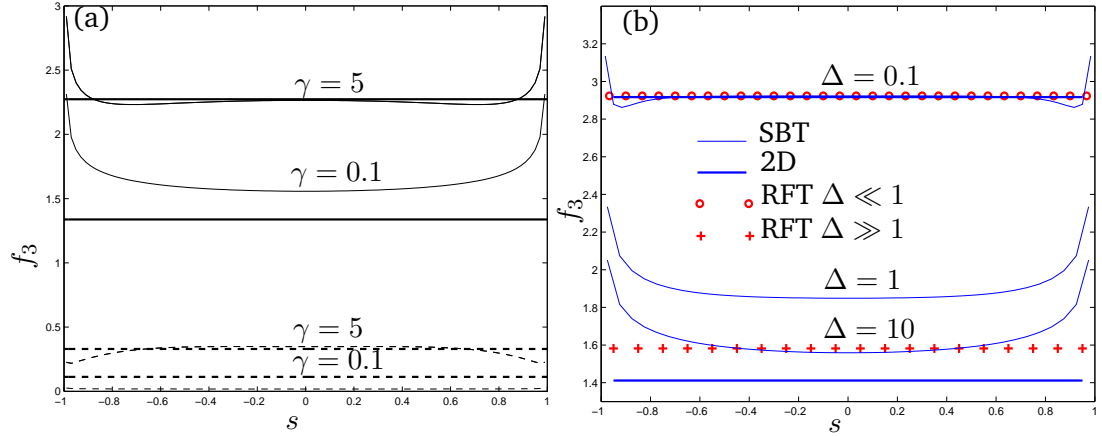


FIGURE 3.2: (a) γ -screening: real (solid line) and imaginary (dashed line) parts of f_3 when $\Delta = 100$, $\epsilon = 10^{-3}$, $\alpha = 0$ for $\gamma = 0.1$ and 5. Thick solid and dashed lines show the corresponding two-dimensional unsteady unbounded drag result (2.19). (b) Δ -screening: f_3 in the quasi-steady limit ($\gamma = 0.01$) for $\Delta = 0.1, 1$ and 10 and $\epsilon = 10^{-3}$. Thick lines show the two-dimensional quasi-steady drag result (2.13), whilst markers show RFT with leading-order wall correction for a cylinder either far away from the wall (3.22, plus signs) or very close to it (3.23, circles).

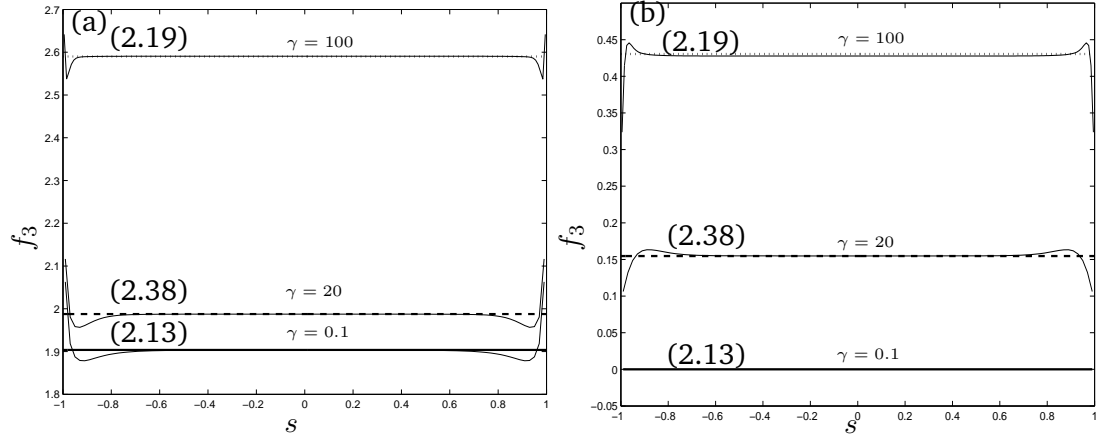


FIGURE 3.3: Comparisons with various two-dimensional models showing (a) real and (b) imaginary parts of Stokeslet strength profiles f_3 arising from USBT computations when $\Delta = 0.1$, $\gamma = 0.1, 20, 100$, $\epsilon = 10^{-4}$ and $\alpha = 0$. The thick lines correspond to two-dimensional results (2.38), (2.19) and (2.13). Note that $\text{Im}(f_3)$ is too small to be distinguishable in (b) when $\gamma = 0.1$.

Stokeslet distributions. In figure 3.2(a) the separation distance is large ($\Delta = 100$), making the wall's presence largely irrelevant when $\gamma = 0.1$ and $\gamma = 5$. Vorticity diffuses $O(\gamma^{-1})$ distances with respect to the cylinder's length and consequently we expect finite-length effects to cover similar distances. This is confirmed in figure 3.2(a), where for $\gamma^{-1} = 10$ vorticity diffuses distances greater than the cylinder length and the Stokeslet profile is everywhere non-uniform. However, when $\gamma^{-1} = 0.2$, not only do we see a decrease in the strength of the profiles, but finite-length effects are indeed restricted to $O(\gamma^{-1})$ distances of the ends. The two-dimensional model (2.19) then provides an accurate picture of the Stokeslet profile over much of the cylinder; we shall refer to this as γ -screening. Agreement with (2.19) provides useful validation of the USBT computations.

Δ -dependence is explored in figure 3.2(b), where the separation distance between the cylinder and the wall is decreased to reveal another mechanism by which end-effects are suppressed. We expect finite-length effects to be confined to within an $O(\gamma^{-1})$ distance or an $O(\Delta)$ distance (when $\Delta \ll \gamma^{-1}$) of the cylinder ends. Therefore when $\gamma \ll 1$ and $\Delta = 10$ (figure 3.2b) the finite-length character of the flow is evident along the cylinder's entire length and the quasi-steady two-dimensional approximation (2.13) proves inadequate. However when $\Delta = 0.1$, the Stokeslet distribution increases in strength and becomes uniform away from the ends, where it is approximated well by (2.13); we call this Δ -screening. It is also instructive to compare these quasi-steady predictions to others in the literature, summarized by Brennen and Winet (1977). In the large- Δ limit, the leading-order finite-length effects are captured by (Brennen and Winet 1977)

$$f_3 = 4\pi u_3 (\ln(2/\epsilon) + 0.193 - (3/2)\Delta^{-1})^{-1}, \quad (3.22)$$

which predicts a uniform Stokeslet distribution that is closer than (2.13) to the computed result when $\Delta = 10$ (figure 3.2b). For small Δ , (2.13) reduces to a simpler form (Brennen and Winet 1977)

$$f_3 = 4\pi u_3 (\ln(2\epsilon/\Delta) - 1)^{-1} \quad (3.23)$$

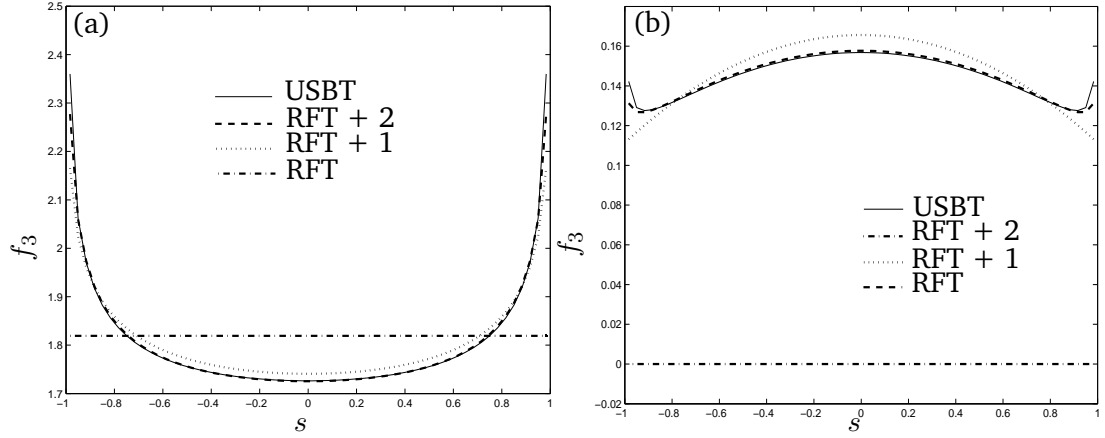


FIGURE 3.4: The real (a) and imaginary (b) parts of the vertical component of Stokeslet strength f_3 along the cylinder's axis. The predictions of modified RFT (3.17–3.18) using n corrective terms (RFT + n) are shown against USBT computations (3.10) for a horizontal cylinder ($\alpha = 0$) when $\gamma = 1$, $\epsilon = 10^{-3}$ and $\Delta = 40$.

which works well when $\Delta = 0.1$ (figure 3.2b), providing further validation of the numerical scheme.

Figure 3.3 demonstrates the transition between various two-dimensional models through γ - and Δ -screening. For $\Delta = \gamma = 0.1$, vorticity diffuses much further from the cylinder than the separation distance and so in this case the quasi-steady model (2.13) is appropriate. However, when $\gamma = 20$ vorticity diffuses distances comparable to $\Delta = 0.1$ and so unsteady inertia is important in the wall interaction, with (2.38) accurately reproducing the uniform portion of the Stokeslet distribution. Finally, when $\gamma = 100$ vorticity is confined very close to the cylinder surface, leaving wall interactions governed by weak inertial effects. Under these circumstances Stokes' (1851) classical result (2.19) works well.

3.3.2 Modified resistive-force-theory

Figures 3.4 and 3.5 assess the performance of modified RFT and its higher-order corrections (3.17–3.18) in capturing the non-uniform Stokeslet distribution. Comparisons are made with the USBT computations (3.10) at both moderate and high frequencies for a

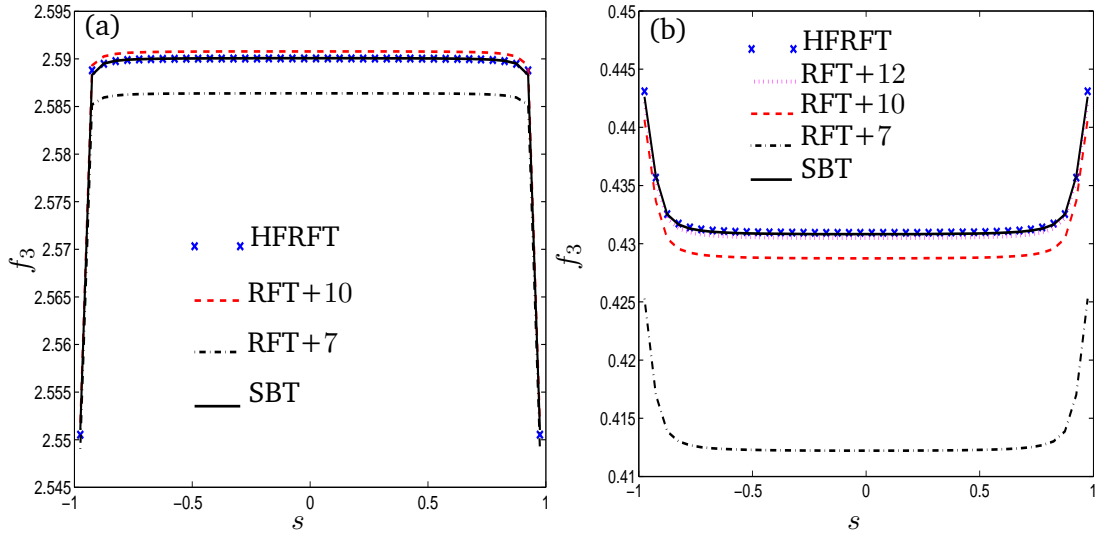


FIGURE 3.5: Vertical component of Stokeslet strength f_3 showing (a) real and (b) imaginary parts along cylinder axis, for $\gamma = 100$, $\epsilon = 10^{-4}$ and $\Delta = 100$. Profiles are computed using RFT plus higher-order corrections (3.17-3.18) and also by exploiting a high-frequency local force-velocity relationship (HFRFT, (3.21)).

cylinder far from the wall. When $\gamma = 1$ (figure 3.4a,b), the leading-order uniform RFT profile is modified at higher orders to capture the distribution's non-uniform character (with just two corrective terms proving sufficient), with only small deviations from USBT very close to the ends of the cylinder. However, when the frequency is increased to $\gamma = 100$ (figure 3.5), convergence of the modified RFT iterative scheme is slower. Under these circumstances the high-frequency expression (3.21) (which is equivalent to (2.19) away from the ends of the cylinder) is an effective and direct approximation.

3.3.3 Drag

Integrating the Stokeslet distribution along the length of the cylinder yields the drag. This is plotted in figure 3.6 under various conditions, against modified RFT predictions (3.17) and the two-dimensional approximation (2.38). Panels (a,b) illustrate the effect of varying Δ , namely an increase in drag amplitude and a decrease in its phase at smaller separations. When γ is decreased both drag amplitude and phase decrease

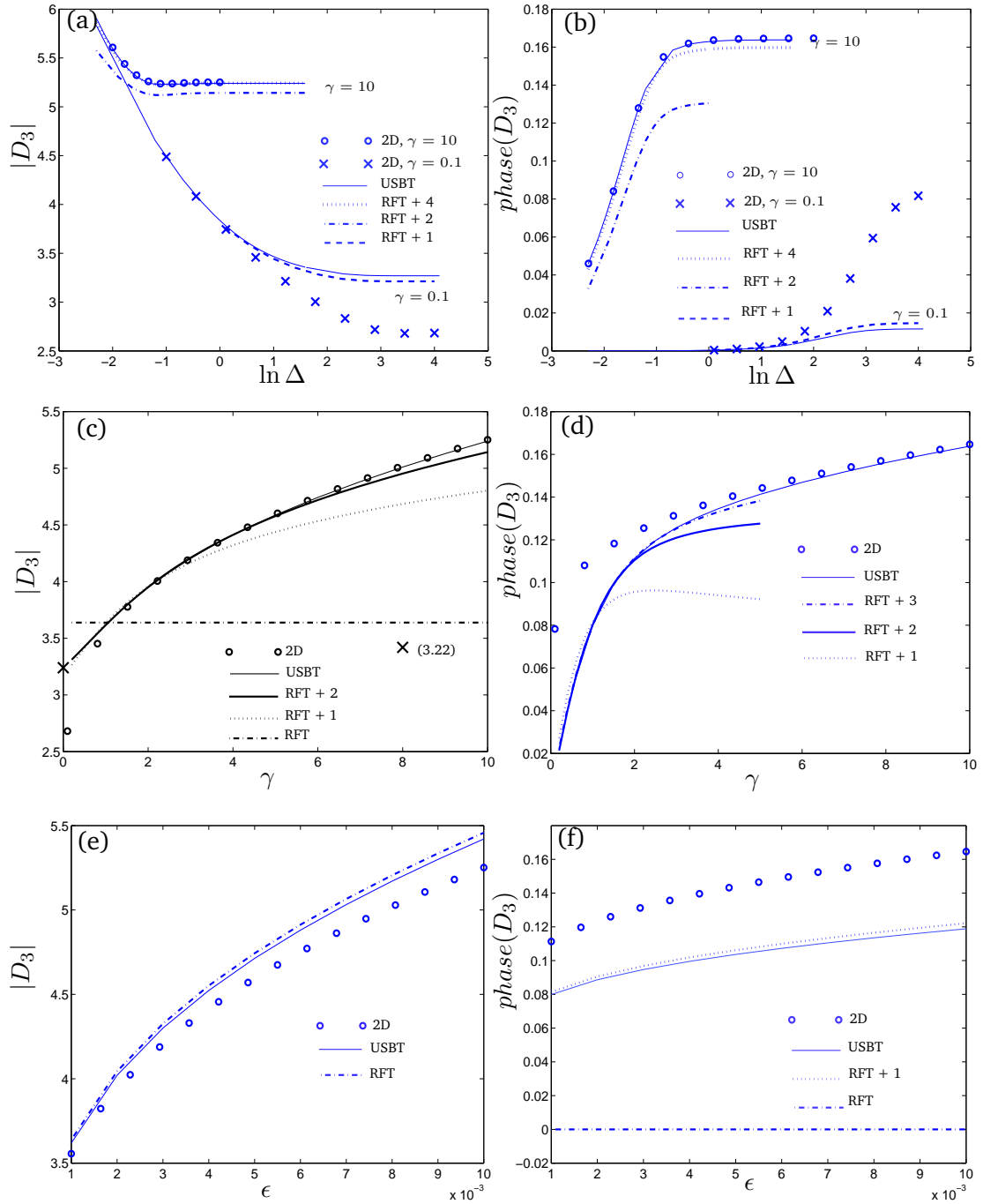


FIGURE 3.6: Drag on a slender horizontal cylinder ($\alpha = 0$) computed using USBT (3.10) and modified RFT (3.17–3.18) over (a,b) a range of Δ when $\epsilon = 10^{-3}$ and $\gamma = 0.1, 10$, (c,d) a range of γ when $\epsilon = 10^{-3}$, $\Delta = 40$ and (e,f) a range of ϵ when $\Delta = 40$ and $\gamma = 1$. Drag amplitudes are shown in (a,c,e), with phases given in (b,d,f). Markers correspond to two-dimensional drag predictions (2.38) and the cross in (c) to (3.22).

(*c,d*), as is also the case when the slenderness ratio is reduced (*e,f*).

At large separation distances and low frequencies (figure 3.6(*a, b*), $\gamma = 0.1$) there is no screening of finite-length effects and so the three-dimensional drag compares unfavourably with the two-dimensional result (2.38). In particular, for two-dimensional flow we observe a continuing change in drag with Δ (due to Stokes' paradox), which saturates via weak inertial effects only at very large Δ , whereas the algebraic far-field decay of the three-dimensional steady flow causes the drag to approach a limiting value more quickly as Δ increases. However, as Δ is decreased the two-dimensional drag prediction becomes more effective through Δ -screening, an effect enhanced when $\gamma = 10$.

Panels 3.6(*c,d*) further emphasise the drag's frequency dependence. At small γ , vorticity diffuses distances comparable with the cylinder length and end-effects once again exert a strong influence over the drag, causing it to diverge from the two-dimensional approximation. However the quasi-steady approximation (3.22) that captures leading-order end effects agrees with the predicted drag as $\gamma \rightarrow 0$. As γ is increased, finite-length effects decay more rapidly away from the ends and this induces two-dimensionality in the flow along much of the cylinder length, leading to improved agreement with the two-dimensional approximation. In panels (*e,f*) we observe the expected breakdown of the two-dimensional approximation as the cylinder is made less slender, due to the increasing importance of geometrically-controlled end effects.

Figure 3.6 also demonstrates the accuracy of modified RFT. Panels (*a,c*) demonstrate that for $\gamma = 0.1$ the first RFT correction proves suitable over a wide range of Δ , but achieves greatest accuracy at smaller separations. The iterative scheme struggles at high frequencies irrespective of the separation distance (figure 3.6*a,b*, $\gamma = 10$), where four corrective terms are still not sufficient to reach agreement with the USBT computations. The dependence of asymptotic accuracy upon γ is emphasized further in figure 3.6(*c,d*), where fewer corrective terms are seen to be required when γ is small. Since RFT is based on an expansion in powers of $\log 1/\epsilon$, the number of corrections required is relatively insensitive to the value ϵ (figure 3.6*e,f*). In summary, modified RFT works well in situations where the two-dimensional model breaks down, specifically at

low and moderate frequencies, when separation distances are large.

3.3.4 Tilt

So far we have considered a cylinder with its axis parallel to a plane wall. However, USBT allows us to tilt the cylinder relative to the wall. The variation in the normal drag for a cylinder driven perpendicularly to its axis at fixed γ and varying Δ is plotted in figure 3.7(a,b) for several inclination angles. As the cylinder is brought closer to the wall the drag increases and the phase decreases, more so at low tilt angles where the influence of the wall is greatest. At large Δ the normal drag is insensitive to the angle of tilt, since the wall induces negligible axial flows. Only for $\Delta \lesssim 20$ (with $\gamma = 0.1$) do wall interactions influence the normal drag at larger tilt angles. The effects of tilt are also reduced by increasing the frequency of oscillation, which results in wall interactions being governed by weaker inviscid effects. Figure 3.7(c,d) shows that for $\gamma \gtrsim 50$ (with $\Delta = 0.1$) the normal drag is largely independent of inclination angle and in this limit γ -screening means that the two-dimensional drag result (2.38) works well (applied in a frame of reference in which the cylinder axis is horizontal).

When the cylinder is tilted but driven vertically we can make meaningful comparisons with two-dimensional models over a wider range of Δ . Although at large Δ wall interactions are weak, vertical driving generates non-negligible axial flows which affect the vertical drag, particularly at large tilt angles (figure 3.8) and two-dimensional models are a poor approximation. When the separation distance is decreased, however, the effects of Δ -screening lead to improved agreement between two-dimensional results and USBT computations, although at severe tilt ($\alpha = \pi/4$) full convergence is never quite reached.

The three-dimensional nature of the flow due to a tilted cylinder oscillating near a wall is illustrated in figure 3.9, which visualizes the flow field from different angles. The arrows (all normalized to unit length) give the flow direction with the background shading indicating the flow speed (lighter shading corresponds to faster flow). Panel (a) gives a side-on view of the cylinder, clearly demonstrating the change in flow over the length of the cylinder body. This is further emphasized through two cross-sectional

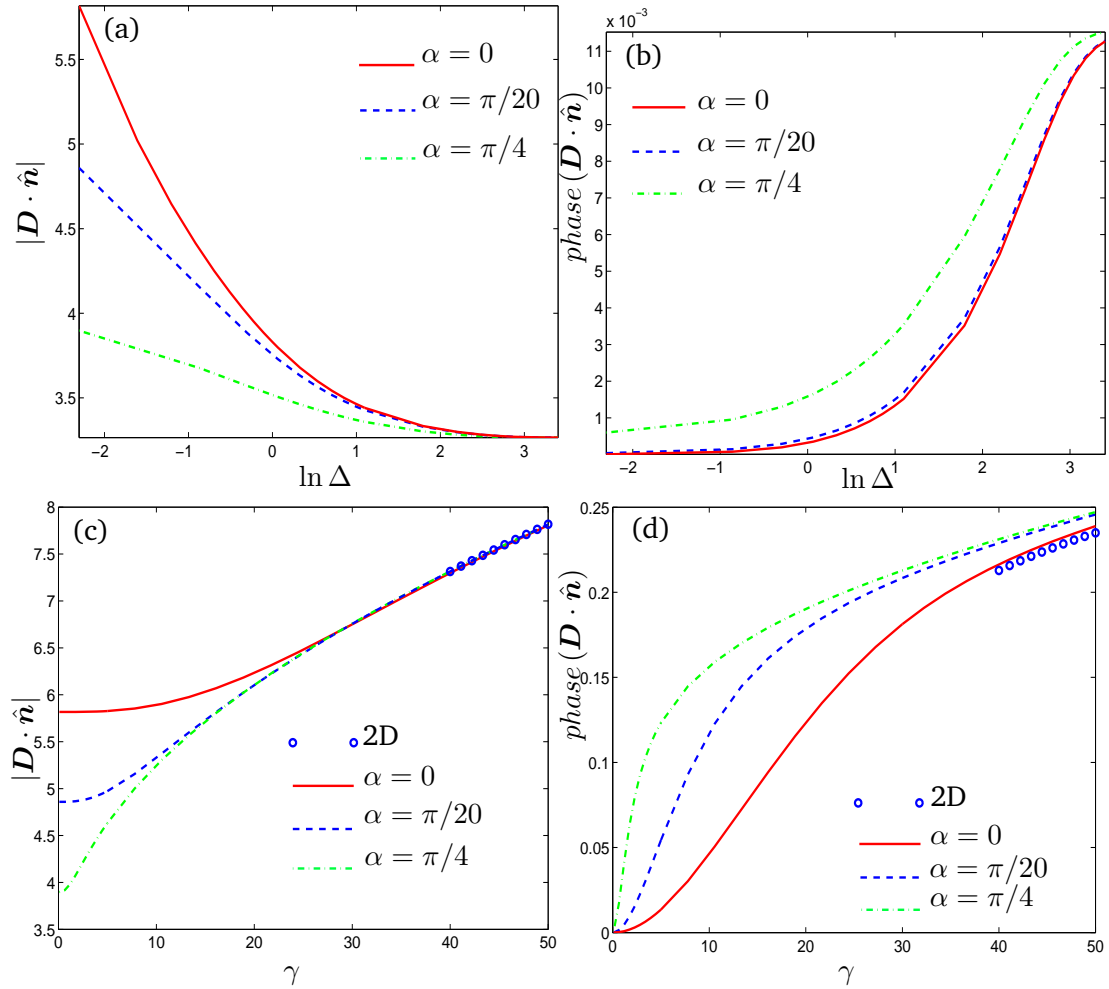


FIGURE 3.7: Curves show the behaviour of the drag (a,c) amplitude and phase (b,d) in a direction normal to the axis for a cylinder ($\epsilon = 10^{-3}$) at various angles of inclination ($\alpha = 0, \pi/20$ and $\pi/4$), as a function of (a,b) separation distance Δ for $\gamma = 0.1$ and (c,d) frequency γ for $\Delta = 0.1$. The markers correspond to results obtained using the two-dimensional unsteady drag (2.38).

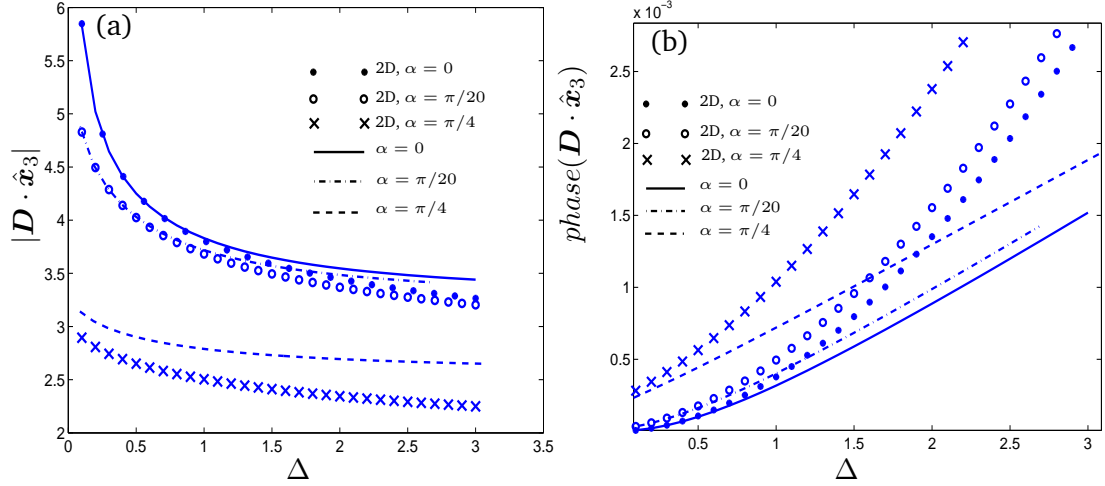


FIGURE 3.8: Curves show the behaviour of the drag amplitude (a) and phase (b) of a cylinder ($\epsilon = 10^{-3}$) driven vertically at various angles of inclination ($\alpha = 0, \pi/20$ and $\pi/4$), as a function of separation distance Δ when $\gamma = 0.1$. The markers correspond to results obtained using the two-dimensional unsteady drag (2.38).

perspectives of the flow, one taken near the raised end of the cylinder (b) and another at its lowered end (c), where it can be seen that the location of recirculating flow changes relative to the cylinder, over its length.

3.4 Discussion

We have developed a novel unsteady slender-body theory (USBT) approximation to describe the flow generated by oscillations of a finite-length cylinder in the presence of a plane wall. We assumed throughout that oscillation amplitudes were sufficiently small to allow linearization of the Navier-Stokes equations and boundary conditions. The flow was modelled using an axial distribution of three-dimensional oscillatory Stokeslets and dipoles (plus appropriate images) in a way which, to leading-order in the slenderness parameter ϵ , satisfied no-slip and no-penetration on the cylinder surface and the wall. The singularity distribution was determined both numerically and by perturbing about the local velocity–force relationship (a modification of resistive-force theory). The slender-body approximation holds for $\Delta \gg \epsilon$ and $\gamma \ll \epsilon^{-1}$ (figure 3.10), breaking

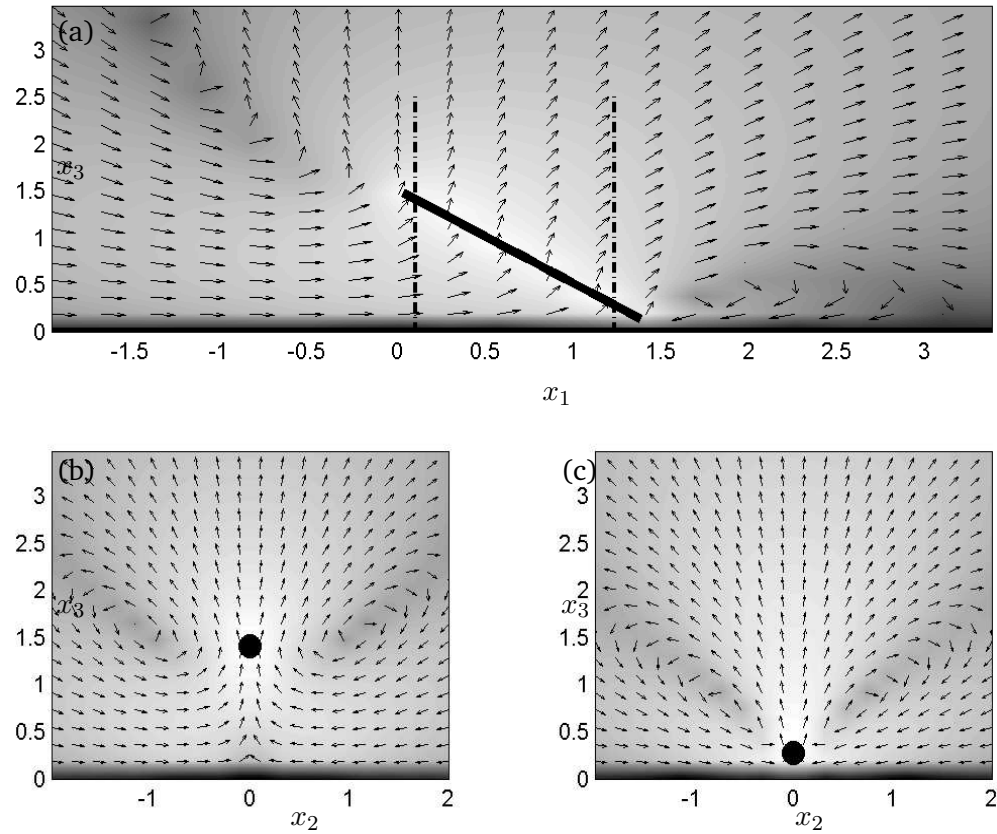


FIGURE 3.9: Flow fields for a cylinder ($\epsilon = 10^{-3}$) oscillating with $\gamma = 0.1$, tilted at angle $\pi/4$ when $\Delta = 0.1$. The arrows (all normalized to unit lengths) give the flow velocity and background rendering indicates flow speeds, with faster flow shown in lighter shades. Panel (a) gives the flow profile along a plane intersecting the cylinder axis longitudinally and dashed-dotted lines mark the location of cross-section slices shown in more detail in (b) and (c).

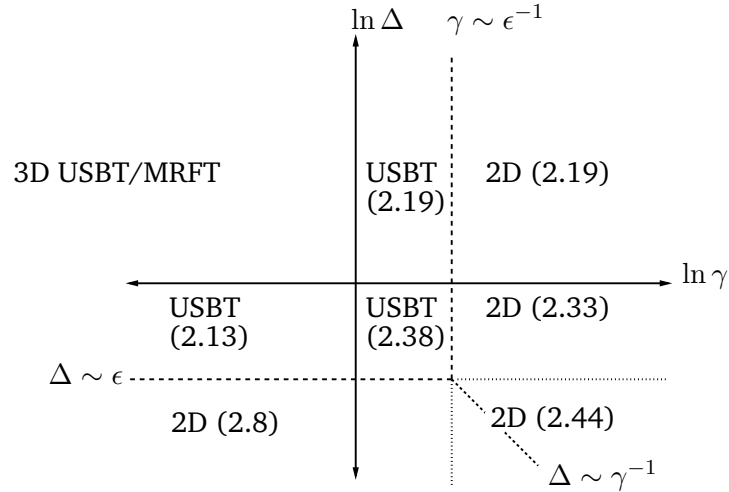


FIGURE 3.10: (Δ, γ) -parameter space for a non-tilted cylinder, indicating the domain accessible to USBT and the regions where USBT gives good agreement with existing two-dimensional models through γ - or Δ -screening. The thick dashed line represents the boundary of parameter space which is inaccessible to USBT but which is described well by two-dimensional models.

down either when the wall separation distance or viscous boundary layers are comparable to the cylinder radius.

When the cylinder is parallel to the wall, two mechanisms suppress finite-length effects and leave the flow two-dimensional along much of the cylinder's length. Under such circumstances we can exploit our extensive range of asymptotic drag approximations for two-dimensional flow (see chapter 2). Increasing the frequency of oscillation, γ , or decreasing the separation distance between the cylinder and the wall, Δ , both limit the range of end effects, and the Stokeslet distribution away from the ends rapidly attains the uniform value given by two-dimensional flow models. When $\epsilon \ll \Delta \ll \min(1, \gamma^{-1})$ vorticity diffuses distances much greater than Δ and we can appeal to a quasi-steady two-dimensional drag (2.13). When $\epsilon \ll \Delta \sim \gamma^{-1} \ll 1$ we can use a result which exploits unsteady image-Stokeslets (2.38). For $\max(1, \Delta^{-1}) \ll \gamma \ll \epsilon^{-1}$, wall interactions are inviscid and weak, allowing us to exploit an unbounded drag result (2.19). Flows at higher frequencies ($\epsilon^{-1} \lesssim \gamma$) and lower separations ($\Delta \lesssim \epsilon$) can be described using additional two-dimensional models (see figure 3.10). USBT can describe

the genuinely three-dimensional flow which occurs when $\gamma \lesssim 1 \lesssim \Delta$, i.e. when the viscous lengthscale $\sqrt{\mu/\rho\omega}$ and the wall separation distance are both comparable to, or larger than, the cylinder length. (For reference, a 100 μm long cylinder oscillating in water at 400 Hz has $\gamma = 1$.) Therefore, used in conjunction, USBT and two-dimensional models are able comprehensively to cover (γ, Δ) -parameter space.

When the cylinder is tilted and driven normal to its axis, large separation distances and high-frequencies render the drag largely insensitive to the angle of inclination, due to the weak character of wall interactions (figure 3.7). Alternatively, when the cylinder is tilted but driven vertically, axial flows result in drag differences at different angles of inclination, even in the absence of wall interactions (figure 3.8). At small separations, however, there is good agreement between the two-dimensional prediction (2.38) and USBT computations provided that the angle of inclination is not too great.

We also developed a modified form of RFT which exploits the approximately uniform local relationship between velocity and force in the USBT equations (3.3) that arises at leading order under quasi-steady conditions. Higher-order corrections in $1/\ln \epsilon$, computed iteratively, account for non-local geometry and the effects of flow inertia. For $\gamma = O(1)$, just one or two corrections in the RFT expansion are generally sufficient for convergence to the USBT computations for sufficiently slender cylinders. It was shown how interaction with the wall leads to off-diagonal elements in the cylinder's resistance matrix (through W_i in (3.17c)). In the low-frequency limit ($\gamma \ll 1$) the quasi-steady SBT formulation of Blake (1974) is recovered. At high-frequencies convergence of the modified RFT is slow; however, γ -screening means that the high-frequency limit (3.21) (which extends Stokes' classical result (2.19) to capture end effects) works effectively.

Our calculations provide justification for the use of simpler two-dimensional models in many practically relevant circumstances (depending, for example, on the level of cantilever tilt) and they provide a relatively straightforward mechanism (particularly through our modification of RFT) for capturing genuinely three-dimensional effects if necessary. As shall be seen later (chapters 5 and 6), when coupled to models of flexible cantilevers, the simplifications offered by modified RFT or by two-dimensional approx-

imations offer considerable computational benefits, when computing sinusoidally or thermally driven responses.

Although USBT provides important information into the extent of finite-length effects, in its present form it is unable to represent flows generated by a body with significant width. As such, we next look to variations on the above ideas that will work for oscillating rigid plates.

Chapter 4

Flows generated by a thin rectangular plate

Up to this point we have examined the flow generated by a body of circular cross section, a geometry which lends itself to a degree of analytical treatment. In practice many AFM cantilevers (and MEMS components) have rectangular cross sections and so we now consider driven vertical oscillations of a rigid rectangular plate of length $2L$, width $2R$ and thickness $2\mathcal{D}$ with its plane of vertical symmetry (parameterised by coordinates ξ and η) at a distance \mathcal{H} above a plane wall which is located at $x_3 = 0$ (see figure 4.1). The plate's velocity is $\text{Re}(Ve^{i\omega t})$, where $V = \mathcal{A}\omega$, ω is the driving frequency and $\mathcal{A} \ll R$ is the amplitude of oscillation. In addition to γ (1.9), the flow dynamics are characterized by two geometric parameters ($\epsilon = R/L$ and $d = \mathcal{D}/L$) as well as the dimensionless separation distance $\Delta = (\mathcal{H} - \mathcal{D})/L$.

We begin by assuming that the plate is sufficiently long that the flow is principally two-dimensional away from the ends of the body. This is examined in § 4.1 using a boundary-integral formulation for oscillatory viscous flow. Due to the limitations of this technique at high frequencies we also include a boundary-layer analysis (§ 4.1.1), with boundary-integral techniques employed once more to solve the outer inviscid

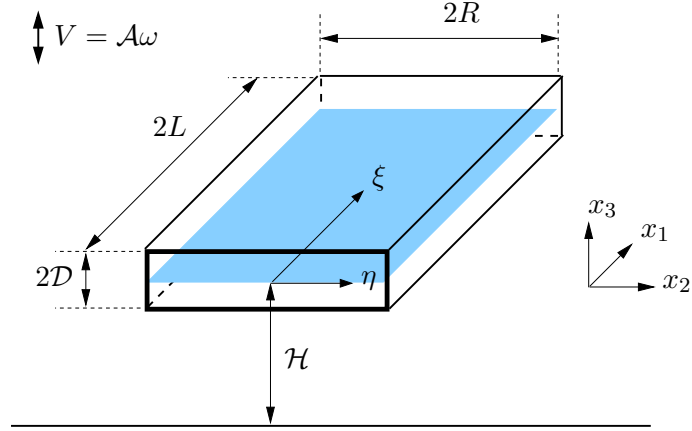


FIGURE 4.1: A plate with length $2L$, width $2R$ and thickness $2D$ oscillates with frequency ω and amplitude \mathcal{A} normal to a plane wall ($x_3 = 0$). The plate's plane of vertical symmetry, parameterized by (ξ, η) , lies a distance \mathcal{H} from the wall. The plate surface is denoted by S with the perimeter of a cross-sectional slice given by S_X

flows. The boundary-integral flow representations are solved using boundary-element methods (BEM) and the numerical scheme is laid out in § 4.1.2. If we impose the additional constraint that the plate thickness is much less than its width we can derive a two-dimensional thin-plate-theory (TPT) approximation for the two-dimensional flow, which requires only a distribution of image Stokeslets (3.6) along the cross section's mid-plane ($x_3 = \mathcal{H}$) (§ 4.2). In the high-frequency (§ 4.2.1) and small-separation (§ 4.2.2) limits we explain how further flow approximations can be made.

The three-dimensional flow can be described using the boundary integral methods described in § 4.1. However the computational overheads are prohibitive, so in § 4.3 we explore the three-dimensional TPT, this time placing a two-dimensional distribution of Stokeslets over the plate's mid-plane. Once again, simplifications can be made in the case of small separation (§ 4.3.2). Results are presented in § 4.4 and their implications discussed in § 4.5.

4.1 Two-dimensional boundary-integral formulation

For two-dimensional oscillating rectangular cantilevers we rescale lengths on R , giving (1.8) in the form

$$i(\epsilon\gamma)^2 \mathbf{u} = -\nabla p' + \nabla^2 \mathbf{u}, \quad \nabla \cdot \mathbf{u} = 0, \quad (4.1)$$

where $\epsilon\gamma = R\sqrt{\omega/\nu}$ and $p' = \epsilon p$ is the pressure scaled on $\mu V/R$. This must be solved subject to the boundary conditions

$$\mathbf{u}|_{\mathcal{S}_X} = \hat{\mathbf{x}}_3, \quad \mathbf{u}(x_2, 0) = \mathbf{0}, \quad \mathbf{u} \rightarrow \mathbf{0} \text{ as } |\mathbf{x}| \rightarrow \infty \text{ for } x_3 \geq 0, \quad (4.2)$$

where $\hat{\mathbf{x}}_3 \equiv (0, 0, 1)$ and \mathcal{S}_X is the cross-sectional perimeter. Since lengths are scaled on R , it is more meaningful to take Δ/ϵ as our dimensionless separation distance.

We now follow Pozrikidis (1989b) and Loewenberg (1994b) by using a two-dimensional version of their boundary-integral formulation. For transverse oscillations, Pozrikidis (1989b) gives the following first-kind Fredholm equation for the velocity field \mathbf{u} in a domain with boundary \mathcal{S}_X and outward unit normal $\hat{\mathbf{n}}$

$$u_i(\mathbf{X}) = -\frac{1}{4\pi} \int_{\mathcal{S}_X} f'_j(\mathbf{x}) S_{ij}^w(\hat{\mathbf{x}}) \, ds(\mathbf{x}), \quad f'_j(\mathbf{x}) = \sigma'_{jk} n_k - i(\epsilon\gamma)^2 u_k x_k \hat{n}_j, \quad (4.3)$$

where $\mathbf{X} \in \mathcal{S}_X$, $\boldsymbol{\sigma}'$ is the stress tensor (1.1b) (non-dimensionalized on $\mu V/R$), $\hat{\mathbf{x}} = \mathbf{x} - \mathbf{X}$ and S_{ij}^w is the two-dimensional oscillatory Stokeslet which satisfies no-slip and no-penetration on the wall $x_3 = 0$. Chu and Kim (2001) showed that

$$S_{ij}^w(\mathbf{x}, \mathbf{X}; \epsilon\gamma) = S_{ij}(\hat{\mathbf{x}}; \epsilon\gamma) + \Lambda_{ij}(\mathbf{x}, \mathbf{X}; \epsilon\gamma), \quad (4.4a)$$

where S_{ij} is the two-dimensional oscillatory free-space Stokeslet (Avudainayagam and Geetha 1998)

$$S_{ij}(\hat{\mathbf{x}}; \epsilon\gamma) \equiv \frac{2}{i(\epsilon\gamma)^2} \left(\frac{\delta_{ij}}{\hat{r}^2} - \frac{2\hat{x}_i \hat{x}_j}{\hat{r}^4} \right) - 2K_0(\sqrt{i\epsilon\gamma\hat{r}}) \left(\delta_{ij} - \frac{\hat{x}_i \hat{x}_j}{\hat{r}^2} \right) - \frac{2K_1(\sqrt{i\epsilon\gamma\hat{r}})}{\sqrt{i\epsilon\gamma\hat{r}}} \left(\delta_{ij} - \frac{2\hat{x}_i \hat{x}_j}{\hat{r}^2} \right), \quad (4.4b)$$

($\hat{r} = |\hat{\mathbf{x}}|$) and

$$\Lambda_{ij}(\mathbf{x}, \mathbf{X}; \epsilon\gamma) = (-1)^{\delta_{i1}} \partial_i \Psi_j(\mathbf{x}, \mathbf{X}; \epsilon\gamma), \quad (4.4c)$$

where

$$\Psi_1(\mathbf{x}, \mathbf{X}; \epsilon\gamma) = \frac{1}{2\pi(\sqrt{i\epsilon\gamma})^2} \int_0^\infty \frac{1}{q-k} \left((q+k) \left(e^{-k(x_3+X_3)} + e^{-q(x_3+X_3)} \right) - 2qe^{-kx_3-qX_3} - 2ke^{-qx_3-kX_3} \right) \cos kx_2 \, dk, \quad (4.4d)$$

$$\Psi_2(\mathbf{x}, \mathbf{X}; \epsilon\gamma) = \frac{1}{2\pi(\sqrt{i\epsilon\gamma})^2} \int_0^\infty \frac{1}{q(q-k)} \left((q+k) \left(qe^{-k(x_3+X_3)} + ke^{-q(x_3+X_3)} \right) - 2kq \left(e^{-kx_3-qX_3} + e^{-qx_3-kX_3} \right) \right) \sin kx_2 \, dk \quad (4.4e)$$

($q = \sqrt{k^2 + i\epsilon^2\gamma^2}$, $\partial_i = \partial/\partial x_i$) is the wall-interaction term (calculated using Fourier transforms) which cancels out any slip and penetrating flow at the wall due to the presence of the free-space Stokeslet

4.1.1 High-frequency limit

High demands on the resolution required to capture viscous boundary layers and the oscillatory nature of the kernel, both place a practical upper limit on the size of $\epsilon\gamma$ and for this reason we also employ a boundary-layer formulation at high frequencies. Here an approximation for the drag on the body is obtained by solving separately for the leading-order inviscid flow, Stokes layers on the solid boundaries and the second-order inviscid flow driven by fluid ejected from the Stokes layers (this secondary inviscid flow makes an $O(\epsilon\gamma)$ drag contribution, comparable in size to the boundary-layer contribution; note that this linear inviscid flow is distinct from the nonlinear streaming flows (see § 1.2.4) that are also generated by Stokes layers, but which we here neglect). The inviscid flows are determined using the standard boundary-integral formulation for the potential flow $\mathbf{u} = \nabla\phi$ (Pozrikidis 1996)

$$\phi(\mathbf{X}) = \frac{1}{\pi} \int_{S_X} \mathbf{V}' \cdot \hat{\mathbf{n}} \ln \hat{r} \, ds(\mathbf{x}) - \frac{1}{\pi} \oint_{S_X} \frac{\hat{\mathbf{x}} \cdot \hat{\mathbf{n}}}{\hat{r}^2} \phi(\mathbf{x}) \, ds(\mathbf{x}), \quad (4.5)$$

with the second integral taking its Cauchy principal value. Setting $\mathbf{V}' = \hat{\mathbf{x}}_3$ on the cylinder and $\mathbf{V}' = \mathbf{0}$ on the wall in (4.5) yields an expression for the potential of

the primary inviscid flow $\phi^{(1)}$. Boundary layers on the solid surfaces drive a secondary potential flow $\phi^{(2)}$, which can be expressed using (4.5) once we have extracted the value of \mathbf{V}' from the boundary-layer flows. Within this asymptotic limit, an approximation for the drag per unit length (lengths scaled on R) is then given by

$$D_3 = i \int_{S_X} \left((\epsilon\gamma)^2 \phi^{(1)} + \epsilon\gamma \phi^{(2)} \right) ds(\mathbf{x}) + \sqrt{i} \int_{S_X^v} \epsilon\gamma (v^s - 1) ds(\mathbf{x}), \quad (4.6)$$

where S_X^v represents the vertical sides of the cantilever and $v^s = \partial\phi^{(1)}/\partial x_3$ is the slip velocity on these vertical sides. (The corresponding asymptotic expression for the drag on a circular cantilever was derived in §2.2.2.)

4.1.2 Numerical treatment

Boundary-element methods provide a computational route to solving (4.3) and (4.5) for the modified traction $\mathbf{f}(\mathbf{x})$ and flow potential $\phi(\mathbf{x})$, respectively. Discretizing the cantilever's surface and the wall into N boundary elements, approximating the geometry of the boundary in the k th element with the simple polynomial curve B_k , with mid-point $\mathbf{X}^{(k)}$ and assuming that $\mathbf{f}(\mathbf{x})$, $\phi(\mathbf{x})$ are constant on each boundary element, we can rewrite (4.3) and (4.5) as the following systems of linear equations, respectively

$$u_i(\mathbf{X}^{(m)}) = -\frac{1}{4\pi} \sum_{k=1}^N A_{ij}^k(\mathbf{X}^{(m)}) f_j'(\mathbf{X}^{(k)}), \quad A_{ij}^k(\mathbf{X}^{(m)}) = \int_{B_k} S_{ij}(\mathbf{x}, \mathbf{X}^{(m)}) ds(\mathbf{x}), \quad (4.7a)$$

$$\phi(\mathbf{X}^{(m)}) = \frac{1}{\pi} \sum_{k=1}^N \left((\mathbf{V}' \cdot \mathbf{n})_k \int_{B_k} \ln |\mathbf{x} - \mathbf{X}^{(m)}| ds(\mathbf{x}) - \phi_k \int_{B_k} \frac{(\mathbf{x} - \mathbf{X}^{(m)}) \cdot \hat{\mathbf{n}}}{|\mathbf{x} - \mathbf{X}^{(m)}|^2} ds(\mathbf{x}) \right), \quad (4.7b)$$

for $m = 1, \dots, N$, where $\phi_k = \phi(\mathbf{X}^{(k)})$, which are solved by Gaussian elimination. Logarithmic singularities at $\mathbf{x} = \mathbf{X}$ are dealt with in the usual fashion, namely an interval is taken around the singularity, within which the asymptotically expanded kernel is integrated analytically.

The non-smooth shape of the cantilever also requires special attention, as there exists an integrable singularity in $|\boldsymbol{\sigma} \cdot \hat{\mathbf{n}}|$ at the cantilever edges. We follow Loewenberg

(1994b) and adjust the spacing of the boundary elements at the edges to account for $O(s^{-\alpha_0})$ and $O(s^{-\beta_0})$ viscous and inviscid singularities, respectively, where s measures the distance from the edge, $\alpha_0 \approx 1/2$ and $\beta_0 \approx 1/3$. The contributions to the drag from the two-dimensional boundary layers wrapped around each edge are sub-dominant to terms in (4.6) (Loewenberg 1994b).

All sides of the square cantilever had 15 clustered boundary elements per half-length (or 10 for higher aspect ratios). Numerical convergence was verified by doubling the number of boundary elements on all surfaces and results are presented in §4.4.1 below.

4.2 Two-dimensional thin-plate formulation

When the thickness of a two-dimensional plate is small compared with its width (D/R , $D/\mathcal{H} \ll 1$) we can expand the surface distribution of Stokeslets in (4.3) about the mid-plate ($x_3 = \mathcal{H}$) and approximate the flow through a distribution of two-dimensional image Stokeslets along this line. Although similar in approach to the slender-body formulation (3.3), the change in geometry leads to important differences in the local integral contributions about a point \mathbf{X} located on the upper or lower surface of the plate, where $\eta = \mathbf{X} \cdot \hat{\mathbf{x}}_2$

$$\int_{\eta-\delta}^{\eta+\delta} S_{ij}^w(\hat{\mathbf{x}}; \epsilon\gamma) dt = \begin{cases} O(\delta \ln(d/\epsilon)), & i = j = 1 \\ O(\delta), & \text{otherwise} \end{cases} \quad (4.8a)$$

($d/\epsilon \ll \delta \ll 1$). Unlike the finite-length circular cylinder, small intervals about η make no leading-order contribution in δ . Outside of this interval $\hat{r} \gg (d/\epsilon)$ and because $\hat{\mathbf{x}} \cdot \hat{\mathbf{x}}_3 = O(d/\epsilon)$ no distinction is made between the top and bottom of the plate to leading order in ϵ . Hence for a thin two-dimensional plate a line distribution of Stokeslets can satisfy prescribed boundary conditions over the whole body (i.e. no dipoles are required, to leading order in ϵ). Therefore, without loss of generality, we can restrict attention to the top surface of the plate and define mid-plane and upper-surface points by

$$\mathbf{x} = t \hat{\mathbf{x}}_1 + (\Delta + (d/2\epsilon)) \hat{\mathbf{x}}_3, \quad \mathbf{X} = \eta \hat{\mathbf{x}}_1 + (\Delta + (d/\epsilon)) \hat{\mathbf{x}}_3, \quad (4.9)$$

respectively. Expanding the Stokeslet distribution about the mid-plane then gives

$$u_i(\eta) = -\frac{1}{4\pi} \int_{-1}^1 S_{ij}^w(\mathbf{x}, \mathbf{X}; \epsilon\gamma) f_j'(t) dt. \quad (4.10)$$

The absence of a local dominance in the integrand about η , however, means that the leading-order flow at a station along the plate is influenced by the entire geometry of the plate. Consequently, at moderate $\epsilon\gamma$, we no longer have a local force–velocity relationship which can be corrected for unsteady non-local effects through iteration and we are left needing to solve (4.10) numerically. As before, we discretize the line of vertical symmetry into N elements and assume that the f_j are constant on each one; the Stokeslet integrals are evaluated by numerical quadrature. This results in an $N \times N$ linear system which is solved by Gaussian elimination. Results are presented in § 4.4.2, where comparisons are made with full BEM computations.

4.2.1 High-frequency limit

Although no local force–velocity relationship exists in general for a two-dimensional thin plate, when the frequency of oscillation is high ($\epsilon\gamma \gg 1$) viscous effects do become localized, which can lead to significant simplifications. This can be seen by splitting the unsteady free-space Stokeslet (4.4b) into its viscous and inviscid components

$$\begin{aligned} u_i(\eta) &= \frac{1}{4\pi} \int_{-1}^1 S_{ij}(\hat{\mathbf{x}}; \epsilon\gamma) f_j'(t) dt = \\ &= -\frac{1}{2\pi} \int_{-1}^1 \left(K_0(\sqrt{i}\epsilon\gamma\hat{r}) \left(\delta_{ij} + \frac{\hat{x}_i\hat{x}_j}{\hat{r}^2} \right) - \frac{K_1(\sqrt{i}\epsilon\gamma\hat{r})}{\sqrt{i}\epsilon\gamma\hat{r}} \left(\delta_{ij} - \frac{2\hat{x}_i\hat{x}_j}{\hat{r}^2} \right) \right) f_j'(t) dt \\ &\quad + \frac{1}{2\pi(\sqrt{i}\epsilon\gamma)^2} \int_{-1}^1 Q_{ij}(\hat{\mathbf{x}}) f_j'(t) dt. \end{aligned} \quad (4.11)$$

The first integral contains the viscous terms, whilst the second integral contains a distribution of two-dimensional dipoles

$$Q_{ij} \equiv \frac{\delta_{ij}}{\hat{r}^2} - \frac{2\hat{x}_i\hat{x}_j}{\hat{r}^4}. \quad (4.12)$$

The modified Bessel functions $K_0(z)$ and $K_1(z)$ in the viscous expression exhibit exponential decay for $|z| \gg 1$ and so we only expect a non-negligible contribution to the

first integral (viscous contribution) over an $O((\epsilon\gamma)^{-1})$ interval about η . This suggests the rescaling $t = \eta + (\epsilon\gamma)^{-1}t'$, in which case

$$u_i(\eta) = \frac{1}{2\pi(\sqrt{i}\epsilon\gamma)^2} \int_{-1}^1 Q_{ij}(\hat{\mathbf{x}}) f'_j(t) dt - \frac{1}{2\pi} I_{ij} f'_j(\eta) + O((\epsilon\gamma)^{-1}), \quad (4.13)$$

where

$$I_{ij} = \int_{-\epsilon\gamma(1+\eta)}^{\epsilon\gamma(1-\eta)} \left(K_0(\sqrt{i}\tilde{r}) \left(\delta_{ij} + \frac{\tilde{x}_i \tilde{x}_j}{\tilde{r}^2} \right) - \frac{K_1(\sqrt{i}\tilde{r})}{\sqrt{i}\tilde{r}} \left(\delta_{ij} - \frac{2\tilde{x}_i \tilde{x}_j}{\tilde{r}^2} \right) \right) dt' \quad (4.14)$$

and $\tilde{x}_2 = t'$, $\tilde{x}_3 = d/\epsilon$ and $\tilde{r}^2 = t'^2 + (\gamma\epsilon)^2$. Hence in this high-frequency limit the leading-order inviscid flow depends upon the full geometry of the plate and requires a distribution of dipoles along its line of symmetry, whereas viscous contributions are observed to be local to a given point. Although (4.13) still must be solved numerically, by discretizing into elements along the line of symmetry and assuming the f'_j are constant on each element, this approach offers substantial computational savings, since we can integrate the dipoles analytically over each element, thereby dispensing with the greatest overhead, numerical quadrature. Moreover, as there is no need to compute explicitly the boundary layers and secondary inviscid flow, (4.13) also offers significant advantages over the boundary-layer approach (4.5).

4.2.2 Lubrication limit

Computing the integrals in the unsteady-image Stokeslet (4.4c–e) becomes more computationally demanding as the separation distance decreases. Therefore it proves practical to derive a lubrication theory expression for the drag when $\Delta/\epsilon \ll 1$. This is calculated analogously to the circular cantilever case (§ 2.2.1), but with the rescalings

$$x_3 = (\Delta/\epsilon)\check{x}_3, \quad x_2 = \check{x}_2, \quad u_3 = \check{u}_3, \quad u_2 = (\Delta/\epsilon)^{-1}\check{u}_2, \quad p = (\Delta/\epsilon)^{-3}\check{p}, \quad D = (\Delta/\epsilon)^{-3}\check{D}. \quad (4.15)$$

An analysis similar to that in §2.2.3 gives the pressure

$$\check{p} = \frac{i\sqrt{i}(\check{x}_2^2 - 1)\tau^3 \sinh \sqrt{i}\tau}{4 - 4 \cosh \sqrt{i}\tau + 2\sqrt{i}\tau \sinh \sqrt{i}\tau}, \quad (4.16)$$

($\tau = \Delta\gamma$) which produces the lubrication drag

$$D_3 = \frac{2}{3}i(\Delta/\epsilon)^{-1}(\epsilon\gamma)^2 \left(\frac{\sqrt{i}\tau \sinh \sqrt{i}\tau}{2 - 2 \cosh \sqrt{i}\tau + \sqrt{i}\tau \sinh \sqrt{i}\tau} \right), \quad (4.17)$$

subject to an $O((\epsilon\gamma)^2)$ correction due to flow outside of the gap. The impact on this drag of introducing slip is examined in Appendix A.2.

In the quasi-steady limit, $\tau \rightarrow 0$, (4.17) reduces to $D = 8(\Delta/\epsilon)^{-3}$, in agreement with Kim et al. (2001b), who also calculated the first drag correction arising from a quasi-steady outer flow when the plate is infinitely thin. Asymptotically matching the lubrication flow to a local flow at the cantilever's edges and to an outer flow where the presence of the plate is accounted for by point sources on the wall, they obtained

$$D_3 = 8(\Delta/\epsilon)^{-3} + 14.8560(\Delta/\epsilon)^{-2}. \quad (4.18)$$

The results in § 4.4 will illustrate the improvements offered by (4.18) over (4.17) in the quasi-steady limit, both of which also act as useful validation of the numerical scheme.

4.3 Three-dimensional thin-plate formulation

In three dimensions (where lengths are scaled on L), the flow is governed by (1.8)

$$i\gamma^2 \mathbf{u} = -\nabla p + \nabla^2 \mathbf{u}, \quad \nabla \cdot \mathbf{u} = 0, \quad (4.19)$$

subject to the boundary conditions

$$\mathbf{u}|_{\mathcal{S}} = \hat{\mathbf{x}}_3, \quad \mathbf{u}(x_1, x_2, 0) = \mathbf{0}, \quad \mathbf{u} \rightarrow \mathbf{0} \text{ as } |\mathbf{x}| \rightarrow \infty \text{ for } x_3 \geq 0, \quad (4.20)$$

where \mathcal{S} is the plate's surface.

A boundary-integral representation of the flow exists which is analogous to the two-dimensional representation presented in § 4.1

$$u_i(\mathbf{X}) = \frac{1}{8\pi} \int_{\mathcal{S}} f_j(\mathbf{x}) S_{ij}^w(\hat{\mathbf{x}}) dA, \quad f_j(\mathbf{x}) = \sigma_{jk} n_k - i\gamma^2 u_k x_k \hat{n}_j, \quad (4.21)$$

where $\mathbf{X} \in \mathcal{S}$, $\hat{\mathbf{n}}$ is the outward normal and S_{ij}^w now represents the three-dimensional Stokeslet plus images given in (3.6). Solving (4.21) numerically poses a formidable challenge, due to the number of boundary elements required to cover the three-dimensional surface and the number of numerical quadratures that this entails. A full boundary-element treatment of the three-dimensional flow is therefore computationally prohibitive. However, following the same reasoning as before, when the plate thickness is small

compared with the other dimensions (\mathcal{D}/R , \mathcal{D}/L , $\mathcal{D}/\mathcal{H} \ll 1$) we can expand the surface distribution of Stokeslets in (4.21) about the plane of vertical symmetry $x_3 = \mathcal{H}$ and approximate the flow through a two-dimensional distribution of three-dimensional image Stokeslets over this plane

$$u_i(\xi, \eta) = \frac{1}{8\pi} \int_{-\epsilon}^{\epsilon} \int_{-1}^1 S_{ij}^w(\mathbf{x}, \mathbf{X}; \gamma, \Delta) f_j(s, t) \, ds \, dt, \quad (4.22)$$

where $\mathbf{x} = s \hat{\mathbf{x}}_1 + t \hat{\mathbf{x}}_2 + (\Delta + d/2) \hat{\mathbf{x}}_3$ is a point in the mid-plane and $\mathbf{X} = \xi \hat{\mathbf{x}}_1 + \eta \hat{\mathbf{x}}_2 + (\Delta + d) \hat{\mathbf{x}}_3$ is a point on the upper surface. For the same reasons as those discussed in § 4.2, no distinction is made between the lower and upper surfaces at leading order in this flow approximation and therefore no dipoles or higher-order viscous singularities are required.

4.3.1 Numerical scheme

In analogous fashion to the numerical treatment of finite-length circular cylinders described in § 3.1, we computationally solve the thin-plate equation (4.22) by discretizing the plate into $N_\xi \times N_\eta$ equally-sized panels, setting $\xi_m = m/N_\xi$ and $\eta_k = k\epsilon/N_\eta$. We assume that the Stokeslet distribution \mathbf{f} is constant over each panel and define

$$\mathbf{V} = \left(u_1(\xi_1, \eta_1), u_2(\xi_1, \eta_1), u_3(\xi_1, \eta_1), \dots, u_1(\xi_{N_\xi}, \eta_1), u_2(\xi_{N_\xi}, \eta_1), u_3(\xi_{N_\xi}, \eta_1), \dots, \right. \\ \left. u_1(\xi_1, \eta_{N_\eta}), u_2(\xi_1, \eta_{N_\eta}), u_3(\xi_1, \eta_{N_\eta}), \dots, u_1(\xi_{N_\xi}, \eta_{N_\eta}), u_2(\xi_{N_\xi}, \eta_{N_\eta}), u_3(\xi_{N_\xi}, \eta_{N_\eta}) \right), \quad (4.23a)$$

$$\mathbf{F} = \left(f_1(\xi_1, \eta_1), f_2(\xi_1, \eta_1), f_3(\xi_1, \eta_1), \dots, f_1(\xi_{N_\xi}, \eta_1), f_2(\xi_{N_\xi}, \eta_1), f_3(\xi_{N_\xi}, \eta_1), \dots, \right. \\ \left. f_1(\xi_1, \eta_{N_\eta}), f_2(\xi_1, \eta_{N_\eta}), f_3(\xi_1, \eta_{N_\eta}), \dots, f_1(\xi_{N_\xi}, \eta_{N_\eta}), f_2(\xi_{N_\xi}, \eta_{N_\eta}), f_3(\xi_{N_\xi}, \eta_{N_\eta}) \right). \quad (4.23b)$$

The integral equation (4.22) can then be approximated by the linear system

$$V_{\alpha'} = G_{\alpha'\beta}^V F_\beta, \quad G_{\alpha'\beta}^V = \frac{1}{8\pi} \int_{\eta_{k-1}}^{\eta_k} \int_{\xi_{m-1}}^{\xi_m} S_{ij}^w(\mathbf{x}_M, \mathbf{X}_M; \gamma, \Delta) \, ds \, dt, \quad (4.24)$$

where the values of $1 \leq \alpha', \beta \leq 3N_\xi N_\eta$ determine the force and velocity component indices $1 \leq i, j \leq 3$ through the equalities

$$\alpha' = 3(k' - 1)N_\xi + 3(m' - 1) + i, \quad \beta = 3(k - 1)N_\xi + 3(m - 1) + j, \quad (4.25)$$

where $1 \leq k, k' \leq N_\eta$, $1 \leq m, m' \leq N_\xi$ and (k', m') and (k, m) index the panels on which velocity and force, respectively, are being evaluated. Profiles were generated on a 30×30 mesh, with convergence verified on a 50×50 mesh.

4.3.2 Lubrication limit

As in § 4.2.2, when $\Delta \sim \gamma^{-1} \ll \epsilon$ the dominant drag contribution will come from an unsteady lubrication region between the wall and the plate. The flow in this gap can be examined by rescaling distances, velocities and pressures in the usual way

$$x_1 = \tilde{x}_1, x_2 = \tilde{x}_2, x_3 = \Delta \tilde{x}_3, u_1 = \Delta^{-1} \tilde{u}_1, u_2 = \Delta^{-1} \tilde{u}_2, u_3 = \tilde{u}_3, p = \Delta^{-3} \tilde{p}. \quad (4.26)$$

The leading-order flow is then governed by (dropping tildes)

$$i\tau^2 u_1 = -\frac{\partial p}{\partial x_1} + \frac{\partial^2 u_1}{\partial x_3^2}, \quad i\tau^2 u_2 = -\frac{\partial p}{\partial x_2} + \frac{\partial^2 u_2}{\partial x_3^2}, \quad \frac{\partial p}{\partial x_3} = 0, \quad \nabla \cdot \mathbf{u} = 0, \quad (4.27)$$

($\tau = \gamma\Delta$) subject to the no-slip and no-penetration conditions under prescribed plate velocity $w(x_1, x_2)$

$$\mathbf{u}(x_1, x_2, 0) = \mathbf{0}, \quad \mathbf{u}(x_1, x_2, 1) = w(x_1, x_2) \hat{\mathbf{x}}_3. \quad (4.28)$$

This is solved by

$$u_1 \hat{\mathbf{x}}_1 + u_2 \hat{\mathbf{x}}_2 = \mathbf{A} e^{\sqrt{i\tau} x_3} + \mathbf{B} e^{-\sqrt{i\tau} x_3} - \frac{1}{i\tau^2} \nabla_s p, \quad (4.29a)$$

$$u_3 = \nabla_s \cdot \mathbf{B} \frac{e^{-\sqrt{i\tau} x_3}}{\sqrt{i\tau}} - \nabla_s \cdot \mathbf{A} \frac{e^{\sqrt{i\tau} x_3}}{\sqrt{i\tau}} + x_3 \frac{\nabla_s^2 p}{i\tau^2} + C, \quad (4.29b)$$

where $\nabla_s = (\partial/\partial x_1, \partial/\partial x_2)$ and

$$\mathbf{A} = \frac{\nabla_s p}{2i\tau^2} \left(\frac{1 - e^{-\sqrt{i\tau}}}{\sinh \sqrt{i\tau}} \right), \quad \mathbf{B} = \frac{\nabla_s p}{2i\tau^2} \left(\frac{e^{\sqrt{i\tau}} - 1}{\sinh \sqrt{i\tau}} \right), \quad C = \nabla_s^2 p \left(\frac{1 - \cosh \sqrt{i\tau}}{i^{3/2} \tau^3 \sinh \sqrt{i\tau}} \right). \quad (4.29c)$$

The no-penetration condition at $x_3 = 1$ then provides a Poisson equation for the pressure

$$\nabla_s^2 p = k_0(\tau) w(x_1, x_2), \quad (4.30a)$$

$$k_0(\tau) = \frac{(\sqrt{i\tau})^3 \sinh \sqrt{i\tau}}{(2 - 2 \cosh \sqrt{i\tau} + \sqrt{i\tau} \sinh \sqrt{i\tau})}, \quad (4.30b)$$

$$p(\mathcal{S}_b) = 0, \quad (4.30c)$$

where we have specified the pressure on the rim of the plate's underside \mathcal{S}_b to be zero, to leading-order in Δ . In the quasi-steady limit $\tau \rightarrow 0$, where vorticity diffuses distances much greater than the gap thickness, $k_0(\tau) \rightarrow 12$ in agreement with Kim et al. (2001b).

When the prescribed velocity is uniform ($w(x_1, x_2) = w$) there is a closed solution for (4.30) which is obtained by splitting the pressure into an inhomogeneous solution

$$p_I = (x_1^2 - 1)k_0(\tau)w/2, \quad (4.31)$$

which violates the zero-valued boundary condition on $x_2 = \pm\epsilon$ and an harmonic solution p_h which restores the boundary conditions, i.e.

$$\nabla^2 p_h = 0, \quad p_h(\pm 1, x_2) = 0, \quad p_h(x_1, \pm\epsilon) = (1 - x_1^2)k_0(\tau)w/2. \quad (4.32)$$

Then, solving Laplace's equation by separation of variables, we arrive at

$$p(x_1, x_2) = k_0(\tau)w \left(\frac{(x_1^2 - 1)}{2} + \frac{16}{\pi^3} \sum_{\substack{k=1 \\ k \text{ odd}}}^{\infty} \frac{\sin(k\pi(1+x_1)/2)a_k(x_2)}{k^3 a_k(\epsilon)} \right), \quad (4.33a)$$

where

$$a_k(x_2) = \sinh(k\pi(1+x_2)/2) + \sinh(k\pi(1-x_2)/2). \quad (4.33b)$$

Narrow plate limit ($\epsilon \ll 1$)

In preparation for later work on elastic plates (§ 5.2.1), we consider the case where the plate is narrow ($\epsilon \ll 1$) and the plate velocity is dependent upon x_1 alone. Rescaling $x_2 = \epsilon \tilde{x}_2$, (4.30) then takes the form

$$\frac{\partial^2 p}{\partial \tilde{x}_2^2} + \epsilon^2 \frac{\partial^2 p}{\partial x_1^2} = \epsilon^2 k_0(\tau)w(x_1), \quad (4.34)$$

subject to $p(0) = p(1) = 0$. Expanding the pressure $p = p^{(0)} + \epsilon^2 p^{(1)} + \epsilon^4 p^{(2)} + \dots$ and respecting symmetry about $\tilde{x}_2 = 0$, at leading order we find the trivial solution and its first-order correction

$$p^{(0)} = 0, \quad p^{(1)} = \frac{1}{2}k_0(\tau)w(x_1)(\tilde{x}_2^2 - 1). \quad (4.35)$$

This outer solution is unable to satisfy both zero pressure and non-zero deflection conditions at $x_1 = 0$ and $x_1 = 1$ at the same time. We therefore consider the end region where $x_1 = O(\epsilon)$ by rescaling $x_1 = \epsilon \tilde{x}_1$, which leaves us needing to solve

$$\frac{\partial^2 p^{(1)}}{\partial \tilde{x}_2^2} + \frac{\partial^2 p^{(1)}}{\partial \tilde{x}_1^2} = k_0(\tau)w(0) \quad (4.36a)$$

for the non-trivial pressure, subject to

$$p^{(1)}(0, \tilde{x}_2) = p^{(1)}(\tilde{x}_1, 0) = 0, \quad p^{(1)}(\tilde{x}_1, \tilde{x}_2) \rightarrow \frac{1}{2}k_0(\tau)w(0)(\tilde{x}_2^2 - 1) \text{ as } \tilde{x}_1 \rightarrow \infty. \quad (4.36b)$$

As before, this Poisson equation can be solved by posing the inhomogeneous solution

$$p_I^{(1)} = \frac{1}{2}k_0(\tau)w(0)(\tilde{x}_2^2 - 1), \quad (4.37)$$

which matches the outer solution as $\tilde{x}_1 \rightarrow \infty$ and then calculating the harmonic function which cancels the non-zero values of the pressure at $\tilde{x}_1 = 0$ and decays at large \tilde{x}_1

$$\begin{aligned} \nabla^2 p_h^{(1)} &= 0, \\ p_h^{(1)}(0, \tilde{x}_2) &= \frac{1}{2}k_0(\tau)w(0)(1 - \tilde{x}_2^2), \quad p_h^{(1)}(\tilde{x}_1, 1) = 0, \quad p_h^{(1)} \rightarrow 0 \text{ as } \tilde{x}_1 \rightarrow \infty. \end{aligned} \quad (4.38)$$

Separation of variables then gives us the end-region pressure near $x_1 = 0$

$$p(\tilde{x}_1, \tilde{x}_2) = k_0(\tau)w(0) \left(\frac{(\tilde{x}_2^2 - 1)}{2} + \frac{16}{\pi^3} \sum_{\substack{k=1 \\ k \text{ odd}}}^{\infty} \frac{\sin(k\pi(1 + \tilde{x}_2)/2)e^{-k\pi\tilde{x}_1/2}}{k^3} \right). \quad (4.39)$$

(Similar analysis gives the end-region pressure near $x_1 = 1$.) Hence the pressure can then be expressed as the following composite expansion:

$$\begin{aligned} p^{(1)}(x_1, x_2) &= \frac{1}{2}k_0(\tau)w(x_1)(x_2^2 - \epsilon^2)/\epsilon^2 \\ &+ \frac{16k_0(\tau)w(0)}{\pi^3} \sum_{\substack{k=1 \\ k \text{ odd}}}^{\infty} \frac{\sin(k\pi(\epsilon + x_2)/2\epsilon)e^{-k\pi x_1/2\epsilon}}{k^3} \\ &+ \frac{16k_0(\tau)w(1)}{\pi^3} \sum_{\substack{k=1 \\ k \text{ odd}}}^{\infty} \frac{\sin(k\pi(\epsilon + x_2)/2\epsilon)e^{-k\pi(1-x_1)/2\epsilon}}{k^3}. \end{aligned} \quad (4.40)$$

In § 4.4 we compare pressure profiles obtained using this composite expression against the numerical solutions of (4.30) when w is a prescribed function of x_1 . Note that this numerical scheme has been developed primarily to solve a more general class of deflections which depend upon both x_1 and x_2 (see § 5.2.1).

4.4 Results

We begin by examining the two-dimensional flow generated by plate of finite thickness (§ 4.4.1) computed using both viscous and inviscid boundary-elements methods (BEM). The flow is visualized through surface stress plots and via flowfield representations. Drag results reveal the impact of varying γ , Δ and the aspect ratio, making comparison with the drag experienced by a cylinder with circular cross-section, computed in chapter 2, as well as lubrication theory (4.17). The validity of the two-dimensional TPT approximation (4.10) is tested in § 4.4.2, together with its high-frequency limit. Finally, § 4.4.3 looks at the limitations of a two-dimensional flow assumption, by comparing three-dimensional TPT profiles (4.22) against two-dimensional BEM predictions (4.3), as well as presenting three-dimensional lubrication theory results.

4.4.1 Two-dimensional finite-thickness plate

Stokeslet profiles and flow visualization

Surface stresses are readily obtainable using BEM and serve to illustrate the impact of the nearby wall. Figure 4.2 shows the vertical component of the surface stress on the wall and the infinite-length square cantilever for the case where $\epsilon\gamma = \Delta/\epsilon = 1$. The difference in stress profiles on the top and bottom of the cantilever, as well as the skewed shear stress on the cantilever's side, are both a sign of the wall's influence. The integrable stress singularities at each edge of the body are evident, although in practice it is likely that geometrical smoothing or wall slip (particularly in gases) would act to regularize this singular behaviour.

Once the stress profile is known, it can be substituted back into (4.3) to yield the velocity at a given point in the flow. This has been done in figure 4.3 and the resulting flowfields demonstrate, at a given instant in time ($t = 0$), the formation of boundary layers on the body surface as γ is increased (figure 4.3*a,b*), as well as the flow's fore-aft asymmetry when the wall is nearby (figure 4.3*c*).

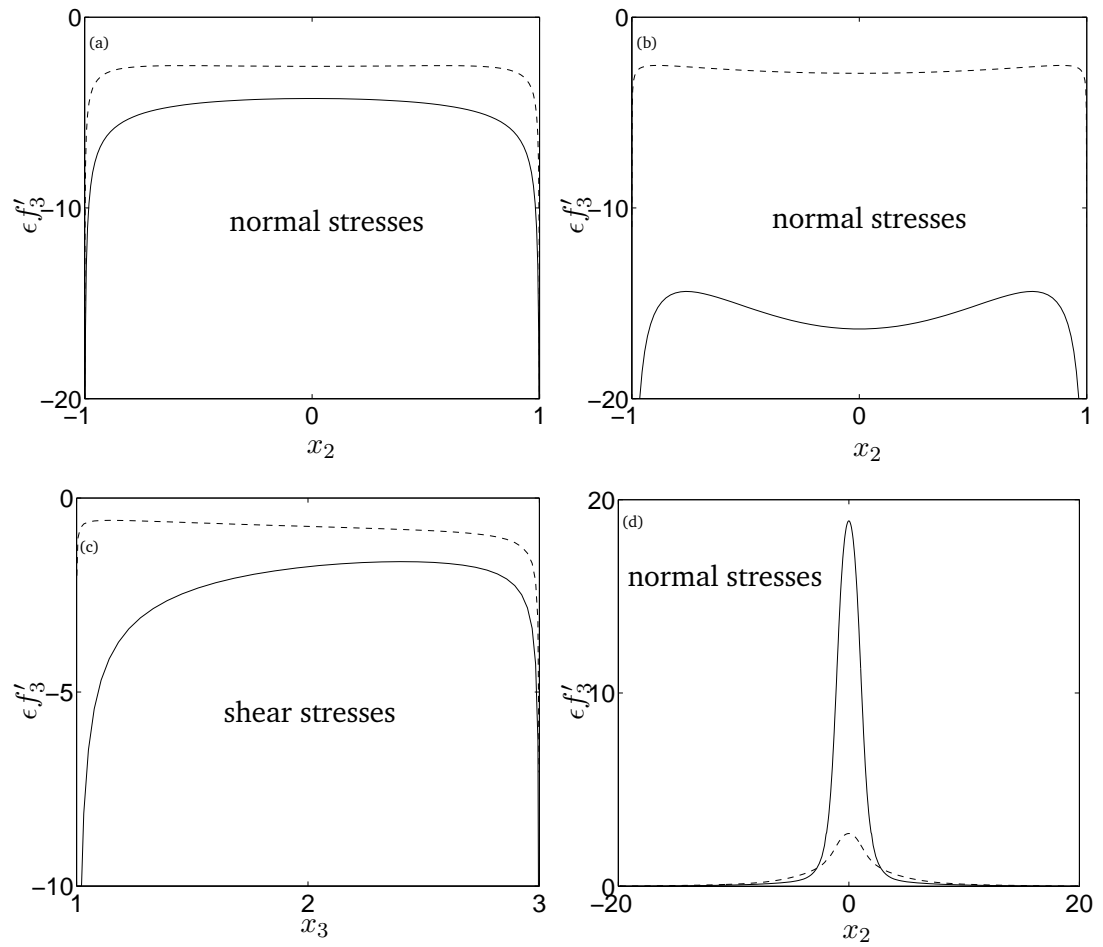


FIGURE 4.2: Normal component of surface stress on (a) top, (b) bottom and (c) side of rectangular cantilever with $d/\epsilon = 1$, when $\epsilon\gamma = 1$ and $\Delta/\epsilon = 1$. Plot (d) shows the normal component of surface stress on the wall. Real parts are given by a full line and imaginary parts by a dashed line.

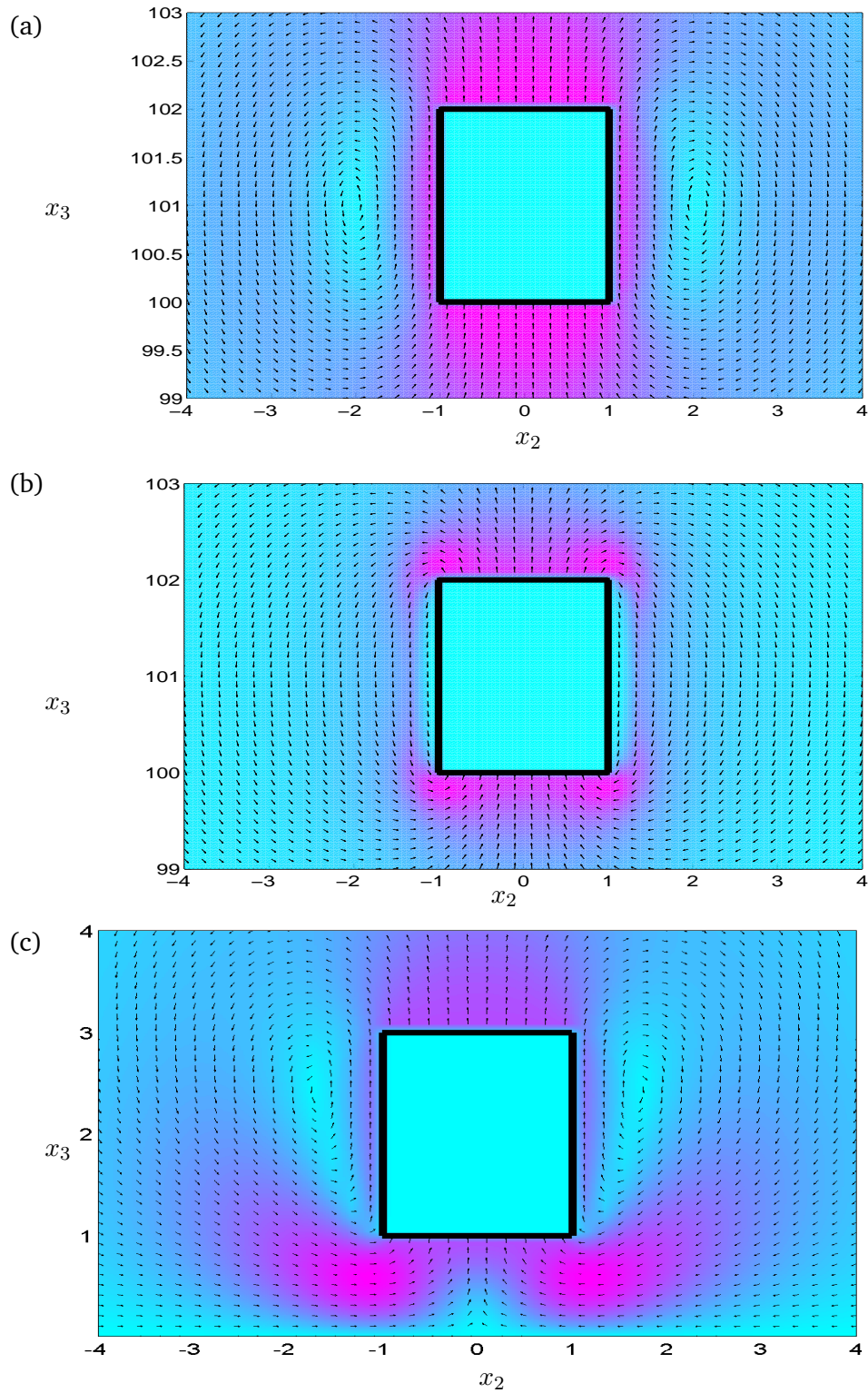


FIGURE 4.3: Flow fields for a plate (lengths scaled on R) with unit aspect ratio ($d/\epsilon = 1$) at time $t = 0$ oscillating with (a) $\epsilon\gamma = 1$ with $\Delta/\epsilon = 100$, (b) $\epsilon\gamma = 10$ with $\Delta/\epsilon = 100$ and (c) $\epsilon\gamma = 1$ when $\Delta/\epsilon = 1$, computed using boundary-element methods (4.3). The arrows (all of unit length) indicate the direction of the flow velocity and shading represents the flow speed $|\mathbf{u}|$.

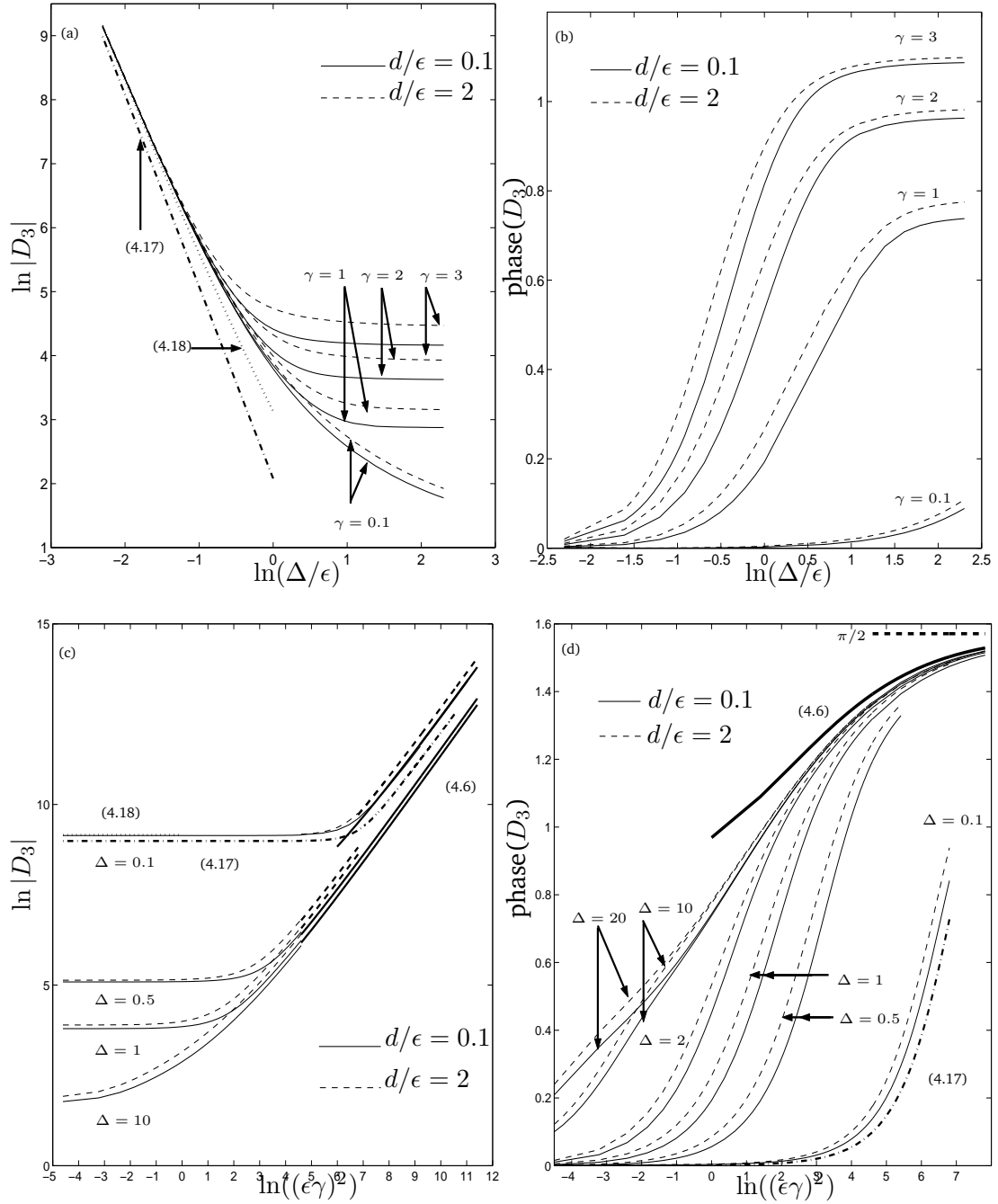


FIGURE 4.4: Modulus (a) and phase (b) of the drag on a cantilever, when $d/\epsilon = 0.05$ (solid line) or $d/\epsilon = 1$ (dashed line), over a range of Δ and the modulus (c) and phase (d) of the drag over a range of γ . The unsteady lubrication limit (4.17), for an infinitely thin plate, is marked by a thick dash-dotted line, and is plotted alongside a quasi-steady limit which accounts for the full geometry (4.18). The thick solid lines in (c, d) show drag predictions computed using a separate boundary-element scheme for the potential flow (4.6).

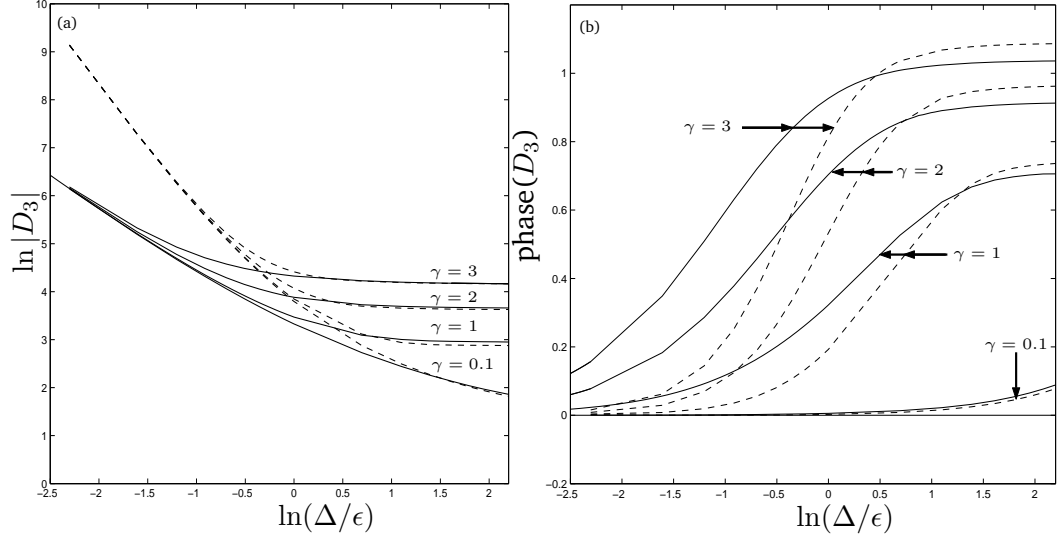


FIGURE 4.5: Comparison between (a) the modulus and (b) the phase of the drag on a circular cantilever (full line) and rectangular cantilever with $d/\epsilon = 0.1$ (dashed line).

Drag

Rectangular cantilever drag results are presented in figure 4.4 for two different cantilever shapes, thin (aspect ratio 20) and square. The dependence of modulus and phase on Δ and γ is broadly similar to the circular case, however, we are now in a position to assess the impact of differing aspect ratio. The dash-dotted lines represent a lubrication limit for the drag on the cantilever (4.17).

Figures 4.4(a, c) illustrate the improvements offered by the quasi-steady $\Delta/\epsilon \ll 1$ drag prediction (4.18), which corrects the standard lubrication drag $D = 8(\Delta/\epsilon)^{-3}$ to account for the full plate geometry. Moreover, figures 4.4(c, d) demonstrate the effectiveness of (4.17) in capturing the influence of flow inertia on the drag in the lubrication regime, as well as the effectiveness of the inviscid BEM predictions (4.6) at high frequencies.

These results confirm that thin cantilevers experience less drag than square ones, but this distinction is diminished when quasi-steady effects dominate the drag, i.e. when either $\epsilon\gamma$ or Δ/ϵ become sufficiently small. If the cantilever is sufficiently close to the wall, the phase of the drag is independent of the cantilever's aspect ratio. However,

as the separation is increased, the phases in each case differ, particularly at higher frequencies. If the separation is increased still further, the sensitivity of the drag's phase to the cantilever's thickness begins to diminish.

Comparing circular and rectangular cantilevers (figure 4.5) we see that the drag on a thin rectangular cantilever is similar to that on a circular cantilever of the same width for sufficiently large wall–cantilever separations. The similarity between the drag for an oscillating infinitely thin plate and an oscillating cylinder in an unbounded fluid, first noted by Tuck (1964), persists at moderate distances from a rigid wall (and moreover, as shown in figure 4.4(a), extends to cantilevers of other aspect ratios at low frequencies). However, the drag on a thin cantilever diverges significantly from that on a circular cantilever as Δ is decreased, as we would expect. For separations less than roughly one cantilever width, there is a dramatic increase in the drag's modulus and a significant drop in its phase (the former more so and the latter less so at low frequencies; see figure 4.5, reflecting the differing size of the lubrication regions in each case. So whilst the circular cylinder approximation to an AFM cantilever works well when the sample–cantilever interaction is of little interest (e.g. perhaps during cantilever calibration), but shape is otherwise an important factor.

4.4.2 Two-dimensional thin-plate theory

Stokeslet profiles

In the two-dimensional thin-plate-theory (TPT) limit ($d/R \ll 1$) (4.10) approximates the flow using a distribution of Stokeslets along the plate's centre-line, plotted in figure 4.6 for the cases where (a) $\Delta/\epsilon = 100$, $\epsilon\gamma = 3$, (b) $\Delta/\epsilon = 1$, $\epsilon\gamma = 1$ and (c) $\Delta/\epsilon = 100$, $\epsilon\gamma = 50$. As (4.10) is a limiting case of the boundary-integral formulation (4.3), we expect the centre-line Stokeslet distribution to be equal to the sum of the upper and lower Stokeslet distributions in the full BEM computations. Figures 4.6(a,b) show that this is indeed the case. Additionally, panel (c) demonstrates the effectiveness of high-frequency thin-plate-theory (HFTPT) (4.13), by comparing the Stokeslet distribution against that computed using the more general TPT method (4.10). Away from the

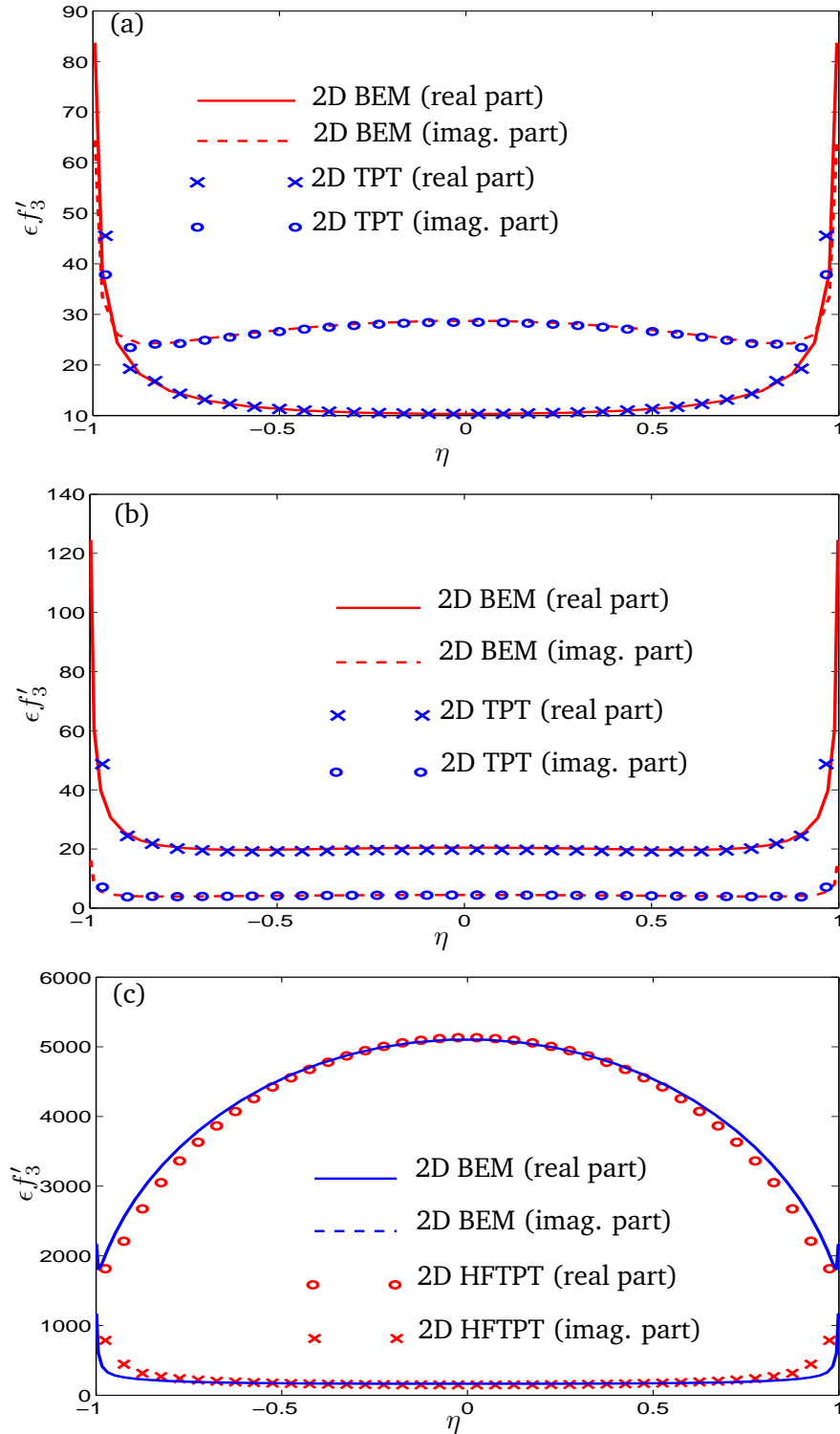


FIGURE 4.6: Vertical component of Stokeslet strength f_3 for a thin two-dimensional plate ($\epsilon = 10^{-2}$) computed using two-dimensional BEM (a-c) (4.3) (lines) plus (a,b) two-dimensional thin-plate-theory TPT (4.10) (markers) and (c) high-frequency thin-plate theory HFTPT (4.13) (markers) when (a) $\Delta/\epsilon = 100$, $\epsilon\gamma = 3$, (b) $\Delta/\epsilon = 1$, $\epsilon\gamma = 1$ and (c) $\Delta/\epsilon = 100$, $\epsilon\gamma = 50$.

ends (where the Stokeslet distribution and its derivatives are singular) (4.13) is seen to perform well in capturing the highly non-uniform Stokeslet distribution, caused by the sensitivity of inviscid flow to plate geometry.

4.4.3 Three-dimensional thin-plate theory

Stokeslet profiles

Figures (4.7, 4.8) show the mid-plane Stokeslet distributions f_3 , obtained using three-dimensional TPT (4.22) in the absence of any wall. As with oscillating finite-length circular cylinder studied in chapter 3, we see how the frequency of oscillation can control the range of finite-length effects. When $\gamma^{-1} = 100$, as in figure 4.7, the length scale over which vorticity diffuses is much larger than the plate length and so the cross-sectional Stokeslet profile differs from the two-dimensional BEM predictions. However, when we increase the frequency of oscillation so that $\gamma^{-1} = 0.1$ (figure 4.8), vorticity is confined to the plate edges (γ -screening). Consequently when the plate is considerably longer than it is wide, a Stokeslet cross-section at $\xi = 0$ is seen to give good agreement with two-dimensional BEM computations, with deviation from this profile only occurring at $O(\epsilon)$ distances from $\xi = \pm 1$. The same is not necessarily true for a cross section taken along $\eta = 0$, however, because the long edges ($\eta = \pm 1$) are capable of generating three-dimensional flows over $O(1)$ distances. So whilst very close to both the long edges and short edges ($\xi = \pm 1$) we expect an $O(s^{-\alpha_0})$ singularity in the Stokeslet profile, where $\alpha_0 \approx 0.5$ for viscous flow around a flat plate (Dean and Montagnon 1949), the flows away from these very localized regions differ at the two edge types (as observed in figures 4.7 and 4.8). By contrast, long edges are largely unaffected by the limited $O(\epsilon)$ range of short-edge flows, (hence the need for both a narrow plate and γ -screening for good agreement with two-dimensional theory at $\xi = 0$). The flow near the corners is more complex, with no simple canonical flow providing the strength of the singularity, although the profiles would suggest that this corner flow is more singular than along the edges.

By integrating the two-dimensional Stokeslet distribution over the plate surface we

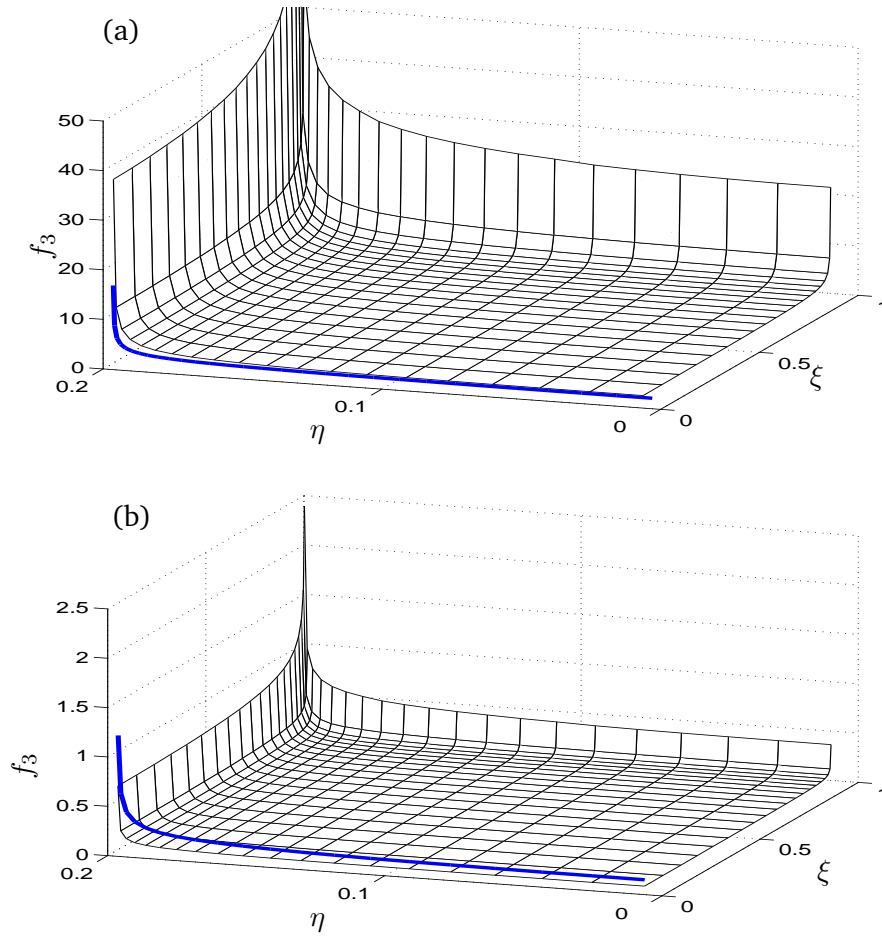


FIGURE 4.7: Real (a) and imaginary (b) parts of the vertical component of the Stokeslet distribution f_3 , computed using three-dimensional thin-plate-theory (TPT) (4.22) when $\gamma = 0.01$, $d/\epsilon = 10^{-2}$, in the absence of a wall. The thick line gives the predictions of two-dimensional BEM (4.3).

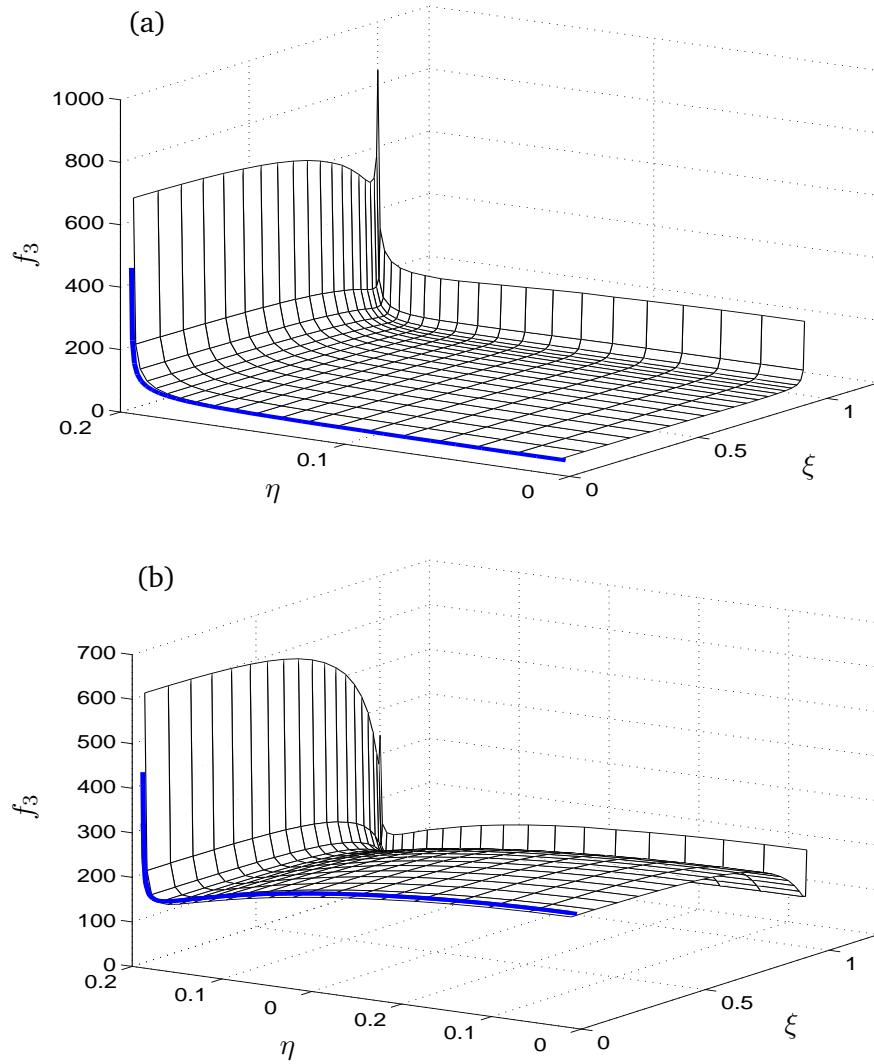


FIGURE 4.8: Real (a) and imaginary (b) parts of the vertical component of the Stokeslet distribution f_3 computed using three-dimensional TPT (4.22) when $\gamma = 10$, $\epsilon = 0.2$ and $d/\epsilon = 10^{-2}$, in the absence of a wall. The superimposed thick line gives the predictions of two-dimensional BEM (4.3).

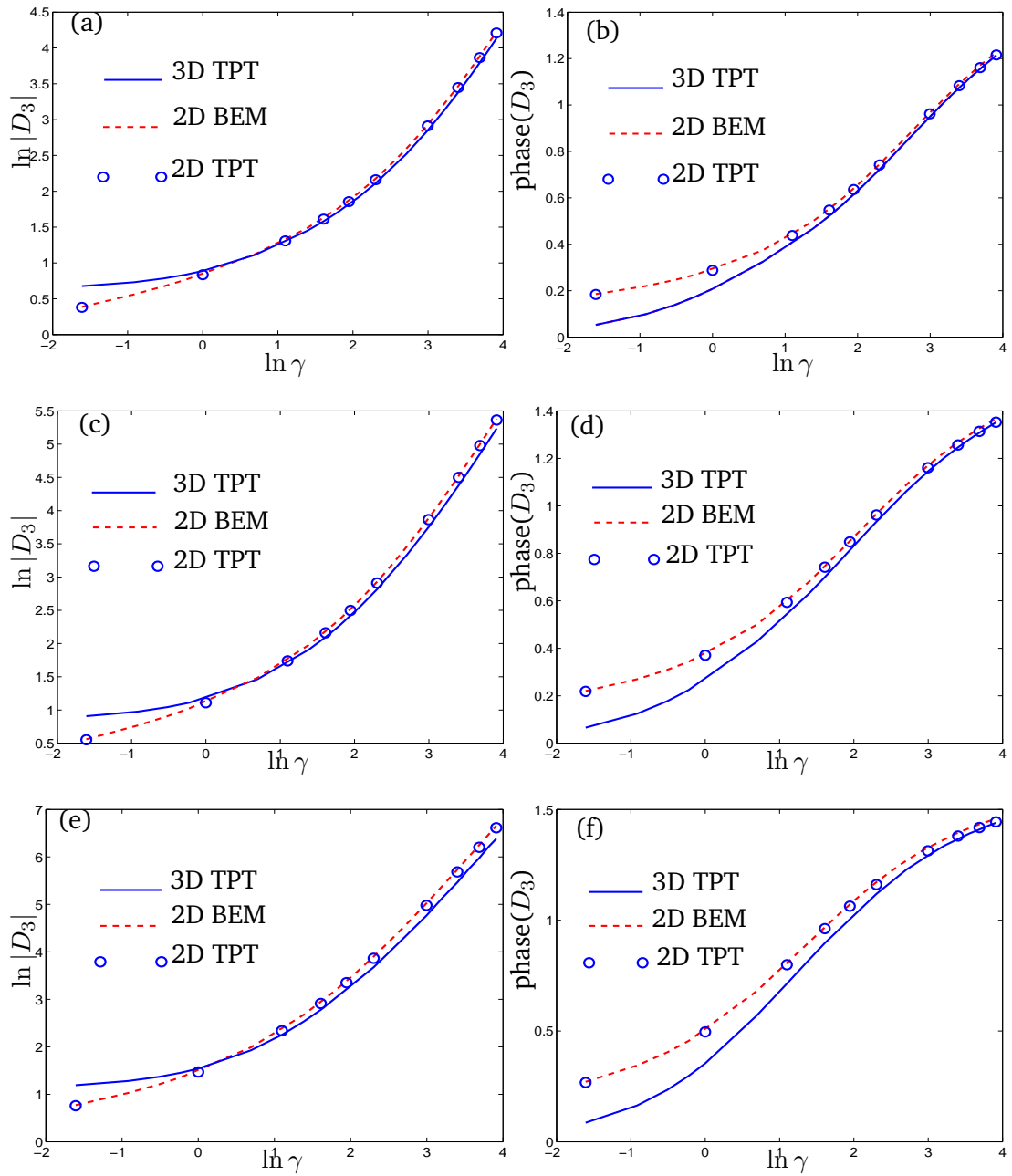


FIGURE 4.9: Modulus (a,c,e) and phase (b,d,f) of the three-dimensional TPT drag (full line) evaluated over a range of γ , compared with the two-dimensional BEM drag (dashed line) and the two-dimensional TPT formulation (markers) when (a,b) $\epsilon = 0.1$, (c,d) $\epsilon = 0.2$ and (e,f) $\epsilon = 0.4$, in the absence of a wall.

can obtain the drag, as plotted in figure 4.9 as a function of γ for several different aspect ratios, computed using two-dimensional TPT and BEM in addition to three-dimensional TPT techniques. In two-dimensions, TPT and BEM predictions are seen to be in consistent agreement. In contrast, when comparing two- and three-dimensional drags, we see the expected divergence between two- and three-dimensional predictions at low γ due to the increasing influence of three-dimensionality via long-ranged viscous length-scales. When the frequency of oscillation is increased, the two- and three-dimensional drags initially converge, as viscous end effects become shorter ranged. However, γ -screening is unable to prevent the three-dimensional flows generated by finite-width effects and these ultimately lead to the eventual divergence between the two- and three-dimensional drags at large γ (still within AFM operating range), with the rate of this divergence increased as the plate becomes wider.

4.4.4 Three-dimensional lubrication theory

Figure 4.10 demonstrates the two-dimensional nature of the flow over much of the plate's surface at small separations ($\Delta = 0.01$), when using three-dimensional lubrication theory under prescribed uniform velocity (4.33). End effects ($x_1 = 0$ and $x_1 = 1$) are clearly in evidence (figures 4.10*a,b*) in the three-dimensional pressure profiles, however, cross-sections taken away from the ends ($x_1 = 0.5$) show good agreement with the two-dimensional result (4.16) (figures 4.10*c,d*). Noting that $\gamma = 0.01$, which figure 4.7 has demonstrated is too low for γ -screening, we deduce that the two-dimensionality arises from Δ -screening effects. Integrating the three-dimensional pressure distribution over the plate surface yields the drag, which is shown by figures 4.10(*e,f*) to agree well with the predictions of two-dimensional lubrication theory. When the prescribed velocity is not uniform, but rather depends upon x_1 , we are still able to determine the pressure profile over the plate asymptotically, provided that it is sufficiently narrow. Figure 4.11 presents the pressure profiles when the velocity is given by $w = \cos x_1$, which have been calculated both numerically by solving (4.30) using a finite-difference scheme and also using the composite expansion (4.40). As can be seen, agreement between the two is excellent, with the composite expansion fully accounting for the

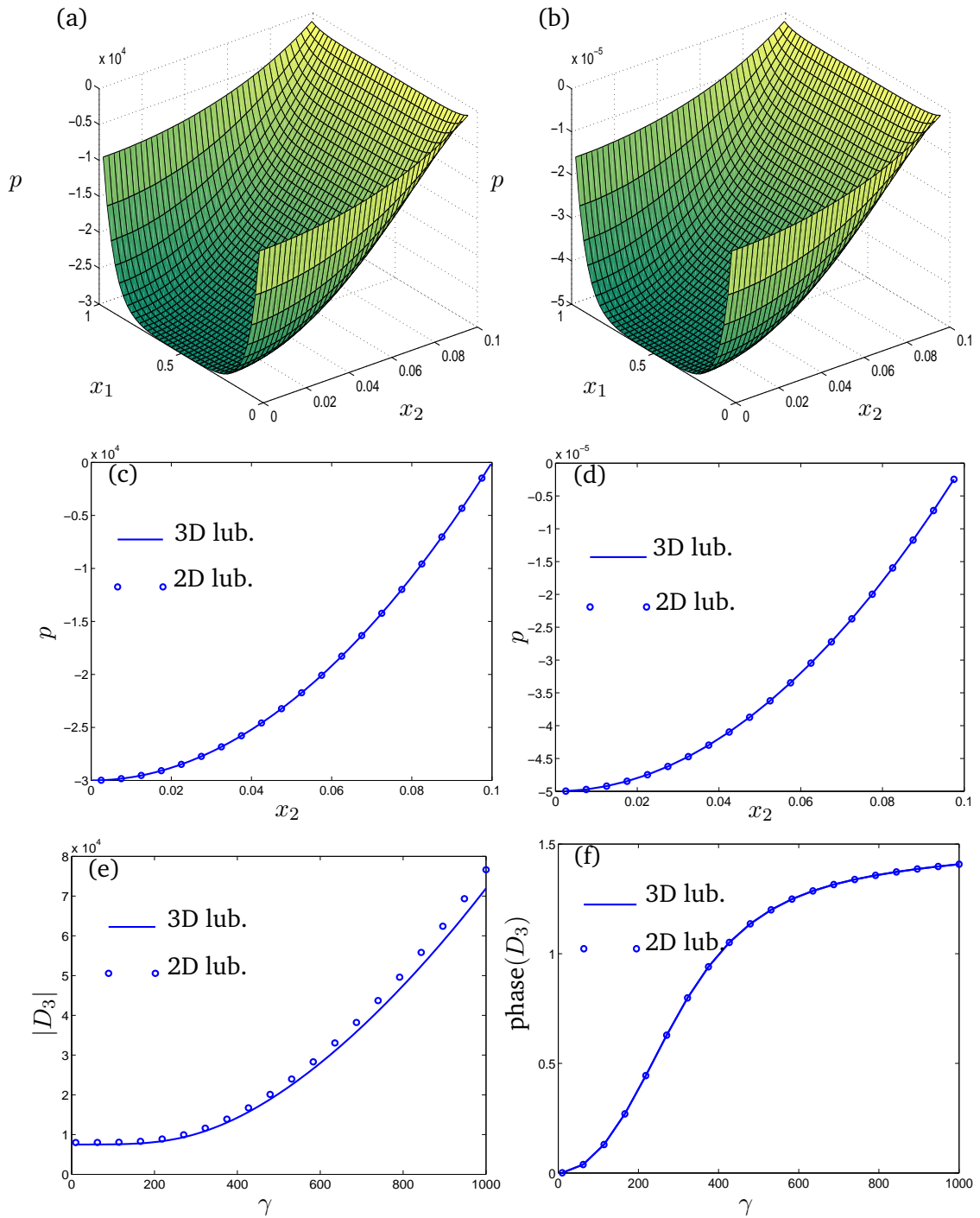


FIGURE 4.10: Real (a) and imaginary (b) parts of the three-dimensional pressure profile in the lubrication limit (4.33) for a plate with aspect ratio $\epsilon = 0.1$ when $\gamma = 0.01$ and $\Delta = 0.01$, with uniform prescribed velocity $w = 1$. Cross-sectional slices taken at $x_1 = 0$ are compared against real (c) and imaginary (d) components of the two-dimensional lubrication pressure profiles ((4.16), markers). The amplitude (e) and phase (f) of the corresponding two- (4.17, markers) and three-dimensional drags are plotted for $\Delta = 0.01$ over a range of γ .

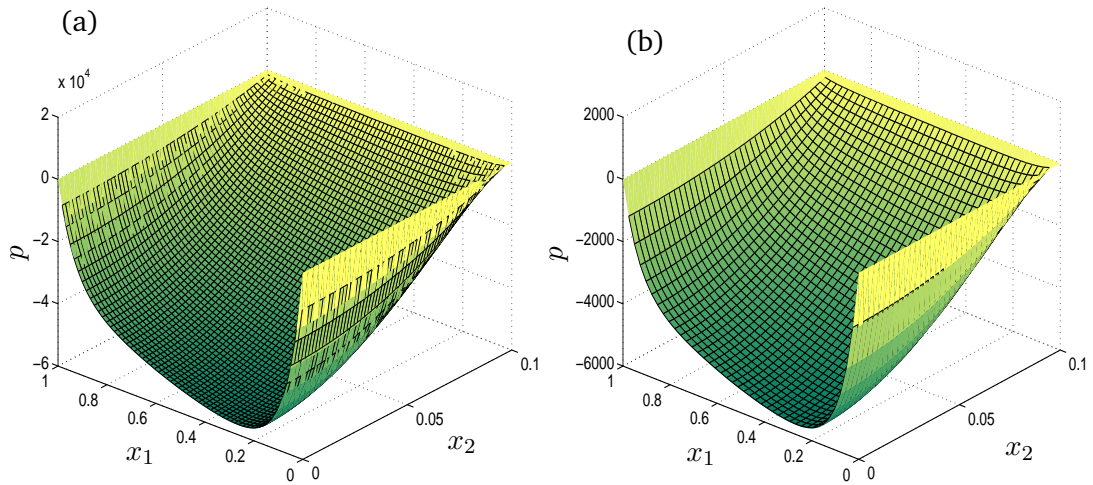


FIGURE 4.11: Real (a) and imaginary (b) parts of the pressure profile under a plate when $\gamma = 100$, $\Delta = 0.01$ and $\epsilon = 0.1$ when the velocity is prescribed as $w(x_1) = \cos x_1$, computed by solving Poisson's equation (4.30) numerically (shaded surface) and using narrow-plate asymptotics (4.40) (wire mesh).

rapidly changing pressure profile at $x_1 = 0$ and $x_1 = 1$.

4.5 Discussion

We have examined the flow generated by oscillating plates using a variety of techniques. For a plate which is much greater in length than in width, we made a two-dimensional flow assumption which reduced the plate geometry down to a rectangle. For a plate of arbitrary thickness, the flow was formulated in terms of a boundary-integral representation which distributed oscillatory image-Stokeslets over the two-dimensional cross-sectional surface. In the high-frequency case, a boundary-layer approximation was adopted, where the inviscid flow was again formulated in terms of a boundary-integral. These boundary-integral representations were then solved using boundary-element methods (BEM). Note that parallel and independent work by Green and Sader (2005) also recognises the importance of wall effects in the AFM and uses BEM to study the two-dimensional flow generated by a rectangular cylinder. Their boundary-integral

representation uses the streamfunction-pressure formulation proposed by Tuck (1964) and, as such, cannot be extended to study three-dimensional plates as we have done here.

In the limiting case of a thin plate we developed thin-plate-theory (TPT) formulation which approximated the surface distribution of Stokeslets using one-dimensional distribution over the plate's centre-line. Under a high-frequency constraint, the formulation was further simplified to a line distribution of dipoles, with viscous effects captured by a local force-velocity coefficient. This TPT formulation was then extended into three dimensions, using a two-dimensional distribution of Stokeslets over the plate's mid-plane. In the small separation limit two- and three-dimensional lubrication theory was able to describe the flow.

For two-dimensional rectangular cantilevers oscillating at high frequency, the wall has a substantial effect. For $\gamma^{-1} \ll \Delta \ll 1$, the unsteady acceleration of liquid along the narrow gap dominates the drag (see (4.17); this is an inviscid lubrication regime); for $\Delta \sim \gamma^{-1}$ the Stokes layers fill the gap, and then for $\Delta \ll \gamma^{-1}$ the dominant drag is from viscous lubrication forces.

One of the most striking findings from the two-dimensional BEM computations is the very weak dependence of drag on aspect ratio. Comparing rectangular cantilevers with $d/\epsilon = 1$ and $d/\epsilon = 0.05$, figure 4.4 shows (not surprisingly) negligible difference in the thin-gap limit ($\Delta/\epsilon \ll 1$) and differences of only a few percent at high frequencies. This high-frequency insensitivity is also demonstrated in figure 4.5, which reflects Tuck's (1964) observation that a plate of the same width serves as a good model for a cylinder (in the absence of a wall). However, figure 4.5 provides clear evidence of the limitations of using the drag on a two-dimensional circular cylinder (2.19), an approximation used commonly in AFM studies (e.g. Sader 1998): the drag on a thin rectangular cylinder rises dramatically (note the logarithmic scale in figure 4.5) and the phase falls substantially as Δ falls below $O(1)$ values, an experimentally realized regime.

The thin-plate-theory (TPT) formulation was developed to lower computation overheads when $d/\epsilon \ll 1$ by using only a centre-line distribution of Stokeslets to approxi-

mate the flow. The Stokeslet profiles obtained using this method were shown to approximate the full BEM computations well (figure 4.6). Near to the wall, profiles differed on the upper and lower surfaces using BEM; TPT correctly predicts, however, the additive profile (i.e. top plus bottom) which is all that is required for determining the overall drag (figure 4.6*b*). When $\gamma \gg 1$ further simplifications are possible; in high-frequency thin-plate-theory (HFTPT), viscous effects are captured by a local coefficient and all non-local phenomena are contained by a dipole distribution, which can be treated analytically, thereby eliminating the need for numerical quadrature. Figure 4.6(*c*) demonstrates the effectiveness of HFTPT by comparing with profiles obtained using the more demanding BEM formulation (4.3). Only near the ends does HFTPT differ noticeably, suggesting the need to include $O(\gamma^{-1})$ corrective terms.

The benefits of the TPT formulation are especially realised in three dimensions, where we can use it to compute flows which would otherwise be unfeasible using BEM under conventional processing power. Consideration of narrow plates provides the opportunity to validate the numerical scheme, since at large enough frequencies γ -screening leaves cross-sectional profiles away from the ends in good agreement with two-dimensional BEM results (figure 4.8). Drag results showed good agreement between three-dimensional TPT predictions and two-dimensional BEM results for moderate γ , with the ϵ -dependent breakdown in this agreement at higher γ attributed to three-dimensional end-flow, the range of which scales with the plate's width. Although not presented here, at higher frequencies it should be possible to derive a three-dimensional version of HFTPT, by following the procedures laid out in § 4.2.1 for two dimensions.

Although the three-dimensional TPT formulation allows us to use image Stokeslets (3.4), the fact that their evaluation requires additional numerical integration makes their use prohibitively expensive. We do have, however, the three-dimensional lubrication result (4.33) for uniform plate velocity, which shows us how edge-effects are confined by Δ -screening (figure 4.10*a-d*), leading to a total drag on the plate which is well-approximated (see figure 4.10*e,f*) by two-dimensional lubrication theory (4.16). These end effects in the pressure profile can be captured asymptotically, as illustrated for the case where the prescribed plate velocity is a function of x_1 (figure 4.11). The

gently varying outer pressure profile is matched to end regions where the pressure varies rapidly, resulting in a uniformly valid expression for the pressure (4.40).

The plate hydrodynamics developed here give us further options for describing the fluid mechanics at work within an AFM and allow us to verify the limitations of earlier flow approximations. The next step is to couple the various flow models to an elastic description of a flexible body, which is the goal of the remaining two chapters.

Chapter 5

Damped dynamics of a sinusoidally-driven cantilever

Up to now we have considered the drag exerted upon a rigid body undergoing prescribed motion, yet in practice the AFM is a flexible body and its motion depends upon the drag generated by its dynamics. Determining this motion therefore requires an elasto-hydrodynamic treatment of the coupled fluid-structure system. This task is made easier by the restrictions on the magnitude of cantilever deformation, which allows us to linearize the flow equations and their boundary conditions, as well as the elasticity equations which describe flexural vibrations of the cantilever.

In § 5.1 we introduce the Bernoulli–Euler beam equation used to describe the spanwise (η -independent) deflections of a narrow cantilever which is subject to a hydrodynamic loading described by (i) two-dimensional flow models (§ 5.1.1), (ii) slender-body theory (§ 5.1.2) and (iii) modified-resistive-force theory (§ 5.1.3). In § 5.2 we extend the study to consider elastic plates whose deflection is a function of both ξ and η and which can be described using linear plate theory. The hydrodynamic loading is described using either (i) lubrication drag (§ 5.2.1) or (ii) TPT hydrodynamics (§ 5.2.2). The results are presented in § 5.3, with their implications discussed in § 5.4.

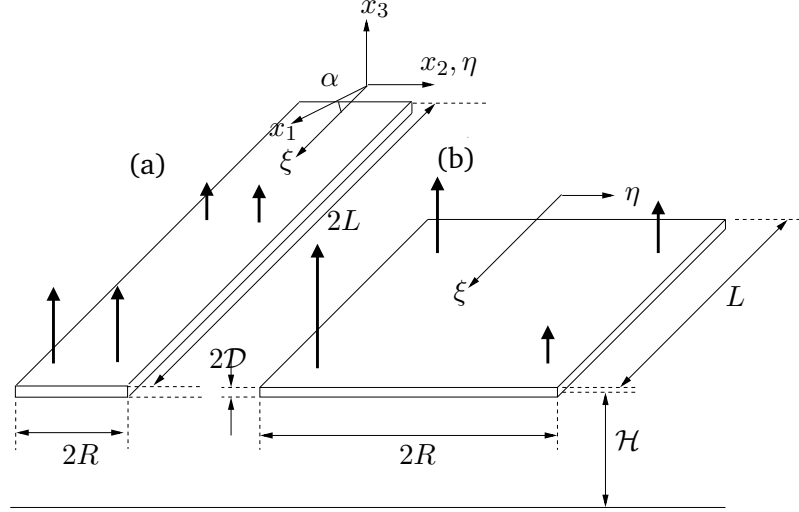


FIGURE 5.1: The elastic behaviour of a thin cantilever with length width $2R$ and thickness $2D$, with its mid-plane a distance \mathcal{H} from a rigid plane wall, can be described using linear elasticity theory. When the plate is (a) narrow (length $2L$, $D \ll R \ll L$) span-wise deflections in the η direction are negligible and the one-dimensional elastic dynamics can be described using the Euler–Bernoulli beam equation (5.1). Wider cantilevers (b) (length L , $D \ll R, L$) experience non-negligible span-wise deflections which must be described by the linear plate equation (5.7).

5.1 One-dimensional beams

We consider deflections $\mathcal{W}(\xi, \eta, t)$ in the \hat{x}_3 direction of a thin elastic beam of length $2L$, width $2R$ and thickness $2D$ ($D \ll R, L$), which is driven sinusoidally at a clamped end, tilted at angle α from the horizontal, with frequency ω and amplitude \mathcal{A} ($\mathcal{A} \ll D, R, L$) and where the non-clamped end is free. The mid-plane of this beam lies at a minimum distance \mathcal{H} from a rigid plane wall located at $\hat{x}_3 = 0$ (see figure 5.1a).

If we impose the further restriction that the cantilever is narrow ($R \ll L$), we expect little span-wise deflection and the one-dimensional planar deflections can be well-described by the Bernoulli–Euler beam equation, which is valid when

- (i) cantilever motion is confined to planar transverse deflections (i.e. no twisting or lateral movement),

- (ii) shear deformation is negligible compared to the bending deformation,
- (iii) rotation is negligible compared with transverse deflection.

Seeking oscillatory solutions $\mathcal{W}(\xi, t) = \text{Re}(w(\xi)e^{i\omega t})$, the (non dimensional) beam equation is given by (Kelly 1993)

$$w_{\xi\xi\xi\xi} - M\gamma^4 w = iM\Omega\gamma^2 \mathcal{F}(\xi; \gamma, \Delta), \quad (5.1a)$$

where subscripts denote derivatives. $\mathcal{F}(\xi; \gamma, \Delta)$ represents the hydrodynamic loading on the cantilever per unit length (scaled on $\mu\mathcal{A}\omega$) in the direction normal to the cantilever's axis, $\Omega \equiv \rho L^2/m_c$ depends upon the fluid to cantilever density ratio as m_c is the cantilever's mass per unit length and $M \equiv m_c\mu^2/\rho^2 EI$, where E and I are the cantilever's Young's modulus and moment of inertia, respectively. For a cantilever of given dimensions and density, operating in a fluid of given viscosity, M therefore characterizes its stiffness. For typical AFM experiments, $E \approx 10^{12} \text{gcm}^{-1}\text{s}^{-2}$, $I \approx 10^{-8} \text{cm}^4$, $\omega \approx 10^4 \text{s}^{-1}$ and $\rho_c \approx 1 \text{gcm}^{-3}$, resulting in $\gamma = 10^4$, $M \approx 10^{-4}$, $\Omega \approx 10^3$.

In simulating TM-AFM (see § 1.1.2), we are interested in a cantilever sinusoidally-driven in a direction normal to its axis, clamped at one end at an angle α to the horizontal. The driving amplitudes $\mathcal{A} \ll D$ are sufficiently small that at leading order the cantilever lies undeflected at an angle α to the horizontal. We analyse the normal deflections to this base state and hence (5.1) must be solved subject to clamped conditions at $\xi = -1$ and no-stress conditions at $\xi = 1$

$$w(-1) = 1, \quad w_\xi(-1) = w_{\xi\xi}(1) = w_{\xi\xi\xi}(1) = 0. \quad (5.1b)$$

5.1.1 Two-dimensional hydrodynamics

When the cantilever is horizontal ($\alpha = 0$) and when finite-length effects are confined to the cylinder ends ($\gamma \gg 1$ or $\Delta \ll 1$), we may assume that the hydrodynamic loading is essentially two-dimensional and (5.1a) then simplifies to

$$w_{\xi\xi\xi\xi} - \kappa^4 w(\xi) = 0 \quad (5.2a)$$

subject to (5.1b) with

$$\kappa = (M\gamma^4 + iM\Omega\gamma^2\Gamma(\epsilon\gamma, \Delta)\cos\alpha)^{1/4}, \quad (5.2b)$$

where $\Gamma(\epsilon\gamma, \Delta)$ is the two-dimensional drag coefficient appropriate for the particular parameter values (see chapter 2). This is solved by

$$w(\xi) = A_1 \cos \kappa\xi + A_2 \sin \kappa\xi + A_3 e^{\kappa\xi} + A_4 e^{-\kappa\xi}, \quad (5.3a)$$

where

$$A_1 = \frac{e^{2\kappa} + 1}{2(e^{2\kappa} \cos \kappa + e^{2\kappa} \sin \kappa + \cos \kappa - \sin \kappa)}, \quad (5.3b)$$

$$A_2 = \frac{e^{2\kappa} - 1}{2(e^{2\kappa} \cos \kappa - e^{2\kappa} \sin \kappa + \cos \kappa + \sin \kappa)}, \quad (5.3c)$$

$$A_3 = \frac{e^\kappa (e^{2\kappa} + 2 \cos^2 \kappa - 2 \sin \kappa \cos \kappa - 1)}{2(2e^{4\kappa} \cos^2 \kappa - e^{4\kappa} + 2e^{2\kappa} + 2 \cos^2 \kappa - 1)}, \quad (5.3d)$$

$$A_4 = \frac{e^\kappa (2e^{2\kappa} \sin \kappa \cos \kappa - e^{2\kappa} + 2e^{2\kappa} \cos^2 \kappa + 1)}{2(2e^{4\kappa} \cos^2 \kappa - e^{4\kappa} + 2e^{2\kappa} + 2 \cos^2 \kappa - 1)}. \quad (5.3e)$$

The validity of (5.3) is in doubt, however, when the two-dimensional flow assumption is unreasonable. Hence we look to the previously developed three-dimensional flow models.

5.1.2 Slender-body-theory hydrodynamics

When the two-dimensional flow assumption is unrealistic for a circular cylinder, due either to long-range end effects ($\gamma^{-1}, \Delta \gg 1$) or non-horizontal orientation ($\alpha \neq 0$), we may turn to USBT to provide the hydrodynamic forcing in (5.1). For a tilted cantilever we shall consider two distinct motions, vertical oscillations and oscillations normal to the axis. In the absence of a wall, normal oscillations should simply amount to a change in the frame of reference and therefore not directly generate any axial flow; vertical oscillations, on the other hand, are capable of producing axial flow. Furthermore, when describing non-normal cantilever oscillations, we assume that the cantilever is inextensible and so any axial body motion is transmitted unchanged through the cantilever.

Therefore, in Cartesians, the distribution of Stokeslets \mathbf{f} is related to cantilever deflection $w(\xi)$ by (c.f. (3.3))

$$\begin{pmatrix} i\gamma^2 w \sin \alpha \\ 0 \\ i\gamma^2 w \cos \alpha \end{pmatrix} = \frac{1}{8\pi} \int_{-1}^1 (S_{ij}^w(\mathbf{x}, \mathbf{X}; \gamma, \Delta) + a_{kj} Q_{ik}(\hat{\mathbf{x}})) f_j(s; \gamma, \Delta) ds, \quad (5.4)$$

which we solve in conjunction with the beam equation (5.1), by discretizing the cantilever axis into N elements and assuming that the deflection w and loading \mathbf{f} are constant on each element $s_m = [(2(m-1)/N) - 1, (2m/N) - 1]$. The Stokeslets and dipoles $S_{ij}^w(\mathbf{x}, \mathbf{X}; \gamma, \Delta)$, $Q_{ik}(\hat{\mathbf{x}})$ are numerically integrated along each (possibly tilted) element of the beam. This leaves us needing to solve the $4N \times 4N$ system

$$\mathbf{\Pi} \mathbf{y} = \mathbf{b}_1 \quad (5.5a)$$

where

$$\mathbf{y} = (w_1, \dots, w_N, f_1, \dots, f_{3N}) \quad (5.5b)$$

is the Stokeslet distribution vector (3.9a), augmented with the discretized cantilever deflections

$$\mathbf{w} = (w(\mathbf{x}_1), \dots, w(\mathbf{x}_N)), \quad (5.5c)$$

whilst

$$\mathbf{b}_1 = (-4, 1, 0, \dots, 0) \quad (5.5d)$$

captures the boundary conditions (5.1b) and

$$\mathbf{\Pi} \equiv \begin{pmatrix} \mathbf{E} & \mathbf{I}_1 \\ \mathbf{I}_2 & \mathbf{G} \end{pmatrix}, \quad (5.5e)$$

where the matrix \mathbf{E} ($N \times N$) holds the finite-difference approximation to the derivatives on the left-hand side of (5.1a). The $N \times 3N$ matrix \mathbf{I}_1 , which incorporates the normal drag per unit length into the beam equation, contains zeroes except for $-M\Omega\gamma^2 \cos \alpha$ and $-M\Omega\gamma^2 \sin \alpha$ entries in the elements indexed by $(i, N + 3(i-1) + 3)$ and $(i, N +$

$3(i-1)+1$ ($i = 1 \dots N$), respectively. The $3N \times N$ matrix \mathbf{I}_2 captures the velocity dependence on the right-hand side of (5.4) and consists of zeros except for $-\cos \alpha$ and $-\sin \alpha$ in the $(N+3(i-1)+3, i)$ and $(N+3(i-1)+1, i)$ -indexed entries, respectively ($i = 1 \dots N$). The $3N \times 3N$ matrix \mathbf{G} is given by (3.10). This linear system is solved by Gaussian elimination, to give both the cantilever deflection and the three components of the singularity distribution \mathbf{f} .

5.1.3 Modified resistive-force-theory

The numerical scheme described by (5.5) is somewhat inefficient for our purposes, since it requires us to compute all three components of \mathbf{f} when only f_3 is required for a horizontal cantilever, supplemented with f_1 when the cantilever is tilted. Therefore, as a less arduous alternative, we estimate the hydrodynamic loading in (5.1) using RFT (3.17b,c) plus its first-order correction (thereby neglecting $O(1/(\ln \epsilon)^3)$ drag terms and smaller). We established in § 3.2 that the non-diagonal elements in the resistance matrix come solely from wall interactions, therefore axial motion contributes to the normal drag \mathcal{F} only through the W_i terms. By working in a frame of reference aligned with the cantilever axis, we obtain an integro-differential equation for cantilever deflection

$$\begin{aligned} \frac{\partial^4 w(\xi)}{\partial \xi^4} - M\gamma^4 w(\xi) &= -iM\Omega\gamma^2 \left(\frac{4\pi}{\ln \epsilon} + \frac{2\pi H_3(\xi; \gamma)}{(\ln \epsilon)^2} \right) w(\xi) \\ - \frac{4\pi i M \Omega \gamma^2}{(\ln \epsilon)^2} \int_{-1}^1 &\left(\frac{e^{-\sqrt{i}\gamma|s-\xi|}}{\sqrt{i}\gamma|s-\xi|^2} - \frac{i(e^{-\sqrt{i}\gamma|s-\xi|} - 1)}{\gamma^2|s-\xi|^3} + \frac{e^{-\sqrt{i}\gamma|s-\xi|}}{|s-\xi|} \right) (w(s) - w(\xi)) \, ds \\ &- \frac{2\pi i M \Omega \gamma^2}{(\ln \epsilon)^2} W_3(\xi, \alpha, w; \gamma, \Delta), \end{aligned} \quad (5.6)$$

where we have exploited the simple relationships $\mathbf{u} \cdot \hat{\mathbf{n}} = i\gamma^2 w$. In § 5.3.1 we compare this asymptotic treatment with the full USBT computations.

5.2 Two-dimensional plates

We consider deflections $\mathcal{W}(\xi, \eta, t)$ in the \hat{x}_3 direction of a thin rectangular elastic plate of length L , width $2R$ and thickness $2D$ ($D \ll R, L$) which is driven sinusoidally at a horizontally clamped end ($\alpha = 0$) with frequency ω and amplitude \mathcal{A} ($\mathcal{A} \ll D, R, L$),

with all other edges free. The mid-plane of this plate lies at a distance \mathcal{H} from a rigid plane wall located at $\hat{x}_3 = 0$ (see figure 5.1b).

The results of chapter 4 demonstrated the highly non-uniform character of the hydrodynamic loading over the surface of a thin plate, in both the span-wise and length-wise directions. We are interested in knowing whether, in spite of the narrowness of an AFM cantilever, the rapidly varying fluid loading at the plate edges can generate significant span-wise deflections (see figure 5.1b). We therefore seek an elastic description of a plate which allows span-wise deflections and the assumption that the thickness and amplitude are both small with respect to other plate dimensions once again permits the use of linear elasticity theory. In particular, flexural vibrations of a two-dimensional plate can be studied using linear elastic plate theory, which assumes

- (i) the plate has a uniform thickness and
- (ii) the shear deformation, stress in the transverse direction and rotational inertia are all negligible.

Expressing strains in terms of plate curvature and assuming Hookean stress–strain relationships, vertical force balances and moment equilibria lead to the plate equation (Timoshenko and Woinowsky-Krieger 1959)

$$\mathcal{D}\nabla^4\mathcal{W} + \rho_p\mathcal{D}\mathcal{W}_{tt} = \mathcal{F}(\xi, \eta; \gamma, \Delta), \quad (5.7)$$

where $\nabla^4 \equiv \partial_\xi^4 + \partial_\eta^4 + 2\partial_\xi^2\partial_\eta^2$, $\mathcal{D} = ED^3/12(1 - \nu_p^2)$ is the flexural rigidity of the plate, depending on its Young's modulus E , Poisson ratio ν_p (the ratio of transverse over compressive strain, which is approximately 0.3 for AFM cantilevers) and thickness D . The plate density is given by ρ_p and \mathcal{F} is the externally applied vertical load per unit area. Seeking oscillatory solutions $\mathcal{W}(\xi, \eta, t) = \text{Re}(w(\xi, \eta)e^{i\omega t})$, we consider a plate assuming that the deflection is symmetric about $\eta = 0$

$$w(\xi, -\eta) = w(\xi, \eta), \quad w_\eta(\xi, 0) = 0, \quad (5.8a)$$

that is clamped at $\xi = 0$ and sinusoidally driven

$$w(0, 0 \leq \eta \leq \epsilon) = 1, \quad w_\xi(0, 0 \leq \eta \leq \epsilon) = 0 \quad (5.8b)$$

and is free along the other edges, i.e. experiences no bending

$$w_{\xi\xi} + \nu_p w_{\eta\eta} = 0 : \quad \xi = 1, \quad 0 \leq \eta \leq \epsilon, \quad (5.8c)$$

$$w_{\eta\eta} + \nu_p w_{\xi\xi} = 0 : \quad 0 \leq \xi \leq 1, \quad \eta = \epsilon \quad (5.8d)$$

and no shearing or twisting; to avoid an over-prescribed system, the twisting moment is expressed in terms of shearing forces (see Timoshenko and Woinowsky-Krieger 1959) leading to the boundary condition

$$w_{\xi\xi\xi} + (2 - \nu_p)w_{\xi\eta\eta} = 0 : \quad \xi = 1, \quad 0 \leq \eta \leq \epsilon, \quad (5.8e)$$

$$w_{\eta\eta\eta} + (2 - \nu_p)w_{\xi\xi\eta} = 0 : \quad \eta = \epsilon, \quad 0 \leq \xi \leq 1. \quad (5.8f)$$

Scaling lengths on L , time on ω^{-1} , deflection on \mathcal{A} and hydrodynamic loading on $\mathcal{A}\omega\mu/L$ gives us (5.7) in non-dimensional form

$$\nabla^4 w - \gamma^4 M_p w = i\gamma^2 M_p \Omega_p f(\xi, \eta), \quad (5.9)$$

where $M_p \equiv \nu^2 \rho_p \mathcal{D}/\mathcal{D} \approx 10^{-7}$ and $\Omega_p = \rho/\rho_p d \approx 10^2$ for typical AFM regimes. For computational purposes, we prefer to decompose the fourth-order equation (5.9) into a pair of coupled second-order equations

$$\nabla^2 v - \gamma^4 M_p w = i\gamma^2 M_p \Omega_p f(\xi, \eta), \quad (5.10a)$$

$$\nabla^2 w = v, \quad (5.10b)$$

with the boundary conditions on the non-clamped edges (5.10c–f) becoming

$$\nu_p v + (1 - \nu_p)w_{\xi\xi} = 0, \quad (2 - \nu_p)v_\xi + (\nu_p - 1)w_{\xi\xi\xi} = 0 : \quad \xi = 1, \quad 0 \leq \eta \leq \epsilon \quad (5.10c)$$

$$\nu_p v + (1 - \nu_p)w_{\eta\eta} = 0, \quad (2 - \nu_p)v_\eta + (\nu_p - 1)w_{\eta\eta\eta} = 0 : \quad \eta = \epsilon, \quad 0 \leq \xi \leq 1. \quad (5.10d)$$

We have two options for the choice of hydrodynamic loading and we discuss both in the following two sections.

5.2.1 Lubrication hydrodynamics

In the limit $\Delta \ll \epsilon$, $\Delta \sim \gamma$ we can approximate the hydrodynamic loading using three-dimensional lubrication theory (§ 4.3.2). This involves solving Poisson's equation for

the pressure (4.30), which is coupled to the plate's elastic behaviour (5.10) as a result of the deflection-dependent non-homogenous term in (4.30)

$$\nabla^4 w - \gamma^4 M_p w = i\gamma^2 M_p \Omega_p \Delta^{-3} p, \quad (5.11a)$$

$$\nabla^2 p = k_0(\tau) w. \quad (5.11b)$$

We solve the coupled system (5.11) by discretizing the plate surface into $N_\xi \times N_\eta$ panels and assuming that the deflection and pressure are constant on each panel. This leaves us needing to solve the $3N_\xi N_\eta \times 3N_\xi N_\eta$ system

$$\mathbf{\Pi}_p \mathbf{y}_p + \mathbf{M}_0 \mathbf{y}_0 = \mathbf{0}, \quad (5.12a)$$

where

$$\begin{aligned} \mathbf{\Pi}_p &= \begin{pmatrix} \mathbf{E}_p & \mathbf{J}_1 \\ \mathbf{J}_2 & \mathbf{L}_p \end{pmatrix}, \quad \mathbf{E}_p = \begin{pmatrix} \mathbf{L}_p & -\mathbf{I}_p \\ -M_p \gamma^4 \mathbf{I}_p & \mathbf{L}_p \end{pmatrix}, \\ \mathbf{J}_1 &= -\gamma^2 M_p \Omega_p \begin{pmatrix} \mathbf{I}_p \\ \mathbf{0}_p \end{pmatrix}, \quad \mathbf{J}_2 = -k_0(\tau) \begin{pmatrix} \mathbf{I}_p & \mathbf{0}_p \end{pmatrix}. \end{aligned} \quad (5.12b)$$

The $N_\xi N_\eta \times N_\xi N_\eta$ matrix \mathbf{L}_p is the finite-difference approximation to the Laplacian and \mathbf{I}_p , $\mathbf{0}_p$ are the $N_\xi N_\eta \times N_\xi N_\eta$ identity and zero matrices, respectively. Also,

$$\begin{aligned} \mathbf{y}_p &= (w(\xi_1, \eta_1), \dots, w(\xi_{N_\xi}, \eta_1), \dots, w(\xi_1, \eta_{N_\eta}), \dots, w(\xi_{N_\xi}, \eta_{N_\eta}), \\ &\quad v(\xi_1, \eta_1), \dots, v(\xi_{N_\xi}, \eta_1), \dots, v(\xi_1, \eta_{N_\eta}), \dots, v(\xi_{N_\xi}, \eta_{N_\eta}), \\ &\quad p(\xi_1, \eta_1), \dots, p(\xi_{N_\xi}, \eta_1), \dots, p(\xi_1, \eta_{N_\eta}), \dots, p(\xi_{N_\xi}, \eta_{N_\eta})) \end{aligned} \quad (5.12c)$$

contains the values of w , v and p at internal points and

$$\begin{aligned} \mathbf{y}_0 &= (w(1, \eta_1), \dots, w(1, \eta_{N_\eta}), w(\xi_1, 1), \dots, w(\xi_{N_\xi}, 1), \\ &\quad v(1, \eta_1), \dots, v(1, \eta_{N_\eta}), v(\xi_1, 1), \dots, v(\xi_{N_\xi}, 1), v(0, \eta_1), \dots, v(0, \eta_{N_\eta})) \end{aligned} \quad (5.12d)$$

contains the unknown boundary values of w and v , which are positioned for the finite-difference scheme by \mathbf{M}_0 . The values in \mathbf{y}_0 are determined by the boundary conditions given in (5.8, 4.30d), which produce a set of $(2N_\xi + 3N_\eta)$ equations relating internal points to boundary values

$$\mathbf{M}_1 \mathbf{y}_p + \mathbf{M}_2 \mathbf{y}_0 = \mathbf{B}, \quad (5.13)$$

where M_1 , M_2 contain the finite-difference approximation to the derivatives in (5.8b–e) and B contains the clamped condition $w(0, \eta) = 1$. Hence

$$\mathbf{y}_0 = M_2^{-1} \mathbf{B} - M_2^{-1} M_1 \mathbf{y}_p, \quad (5.14)$$

giving, on substitution into (5.12)

$$(\mathbf{\Pi}_p - M_0 M_2^{-1} M_1) \mathbf{y}_p + M_0 M_2^{-1} \mathbf{B} = \mathbf{0}, \quad (5.15)$$

which we solve by Gaussian elimination for \mathbf{y}_p . Results are obtained on a 30×30 mesh with convergence verified by increasing this to 60×60 .

Narrow plate limit ($\Delta \ll \epsilon \ll 1$)

In the narrow-plate limit asymptotic progress can be made determining the plate's deflection. Rescaling $\eta = \epsilon \tilde{\eta}$, (5.11a) becomes

$$\frac{\partial^4 w}{\partial \tilde{\eta}^4} + 2\epsilon^2 \frac{\partial^2 \partial^2 w}{\partial \tilde{\eta}^2 \partial \xi^2} + \epsilon^4 \frac{\partial^4 w}{\partial \xi^4} - \epsilon^4 \gamma^4 M_p w = i\epsilon^4 \gamma^2 M_p \Omega_p \Delta^{-3} p, \quad (5.16a)$$

subject to

$$w(\xi, -\tilde{\eta}) = w(\xi, \tilde{\eta}), \quad w_\eta(\xi, 0) = 0, \quad (5.16b)$$

$$w_{\tilde{\eta}\tilde{\eta}} + \epsilon^2 \nu_p w_{\xi\xi} = 0 \text{ at } \tilde{\eta} = 1, \quad (5.16c)$$

$$w_{\tilde{\eta}\tilde{\eta}\tilde{\eta}} + \epsilon^2 (2 - \nu_p) w_{\tilde{\eta}\xi\xi} = 0 \text{ at } \tilde{\eta} = 1, \quad (5.16d)$$

$$\epsilon^2 w_{\xi\xi} + \nu_p w_{\tilde{\eta}\tilde{\eta}} = 0 \text{ at } \xi = 1, \quad (5.16e)$$

$$\epsilon^2 w_{\xi\xi\xi} + (2 - \nu_p) w_{\xi\tilde{\eta}\tilde{\eta}} = 0 \text{ at } \xi = 1, \quad (5.16f)$$

$$w = 0, \quad w_\xi = 0 \text{ at } \xi = 0. \quad (5.16g)$$

Let us consider the case when $i\gamma^2 M_p \Omega_p \Delta^{-3} = \tilde{M} \epsilon^{-2}$, with $\tilde{M} = O(1)$. Now expanding the deflection and pressure $p(\xi, \tilde{\eta}) = p^{(0)}(\xi, \tilde{\eta}) + \epsilon p^{(1)}(\xi, \tilde{\eta}) + \epsilon^2 p^{(2)}(\xi, \tilde{\eta}) + \dots$, $w(\xi, \tilde{\eta}) = w^{(0)}(\xi, \tilde{\eta}) + \epsilon w^{(1)}(\xi, \tilde{\eta}) + \epsilon^2 w^{(2)}(\xi, \tilde{\eta}) + \dots$ at leading and second orders we find

$$\frac{\partial^4 w^{(0)}}{\partial \tilde{\eta}^4} = \frac{\partial^4 w^{(1)}}{\partial \tilde{\eta}^4} = 0. \quad (5.17)$$

Hence, respecting symmetry about $\tilde{\eta} = 0$

$$w^{(0)} = A_0(\xi) \tilde{\eta}^2 + B_0(\xi), \quad w^{(1)} = A_1(\xi) \tilde{\eta}^2 + B_1(\xi). \quad (5.18)$$

The no-moment condition at $\tilde{\eta} = 1$ (5.16c) then implies that $A_0(\xi) = 0$ and

$$w^{(2)} = -\frac{\nu_p}{2} \frac{\partial^2 w^{(0)}}{\partial \xi^2} \tilde{\eta}^2 + B_2(\xi). \quad (5.19)$$

Hence the leading-order deflection is a function of ξ alone and, using the results of § 4.3.2, the pressure can be approximated by the composite expansion (4.40). Consequently at $O(\epsilon^4)$ we have

$$\frac{\partial^4 w^{(2)}}{\partial \tilde{\eta}^4} + 2 \frac{\partial^4 w^{(1)}}{\partial \xi^2 \partial \tilde{\eta}^2} + \frac{\partial^4 w^{(0)}}{\partial \xi^4} - \gamma^4 M_p w^{(0)} = \tilde{M} p^{(2)} = \tilde{M} k_0(\tau) w^{(0)}(\xi) \frac{(\tilde{\eta}^2 - 1)}{2}, \quad (5.20)$$

hence

$$w^{(2)} = \left(\left(\gamma^4 M_p - \frac{\tilde{M} k_0(\tau)}{2} \right) w^{(0)} - (1 - 2\nu_p) \frac{\partial^4 w^{(0)}}{\partial \xi^4} \right) \frac{\tilde{\eta}^4}{4!} + \tilde{M} k_0(\tau) w^{(0)} \frac{\tilde{\eta}^6}{6!} + A_4(\xi) \frac{\tilde{\eta}^2}{2} + B_4(\xi). \quad (5.21)$$

The no-shear condition at $\tilde{\eta} = 1$ (5.16d) then provides the solvability condition for $w^{(0)}$

$$(\nu_p^2 - 1) \frac{\partial^4 w^{(0)}}{\partial \xi^4} + \left(\gamma^4 M_p - \frac{\tilde{M} k_0(\tau)}{3} \right) w^{(0)} = 0, \quad (5.22)$$

i.e. the Euler–Bernoulli beam equation. Determining the boundary conditions for (5.22) at $\xi = 0$ and $\xi = 1$ requires us to examine the structure of the plate deflection near the free ends. Near $\xi = 1$ we rescale the ξ -coordinate according to $\xi = 1 - \epsilon \tilde{\xi}$ and the deflection in this end region is then governed by

$$\nabla^4 w - \epsilon^4 \gamma^4 M_p w = i \epsilon^4 \gamma^2 M_p \Omega_p \Delta^{-3} p, \quad (5.23)$$

subject to (5.8e,f) and matches the inner limit of the outer solution

$$w \rightarrow w(1) - \epsilon \tilde{\xi} w_{\xi}^{(0)}(1) + \epsilon^2 \left[\frac{\tilde{\xi}^2 w_{\xi\xi}^{(0)}(1)}{2} - \frac{\nu_p}{2} \tilde{\eta}^2 w_{\xi\xi}^{(0)}(1) + B_2(1) \right] + \epsilon^3 \left[-\frac{\tilde{\xi}^3 w_{\xi\xi\xi}^{(0)}(1)}{6} + \frac{\nu_p}{2} \tilde{\eta}^2 \tilde{\xi} w_{\xi\xi\xi}^{(0)}(1) - \tilde{\xi} B_{2,\xi}(1) \right] + O(\epsilon^4) \text{ as } \tilde{\xi} \rightarrow \infty. \quad (5.24)$$

We note that (5.24) satisfies (5.23) up to $O(\epsilon^4)$ corrections and respects the boundary conditions (5.8e,f), provided that

$$w_{\xi\xi}^{(0)}(1) = w_{\xi\xi\xi}^{(0)}(1) = 0, \quad (5.25a)$$

i.e. the two-dimensional no-moment and no-stress free-end conditions. Similarly, the inner limit of the outer solution provides the leading-order solution in the $\xi = 0$ end region, provided

$$w^{(0)}(0) = w_\xi^{(0)}(0) = 0. \quad (5.25b)$$

We therefore recover the familiar clamped boundary conditions for the Euler–Bernoulli beam (5.22), which is solved by

$$w^{(0)} = A_1 \left(e^{\kappa\xi} - \cos \kappa\xi - \sin \kappa\xi - A_2 \left(e^{-\kappa\xi} - \cos \kappa\xi + \sin \kappa\xi \right) \right) + A_3 \left(e^{-\kappa\xi} - \cos \kappa\xi + \sin \kappa\xi \right) + \cos \kappa\xi, \quad (5.26a)$$

where

$$A_1 = \frac{1 + e^{-\kappa} \cos \kappa - e^{-\kappa} \sin \kappa}{4 + 2e^{-\kappa} \cos \kappa + 2e^\kappa \cos \kappa}, \quad A_2 = \frac{e^\kappa + \cos \kappa + \sin \kappa}{e^{-\kappa} + \cos \kappa - \sin \kappa}, \quad (5.26b)$$

$$A_3 = \frac{\cos \kappa}{e^{-\kappa} + \cos \kappa - \sin \kappa}, \quad \kappa = \left(\frac{\tilde{M}k_0(\tau) - 3\gamma^4 M_p}{3(\nu_p^2 - 1)} \right)^{1/4} \quad (5.26c)$$

and in § 5.3.2 we plot this narrow-plate limit against the finite-difference computations.

5.2.2 Thin-plate hydrodynamics

The approach just described in § 5.2.1 is valid when $\Delta \ll 1$, however, a more general situation can be dealt with by using the three-dimensional TPT hydrodynamics developed in § 4.3. Under these circumstances we need to solve the $5N_\xi N_\eta \times 5N_\xi N_\eta$ system

$$\mathbf{\Pi}_v \mathbf{y}_v + \mathbf{M}_0 \mathbf{y}_0 = \mathbf{0}, \quad (5.27a)$$

where

$$\mathbf{y}_v = \left(w(\xi_1, \eta_1), \dots, w(\xi_{N_\xi}, \eta_1), \dots, w(\xi_1, \eta_{N_\eta}), \dots, w(\xi_{N_\xi}, \eta_{N_\eta}), \right. \\ v(\xi_1, \eta_1), \dots, v(\xi_{N_\xi}, \eta_1), \dots, v(\xi_1, \eta_{N_\eta}), \dots, v(\xi_{N_\xi}, \eta_{N_\eta}), \\ f_1(\xi_1, \eta_1), f_2(\xi_1, \eta_1), f_3(\xi_1, \eta_1), \dots, f_1(\xi_{N_\xi}, \eta_1), f_2(\xi_{N_\xi}, \eta_1), f_3(\xi_{N_\xi}, \eta_1), \dots, \\ \left. f_1(\xi_1, \eta_{N_\eta}), f_2(\xi_1, \eta_{N_\eta}), f_3(\xi_1, \eta_{N_\eta}), \dots, f_1(\xi_{N_\xi}, \eta_{N_\eta}), f_2(\xi_{N_\xi}, \eta_{N_\eta}), f_3(\xi_{N_\xi}, \eta_{N_\eta}) \right) \quad (5.27b)$$

and

$$\mathbf{\Pi}_v = \begin{pmatrix} \mathbf{E}_p & \mathbf{J}_3 \\ \mathbf{J}_4 & \mathbf{G} \end{pmatrix}, \quad (5.27c)$$

where \mathbf{E}_p is the finite-difference representation of the elasticity operator (5.12b) and \mathbf{G} is the TPT hydrodynamic matrix defined in (4.24). \mathbf{J}_3 is a zero matrix other than $-\gamma^2 M_p \Omega_p$ values in $(k, 3(k-1) + 3)$ -indexed entries, as is \mathbf{J}_4 except for -1 values in $(3(K-1) + 3, K)$ -indexed entries ($1 \leq k, K \leq N_\xi N_\eta$). \mathbf{y}_0 is determined as in (5.14).

Solving this linear system by Gaussian elimination then provides the plate deflection and the Stokeslet distribution of \mathbf{f} over the plate. Convergence is verified by solving on 30×30 and 50×50 meshes.

Narrow plate limit ($\epsilon \ll 1$)

As for the case of lubrication hydrodynamics, when the plate is narrow we expect a simplified form for dominant plate dynamics. The TPT findings in § 4.4.3 suggest that under such geometric conditions and at sufficiently high frequencies of oscillation, we may expect the flow to be largely two dimensional over much of the plate. Therefore, assuming a ξ -independent loading in (5.9), the plate dynamics take the form

$$\nabla^4 w - \gamma^4 M_p w = i\gamma^2 M_p \Omega_p f'(\eta) w, \quad (5.28)$$

where $f'(\eta)$ is the two-dimensional TPT Stokeslet profile described in § 4.2. We can then solve (5.28) directly (using similar finite-difference methods as before) to assess the importance of three-dimensional flows near the ends of the plate. We may also pursue an asymptotic route as was done when using lubrication hydrodynamics in § 5.2.1. This gives us

$$(\nu_p^2 - 1) \frac{\partial^4 w^{(0)}}{\partial \xi^4} + (\gamma^4 M_p + i\gamma^2 M_p \Omega_p D) w^{(0)} = 0, \quad (5.29)$$

$$D = \int_0^1 f'(\eta) d\eta. \quad (5.30)$$

Note that (5.29) has been derived without special treatment of the singularity in $f'(\eta)$ at $\eta = 1$ and so in § 5.3.2 we check how this naive calculation performs against the full two-dimensional plate computations.

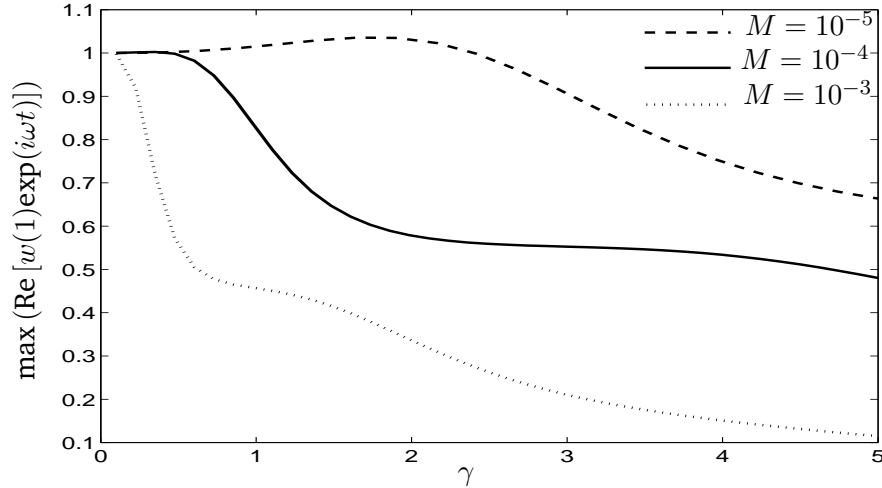


FIGURE 5.2: Maximum amplitude at the tip of a horizontal ($\alpha = 0$) damped cantilever ($\epsilon = 10^{-2}$) driven over a range of frequencies γ when $\Delta = 100$ and $\Omega = 10^4/\pi$. Cantilevers of three different stiffnesses are shown ($M = 10^{-3}$, 10^{-4} and 10^{-5} and the hydrodynamic loading is given by USBT (5.5).)

5.3 Results

These results focus on the amplitude response at the tip of a cantilever which is driven sinusoidally at its clamped end, as a function of oscillation frequency. We look at one-dimensional descriptions of the elastic behaviour using various expressions for the hydrodynamic loading (§ 5.3.1), considering the effects of tilt and the presence of a wall. Non-uniform deflections across the width of the cantilever are accounted for by treating the cantilever as a finite-width elastic plate coupled to either lubrication or TPT loading (without a wall) (§ 5.3.2).

5.3.1 Elastic beams

When the cantilever is horizontal, the tip response can be found through the beam equation subject to hydrodynamic loading described by three-dimensional unsteady slender-body theory (SBT) (5.5) and its modified resistive-force-theory (RFT) limit (5.6) (circular cantilevers only) or two-dimensional drag (5.3) (circular and rectan-

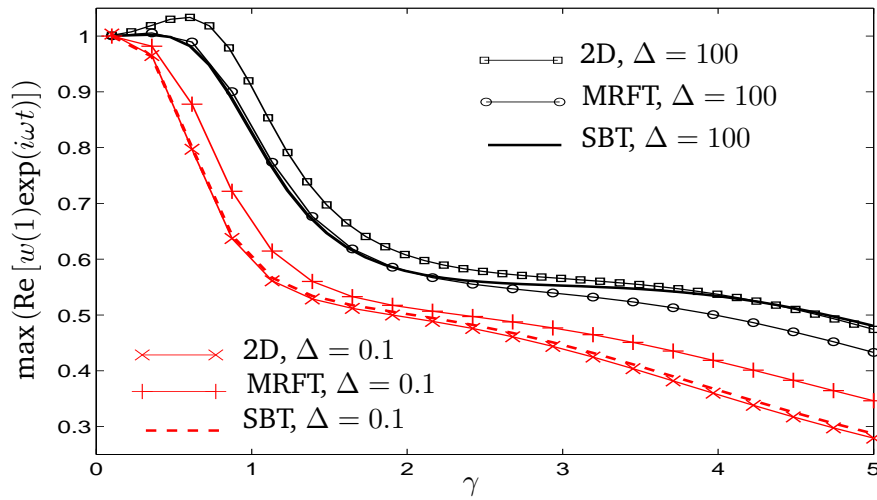


FIGURE 5.3: Maximum amplitude at the tip of a horizontal ($\alpha = 0$) damped cantilever ($\epsilon = 10^{-2}$) driven over a range of frequencies γ . Tip responses are computed with the hydrodynamic loading given by (i) two-dimensional drag (5.3, markers), (ii) full USBT computation (5.5, full line) and (iii) modified RFT (5.6, dashed line) when $M = 10^{-4}$, $\Omega = 10^4/\pi$ and $\Delta = 0.1, 100$.

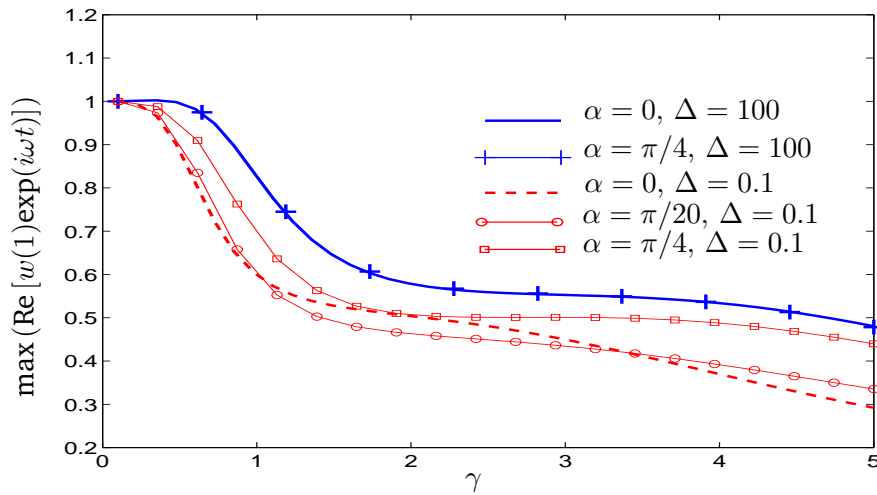


FIGURE 5.4: Maximum amplitude at the tip of a damped cantilever ($\epsilon = 10^{-2}$) tilted at $\alpha = 0, \pi/20$ and $\pi/4$, driven over a range of frequencies γ when $M = 10^{-4}$, $\Omega = 10^4/\pi$ for $\Delta = 0.1$ and $\Delta = 100$, using a USBT description of the hydrodynamics.

gular cantilevers).

The influence of cantilever stiffness M is illustrated in figure 5.2. A decrease in the Young's modulus E leads to an increase in $M \equiv \mu^2 m_c / \rho^2 EI$ (when the other material properties of the cantilever and fluid are kept constant) and we see that this results in more pronounced hydrodynamic damping in the frequency response and a reduction in the resonant frequency.

In figure 5.3 we see the effect on tip oscillations of bringing the cantilever close to the wall. For all three choices of hydrodynamic loading, decreasing Δ from 100 to 0.1 leads to much greater loading on the cantilever, which results in a more damped response, i.e. lower amplitudes and a shift in the resonant peak to lower frequencies. Figure 5.3 also explores the effectiveness of two-dimensional drag and three-dimensional modified RFT as estimates for hydrodynamic loading in the beam equation. At lower γ the two-dimensional drag assumption (5.3) leads to inaccurate results, whilst modified RFT (5.6) performs well. Although the effectiveness of (5.6) lessens as γ is increased (due to increasing demand for higher-order corrections to RFT, see figure 3.6c,d), at this point two-dimensional drag begins to give good agreement with the full slender-body computations due to γ -screening. Hence, for most values of γ , we have an acceptable alternative to (5.5). The impact of Δ -screening on frequency responses is also shown. Even at low γ the presence of the wall results in two-dimensional drag proving a trustworthy approximation, even though at these values of Δ a single correction to RFT proves insufficient to capture the full hydrodynamic loading on the beam.

Figure 5.4 examines the role of tilt in the frequency response of a cantilever which is driven normal to its axis. At large values of Δ the angle of inclination is irrelevant due to the lack of any significant axial flows. Once the separation distance is decreased to $\Delta = 0.1$, however, strong flow interactions with the wall lead to substantial α -dependence in the response.

5.3.2 Elastic plates

When the cantilever has significant width, we expect the plate deflections to vary in the span-wise (η -dependent), as well as in the length-wise (ξ -dependent), direction.

The elastic dynamics are then determined by the plate equation (5.9), subject to either lubrication theory or TPT hydrodynamics.

Lubrication loading

Figure 5.5 shows the real (*a*) and imaginary (*b*) parts of a narrow ($\epsilon = 0.05$) cantilever's deflection when oscillating at high frequency ($\gamma = 200$), whilst situated close to a wall ($\Delta = 0.005$). Under these circumstances we expect lubrication theory to work well at providing the hydrodynamic loading on the plate. Furthermore, as the plate is relatively narrow, we see in figure 5.5(*a,b*) that there is very little span-wise deflection. The narrow-plate asymptotic analysis predicts that the plate will behave like a one-dimensional Euler–Bernoulli beam (5.22) and this is indeed seen to be the case (thick line). The lower two panels (*c,d*) of figure 5.5 show, respectively, the real and imaginary parts of the pressure profile. The dashed thick lines give the outer asymptotic solution for the pressure (4.35), which works well away from the plate ends. Although the end regions are not required for determining the leading-order plate deflection, we see that their inclusion via the composite pressure expansion (4.40) allows the pressure profile to be fully captured over the whole plate (full line). When the plate is made less narrow (figure 5.6) we are able to observe non-negligible span-wise deflections and so our asymptotic analysis is no longer appropriate.

TPT loading

In § 4.4.3 we described how both geometry and oscillation frequency were important in determining the extent of three-dimensionality in the flow generated by a thin rigid plate. By increasing γ , viscous effects become confined to the surface edges and the geometry of the plate dictates the flow structure; making the plate narrow ($\epsilon \ll 1$) results in two-dimensional flow over much of the plate and three-dimensional effects remain significant only within $O(\epsilon)$ distances of the $\xi = 0$ and $\xi = 1$ edges. Although small, these end regions are not necessarily insignificant to the elastic behaviour of a narrow plate, as illustrated by figure 5.7. The TPT Stokeslet distribution (normalised on plate velocity), shown in panels (*a,b*), is seen to attain an ξ -independent profile

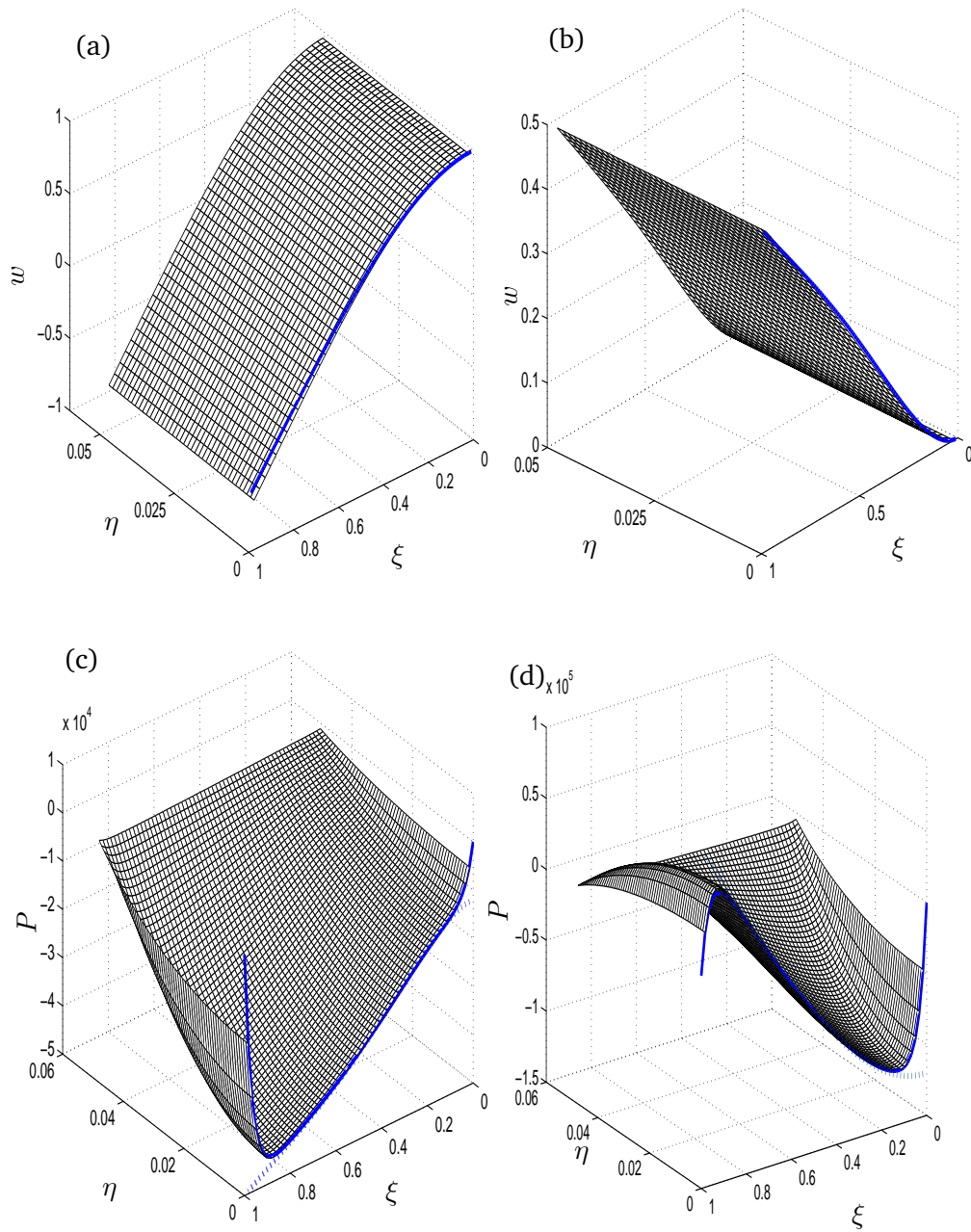


FIGURE 5.5: Real (a) and imaginary (b) components of an elastic cantilever's deflection when $\epsilon = 0.05$, $\Omega_p = 1$, $M_p = 10^{-8}$ and $\nu_p = 0.3$, and where $\gamma = 200$ and $\Delta = 0.005$. Deflections are computed using the three-dimensional lubrication formulation (5.12) and its narrow-plate limit (5.22) (thick line). Panels (c,d) represent the real and imaginary parts of the pressure profile, respectively, with the dashed thick line corresponding to the outer solution in the asymptotic approximation (4.35b), whilst the full thick line represents the full composite expansion (4.40).

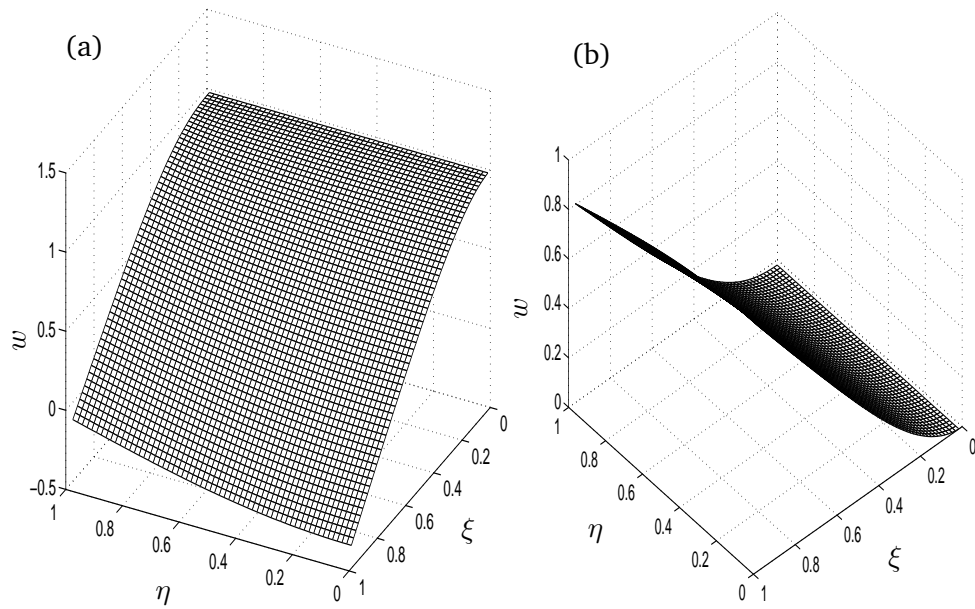


FIGURE 5.6: Real (a) and imaginary (b) components of an elastic cantilever's deflection when $\epsilon = 1$, $d/\epsilon = 10^{-3}$, $\Omega_p = 10^2$, $M_p = 10^{-7}$ and $\nu_p = 0.5$ and where $\gamma = 20$ and $\Delta = 0.05$. Hydrodynamic loading is given by three-dimensional lubrication theory (5.12).

away from $\xi = 0$ and $\xi = 1$ which agrees with two-dimensional BEM predictions (thick red line). For these parameter values, there is good agreement with the deflections predicted with the hydrodynamic loading provided by two-dimensional BEM computations. This is demonstrated in figures 5.7 (c,d), where the thick green line shows a cross-sectional slice of the plate deflection computed using two-dimensional BEM hydrodynamic loading alone. In these plots the thick red line represents the narrow-plate deflection, which satisfies the Euler–Bernoulli beam equation (5.29); clearly the asymptotics do not work as well as in the lubrication limit, possibly due to the singular nature of the TPT Stokeslet profiles near the plate edges. This is further reflected in the frequency responses for a narrow plate, shown in figure 5.8. Here plate deflections under three distinct forms of hydrodynamic loading have been plotted as a function of oscillation frequency. Although all three responses show similar qualitative behaviour, the two-dimensional BEM hydrodynamics are seen to cause a slight shift and over-predict the amplitude and sharpness of the resonant peak, for both beams and plates, which naturally has implications for AFM cantilever responses. Again, this is perhaps due to the importance of edge and end regions in the Stokeslet distribution. When the plate is square, there is non-negligible span-wise deflection and this results in differences between the frequency response measured at the edge compared to that taken at the plate centre (figure 5.9).

5.4 Discussion

We have determined the dynamics of a sinusoidally-driven cantilever by incorporating previous hydrodynamic theory into beam and plate equations, which describe the elastic dynamics. When the cantilever was hydrodynamically modelled as a slender rod, either two-dimensional drag results for an infinitely-long circular cylinder (chapter 2,4.1) or USBT results for a finite-length circular cylinder (chapter 3) were substituted into the one-dimensional beam equation. The deformation of a driven cantilever with finite width was determined using the two-dimensional plate equation, subject to hydrodynamic loading described by TPT or, at small separation, three-dimensional lubri-

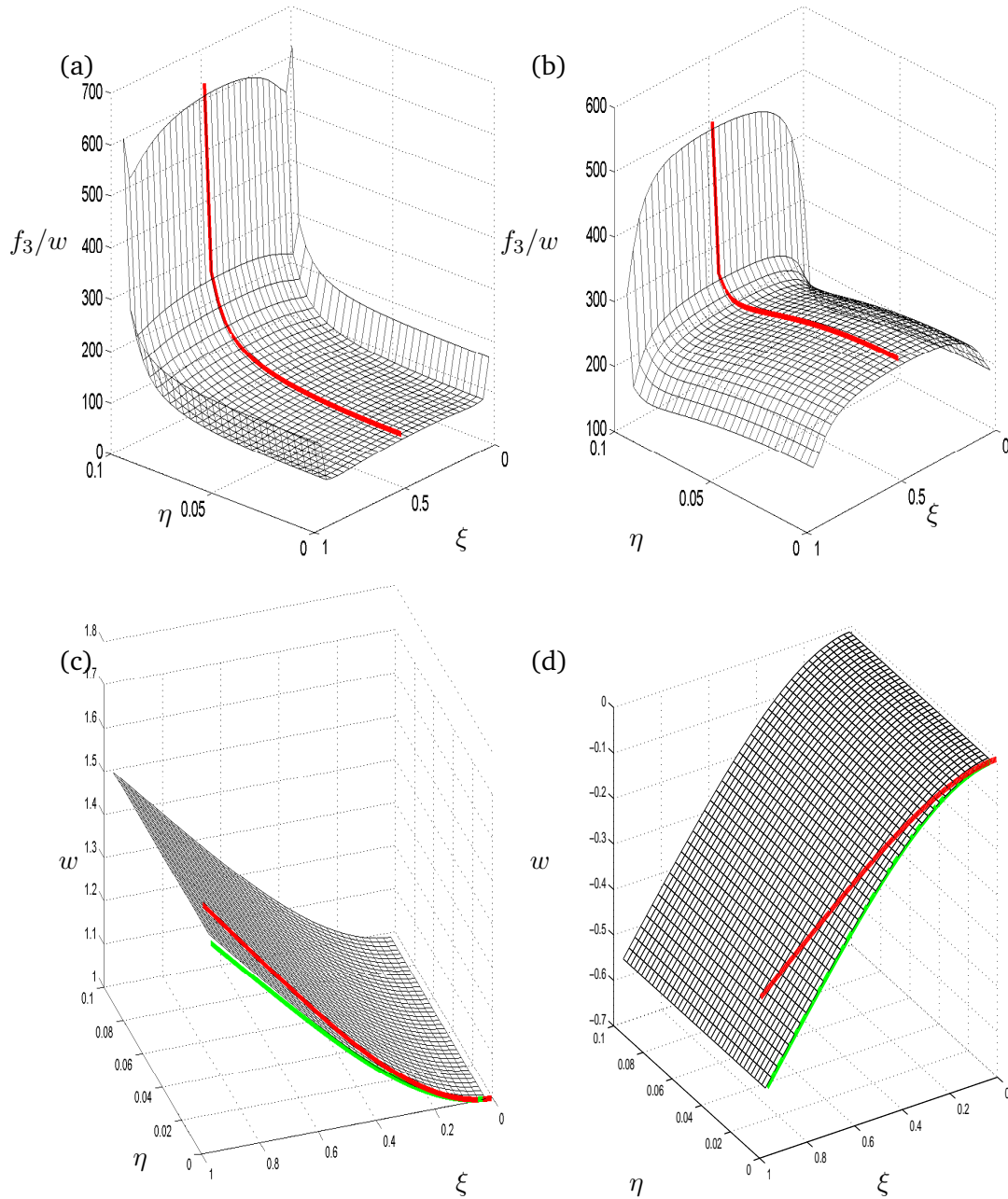


FIGURE 5.7: Panels (a,b) show the real and imaginary parts, respectively, of the three-dimensional TPT Stokeslet profile (mesh) detailing the hydrodynamic loading on a thin narrow plate ($\Omega_p = 10$, $M_p = 10^{-6}$, $\nu_p = 0.3$, $\epsilon = 0.1$, $d/\epsilon = 10^{-2}$) which oscillates in unbounded fluid with $\gamma = 30$, together with the two-dimensional BEM profile (thick line red), all normalised on plate velocity. The corresponding real and imaginary parts of an elastic cantilever's deflection are shown in (c,d), respectively, computed using TPT hydrodynamics (5.27) (shown by mesh) and two-dimensional hydrodynamics given by BEM (4.3) (cross-sectional slice shown by thick green line). The thick red line represents the deflection computed using the leading-order Euler-Bernoulli beam dynamics (5.29).

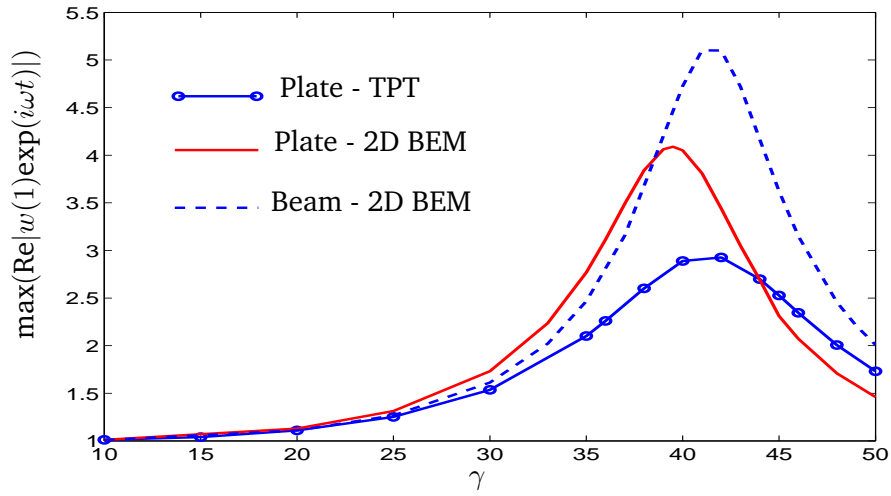


FIGURE 5.8: Frequency response of a narrow plate ($\nu_p = 0.3$, $M_p = 10^{-6}$, $\Omega_p = 10$, $\epsilon = 0.1$, $d/\epsilon = 10^{-2}$) under TPT hydrodynamic loading (full line and markers) and two-dimensional BEM hydrodynamics (full line only), together with the asymptotic description, which is governed by the Euler–Bernoulli beam equation (5.29, dashed line).

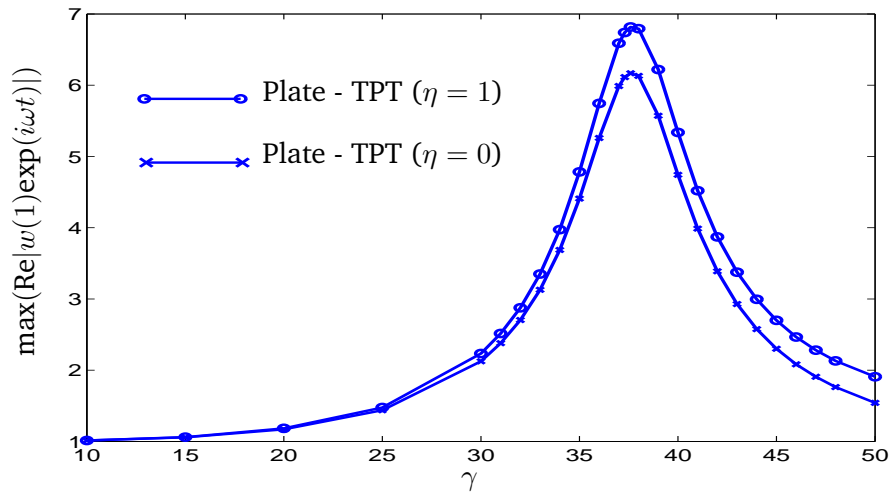


FIGURE 5.9: Frequency response of a square plate ($\nu_p = 0.3$, $M_p = 10^{-6}$, $\Omega_p = 10$, $\epsilon = 1$, $d/\epsilon = 10^{-2}$) under TPT hydrodynamic loading with deflection measured along the edge ($\eta = 1$, circles) or at plate middle ($\eta = 0$, crosses).

cation theory (chapter 4). In both cases the narrow-plate limit lent itself to asymptotic analysis.

The results relating to cantilevers with negligible span-wise deflections showed that bringing the cantilever close to the wall increased the hydrodynamic loading and consequently reduced the amplitude of the tip's response. For regimes where the finite-length flow effects were suppressed, either due to a high cantilever spring constant or the presence of a nearby solid boundary, two-dimensional drag was shown to capture adequately the cantilever tip's response. Importantly, these screening mechanisms were shown to persist at moderate angles of inclination (i.e. values typical of AFM cantilever configurations). In the absence of any screening mechanisms (resulting in long-ranged end effects) or when the cantilever had a large angle of inclination, the two-dimensional flow approximations were found to misrepresent the true hydrodynamic loading on the cantilever. Nevertheless, for the case of a horizontal cantilever without end-effect screening, the integro-differential equation (5.6), derived using modified-resistive-force theory (MRFT) was seen to provide a reliable and computationally less arduous alternative to solving the fully-coupled system (5.5).

We then moved on to consider finite-width cantilevers which could experience span-wise deflections. Using a finite-difference scheme, we were able to solve the coupled lubrication-plate equations to compute the deflection and pressure when $\Delta \sim \gamma^{-1} \ll 1$. A square plate was seen to experience significant span-wise deflections, yet this became less pronounced as AFM cantilever aspect ratios were approached. In this narrow-plate limit ($\Delta \ll \epsilon \ll 1$) an asymptotic analysis showed that the elastic behaviour once more governed by the Euler-Bernoulli beam equation, subject to the familiar one-dimensional clamped and free-end boundary conditions (figure 5.5). Once the deflection was known the pressure profile could also be determined using a uniformly valid asymptotic expansion, which figure 5.5 showed adequately captured the rapid pressure variations at the plate edges $x_1 = 0$ and $x_1 = 1$. Figure 5.6 demonstrated how increasing the plate width and Poisson ratio both lead to non-uniform deflections across the plate.

Application of TPT, rather than lubrication hydrodynamics, allowed us to study plate deflections away from the wall, yet unbounded fluid proved the only case accessible

with conventional processing power. When the plate was narrow and the frequency of oscillation high, figure 5.7 showed that the Stokeslet profile becomes largely two-dimensional away from the $\xi = 0$ and $\xi = 1$ edges. Here two-dimensional BEM could be used to accurately determine plate deflection. In the narrow-plate limit, asymptotic analysis once more lead to Euler-Bernoulli beam mechanics at leading-order, although the agreement was not as strong as for the lubrication case, perhaps due to the rapidly varying hydrodynamic loading near the end and edge regions. These shortcomings lead to a noticeable shift and differences in the amplitude and sharpness of the resonant peaks (figure 5.8). When the plate was no longer narrow, the frequency response curves were seen dependent upon the span-wise measurement location (figure 5.9).

These findings have important implications for deciding the level of elastohydrodynamic sophistication needed to accurately describe the dynamics of a sinusoidally-driven AFM cantilever. It has been demonstrated that, even when the cantilever is narrow (as is the case with the AFM), two-dimensional assumptions may not be entirely dependable, although the cantilevers considered in figures (5.7–5.9) are less stiff and dense than typical AFM cantilevers and so the discrepancy may be somewhat exaggerated here.

Sinusoidally-driven cantilevers give an appropriate description of tapping-mode AFM (TM-AFM, see § 1.1.2). However, there are other ways in which the cantilever can be driven. One alternative (*ex-vacuo*) is to allow the cantilever to fluctuate under Brownian motion. This method is becoming increasingly appealing to experimentalists who wish to drive the cantilever at extremely low amplitudes and, as such, we dedicate the final chapter to describing these thermally-driven modes of operation.

Chapter 6

Damped dynamics of a thermally-driven cantilever

Brownian effects in fluids have long been a source of noise contamination in AFM measurements, but techniques have evolved which exploit the cantilever's low-amplitude thermal fluctuations, as discussed in some detail in § 1.1.3 and § 1.1.4. There is much interest in simulating the Brownian dynamics of AFM cantilevers and we are now in a position to combine the earlier hydrodynamic theory with some results from statistical physics, to predict the behaviour of thermally-fluctuating cantilevers.

We consider deflections \mathcal{W} of a beam-like cantilever of length L , width $2R$ and thickness $2D$, with its mid-plane at a minimum distance \mathcal{H} from a horizontal wall (see figure 5.1a), which fluctuates in a thermal bath at temperature \mathcal{T} under the action of Brownian motion.

In § 6.1 we describe an existing model for describing the thermal cantilever fluctuations which enjoys great popularity in the AFM community, but which suffers from some shortcomings. The physics behind an alternative approach for probing microscopic Brownian-induced fluctuations, by analysing the macroscopic behaviour of the system, will be presented in § 6.2 and specific application to cantilevers will be made in

§ 6.3. When the flow is assumed to be two-dimensional (§ 6.3.1) the thermal spectrum can be expressed in terms of discrete and continuous contributions. The numerical approximation of fully three-dimensional flow is then briefly outlined in § 6.3.2. Results are presented in § 6.4, including comparison to experimental data and implications are then discussed in § 6.5.

6.1 Equipartition of energy approach

Sader (1998) modelled the cantilever's elastic behaviour using the Euler–Bernoulli beam equation (5.1) and the two-dimensional drag experienced by an infinite circular cylinder in unbounded fluid (2.19). The response to thermal noise was determined by first decomposing the deflection into spatially orthogonal vacuum eigenmodes ϕ_k , which form a basis for describing any arbitrary deflection. In this way the deflection was expressed as

$$\mathcal{W}(\xi, t) = \sum_{k=1}^{\infty} \alpha_k \phi_k(\xi) e^{i c_k t}, \quad (6.1a)$$

$$\phi_k(\xi) = \cos c_k \xi - \cosh c_k \xi + \left(\frac{\cos c_k + \cosh c_k}{\sin c_k + \sinh c_k} \right) (\sinh c_k \xi - \sin c_k \xi), \quad (6.1b)$$

where the eigenfrequencies c_k satisfy

$$1 + \cos c_k \cosh c_k = 0 \quad (6.2)$$

and ϕ_k satisfy homogeneous boundary conditions

$$\phi_k(0) = \phi_{k,\xi}(0) = \phi_{k,\xi\xi}(1) = \phi_{k,\xi\xi\xi}(1) = 0. \quad (6.3)$$

Hydrodynamic loading was introduced by weighting these vacuum modes through the use of a transfer function (projecting the damped response, under steady uniform loading over the cantilever length, onto each vacuum mode). Equipartition of energy was then invoked to determine the amplitude α_k of each weighted mode under Brownian forcing, by equating the potential energy of each mode in this linear decomposition to $\frac{1}{2} k_B \mathcal{T}$ of energy, where $k_B \approx 1.38 \times 10^{-16}$ is Boltzmann's constant. This analysis lead to the following expression for the thermal power spectra of the tip's displacement P_{eq} ,

for a cantilever with spring constant k_e as a function of the oscillation frequency of the cantilever's tip ω

$$P_{eq}(\omega) = \frac{3\pi k_B \mathcal{T}}{k_e} \sum_{k=1}^{\infty} |\alpha_k(\omega)|^2 \left(c_k^4 \int_0^{\infty} |\alpha_k(\varpi')|^2 d\varpi' \right)^{-1} \phi_k^2(1), \quad (6.4a)$$

$$\alpha_k(\omega) = \frac{2 \sin c_k \tan c_k}{c_k (c_k^4 - \kappa(\omega)^4) (\sin c_k + \sinh c_k)}, \quad (6.4b)$$

$$\kappa = c_1 \omega_v^{-1/2} (\omega^2 - i\omega(\rho R^2/m_c)\Gamma(\omega))^{1/4}, \quad (6.4c)$$

where Γ is the expression for the drag on a circular cylinder of width R and mass per unit length m_c oscillating in an unbounded fluid of density ρ , as given in (2.19) and ω_v is the fundamental resonant frequency in vacuo. $\phi_{k,x}$ are derivatives of the vacuum modes (6.1b). The dangers of such analysis, however, were highlighted by Hinch (1975) who discussed the need to consider absorption of thermal energy by both the solid body and the fluid. Equation (6.4) does not allocate any thermal energy to the flow.

A second shortcoming of (6.4) lies in its assumption that the Brownian noise is δ -correlated, which is incorrect for time-dependent drag. A well-documented failing of the δ -correlation assumption was observed in the molecular dynamic simulations of liquid argon by Rahman (1964), where the auto-correlation function exhibited a $t^{-3/2}$ decay, rather than the e^{-t} decay predicted from δ -correlated forcing. The correct analysis, due to Zwanzig and Bixon (1970), took account of memory effects in the drag (as well as compression effects in the gas) and gave the correct algebraic decay. In § 6.3.1 we demonstrate this algebraic decay of auto-correlations for a thermally-driven cantilever experiencing two-dimensional drag.

6.2 Fluctuations in the canonical ensemble

Our approach avoids the equipartition of energy and δ -correlation assumptions and follows that recently suggested by Paul and Cross (2004), who made use of the Fluctuation-Dissipation theorem. This theorem, a fundamental result from statistical physics, connects microscopic fluctuations with macroscopic energy dissipation in the system.

Under Brownian forcing the cantilever fluctuations are stochastic in nature, although deterministic information is available by analysing the correlations of these

fluctuations over time. Chandler (1987) provides a description of how the fluctuation–dissipation theorem is able to connect microscopic fluctuations to macroscopically observed quantities using a classical mechanics approach, which we outline here. Our system consists of two subsystems (i) a cantilever consisting of n particles and (ii) a thermal bath made up of N particles, whose microscopic states can be characterized in phase space by the points $(\mathbf{q}^n, \mathbf{p}^n) \equiv (q_1, \dots, q_n; p_1, \dots, p_n)$, $(\mathbf{Q}^{3N}, \mathbf{P}^{3N}) \equiv (\mathbf{Q}_1, \dots, \mathbf{Q}_{3N}; \mathbf{P}_1, \dots, \mathbf{P}_{3N})$, corresponding to the motion of cantilever particles (constrained to one degree of freedom) and bath particles, respectively. The energy associated with the cantilever at given time t is then given by the Hamiltonian $\mathcal{H}_c(\mathbf{p}^n, \mathbf{q}^n)$ and the energy of the thermal bath by $\mathcal{H}_b(\mathbf{Q}^{3N}, \mathbf{P}^{3N})$, where both systems are in thermal equilibrium. The subsystems are closed (the number of particles and volume remain constant) but are not isolated (energy can be exchanged between the subsystems provided that the total energy of the system $\mathcal{E} = \mathcal{H}_c(\mathbf{q}^n, \mathbf{p}^n) + \mathcal{H}_b(\mathbf{Q}^{3N}, \mathbf{P}^{3N})$ remains fixed). These two conditions define a *canonical ensemble*.

For a given cantilever state $(\mathbf{q}^n, \mathbf{p}^n)$ with energy $\mathcal{H}_c(\mathbf{q}^n, \mathbf{p}^n)$ there are multiple microscopic states for the thermal bath consistent with the constraint $\mathcal{H}_b(\mathbf{Q}^{3N}, \mathbf{P}^{3N}) = \mathcal{E} - \mathcal{H}_c(\mathbf{q}^n, \mathbf{p}^n)$ and we denote their total number by $\Omega_b(\mathcal{E} - \mathcal{H}_c(\mathbf{q}^n, \mathbf{p}^n))$. As there is nothing in the physics which favours any particular microstate, it is assumed that they are all equally likely. Consequently the probability of observing the cantilever in state $(\mathbf{q}^n, \mathbf{p}^n)$ is proportional to $\Omega_b(\mathcal{E} - \mathcal{H}_c(\mathbf{q}^n, \mathbf{p}^n))$, i.e.

$$P(\mathbf{q}^n, \mathbf{p}^n) \propto \Omega_b(\mathcal{H}_b(\mathbf{Q}^{3N}, \mathbf{P}^{3N})) = \Omega_b(\mathcal{E} - \mathcal{H}_c(\mathbf{q}^n, \mathbf{p}^n)). \quad (6.5)$$

Connection with the thermodynamics is obtained by rewriting (6.5) in the form

$$P(\mathbf{q}^n, \mathbf{p}^n) \propto \exp(\ln(\Omega_b(\mathcal{E} - \mathcal{H}_c(\mathbf{q}^n, \mathbf{p}^n)))) \quad (6.6)$$

and using the fact that the thermal bath is sufficiently large that its energy levels effectively form a continuum and that its energy greatly exceeds that of the cantilever ($\mathcal{E} \gg \mathcal{H}_c(\mathbf{q}^n, \mathbf{p}^n)$). This allows us to expand the exponent about the total energy \mathcal{E}

$$\ln \Omega_b(\mathcal{E} - \mathcal{H}_c) = \ln \Omega_b(\mathcal{E}) - \mathcal{H}_c \left. \frac{d(\ln \Omega_b)}{d\mathcal{H}_b} \right|_{\mathcal{H}_b=\mathcal{E}} + \dots \quad (6.7)$$

The leading-order term in this expansion is proportional to the Gibbs entropy of the bath $S(\mathcal{H}_b) \equiv k_B \ln \Omega_b(\mathcal{H}_b)$, which counts the number of microscopic states at a given energy and provides a link between the bath's energy and its temperature, so that

$$k_B \frac{d(\ln \Omega_b)}{d\mathcal{H}_b} = \frac{dS}{d\mathcal{H}_b} \equiv 1/\mathcal{T}. \quad (6.8)$$

Since $\ln \Omega_b(\mathcal{E})$ is constant,

$$P(\mathbf{q}^n, \mathbf{p}^n) = \mathcal{Z}^{-1} \exp(-\beta \mathcal{H}_c(\mathbf{q}^n, \mathbf{p}^n)), \quad (6.9a)$$

where $\beta = (k_B \mathcal{T})^{-1}$ is computed at the bath's maximum temperature (since Ω_b is a monotonically increasing function of \mathcal{H}_b). Hence the probability of observing a microscopic cantilever state decreases exponentially as the energy of this state increases (Boltzmann distribution). The normalisation coefficient, found by taking the (conventionally-named) classical trace

$$\mathcal{Z} = \text{Tr} [\exp(-\beta \mathcal{H}_c)] \equiv \int \int d\mathbf{p}^n d\mathbf{q}^n \exp(-\beta \mathcal{H}_c(\mathbf{q}^n, \mathbf{p}^n)) \quad (6.9b)$$

is referred to as the *canonical partition function*. The equilibrium average $\langle \cdot \rangle_{eq}$ of a dynamical variable $\mathcal{K}(\mathbf{q}^n, \mathbf{p}^n, t)$ is then defined as

$$\langle \mathcal{K} \rangle_{eq} \equiv \text{Tr} [\mathcal{K}(\mathbf{q}^n, \mathbf{p}^n, t) e^{-\beta \mathcal{H}_c}] / \mathcal{Z} \quad (6.10)$$

and the stationary character of the equilibrium state means that this average is time-independent $\langle \mathcal{K}(\mathbf{q}^n, \mathbf{p}^n, t) \rangle_{eq} = \langle \mathcal{K}(\mathbf{q}^n, \mathbf{p}^n, 0) \rangle_{eq}$.

6.2.1 Microscopic equilibrium fluctuations

Equilibrium fluctuations are probed by placing the system into a non-equilibrium state through application of a small force to the n th particle, which takes the constant value $F \ll 1$ when $t \leq 0$ and is zero for $t > 0$. The system will reach a macroscopically steady non-equilibrium configuration (at $t = 0$); it is the indeterminate nature of this initial state which leads to stochasticity, since the decay back to equilibrium from a known initial condition is deterministic. For simplicity let us take this time-independent equilibrium value to be zero, i.e. $\langle q_n \rangle_{eq} = 0$. Consequently, the average value at a given

time $t > 0$ can be found by averaging all possible initial conditions. Recalling from (6.9) that the probability density function for initial non-equilibrium states is given by

$$P(\mathbf{q}^n(0), \mathbf{p}^n(0)) = \frac{\exp(-\beta(\mathcal{H}_c - F q_n(0)))}{\text{Tr}[\exp(-\beta(\mathcal{H}_c - F q_n(0)))]}, \quad (6.11)$$

the non-equilibrium average $\langle q_n(t) \rangle_{neq}$ at time t can be written as

$$\langle q_n(t) \rangle_{neq} \equiv \frac{\text{Tr}[\exp(-\beta(\mathcal{H}_c - F q_n(0))) q_n(t; 0)]}{\text{Tr}[\exp(-\beta(\mathcal{H}_c - F q_n(0)))]}, \quad (6.12)$$

where $q_n(t; 0)$ is the deterministic state at time t relating to a particular initial state $q_n(0)$. The trace is therefore an integral over all possible initial conditions.

Since $F \ll 1$ we can expand the non-equilibrium Hamiltonian about its equilibrium form

$$\begin{aligned} \langle q_n(t) \rangle_{neq} &= \frac{\text{Tr}[q_n(t; 0) e^{-\beta \mathcal{H}_c}]}{\text{Tr}[e^{-\beta \mathcal{H}_c}]} + \beta F \frac{\text{Tr}[q_n(0) q_n(t; 0) e^{-\beta \mathcal{H}_c}]}{\text{Tr}[e^{-\beta \mathcal{H}_c}]} \\ &\quad - \beta F \frac{\text{Tr}[q_n(0) e^{-\beta \mathcal{H}_c}] \text{Tr}[q_n(t; 0) e^{-\beta \mathcal{H}_c}]}{\text{Tr}[e^{-\beta \mathcal{H}_c}]^2} + O(F^2). \end{aligned} \quad (6.13)$$

Now $\exp(-\beta \mathcal{H}_c)$ is the probability density function for the system in the absence of the point force and so the non-equilibrium mean displacement (6.12) can be expressed in terms of the equilibrium averages

$$\begin{aligned} \langle q_n(t) \rangle_{neq} &= \langle q_n(t; 0) \rangle_{eq} + \beta F \left(\langle q_n(0) q_n(t; 0) \rangle_{eq} - \langle q_n(0) \rangle_{eq} \langle q_n(t; 0) \rangle_{eq} \right) + O(F^2) \\ &= \beta F \langle q_n(t; 0) q_n(0) \rangle_{eq} + O(F^2), \end{aligned} \quad (6.14)$$

as $\langle q_n(0) \rangle_{eq} = \langle q_n(t; 0) \rangle_{eq} = 0$. The right-hand side of (6.14) contains the autocorrelation function

$$C_{nn}(t) \equiv \langle q_n(t; 0) q_n(0) \rangle_{eq}, \quad (6.15)$$

which measures the correlation between initial fluctuations of the tip about the equilibrium displacement and those at time t . Rewriting (6.14) in the form

$$\langle q_n(t) \rangle_{neq} = \beta F C_{nn}(t) + O(F^2) \quad (6.16)$$

gives us a version of the celebrated fluctuation-dissipation theorem, relating microscopic fluctuations to the macroscopic relaxation of a system which, in turn, is linked to energy dissipation (see Chandler 1987).

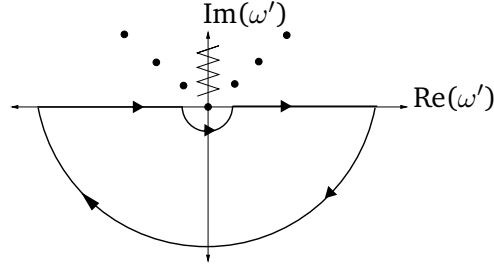


FIGURE 6.1: In general $\chi(\omega') \omega'^{-1} e^{-i\omega' t}$, with ω' complex, possesses poles and a branch cut (jagged line) in the upper-half of the complex plane, in addition to the pole at zero. By the residue theorem the contour integral is zero, with the only non-negligible contributions coming from the integrals around $\omega' = 0$ and along the real axis.

6.2.2 Thermal spectra

The connection between the laws governing the micro- and macroscopic dates back to the regression hypothesis of Onsager (1931), which states that the regression of spontaneous microscopic fluctuations in an equilibrium system are governed by the same laws which describe the relaxation of macroscopic non-equilibrium disturbances. These macroscopic disturbances are simply the averaged microscopic state $\langle q_n(t) \rangle_{neq}$ defined in (6.12). Given the linearity of the system, there exists a function $K(t)$ which relates any time-dependent force $F_n(t)$ applied to particle n to its macroscopic response

$$\langle q_n(t) \rangle_{neq} = \int_{-\infty}^{\infty} K(t - \tau') F_n(\tau') d\tau', \quad (6.17)$$

which in Fourier space takes the form

$$\langle \widehat{q_n(\omega')} \rangle_{neq} = \chi(\omega') \widehat{F_n(\omega')}, \quad (6.18)$$

where $\chi(\omega') \equiv \widehat{K(t)}$ is commonly referred to as the system's susceptibility and can be determined by choosing $F_n(t)$ to be the temporal Dirac-delta function ($\delta(t)$). With the susceptibility known, the response to the Fourier-transformed Heaviside forcing

$$\widehat{F_n(\omega')} = F \left(\pi \delta(\omega') + \frac{i}{\omega'} \right) \quad (6.19)$$

(see Reichl 1987) can readily be computed. The fluctuation–dissipation theorem then gives us the autocorrelation function through an inverse-Fourier transform of (6.18)

$$\begin{aligned} C_{nn}(t) &= \frac{k_B \mathcal{T}}{F} \langle q_n(t) \rangle_{neq} = \frac{k_B \mathcal{T}}{2\pi F} \int_{-\infty}^{\infty} \chi(\omega') \widehat{F}_n(\omega') e^{i\omega' t} d\omega' \\ &= \frac{k_B \mathcal{T}}{2F} \chi(0) + \frac{ik_B \mathcal{T}}{2\pi F} \int_{-\infty}^{\infty} \frac{\chi(\omega')}{\omega'} e^{i\omega' t} d\omega'. \end{aligned} \quad (6.20)$$

Because the fluid drag is time-dependent, $\chi(\omega')$ contains a branch cut along the positive imaginary axis (see figure 6.1) which must be navigated when taking the inverse transform and this has important consequences (see § 6.3.1).

The auto-correlation function (6.20) can be simplified further using the residue theorem. Following a closed contour in the complex plane, which avoids the branch cut and any poles of $\chi(\omega')$ (see figure 6.1), gives us

$$\pi \chi(0) = -i \int_{-\infty}^{\infty} \frac{\chi(\omega') e^{-i\omega' t}}{\omega'} d\omega', \quad (6.21)$$

where integration is defined in the Cauchy-Principal-Value sense. Consequently

$$\begin{aligned} C_{nn}(t) &= \frac{ik_B \mathcal{T}}{2\pi F} \int_{-\infty}^{\infty} \left(\frac{\chi(\omega')}{\omega'} e^{i\omega' t} d\omega' - \frac{\chi(\omega')}{\omega'} e^{-i\omega' t} d\omega' \right) \\ &= \frac{-k_B \mathcal{T}}{\pi F} \int_{-\infty}^{\infty} \frac{\chi(\omega')}{\omega'} \sin \omega' t d\omega'. \end{aligned} \quad (6.22)$$

The thermal spectrum of the cantilever can now be found by taking the Fourier-cosine transform of (6.22)

$$\begin{aligned} P(\omega) &\equiv 2 \int_0^{\infty} C_{nn}(t) \cos \omega t dt \\ &= -\frac{2k_B \mathcal{T}}{\pi F} \int_0^{\infty} \cos \omega t dt \int_{-\infty}^{\infty} \frac{\chi(\omega')}{\omega'} \sin \omega' t d\omega' \\ &= -\frac{2k_B \mathcal{T}}{\pi F} \int_{-\infty}^{\infty} \frac{\chi(\omega')}{\omega'^2 - \omega^2} d\omega' \\ &= -\frac{k_B \mathcal{T}}{\pi F \omega} \int_{-\infty}^{\infty} \left(\frac{\chi(\omega')}{\omega' - \omega} - \frac{\chi(\omega')}{\omega' + \omega} \right) d\omega' \\ &= -\frac{ik_B \mathcal{T}}{F} \frac{(\chi(\omega) - \chi(-\omega))}{\omega} \\ &= \frac{2k_B \mathcal{T}}{F} \frac{\Im(\chi(\omega))}{\omega}. \end{aligned} \quad (6.23)$$

Hence we have the thermal spectrum, a quantity which is measurable in AFM experiments, in terms of the susceptibility χ , which can be computed deterministically.

6.3 Fluctuating beams

For the specific case of cantilever fluctuations, AFM experimentalists measure the thermal spectrum of the tip. Once we have found the tip's susceptibility $\chi(\omega)$, the thermal spectrum follows immediately by (6.23). Although we have the technology to consider finite-width plates, many of the important features of Brownian-driven fluctuations can be illustrated using an Euler–Bernoulli beam description of the cantilever's elastic behaviour (see § 5.1).

As the cantilever fluctuates under thermal noise, rather than being driven at a fixed frequency at very low temperatures, we rescale time on the natural frequency of the cantilever and the cantilever's kinetic energy on $k_B \mathcal{T}$. The cantilever and flow variables rescale accordingly

$$\begin{aligned} \mathbf{x} &= L\bar{\mathbf{x}}, & \mathcal{W} &= \sqrt{k_B \mathcal{T} L^3 / EI} \bar{\mathcal{W}}, & \omega &= \sqrt{EI / m_c L^4} \varpi, \\ \mathbf{u} &= \sqrt{k_B \mathcal{T} / m_c L} \bar{\mathbf{u}}, & \boldsymbol{\sigma} &= \mu \sqrt{k_B \mathcal{T} / m_c L} \bar{\boldsymbol{\sigma}} \end{aligned} \quad (6.24)$$

(bars are dropped immediately), recalling that \mathbf{u} and $\boldsymbol{\sigma}$ represent the flow velocity and stress tensor. Under these rescalings the Euler–Bernoulli beam equation (Kelly 1993) takes the form

$$w_{\xi\xi\xi\xi} - \varpi^2 w = M^{1/2} \Omega f_n(\xi; \varpi^{1/2} M^{-1/4}, M, \Delta) \quad (6.25a)$$

(subscripts denote derivatives), where M and Ω are as in § 5.1 and f_n represents the hydrodynamic loading on the cantilever, per unit length. Under this frequency-scaling, the Strouhal number, which quantifies the degree of unsteadiness in the flow, is given by $\varpi^{1/2} M^{-1/4}$. The point load balances the shear force at the tip, giving us the boundary conditions (under a temporal Fourier transform)

$$w(0) = w_\xi(0) = w_{\xi\xi}(1) = 0, \quad w_{\xi\xi\xi}(1) = 1. \quad (6.25b)$$

We consider the cases where f_n is given by two-dimensional drag and three-dimensional USBT.

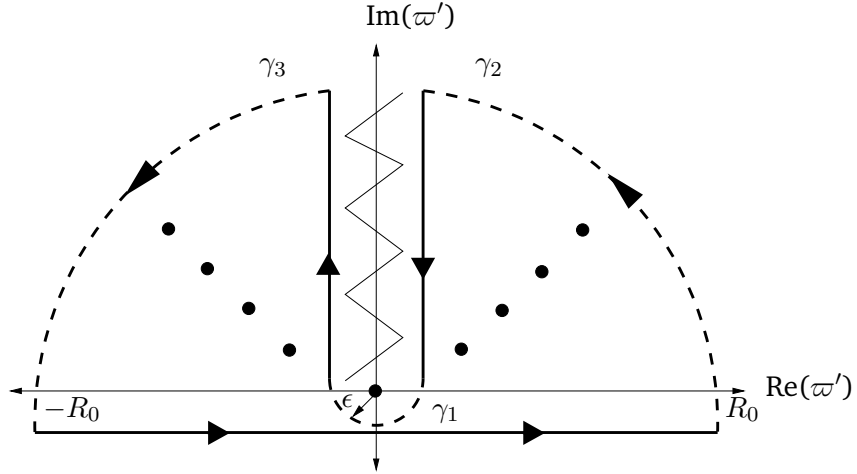


FIGURE 6.2: The inverse Fourier transform in (6.30) can be found by application of the residue theorem. Unsteady drag introduces a branch cut (jagged line) into the complex plane, the navigation of which yields an integral along the positive imaginary axis. Contour segments γ_1 , γ_2 and γ_3 are shown with a dashed line and points denote poles of the susceptibility function $\chi(\sqrt{w'})$.

6.3.1 Two-dimensional drag

Under a two-dimensional flow assumption (lengths rescaled on R in the flow equations) $f_n(\xi; \epsilon\varpi^{1/2}M^{-1/4}, M, \Delta)$ is directly proportional to the local velocity, i.e.

$$f_n(\xi; \epsilon\varpi^{1/2}M^{-1/4}, M, \Delta) = i(\epsilon\varpi^{1/2})^2\Gamma(\epsilon\varpi^{1/2}M^{-1/4}, \Delta)w(\xi), \quad (6.26)$$

where $\Gamma(\epsilon\varpi^{1/2}M^{-1/4}, \Delta)$ is a two-dimensional drag coefficient. Hence

$$w_{\xi\xi\xi\xi} - \kappa^4 w = 0, \quad \kappa = \left(\varpi^2 + iM^{1/2}\Omega\epsilon^2\varpi\Gamma(\epsilon\varpi^{1/2}M^{-1/4}, \Delta)\right)^{1/4}, \quad (6.27)$$

subject to (6.25b), is solved by

$$w(\xi, \omega) = c_1 \left(e^{\kappa\xi} - \cos \kappa\xi - \sin \kappa\xi \right) - c_2 \left(e^{-\kappa\xi} - \cos \kappa\xi + \sin \kappa\xi \right), \quad (6.28a)$$

where

$$c_1 = \frac{e^{-\kappa} + \cos \kappa - \sin \kappa}{4\kappa^3(1 + \cos \kappa \cosh \kappa)}, \quad c_2 = \frac{e^{\kappa} + \cos \kappa + \sin \kappa}{4\kappa^3(1 + \cos \kappa \cosh \kappa)}. \quad (6.28b)$$

The susceptibility for the displacement of the cantilever tip is then given by

$$\chi(\sqrt{\varpi}) \equiv w(1) = \frac{\cos \kappa \sinh \kappa - \sin \kappa \cosh \kappa}{\kappa^3(1 + \cos \kappa \cosh \kappa)}. \quad (6.29)$$

With χ in such a simple form, it is instructive to use the residue theorem to evaluate explicitly the auto-correlation function for tip displacement, where it is useful to note that $\chi(\sqrt{\varpi}) \rightarrow -\frac{1}{3}$ as $\varpi \rightarrow 0$. The fluctuation–dissipation theorem (6.20) requires us to integrate the susceptibility over all frequencies

$$C_{nn}(t) = \frac{k_B \mathcal{F}}{F} \left(-\frac{1}{6} + \frac{i}{2\pi} \int_{-\infty}^{\infty} \frac{\chi(\sqrt{\varpi'})}{\varpi'} e^{i\varpi' t} d\varpi' \right). \quad (6.30)$$

This dependence upon the square root of ϖ' leads to a branch cut along the positive imaginary axis. Using residue theorem when $t > 0$, we are required to close the contour in the upper-half of the complex plane and therefore this branch cut must be circumvented (see figure 6.2).

The non-zero poles a_k of χ are the countably-infinite vacuum eigenfrequencies $\kappa = c_k$ which satisfy the transcendental equation (6.2). The residue theorem then gives us

$$C_{nn} = \frac{k_B \mathcal{F}}{F} \left[-\frac{1}{6} - \sum_{k=1}^{\infty} \text{res} \left\{ \frac{\chi(\sqrt{\varpi'})}{\varpi'} e^{i\varpi' t}; a_k \right\} + \left(\int_{\gamma_1} + \int_{\gamma_2} + \int_{\gamma_3} \right) \frac{\chi(\sqrt{\varpi'})}{\varpi'} e^{i\varpi' t} d\varpi' + \frac{i}{2\pi} \int_{-i\epsilon}^{iR_0} \frac{(\chi^+(\sqrt{\varpi'}) - \chi^-(\sqrt{\varpi'})) e^{i\varpi' t}}{\varpi'} d\varpi' \right], \quad (6.31)$$

where χ^+ and χ^- correspond to values on either side of the branch cut, which differ in sign. In the limit $\epsilon \rightarrow 0$, $R_0 \rightarrow \infty$ the γ_1 contribution cancels the $-1/6$ term, whilst the γ_2 and γ_3 contour integrals become vanishingly small. Hence

$$C_{nn} = -\frac{k_B \mathcal{F}}{F} \left[\sum_{k=1}^{\infty} \text{res} \left\{ \frac{\chi(\sqrt{\varpi'})}{\varpi'} e^{i\varpi' t}; a_k \right\} + \frac{1}{\pi} \int_0^{\infty} \frac{\Im(\chi(i\sqrt{x})) e^{-xt}}{x} dx \right]. \quad (6.32)$$

An expression for the residue at the non-zero pole $\varpi' = a_k$ can be obtained by series expanding $\kappa(\sqrt{\varpi})$ (6.27) about a_k , i.e. $\kappa = \kappa(a_k) + \kappa_1(a_k)(\varpi - a_k)$. This gives

$$1 + \cos \kappa \cosh \kappa = \kappa_1(a_k) (\cos \kappa(a_k) \sinh \kappa(a_k) - \sin \kappa(a_k) \cosh \kappa(a_k)) (\varpi - a_k). \quad (6.33)$$

Substituting (6.33) into (6.29) and extracting the $(\varpi - a_k)^{-1}$ coefficient in the Laurent series then gives

$$\text{res} \left\{ \frac{\chi(\sqrt{\varpi'})}{\varpi'} e^{i\varpi' t}; a_k \right\} = \frac{e^{ia_k t}}{a_k \kappa(a_k)^3 \kappa_1(a_k)}. \quad (6.34)$$

Therefore

$$C_{nn} = -\frac{k_B \mathcal{J}}{F} \left[\sum_{k=1}^{\infty} \frac{e^{ia_k t}}{a_k \kappa(a_k)^3 \kappa_1(a_k)} + \frac{1}{\pi} \int_0^{\infty} \frac{\Im(\chi(i\sqrt{x})) e^{-xt}}{x} dx \right]. \quad (6.35)$$

From (6.35) we see how the branch cut produces a contribution from the continuous spectrum, which modifies the otherwise exponential time decay from the discrete spectrum. This is the same mechanism by which unsteady drag leads to $t^{-3/2}$ long-time behaviour in the auto-correlation of liquid argon (Rahman 1964, see § 6.1) Taking the Fourier-cosine transform of (6.35) then gives us the thermal spectrum as a sum of discrete and continuous spectral contributions

$$\begin{aligned} P(\varpi) &= 2 \int_0^{\infty} C_{nn}(t) \cos(\varpi t) dt \\ &= -2 \frac{k_B \mathcal{J}}{F} \left(i \sum_{k=1}^{\infty} \frac{\kappa(a_k)^{-3} \kappa_1^{-1}(a_k)}{a_k^2 - \varpi^2} + \frac{1}{\pi} \int_0^{\infty} \frac{\Im(\chi(i\sqrt{x}))}{x^2 + \varpi^2} dx \right). \end{aligned} \quad (6.36)$$

Consider the example where $\Gamma(\epsilon \varpi^{1/2} M^{-1/4})$ is the two-dimensional unsteady drag in unbounded fluid (2.19). Then

$$\kappa_1 = \left[\frac{\Lambda(a_k)^{1/4}}{4a_k^{3/4}} + \frac{a_k^{1/4}}{4\Lambda(a_k)^{3/4}} \left((1 - \pi\epsilon^2\Omega) + 2\pi\epsilon^2\Omega \left(\frac{K_1(\epsilon M^{-1/4} \sqrt{ia_k})}{K_0(\epsilon M^{-1/4} \sqrt{ia_k})} \right)^2 \right) \right], \quad (6.37a)$$

$$\Lambda(a_k) = a_k \left(1 + \pi\epsilon^2\Omega \left(1 + \frac{4K_1(\epsilon M^{-1/4} \sqrt{ia_k})}{\epsilon M^{-1/4} \sqrt{ia_k} K_0(\epsilon M^{-1/4} \sqrt{ia_k})} \right) \right), \quad (6.37b)$$

and so

$$\begin{aligned} \text{res} \left\{ \frac{\chi(\sqrt{\varpi'}) e^{i\varpi' t}}{\varpi'}; a_k \right\} &= \\ &= 4 e^{ia_k t} \left(\kappa(a_k)^4 + a_k^2 \left((1 - \pi\epsilon^2\Omega + 2\pi\epsilon^2\Omega \left(\frac{K_1(\epsilon M^{-1/4} \sqrt{ia_k})}{K_0(\epsilon M^{-1/4} \sqrt{ia_k})} \right)^2) \right) \right)^{-1}. \end{aligned} \quad (6.38)$$

The continuous spectral contribution derives solely from unsteadiness in the drag and in § 6.4 we examine its specific effect on the thermal spectrum.

6.3.2 USBT hydrodynamics

As with sinusoidal driving, if the hydrodynamic loading is three-dimensional we can solve the elasticity equation coupled to a USBT description of the flow (see chapter 3).

This can be achieved using the numerical scheme described by (5.5), but with the vector \mathbf{b}_1 now holding the instantaneous point-force boundary conditions (6.25b). Note that under the rescalings (6.24), the USBT frequency constraint becomes $\varpi^{-1/2}M^{1/4} \ll \epsilon$. This approach allows us to analyse the influence of screening effects on the thermal spectra in § 6.4.

6.3.3 Experimental setup ¹

Thermal power spectra experiments were conducted using an Asylum Research (MFP-1D) AFM molecular force probe (MFP), which was equipped with a gold-coated ParkScientific silicon nitride cantilever, fitted with a $2\mu\text{m}$ high pyramidal tip. Cleaved mica was used as a substrate and spectra were collected in both air and water (filtered at $0.2\mu\text{m}$ using an Elga filtering system). Experiments were conducted at approximately 25 degrees Celsius, although the temperature was able to fluctuate slightly. Even though manufacturer estimates were provided, high-resolution of the cantilever dimensions were obtained using scanning-electron microscopy (SEM) whose images (figure 6.3) show that the cantilever has length, width and thickness of $232.4\mu\text{m}$, $20.11\mu\text{m}$ and $0.573\mu\text{m}$, respectively (the manufacturer length estimate was $200\mu\text{m}$). Raw data was passed into commercial signal processing software (Igor Pro), running an Asylum Research power spectrum analyser (fast-Fourier transform (FFT) routines).

Spectra, which were gathered in both air and water, are presented in § 6.4.2 alongside theoretical predictions.

6.4 Results

6.4.1 Theory

The effects of varying the cantilever stiffness and density relative to the fluid are both explored in figure 6.4. Decreasing the cantilever stiffness (i.e. decreasing the Young's

¹Experiments were conducted in the Laboratory of Biophysics and Surface Analysis at the University of Nottingham in collaboration with Anita Turner, a graduate student in the School of Pharmacy.

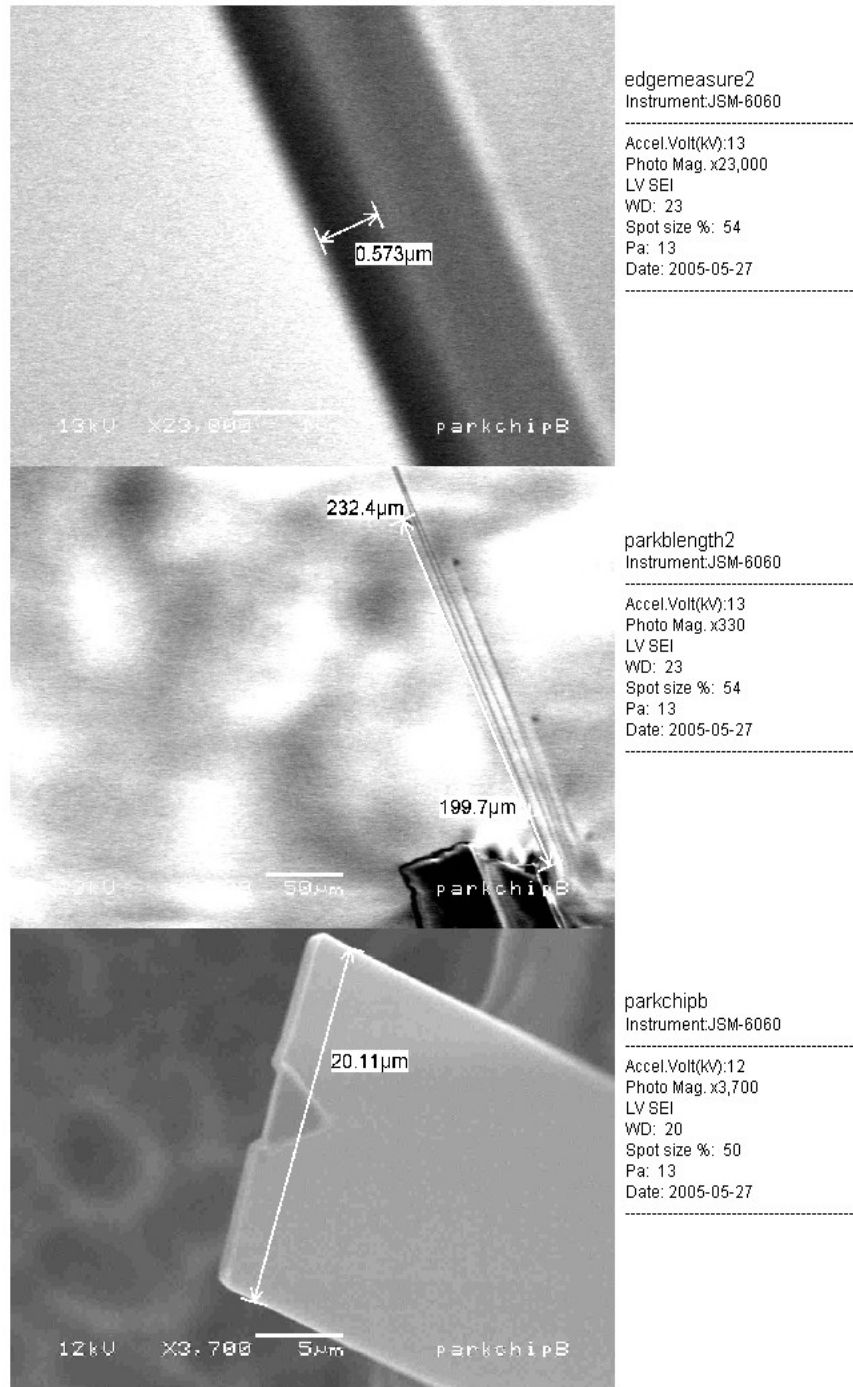


FIGURE 6.3: Scanning-electron microscopic (SEM) images of the cantilever used in the thermal power spectra experiments, showing its thickness, length and width to be $0.573\mu\text{m}$, $232.4\mu\text{m}$ and $20.11\mu\text{m}$, respectively.

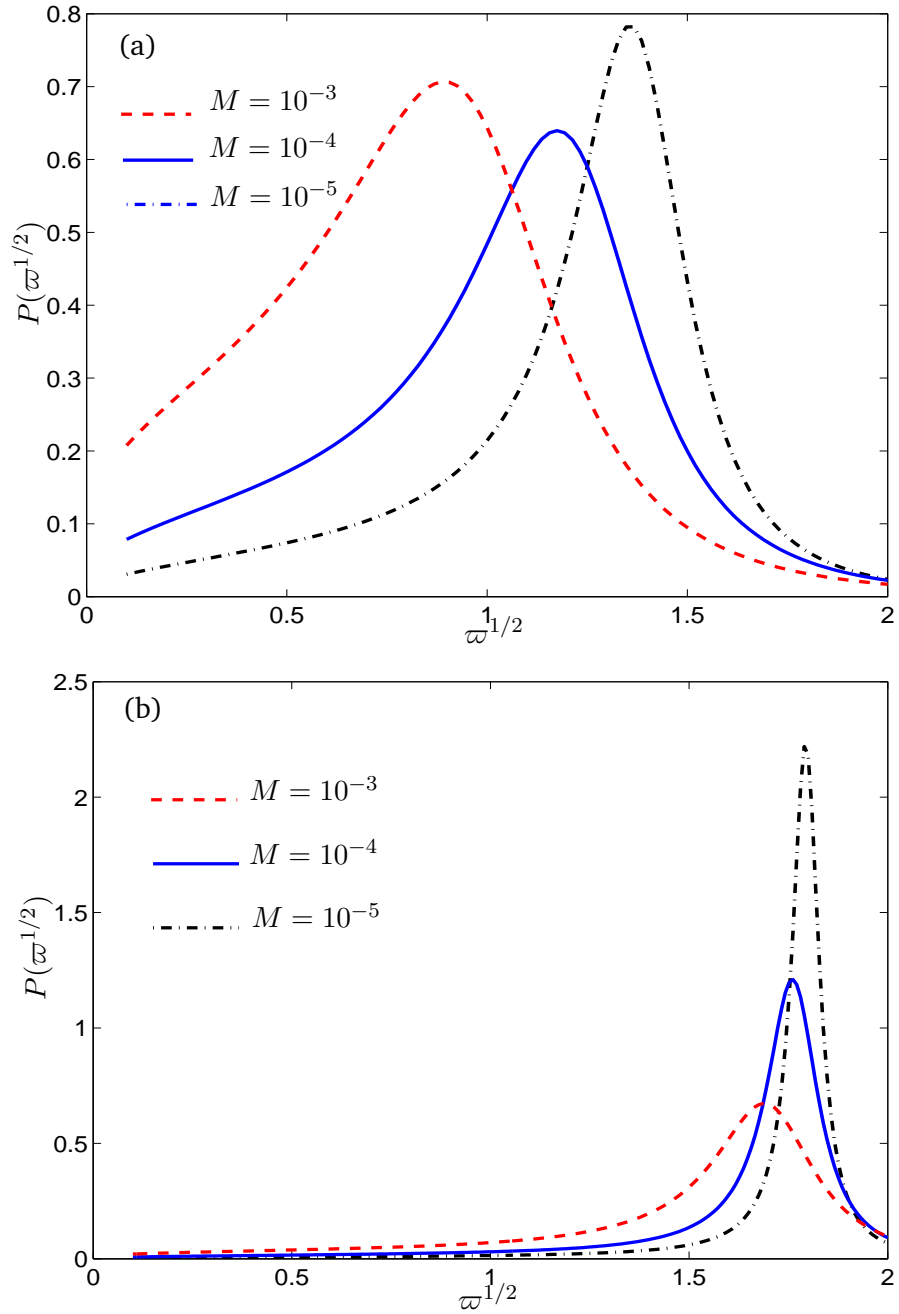


FIGURE 6.4: Theoretical thermal spectra (6.23) of displacement at the tip of a horizontal cantilever ($\alpha = 0$) experiencing two-dimensional hydrodynamic drag (2.38) when $\Delta = 100$, $\epsilon = 0.1$ for $M = 10^{-3}$, 10^{-4} and 10^{-5} and (a) $\Omega = 100/\pi$ or (b) $\Omega = 10/\pi$.

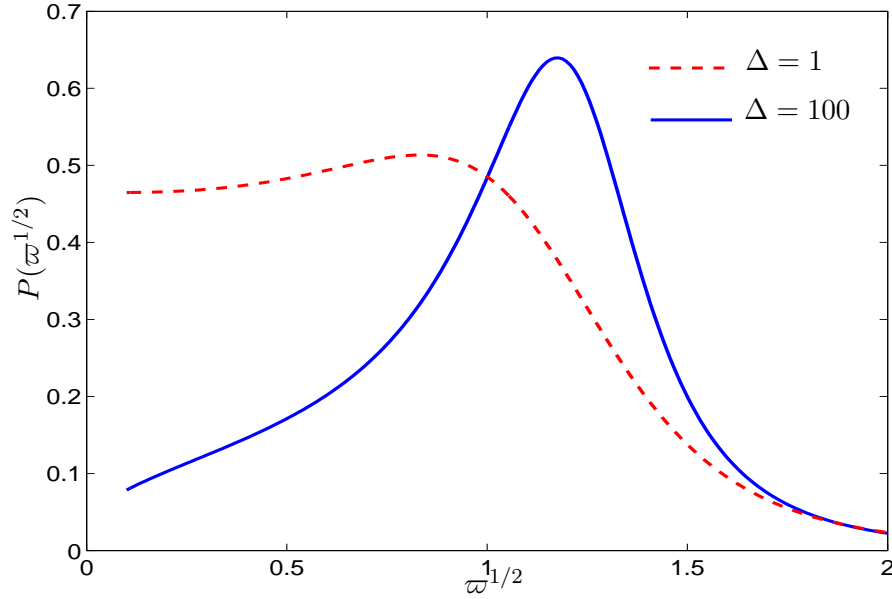


FIGURE 6.5: Theoretical thermal spectra (6.23) of displacement at the tip of a horizontal cantilever ($\alpha = 0$) experiencing two-dimensional hydrodynamic drag (numerically computed, see § 2.1) when $\Delta = 1, 100$, $\epsilon = 0.1$, $M = 10^{-4}$ and $\Omega = 100/\pi$.

modulus E), corresponds to an increase in M and leads to the resonant peak broadening and being shifted to lower frequencies (figure 6.4a), with a similar shift observed when the fluid to cantilever density ratio Ω is increased (figure 6.4b). Both of these phenomena can be linked to a relative decrease in the generated flow's inertia and, consequently, an increase in dissipative effects.

Similar effects can be observed in figure 6.5, which shows variations in the cantilever's thermal spectra as the separation distance Δ is decreased. The small-separation limit is dominated by quasi-steady flow and so, for the reasons just discussed above, this leads to a broadening in the resonant peak accompanied by a shift to lower frequencies. There is also a levelling-off in the spectra at low values of $\varpi^{1/2}$ when Δ is small.

The impact of cross-sectional shape is explored in figure 6.6, where spectra have been produced for cantilevers with circular and thin rectangular cross-sections at $\Delta = 1$ and $\Delta = 10$. At large separation there is little difference between the spectra, a consequence of the similarity between the drag on a plate and that on a circular cylinder

of equivalent width (Tuck 1969). Once the separation has been reduced to $\Delta = 1$, however, the geometrical differences become important. The rectangular cantilever's larger lubrication region with the wall leads to greater hydrodynamic loading and hence more strongly damped thermal spectra.

For the simple case where $\Delta \gg 1$ and the drag is assumed to be two-dimensional, figure 6.7 shows that when we use (6.4), the method of Sader (1998), the levelling-off in the spectra at small $\varpi^{1/2}$ is present even at a large separation ($\Delta = 100$), in contrast to fluctuation-dissipation spectra (6.23) which decay as $\varpi^{1/2}$ tends to zero. This can be attributed to the inherent assumption in (6.4) that the Brownian forcing \mathcal{F}_B is delta-correlated i.e. $\langle \mathcal{F}_B(t), \mathcal{F}_B(0) \rangle = k_B \mathcal{T} \delta(t)$ when, in fact, Hauge and Martin-Löf (1973) demonstrated that for time-dependent drag $\langle \mathcal{F}_B(t), \mathcal{F}_B(0) \rangle = k_B \mathcal{T} \Gamma(|t|)$, where $\Gamma(t)$ is the drag coefficient in physical space ($D(t) = \int_0^t \Gamma(s) U(s) ds$). Application of the residue theorem decomposes the thermal spectrum into discrete (poles) and continuous (branch cut) contributions (6.36) and it can be seen that this branch-cut contribution, which is present due to the unsteadiness of the drag, is responsible for the spectral decay at low frequencies. In figure 6.7(b), where $\Delta = 0.1$, the discrepancy between the two approaches becomes less pronounced. This is because the proximity of the wall results in a drag on the cantilever which is essentially quasi-steady over a large range of $\varpi^{1/2}$ and in this limit the drag becomes independent of earlier motion ($\Gamma(t) \rightarrow \delta(t)$); hence the assumption inherent in the analysis of Sader (1998) becomes applicable for a wide range of the frequencies integrated over in (6.4a).

The effect of wall and frequency-screening (in suppressing three-dimensionality in the flow) in the thermal spectrum is illustrated by figure 6.8. When M is $O(1)$, over moderate frequency ranges $\varpi^{1/2}$ is also $O(1)$ and so, when $\Delta \gg 1$, finite-length effects are felt along the entire cantilever length and the flow is genuinely three-dimensional (figure 6.8a). As was found with the driven spectra, when the separation distance is decreased (figure 6.8b) Δ -screening of end effects results in improved agreement between the two-dimensional and USBT drag. The two-dimensional drag predictions prove applicable at large separations provided that the cantilever is sufficiently stiff. In figure 6.8(c), $M = 10^{-2}$, resulting in $\varpi^{1/2} = O(10)$ over much of the frequency range

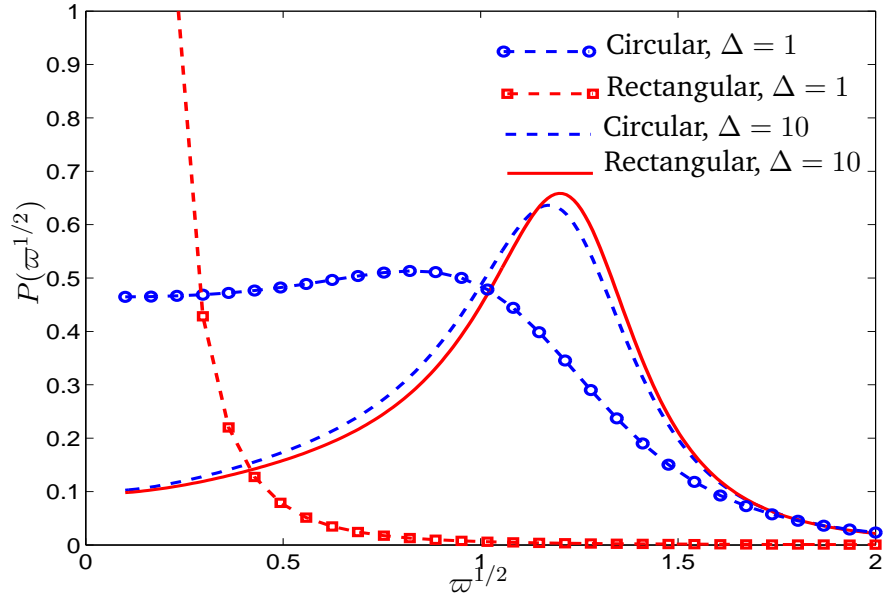


FIGURE 6.6: Theoretical thermal spectra (6.23) of displacement at the tip of two-dimensional circular and thin rectangular ($d/\epsilon = 0.01$) cantilevers when $\Delta = 1$ and $\Delta = 10$, $\epsilon = 0.1$, $\alpha = 0$, $M = 10^{-1}$ and $\Omega = 100/\pi$.

and this proves sufficient for effective frequency screening of three-dimensionality in the flow.

6.4.2 Experiment

Figure 6.9 shows the thermal spectra at the tip of an AFM cantilever, obtained experimentally using the procedures outlined in § 6.3.3. The gold-coated silicon nitride cantilever had a $0.573\mu\text{m}$ thickness, $20\mu\text{m}$ width, $232\mu\text{m}$ length and measurements were made in both air and water, at different distances from a substrate.

The cantilever was gold-coated to improve its reflectivity, which results in a change to the material properties as specified by the manufacturers. Therefore it proved necessary to determine the density ρ_c by fitting to the thermal spectrum collected in air. Varying cantilever density in the theoretical model changes the width-to-height ratio (quality factor) of the first resonant peak and it was found that a density of 5.3gcm^{-3} gave the best fit (in approximate agreement with Chon et al. (2000), who conducted

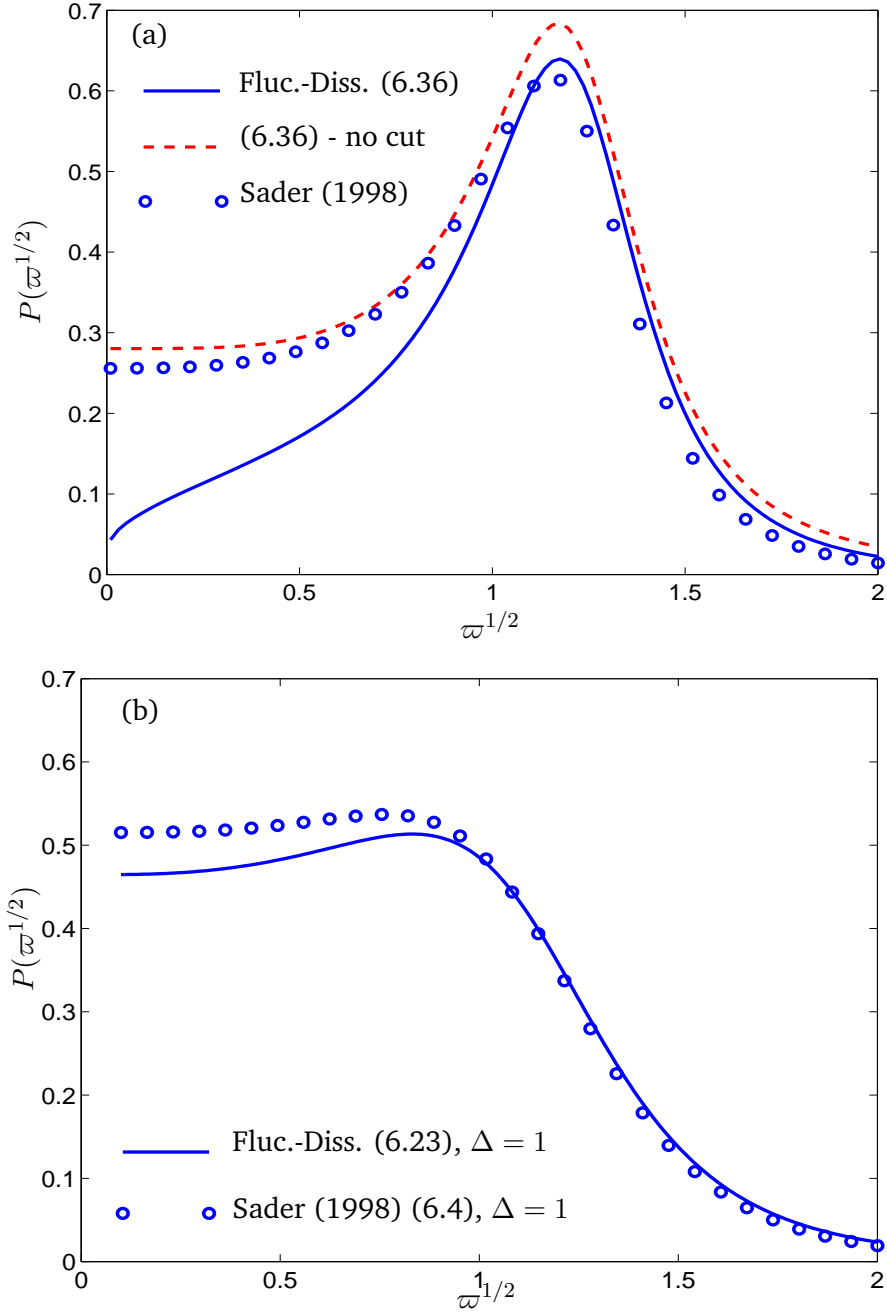


FIGURE 6.7: Theoretical thermal spectra of displacement at the tip of a circular cantilever, obtained using the two-dimensional hydrodynamic drag assumption when $\alpha = 0$, $\epsilon = 0.1$, $M = 10^{-4}$ and $\Omega = 100/\pi$. Comparison can be made between the fluctuation–dissipation theory prediction (6.23) (full line) and that obtained using (6.4) (Sader 1998, markers). In (a) $\Delta \gg 1$ the hydrodynamic loading is given by (2.19) and we use the result derived by application of residue theorem (6.36), with the dashed line showing contributions from the discrete spectrum only (i.e. no branch-cut integral). In (b) $\Delta = 1$ and the drag is computed numerically (see § 2.1) and we must therefore evaluate the power spectrum (6.23) numerically.

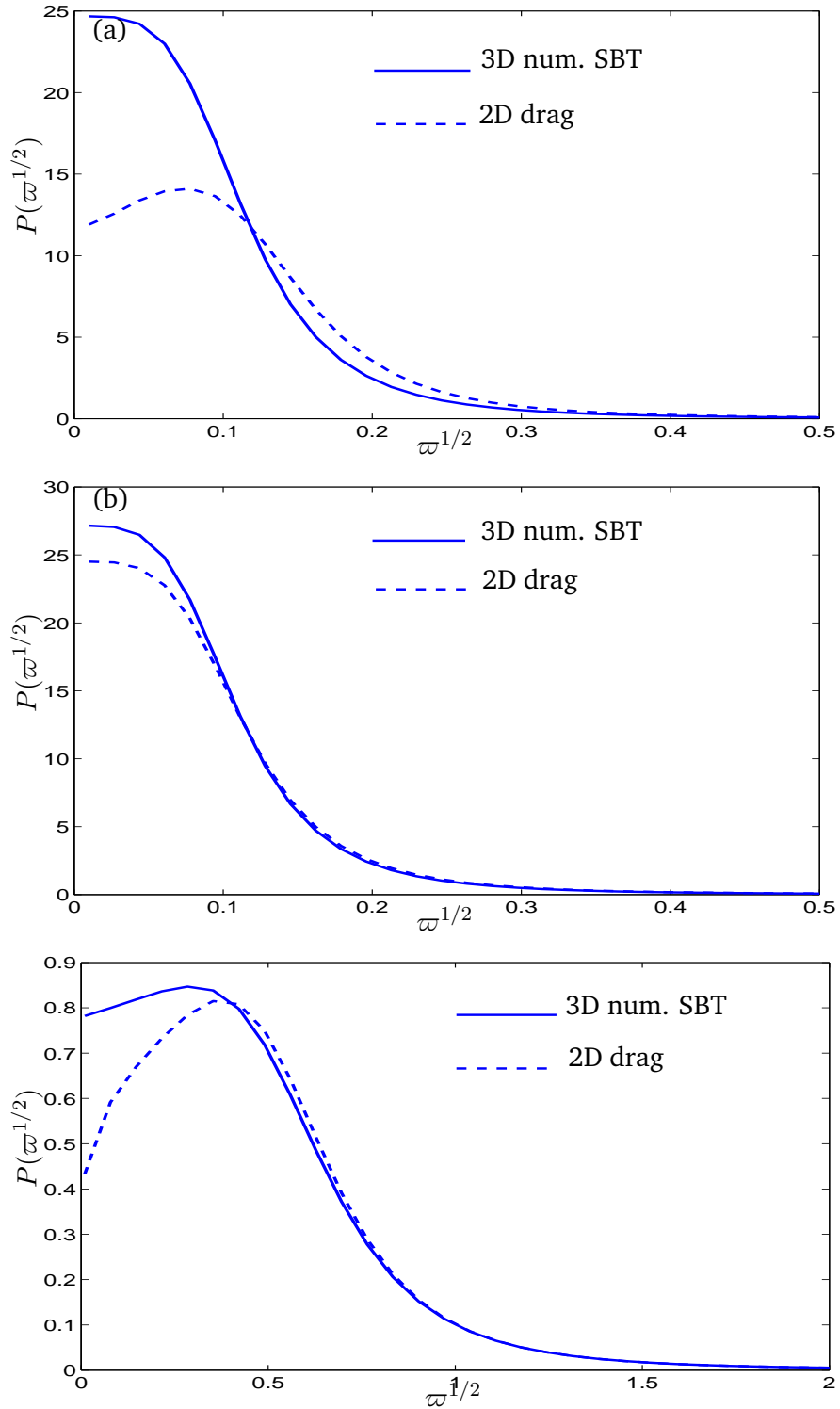


FIGURE 6.8: Theoretical thermal spectra (6.23) of displacement at the tip of a horizontal circular cantilever ($\alpha = 0$) computed using both USBT hydrodynamics (§ 6.3.2, full line) and two-dimensional drag (6.29, dashed line) when $\epsilon = 10^{-2}$, $\Omega = 10/\pi$ and (a) $\Delta = 100$, $M = 1$, (b) $\Delta = 1$, $M = 1$ and (c) $\Delta = 100$, $M = 10^{-3}$.

similar experiments). All other theoretical predictions, including those in water, then used this density value. Furthermore, the first resonant peak in air also provided verification of the manufacturer's estimate for the cantilever's resonant frequency in-vacuo, which typically only varies by a few percent from the value in air (Chon et al. 2000). The software which automatically analyses the experimental data contains *black-box* routines which rescale the thermal power spectrum. For this reason, we normalised our theoretical spectra so that the amplitude of the first resonant peak in air matched the experimental value. This normalisation constant was then used for predictions in water, both near and away from the wall.

As in figure 6.4, the spectra obtained in the lower-density medium exhibit more defined resonant peaks, situated at higher frequencies. A direct comparison is made with the theoretical predictions of (Sader 1998) (6.4), shown by the full thick line and the fluctuation–dissipation theorem (6.23), given by the dashed thick line and in both cases hydrodynamic loading was given by (2.19). In comparing the two sets of theoretical predictions, we note the differences in size of the second harmonic. Sader (1998) predicts a larger response and this may be due to his assumption that all thermal energy goes into moving the cantilever when, in fact, Hinch (1975) tells us that some of that energy is needed to drive the surrounding flow. This only becomes noticeable as flow inertia increases, i.e. at larger frequencies of oscillation, which perhaps explains why the theoretical amplitudes of the first harmonics do not suffer from the discrepancy. (The amplitude of the experimentally-measured second harmonic appears to lie between these two theoretical predictions and this could be due to a number of experimental factors, for example the neglect of axial flows.)

Comparison with the experimental data in figures 6.9(a,b) shows that both theoretical models work reasonably well, capturing the location, amplitude and sharpness of the resonant peaks (especially the principal harmonic) to a high level of accuracy and correctly predicting the shift in these characteristics as the density of the surrounding medium is varied. However, there are certain improvements offered by the fluctuation–dissipation approach and these are best illustrated in figure 6.9(c), which gives a close-up of the first harmonic in water. This provides experimental evidence of the low-

frequency decay of the thermal spectrum which can be captured using fluctuation–dissipation theorem (dashed thick line) but not using the formula given by Sader (1998) (full thick line).

The agreement between theory and experiment is remarkably good, although there are some experimental artifacts which have not been incorporated into the model. The spectra are seen to exhibit a $1/\omega$ behaviour at low frequencies (which is especially noticeable in 6.9a) and this is due to miscellaneous mechanical vibrations, for example from the air conditioning etc. Furthermore, the spectral baseline is non-zero and this is due to low-level white noise produced by the apparatus electronics.

Figure 6.10 shows how wall effects can produce a shift in the spectra which is captured well by the theory. A thermal spectrum obtained experimentally, at a separation distance of $8.87\mu\text{m}$ (including tip, red line) is seen to have a lower amplitude and resonant frequency than at $70\mu\text{m}$, where wall effects are much weaker (green line). These changes are well captured by the fluctuation–dissipation theory (6.23) when the hydrodynamic drag is computed using two-dimensional BEM for a rectangular cantilever near a wall, provided that we acknowledge the finite ($\alpha = \pi/12$) tilt (full blue line). If tilt is ignored (dashed blue line), the hydrodynamic loading on the cantilever is artificially high and the spectra do not agree well. (At large separation distances, the spectrum is not tilt sensitive.) Note, however, that tilt has only been accounted for here in a two-dimensional context, i.e. we have neglected any flows along the cantilever axis.

6.5 Discussion

We have examined the fluctuations at the tip of a thermally-driven cantilever by using the fluctuation–dissipation theorem, which links macroscopic behaviour to microscopic fluctuations; we described its physical basis in some detail using a Hamiltonian description of a cantilever immersed in a thermal bath. Unlike the current leading model of cantilever calibration in fluid (Sader 1998), this approach accounts fully for fluid inertia, in terms of both its energy requirements and its influence on the statistical physics which describe the thermal bath. These considerations were seen to be important at

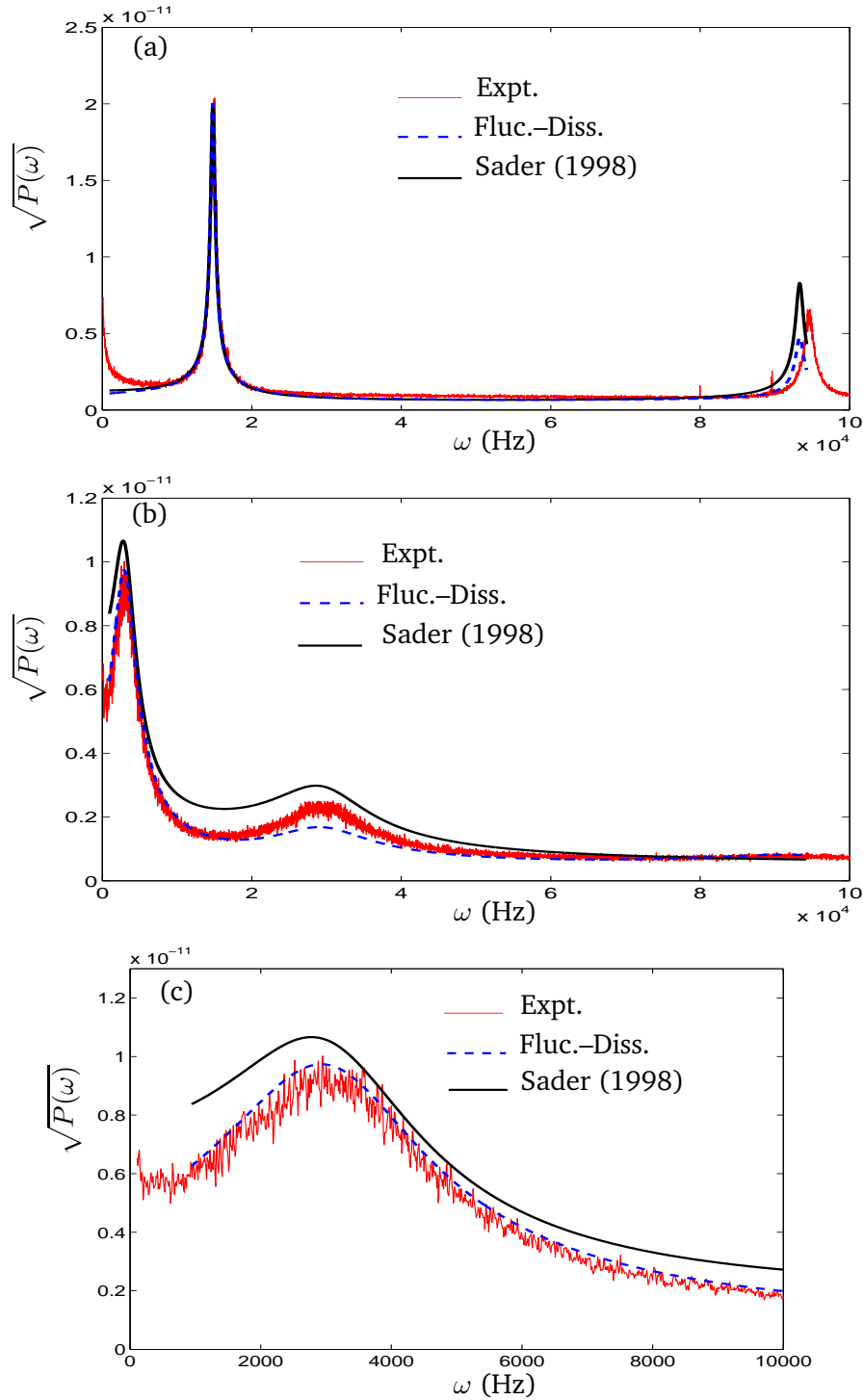


FIGURE 6.9: Experimental thermal power spectra (square rooted, full lines) for the tip of a thermally-driven gold-coated silicon nitride cantilever with thickness $0.573\mu\text{m}$, width $20\mu\text{m}$ and length $232\mu\text{m}$. Measurements are made in (a) air and (b,c) water, both when $\Delta = 10$ and fitting in air gives an effective cantilever density of $\rho_c = 5.3\text{gcm}^{-3}$. A close-up of the first harmonic in water is shown in panel (c). Full thick lines give the spectra due to (Sader 1998, 6.4), whilst dashed thick lines correspond to spectra obtained using the fluctuation–dissipation theorem (6.23). Both were computed using the drag given by (2.19), assuming the cantilever to be horizontal.

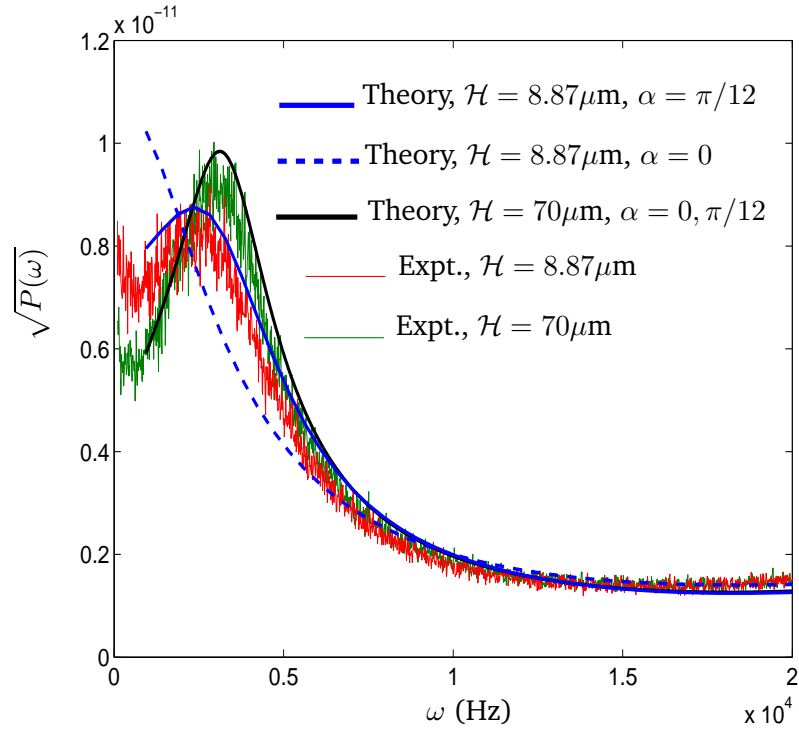


FIGURE 6.10: Thermal power spectra for a silicon nitride cantilever ($\rho_c = 5.3\text{gcm}^{-3}$), tilted at $\alpha = \pi/12$ from the horizontal, with thickness $0.573\mu\text{m}$, width $20\mu\text{m}$ and length $232\mu\text{m}$, thermally driven in water. The thin green line corresponds to experimental data collected at $\mathcal{H} = 70\mu\text{m}$, with the thick black line representing the fluctuation-dissipation predictions (6.23). The blue and red lines correspond to theoretical and experimental spectra measured at $\mathcal{H} = 8.87\mu\text{m}$; the dashed blue line corresponds to zero tilt ($\alpha = 0$) computations and the full blue lines relates to predictions which acknowledge the non-zero inclination angle.

both low and high frequencies. Using this approach, thermal spectra were analysed as a function of cantilever stiffness and shape, as well as wall separation distance. The use of unsteady slender-body theory (USBT) also allowed us to study the influence of frequency and wall screening, both of which suppress three-dimensionality in the flow. Comparison was then made between the theoretical predictions and actual experimental data.

In terms of the qualitative behaviour of the thermal spectra, figure 6.4 shows that increasing the density of the surrounding fluid can shift the resonant peak in the thermal spectrum to lower values, an effect that can also be achieved by decreasing cantilever stiffness, which also broadens the peak (decreases the quality factor). Decreasing the wall-separation distance was seen to flatten the spectra and shift the resonant peak to lower frequencies (figure 6.5). Earlier, in §4.4.1, we demonstrated the divergence in the drag experienced by circular and thin-rectangular cylinders as a wall is approached and figure 6.6 illustrated the consequences of this effect on the thermal spectra, which were seen to be highly sensitive to the cantilever shape when the wall was close.

The low-frequency discrepancies with Sader (1998) (figure 6.7) were attributed to his assumption that the Brownian forcing is δ -correlated, which is only true when the flow has negligible inertia. Insights into the influence of flow inertia were obtained by computing the thermal power spectrum (as described by the fluctuation–dissipation theorem) using complex-variable methods for the simple case of a two-dimensional circular cantilever in unbounded fluid. The mathematical structure of the spectrum at low-frequencies was seen to contain an integral along a branch cut, which results solely from non-negligible flow inertia; it was the influence of this integral which controlled the low-frequency decay observed in the thermal spectrum (figure 6.7a).

We argued that the discrepancies with Sader (1998) in the thermal spectra at high frequencies (figure 6.9), which predict a larger-amplitude second harmonic, are due to his assumption that all of the thermal energy goes into driving the cantilever, when in fact some of this thermal energy must be used to drive the unsteady flow (Hinch 1975). Therefore less energy is available to the cantilever at high frequencies of oscillation. However, the true amplitude of the second harmonic seems to lie somewhere between

the predictions of Sader (1998) and our values; this may be due to neglected factors in the hydrodynamics, such as axial flows generated by finite cantilever tilt and finite-cantilever-width effects.

Direct comparison with experimental data (figure 6.9) demonstrated the effectiveness of the theory for both gases (air) and liquids (water). In gases the method of Sader (1998) and the fluctuation–dissipation theorem approach both gave good estimates for the first harmonic, with comparative accuracies. In water, however, only the fluctuation–dissipation theorem was able to correctly predict the shape of the first resonant peak and this clearly has implications for the analysis of AFM data. Furthermore, in the presence of hydrodynamic wall effects, the theory was able to predict the shift in amplitude and resonant frequency observed in the experimental data. In addition to validating the correct treatment of the physics offered by the fluctuation–dissipation theorem, these results have important consequences for experimentalists wishing to extract properties of the cantilever and the sample through parameter fitting (see Rajagopalan 2000). It is worth noting that in our experiments we were able to take a thermal power spectrum in air, before moving to a liquid environment. The air data yielded sharply defined resonant peaks, which made finding the cantilever density through a fitting exercise relatively straightforward. In addition, the air measurements gave us the opportunity to confirm the manufacturer-stated value for the cantilever’s resonant frequency in-vacuo (which varies little from its value in air). In many biological experiments, however, the tip is functionalized with a chemically-active compound (see § 1.1) which must be kept in a liquid environment. The influence of these compounds on the effective material properties of the cantilever will change if they are allowed to dry out and this underlies the need for in-situ calibration. Therefore, in practice, it may not be possible to obtain confirmation of the vacuum resonant frequency simply by taking measurements in air; fitting may need to be performed using thermal spectra obtained in liquid, where the peaks are less well defined. Nevertheless, this should not present an insurmountable obstacle to the experimental application of the method.

As a final point, we note that the fluctuation–dissipation not only provides a more reliable account of the microscopic dynamics of a single fluctuating diving-board can-

tilever, but is equally applicable to any geometry where the deterministic, damped behaviour under δ -forcing can be computed, for example multiple-cantilever systems (see Paul and Cross 2004). By contrast, the modal analysis approach detailed in § 6.1 is much less flexible in its application.

Chapter 7

Conclusions

In this thesis we have studied hydrodynamic effects at work within an atomic force microscope (AFM), using a variety of computation and asymptotic techniques. After introducing the AFM, the role of hydrodynamics and the relevant fluid dynamics theory in § 1.3, the effort to quantify theoretically fluid effects began in chapter 2, with the modelling of the flow produced an infinitely-long circular cantilever oscillating normal to a flat rigid wall. Such a geometry permits two-dimensional flow only and neglects possibly important effects at the cylinder ends. Therefore in chapter 3 we allowed the circular cantilever to have finite length and approximated the resulting three-dimensional flow by developing an unsteady version of slender-body theory (USBT). Since AFM cantilevers are typically rectangular, rather than circular, in cross section, the use of boundary-element methods (BEM) in chapter 4 to determine the flow generated by oscillations of an infinitely-long rectangular cantilever represented an important geometric step forwards. AFM cantilevers have a typical thickness of $1\mu\text{m}$, much less than their other dimensions and this allowed for significant simplifications when describing the flow that they generate, which became especially useful when extending this rectangular geometry into three dimensions. The development of thin-plate-theory (TPT) followed the rationale behind USBT and provided a computationally more efficient alternative to BEM. Rather than distributing Stokeslets over the entire surface, as in an exact boundary-integral representation, TPT approximated the two-dimensional (three-

dimensional) flow using a one-dimensional (two-dimensional) distribution of Stokeslets over the line (plane) of vertical symmetry. TPT, although unable to distinguish between the different profiles on the top and bottom of the plate (only their additive contribution), nonetheless provided the important information needed for drag calculations. Unlike USBT, however, TPT did not yield any local force-velocity relationship upon which an iterative procedure could be built. At high-frequencies, however, confinement of vorticity did lead to a local force-velocity relationship for viscous effects; the global geometry still exerted its influence, however, through the irrotational flow generated by the presence of dipoles. Nevertheless, this represented an improvement from a computational perspective, because the dipole integrals could be integrated analytically, therefore eliminating the need for numerical quadrature. The damped-dynamics of flexible AFM cantilevers were studied by coupling the fluid mechanics to the elastic dynamics, as described by either linear beam or plate theory, where the cantilever was driven externally (chapter 5) or by Brownian motion (chapter 6).

Even though this work has been directed towards a better understanding of AFM operation, many of the results and techniques are general and apply equally well to any small-scale body oscillating at high frequency in a Newtonian fluid. For this reason we shall summarize some of the key fluid-dynamic results in § 7.1, before going on to discuss their direct relevance to atomic-force microscopy in § 7.2. Finally § 7.3 will outline some possibly relevant areas only touched upon, or not covered at all, which could form the basis for future investigations.

7.1 Hydrodynamic theory

7.1.1 Wall effects

One of our objectives was to assess the influence of a nearby horizontal wall on the drag, which is relevant to the AFM because of the proximity of nearby samples during tapping-mode AFM (TM-AFM), as well as during various other modes of operation. The drag results aimed to quantify how the wall's influence varies with both separation distance and flow inertia.

For the case of an infinite circular cylinder (chapter 2), we were able to construct numerous asymptotic limits to account for the wall's influence. For high-frequencies and moderate separation distances, wall effects were governed by inviscid flow interactions and seen to be weak. At these oscillation frequencies, only as the separation distance became comparable with the boundary-layer thickness, did the presence of the wall become important due to strong lubrication effects in the thin gap. At lower frequencies of oscillation and moderate separations, the wall exerted a significant influence on the drag provided that the viscous length scale was of the same order of magnitude as the wall distance. Once separations became greater than the viscous length scale the wall interactions were once again controlled by weaker inviscid effects.

We investigated how the geometry of the cantilever can impact upon wall effects. Using boundary-element methods (BEM) (chapter 4), we were able to determine the flow generated by a two-dimensional rectangular cylinder oscillating normal to the wall. It was found that the similarity between the drag experienced by a circular cylinder and a rectangular one, first noted by Tuck (1964) in unbounded fluid, persists relatively well up to about one cylinder width away from the wall, after which point the differing geometries produced rapidly differing drags.

When investigating the validity of the two-dimensional-flow assumption, by considering a finite-length circular cylinder (chapter 3), wall effects were seen to play a key role in promoting two-dimensionality. The flow was approximated by developing a novel version of slender-body theory (USBT) which included flow inertia and wall effects through the use of unsteady image Stokeslets. In unbounded flow, the range of the three-dimensional flow created at the cylinder ends was dictated by either the cylinder's radius or the viscous lengthscale, whichever was largest. Therefore at low frequencies of oscillation a long cylinder may still experience significant three-dimensional flow along its entire length. Close to a wall, however, the separation distance Δ becomes the dominant lengthscale in determining the range of end effects and comparison with two-dimensional flows demonstrated this effect. We termed this Δ -screening.

In principal the thin-plate-theory (TPT) formulation, developed in chapter 4 to approximate the flow generated by infinite- and finite-length plates, can automatically

account for a nearby wall through the use of the three-dimensional image Stokeslets. Unfortunately, however, evaluating the image system requires numerical quadrature which, in the context of a three-dimensional plate, puts the computational overheads beyond conventional processing power. As a possible remedy, an approach similar to that used by Chu and Kim (2001), who found a series expression for the integral form of the two-dimensional Stokeslet image system using residue theorem, may uncover a more tractable expression for the three-dimensional image Stokeslet, which lends itself more to computational methods. Alternatively, we could pursue an asymptotic treatment of the boundary-integral representation for the flow generated by a body near a wall, as undertaken by Williams (1966a) in the quasi-steady case.

Nevertheless, at small separations we were able to derive a three-dimensional lubrication description of the thin-gap flow (chapter 4), which resulted in a Poisson equation for the pressure. When the inhomogeneous term in this equation was assumed to be uniform, separation of variables lead to a series solution for the pressure. When the plate was narrow and the inhomogeneous term was assumed to be a function the coordinate parameterizing the plate length, we were able to find a uniformly valid asymptotic expression for the pressure by considering end regions where the pressure changed rapidly. This proved useful for later work on a flexible cantilever near a wall.

7.1.2 Finite-length effects

We have discussed above how the presence of a nearby wall can limit the range of finite-length effects and stated that, in its absence, the range of three-dimensional end flow is governed by the dominant geometric length scale at the end or the viscous length scale, whichever is the largest (chapter 3). For a slender finite-length circular cylinder, the geometric lengthscale is negligible and so flow three-dimensionality is controlled by the frequency of oscillation. Results demonstrated that, at low frequencies of oscillation, the Stokeslet profile in the USBT formulation was non-uniform along the body axis, indicating a genuinely three-dimensional flow. Increasing the oscillation frequency confined viscous effects to the ends and promoted two-dimensionality along much of the body's length, verified by comparison with earlier two-dimensional flow

results. This effect was termed γ -screening.

In the case of a square thin plate (chapter 4), the geometric lengthscale is not negligible and so the flow can remain three-dimensional over the entire surface, even at high frequencies. When the plate is narrow and the oscillation frequency high, however, both the geometric and viscous lengthscales are small and so the flow becomes two-dimensional sufficiently far from the ends. This was checked by comparing a cross-section of the Stokeslet profile with BEM computations for two-dimensional flow, which showed good agreement when the plate was narrow but not when it was square.

7.1.3 Tilt

The variation in the hydrodynamics when the cylinder is tilted, as opposed to horizontal, is also an important consideration, since AFM cantilevers are usually inclined at an angle of about 10 degrees. When a finite-length circular cylinder (chapter 3) is driven normally to its axis well away from the wall, tilt simply corresponds to a change in the frame of reference and does not alter the structure of the flow. This ceases to be the case once the separation distance decreases to about 20 cylinder lengths, where wall interactions cause flows along the cylinder axis. This is reflected in the drag's sensitivity to the angle of inclination near the wall. Increasing the frequency of oscillation sufficiently can result in wall effects becoming inviscid and weaker, thereby decreasing the drag's dependence on the angle of inclination at a given separation distance.

When the tilted cylinder is oscillated vertically, rather than normally to its axis, axial flows are generated even in the absence of any wall, so two-dimensional flow models are limited even in unbounded flow. Under these circumstances, moving the cylinder close to the wall can actually improve the accuracy of two-dimensional predictions through Δ -screening. The comparison with experimental data in § 6.4.2 illustrates quite nicely the need to account for finite tilt.

7.2 AFM implications

Many previous studies which couple fluid dynamics to elastic AFM cantilever behaviour have concentrated on the quasi-steady limit (e.g. Vinogradova et al. 2001; Alcaraz et al. 2002). Equipped with our results for oscillatory viscous flows, we were able to consider elastic interactions with unsteady viscous flows. This has implications not only for AFM techniques associated with rapid movement in fluid, such as tapping-mode (TM-AFM, see § 1.1.2), but also advances in techniques traditionally considered to generate slow-moving flows, such as dynamic-force spectroscopy (DFS) (see § 1.1.3), which are becoming increasingly high-speed in an attempt to counter unwanted effects such as sample drift and also to expand the range of molecular forces which can be measured.

7.2.1 TM-AFM

As has been a theme throughout this work, when simulating TM-AFM by considering the elastic behaviour of a sinusoidally-driven cantilever under hydrodynamic loading, we were interested in the ability of simple models accurately to approximate the dynamics, especially in measuring the hydrodynamic impact of wall effects. In the simplest scenario, two-dimensional flow models were coupled to the one-dimensional Euler–Bernoulli beam equation (§ 5.1). We were able to quantify how an increase in hydrodynamic loading, generated by a decrease in the wall separation distance, damped the response of the beam over a range of oscillation frequencies. We then allowed for three-dimensional flows. First for the case of a slender rod through the use of USBT, where we were able to observe how well two-dimensional models worked at small separation distances and/or high frequencies. On a less positive note, however, the dynamics were seen to be sensitive to the angle of tilt at separations characteristic of the AFM cantilever operating distance (about $1\mu\text{m}$ from the sample). The differences in the cantilever response at angles of 0 and $\pi/20$ (the typical tilt for an AFM cantilever) were not drastic, but perhaps large enough to raise questions over the validity of two-dimensional flow models.

In addition to measuring the transverse deflections, important information can be

extracted by analysing other modes of cantilever motion (see Sader and Green 2002). For this reason we examined the deflections across an elastic plate with finite width, using either lubrication theory or TPT as the source of hydrodynamic loading (§ 5.2). A plate with a Poisson ratio of 0.3 (a typical AFM value), and unit aspect ratio, was seen to undergo both length-wise and span-wise bending, whereas a plate with the narrower AFM cantilever aspect ratio seemed to experienced little span-wise deflection (although we could expect this to change for TM-AFM in the presence of an uneven sample topology). However, two-dimensional flow and elasticity approximations failed to fully account for the cantilever dynamics and this could be due to the importance of neglected end and edge regions in the hydrodynamic loading.

7.2.2 Thermal spectra

Thermally-driven cantilevers formed the subject of chapter 6, due to their growing importance to the AFM community. Thermal spectra offer a popular, non-intrusive method for determining the spring constant of a cantilever (Sader 1998; Paul and Cross 2004) and an accurate knowledge of this constant is critical to the interpretation of any force-measurement experiments (see § 1.1.3). Another application of thermally-driven cantilevers lies in the field of noise analysis, where thermally excited cantilevers provide an ultra-sensitive, low-amplitude method for probing the micro-rheology of soft biological specimens, in a way which minimizes damage to the sample and reduces the risks of unwanted non-linear sample interactions. The nature of the technique means that the cantilever oscillates in close proximity to the substrate and so clearly stands to benefit from an increased understanding of wall effects in oscillatory Stokes flow (as expressed by Ma et al. 2000).

We applied our hydrodynamic results and techniques to provide the cantilever's damping whilst undergoing Brownian motion, the stochastic behaviour of which was described by following an approach exploiting the fluctuation-dissipation theorem rather than a popular, but somewhat flawed, alternative due to Sader (1998). As well as allowing for more general geometric situations, such as three-dimensional flows generated by non-zero angles of inclination, our method correctly predicted the low-frequency

behaviour of the thermal spectra. When compared with experimental data, this was shown to be of great relevance in properly describing the principal harmonic in the power spectrum of a AFM cantilever in water near a wall. This, in turn, could result in substantially improved results during parameter fitting exercises which are designed to determine the cantilever's spring constant or the material properties of a biological specimen (see Rajagopalan 2000)).

7.3 Extensions

7.3.1 Non-linear effects

We have assumed throughout that the amplitude of oscillation is small enough for non-linear effects, such as steady streaming, to be negligible. We implicitly assumed the oscillation amplitude to be much smaller than the boundary-layer thickness, which is a restrictive condition at high frequencies. Furthermore, we have also taken no account of possible flow instabilities. However, in high-speed AFM imaging regimes, the flow is likely to exhibit some interesting weakly nonlinear effects. For a two-dimensional rectangular cantilever oscillating with amplitude \mathcal{A} (scaled on cantilever width R , with $(\epsilon\gamma)^{-1} \ll \Delta/\epsilon \ll 1$), then $O(\mathcal{A}^2)$ steady-streaming flow beneath the cantilever is likely to resemble that in an infinitely long pulsating channel, as described by Scomb (1978). Subsequently Hall and Papegeorgiou (1999) showed how a nonlinear flow synchronous with the oscillating wall arises for (in our variables) $\epsilon\gamma > 3.39/\mathcal{A}$ (this is a large-Reynolds-number asymptotic limit, assuming $\gamma^2\Delta^2 \gg 1$; a similar result was also obtained by Watson et al. (1990)), and that this flow then loses stability to quasi-periodic oscillations for $\epsilon\gamma > 5.99/\mathcal{A}$. This indicates that, even at small amplitudes, an AFM cantilever can experience a steady force (due to steady streaming) as well as a force that fluctuates at a frequency different to that of the driver. At lower Reynolds numbers, the quasi-steady flow between pulsating plates may also be unstable to growing Tollmien–Schlichting waves (Stuart et al. 1990).

7.3.2 Slip

As discussed in § 1.2.1, the microscopic dimensions of AFM cantilevers raise important questions about the validity of both the no-slip condition and the continuum approximation. The effects of slip are illustrated in a couple of two-dimensional examples in Appendix A. In air, when operating far from the wall, we estimate the Knudsen number Kn based on cantilever half-width R to be approximately 0.014. For most practical surfaces the molecular mean-free-path is comparable in magnitude to the slip-length (scaled on the dominant length scale) \mathcal{L}_s (Gad-El-Hak 2001), so that $\mathcal{L}_s \approx \text{Kn}$. \mathcal{L}_s is likely to be smaller in liquids (typically $\mathcal{L}_s \approx 0.004$) provided the cantilever surface is smooth and uncontaminated (Cottin-Bizonne et al. 2005). Figure A.1(a,b) in Appendix A shows how the drag on an unbounded circular cantilever, when $\mathcal{L}_s \lesssim 0.02$, differs from the no-slip value by an $O(\mathcal{L}_s)$ amount, but in a frequency-dependent manner; recent boundary-element computations of unbounded oscillatory flow in a multiple-cantilever system (Ding and Wenjiig 2004) report the same order of magnitude for the drag correction. Slip effects are likely to be more important for cantilevers operating in either air or liquid very close to a substrate, when the drag (at least at sufficiently low frequencies) depends on \mathcal{L}_s/Δ (the ratio of slip length to gap width). In liquids, slip lengths on hydrophobic surfaces of order $1\mu\text{m}$ have been reported (Zhu and Granick 2001) and similarly large values can be anticipated for some coated or biological interfaces. Substrate-dependent slip can then have a leading-order effect on drag (as illustrated by Figure A.1(c,d)). Furthermore, for a cantilever very close to a substrate in air, the present model may lose its validity both through high values of slip and through discrete molecular effects (treated by Gallis and Torczynski (2004)). Since the measurement of drag on AFM cantilever is a popular means by which slip lengths are determined (Vinogradova and Yakubov 2003), typically reliant on simple squeeze-film models, a thorough treatment of slip on AFM cantilevers would be worthwhile.

7.3.3 Cantilever considerations

The focus of this work has been diving-board cantilevers, principally because of their tractable geometry. However, V-shaped cantilevers are also commonly used and we would expect their hydrodynamics and elastic deformations to differ substantially from their diving-board-shaped counterparts. Some previous studies have modelled V-shaped cantilevers, either determining their eigenmodes in vacuo (Stark et al. 2001) or with point-force loading at the tip (Sader and White 1993). Thin-plate theory (TPT, chapter 4) provides an efficient means of introducing hydrodynamic loading to plates with arbitrary geometries, although determining the elastic behaviour of a non-rectangular cantilever lends itself more to finite-element analysis (FEA).

In practice, an AFM cantilever twists as well as bends, especially when in contact with a sample surface and modern AFM's are designed to detect this potentially important degree of freedom. As with bending, these rotational oscillations can be damped by torsional forces exerted by the surrounding fluid and there has been some work done in analysing these effects in two dimensions (Sader and Green 2002, Green and Sader 2005). With slight modification, many of the methods discussed in this work could be applied to rotational motion. For example, a variation of USBT which approximates the flow generated by rotational oscillations of a slender finite-length cylinder could be achieved through a distribution of rotlets along the body axis (c.f. Chwang and Yao-Tsu Wu 1974).

7.3.4 Sample considerations

In TM-AFM it is the uneven sample topology which is of primary interest, yet in this study we have assumed that the substrate is flat. The BEM, USBT and TPT formulations can all be extended to include surface features, although the lack of a convenient Stokeslet image system means that an uneven wall would need to be explicitly included as a discretized surface.

One interesting and potentially useful direction for this work would be to consider compliant substrates. Some experimentalists have already used the AFM to measure

the micro-rheology of soft biological materials such as cells (see § 1.1.3). These measurements could be significantly influenced by elasto-hydrodynamic interactions at the specimen surface. Interaction of compliant walls with fluid provide a rich array of phenomena and some interesting physical effects (Carpenter and Garrad 1985, Carpenter 1986).

7.3.5 AFM Experiments

The thermal spectra presented in § 6.4.2 used the simpler forms for the hydrodynamic drag to illustrate the principal ideas. The full range of hydrodynamic models developed have yet to be put to use in this context. For example, the TPT hydrodynamics offer the opportunity to consider thermally-driven span-wise fluctuations.

Simulations of thermal spectra represent just one use of hydrodynamic theory in an AFM context. TM-AFM senses sample topology through decreases in the cantilever's amplitude response. In the analysis of TM-AFM data, chapter 5 tells us how much of this damping is due to hydrodynamics. Taken further, the fluid mechanics could perhaps form just one component in a more complete picture of AFM interactions, e.g. Lennard-Jones potentials, electrostatic effects etc.

In dynamic-force microscopy (DFS) the cantilever is impulsively retracted once the tip is in contact with a sample and so its motion is discontinuous. This will result in flow transients (§ 1.2.3), which may influence the drag during the crucial force-measurement stage. These flows, however, can be described through studies of oscillatory motion using Fourier analysis.

In closing, we believe that the work presented here represents a major step forward in quantifying the impact of geometry and flow inertia on the drag exerted by an oscillating (possibly flexible) body near a wall, in addition to providing some novel and versatile techniques. So as well as being of specific relevance to the AFM community, we hope that this work will also carry a wider hydrodynamic appeal.

Appendix A

Effects of slip

To illustrate the implications of relaxing the no-slip condition, we revisit the cases of an unbounded circular cantilever (§ 2.2.2) and rectangular cantilever near a wall (§ 4.2.2), recalculating the drag using the Navier-slip condition (1.6), where \mathcal{L}_s/ϵ is the slip-length scaled on R .

A.1 Two-dimensional circular cantilever

In streamfunction form, the flow is governed by (2.2a) subject to

$$u_r = \sin \theta, \quad u_\theta = (\mathcal{L}_s/\epsilon) \frac{\partial}{\partial r} \left(\frac{u_\theta}{r} \right) + \cos \theta \quad (\text{A.1})$$

on the cylinder surface $r = 1$, i.e.

$$\psi(1, \theta) = -\cos \theta, \quad -(1 + (\mathcal{L}_s/\epsilon)) \frac{\partial \psi}{\partial r} \Big|_{r=1} = -(\mathcal{L}_s/\epsilon) \frac{\partial^2 \psi}{\partial r^2} \Big|_{r=1} + \cos \theta, \quad (\text{A.2})$$

with $\mathbf{u} \rightarrow \mathbf{0}$ as $r \rightarrow \infty$. This is satisfied by

$$\psi = \left(\frac{(CK_1(\sqrt{i\epsilon}\gamma) - 1)}{r} - CK_1(\sqrt{i\epsilon}\gamma r) \right) \cos \theta, \quad (\text{A.3})$$

$$C = -\frac{(2 + 3(\mathcal{L}_s/\epsilon))}{\sqrt{i\epsilon}\gamma K_0(\sqrt{i\epsilon}\gamma)} \left(1 + (\mathcal{L}_s/\epsilon) \left(\frac{2K_0(\sqrt{i\epsilon}\gamma) + \sqrt{i\epsilon}\gamma K_1(\sqrt{i\epsilon}\gamma)}{K_0(\sqrt{i\epsilon}\gamma)} \right) \right)^{-1}. \quad (\text{A.4})$$

The drag is then found to be

$$D = -i\pi\epsilon^2\gamma^2 \left(1 - 2CK_1(\sqrt{i}\epsilon\gamma)\right). \quad (\text{A.5})$$

At leading order in \mathcal{L}_s/ϵ we recover the no-slip expression (2.19) and the high-frequency limit $\epsilon\gamma \gg 1$ is dominated by the inviscid contribution $D_{inv} = -i\pi\epsilon^2\gamma^2$. The amplitude and phase of the drag are plotted in figure A.1(a, b) respectively. For small $\epsilon\gamma$ the drag is almost linear in \mathcal{L}_s/ϵ and slip acts to decrease the amplitude and phase of the drag; however, these trends change at much larger $\epsilon\gamma$. Initially the slip's influence increases with $\epsilon\gamma$, yet after a point its impact declines, tending towards a largely slip-insensitive inviscid limit. This phenomenon is displayed in figure A.1(e, f), where it can be seen that there exists a non-zero $\epsilon\gamma$ which maximizes drag variations at a given slip length. We found that the frequency $\epsilon\gamma_0$ which maximizes the reduction in drag amplitude satisfies $(\epsilon\gamma_0)^{-2} \approx 0.4(\mathcal{L}_s/\epsilon)$ (although we could not identify an equivalent relationship for the drag's phase).

A.2 Rectangular cantilever in the lubrication limit

Adopting the rescalings given by (4.15), we can re-derive the lubrication drag on a rectangular cantilever with Navier-slip conditions on both the cantilever and nearby wall. Similar analysis as before gives the leading-order drag as

$$D = -\frac{2\alpha_+(\epsilon\gamma)^3}{3\sqrt{i}} \left(\sqrt{i}\tau\alpha_+ + e^{-\sqrt{i}\tau} - 1 - \frac{(\alpha_+ + \alpha_- e^{-\sqrt{i}\tau}) (\cosh \sqrt{i}\tau - 1 + \sqrt{i}\tau(\mathcal{L}_s/\epsilon) \sinh \sqrt{i}\tau)}{2\sqrt{i}\tau(\mathcal{L}_s/\epsilon) \cosh \sqrt{i}\tau + (1 + i\tau^2((\mathcal{L}_s/\epsilon))^2) \sinh \sqrt{i}\tau} \right), \quad (\text{A.6})$$

where $\tau = \Delta\gamma$ and $\alpha_{\pm} = \sqrt{i}\tau(\mathcal{L}_s/\epsilon) \pm 1$. Expanding in powers of (\mathcal{L}_s/ϵ) ,

$$D = \frac{2}{3}i(\Delta/\epsilon)^{-1}(\epsilon\gamma)^2 \left(\frac{\sqrt{i}\tau \sinh \sqrt{i}\tau}{2 - 2 \cosh \sqrt{i}\tau + \sqrt{i}\tau \sinh \sqrt{i}\tau} - \frac{4i(\mathcal{L}_s/\epsilon)(\Delta/\epsilon)^{-1}(\epsilon\gamma)^2 \sqrt{i}\tau (1 - \cosh \sqrt{i}\tau)^2}{3(2 - 2 \cosh \sqrt{i}\tau + \sqrt{i}\tau \sinh \sqrt{i}\tau)^2} + O((\Delta/\epsilon)^{-3}((\mathcal{L}_s/\epsilon))^2) \right). \quad (\text{A.7})$$

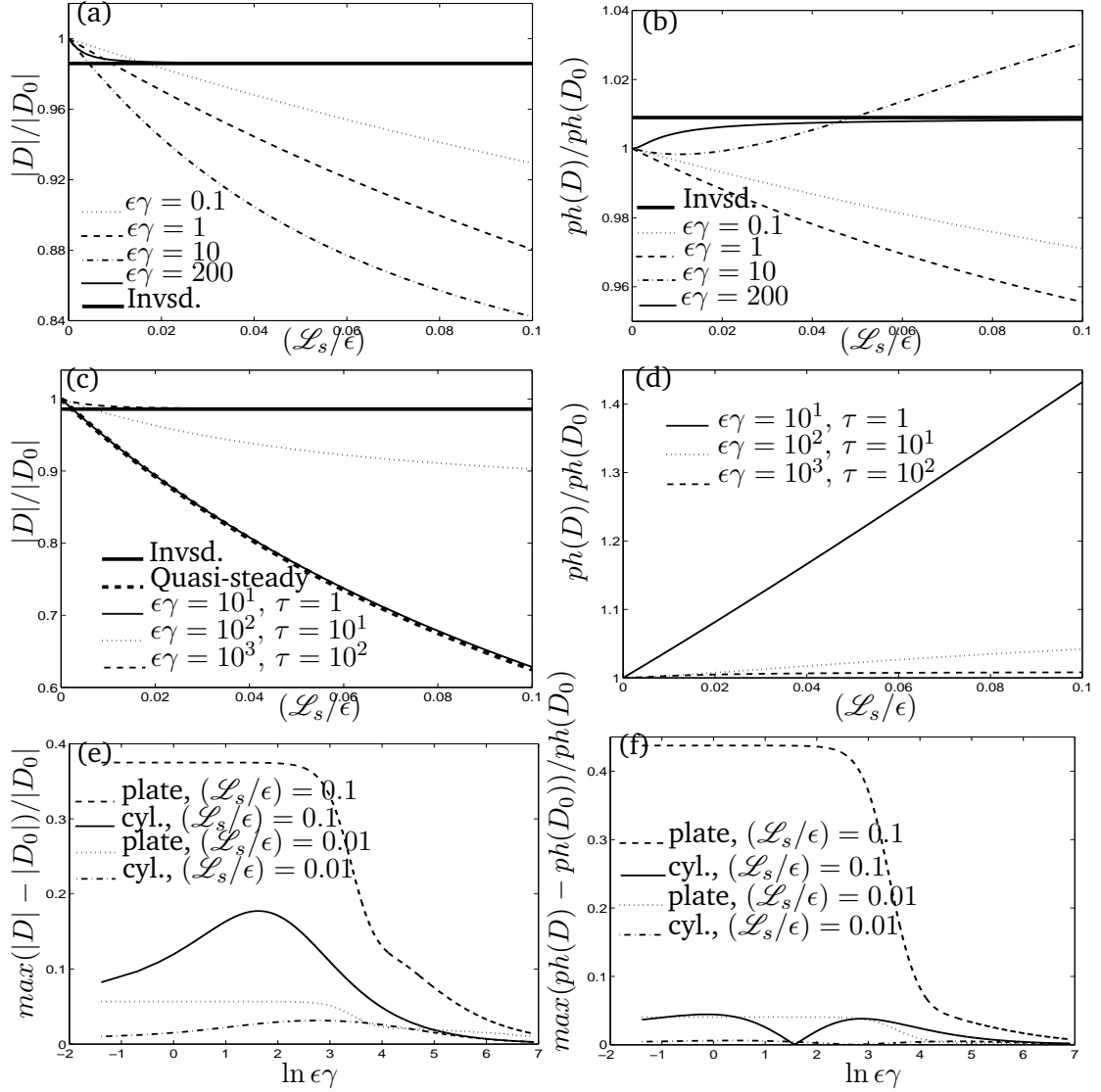


FIGURE A.1: Variation in (a, c) amplitude and (b, d) phase of the drag with slip length (L_s/ϵ) , normalized on the no-slip value D_0 . (a) and (b) relate to an unbounded cylinder oscillating at frequencies $\epsilon\gamma = 0.1, 1, 10$ and 200 (A.5); (c) and (d) correspond to the lubrication drag on a plate oscillating near a wall when $\Delta/\epsilon = 10^{-1}$ and $\epsilon\gamma = 10, 100$ and 1000 (A.6). Inviscid limits are shown with thick solid lines. The maximum deviation in the amplitude (e) and phase (f) of the drag are also plotted as a function of $\epsilon\gamma$ for two different (L_s/ϵ) .

At leading order we recover the no-slip result (4.17). When the gap separation is much smaller than the boundary-layer thickness ($\tau \ll 1$), (A.6) reduces to the quasi-steady limit

$$D = \frac{8(\Delta/\epsilon)^{-3}}{(1 + 6(\mathcal{L}_s/\epsilon))} = 8(\Delta/\epsilon)^{-3} - 48(\mathcal{L}_s/\epsilon)(\Delta/\epsilon)^{-3} + O((\Delta/\epsilon)^{-3}((\mathcal{L}_s/\epsilon))^2). \quad (\text{A.8})$$

Alternatively, in the limit where boundary layers are much thinner than the separation distance ($\tau \gg 1$), the drag (A.6) tends to the inviscid limit $D_{inv} = \frac{2}{3}i(\epsilon\gamma)^2(\Delta/\epsilon)^{-1}$. In figure A.1(c, d) we again see how slip influences the drag. As with the unbounded cylinder, at low $\epsilon\gamma$ the slip–drag relationship is essentially linear, becoming less so as $\epsilon\gamma$ is increased, until finally the inviscid limit is attained where slip matters little. Unlike the cylinder case, however, slip has its greatest influence in the quasi-steady limit, and only a weak effect at high $\epsilon\gamma$ (see figure A.1(e, f)).

Appendix B

Two-dimensional inviscid flow for a cylinder above a wall

In § 2.2.2 we consider the inviscid flow generated by high-frequency oscillations ($\epsilon\gamma \gg 1$) of a circular cylinder when boundary layers are much thinner than the wall–cylinder distance ($\Delta \gg \gamma^{-1}$). Here we derive the leading-order inviscid flow and resulting slip velocities by transforming into bipolar coordinates (2.3), where the flow is governed by

$$\psi_{\xi'\xi'}^{(0)} + \psi_{\eta'\eta'}^{(0)} = 0 \quad (\text{B.1})$$

(subscript denotes derivatives) subject to

$$\psi^{(0)}(\xi', 0) = 0, \quad \psi^{(0)}(0, \eta') = 0, \quad \psi^{(0)}(-\pi, \eta') = 0, \quad (\text{B.2a})$$

$$\psi^{(0)}(\xi', \eta_1) = c \sin \xi' / (\cosh \eta_1 - \cos \xi'), \quad (\text{B.2b})$$

where $\eta_1 \equiv \cosh^{-1}(1 + (\Delta/\epsilon))$. We express $\psi^{(0)}$ as a Fourier series satisfying (B.2a),

$$\psi^{(0)} = \sum_{n=0}^{\infty} a_n \sinh n\eta' \sin n\xi'. \quad (\text{B.3})$$

The coefficients a_n are determined by expressing the remaining boundary condition as

$$\sum_{n=1}^{\infty} a_n \sinh n\eta_1 \sin n\xi' = \frac{c \sin \xi'}{\cosh \eta_1 - \cos \xi'} = 2c \sum_{n=1}^{\infty} e^{-n\eta_1} \sin n\xi', \quad (\text{B.4})$$

($c \equiv \sqrt{(\Delta/\epsilon)((\Delta/\epsilon) + 2)}$) which yields (2.24). The slip velocities on the cylinder surface and on the wall are then

$$u_c^s = \sum_{n=1}^{\infty} \left[(c - d_n)(n-1)e_{n-1} - (c + d_n)(n+1)e_{n+1} + 2d_n n e_n \right] \sinh n\eta_1 \sin n\xi', \quad (\text{B.5a})$$

$$u_w^s = \sum_{n=1}^{\infty} [2ne_n - (n-1)e_{n-1} - (n+1)e_{n+1}] \sin n\xi', \quad (\text{B.5b})$$

respectively, where $d_n = (1 + (\Delta/\epsilon))/\tanh n\eta_1$ and $e_n = e^{-n\eta_1}/\sinh n\eta_1$.

Appendix C

Unsteady two-dimensional image Stokeslets

We here derive the results presented in § 2.2.3, where a two-dimensional cylinder oscillates above a wall with $\Delta/\epsilon \sim (\epsilon\gamma)^{-1} \gg 1$

C.1 Leading-order flow

We postulate a leading-order flow, local to the cylinder surface, which is given by the superposition of a Stokeslet–dipole combination and a uniform flow. In polar coordinates with origin at cylinder’s centre (2.27)

$$\psi = c_1 \left(-A_1 \frac{1}{r} + A_2 \frac{K_1(\sqrt{i\epsilon}\gamma r)}{\sqrt{i\epsilon}\gamma} \right) \cos \theta + c_2 r \cos \theta, \quad (\text{C.1a})$$

$$A_1 = 1 + \frac{2K_1(\sqrt{i\epsilon}\gamma)}{\sqrt{i\epsilon}\gamma K_0(\sqrt{i\epsilon}\gamma)}, \quad A_2 = \frac{2}{K_0(\sqrt{i\epsilon}\gamma)}, \quad (\text{C.1b})$$

Constants c_1 and c_2 must be chosen so that no-penetration and no-slip conditions are satisfied on the solid surfaces. A relationship between c_1 and c_2 is obtained by finding the image system of the Stokeslet–dipole combination in (C.1a) (in Cartesians centred on the cylinder). Both dipole and Stokeslet can be determined in integral form by solving the δ -forced inviscid and unsteady Stokes equations, (2.23) and (2.1a), respectively,

using Fourier transform methods, which in combination give

$$\psi = c_1 \int_0^\infty \left(-A_1 e^{-k|x_3|} + \frac{A_2}{i\epsilon^2 \gamma^2} \frac{k e^{-q|x_3|}}{q} \right) \sin kx_2 \, dk, \quad (\text{C.2a})$$

where $q = \sqrt{k^2 + i\epsilon^2 \gamma^2}$. This is equivalent to the more familiar closed-form expression

$$\psi = c_1 \left(-A_1 \frac{x_2}{r^2} + A_2 \frac{x_2 K_1(\sqrt{i\epsilon} \gamma r)}{\sqrt{i\epsilon} \gamma r} \right). \quad (\text{C.2b})$$

This singularity solution induces the following slip and penetration velocities at the wall ($x_3 = -\Delta/\epsilon$)

$$\frac{\partial \psi}{\partial x_2}(x_2, -\Delta/\epsilon) = c_1 \int_0^\infty \left(\frac{A_2 k^2 e^{-q\Delta/\epsilon}}{i\epsilon^2 \gamma^2 q} - A_1 k e^{-k\Delta/\epsilon} \right) \cos kx_2 \, dk, \quad (\text{C.3a})$$

$$\frac{\partial \psi}{\partial x_3}(x_2, -\Delta/\epsilon) = c_1 \int_0^\infty \left(\frac{A_2 k e^{-q\Delta/\epsilon}}{i\epsilon^2 \gamma^2} - A_1 k e^{-k\Delta/\epsilon} \right) \sin kx_2 \, dk. \quad (\text{C.3b})$$

We require a solution to the unsteady Stokes equations (2.1a) which cancels these wall velocities and this can be found (through linearity) as a combination of a viscous (ψ_1) and an inviscid flow (ψ_2), i.e.

$$\psi \equiv \psi_1 + \psi_2, \quad \nabla^2 \psi_1 - i\epsilon^2 \gamma^2 \psi_1 = 0, \quad \nabla^2 \psi_2 = 0. \quad (\text{C.4})$$

Under a Fourier sine transform (C.4) becomes

$$\frac{\partial^2 \hat{\psi}_1}{\partial x_3^2} - (k^2 + i\epsilon^2 \gamma^2) \hat{\psi}_1 = 0, \quad \frac{\partial^2 \hat{\psi}_2}{\partial x_3^2} - k^2 \hat{\psi}_2 = 0, \quad (\text{C.5})$$

(dropping hats hereafter) which has solutions that decay at large distances of the form

$$\psi = \int_0^\infty \left(A(k) e^{-kx_3} + B(k) e^{-qx_3} \right) \sin(kx_2) \, dk. \quad (\text{C.6})$$

Cancelling the wall velocities C.3 (a,b) then gives us

$$A(k) k e^{k\Delta/\epsilon} + B(k) k e^{q\Delta/\epsilon} = -c_1 \left(\frac{A_2 k^2 e^{-q\Delta/\epsilon}}{i\epsilon^2 \gamma^2 q} - A_1 k e^{-k\Delta/\epsilon} \right), \quad (\text{C.7a})$$

$$k A(k) e^{k\Delta/\epsilon} + q B(k) e^{q\Delta/\epsilon} = c_1 \left(\frac{A_2 k e^{-q\Delta/\epsilon}}{i\epsilon^2 \gamma^2} - A_1 k e^{-k\Delta/\epsilon} \right), \quad (\text{C.7b})$$

from which we deduce

$$A(k) = \frac{c_1}{(k-q)} \left(\frac{2A_2 k e^{-(\Delta/\epsilon)(q+k)}}{i\epsilon^2 \gamma^2} - A_1 e^{-2k\Delta/\epsilon} (k+q) \right), \quad (\text{C.8a})$$

$$B(k) = \frac{c_1}{(k-q)} \left(-\frac{A_2 k e^{-2q\Delta/\epsilon}}{i\epsilon^2 \gamma^2} \left(\frac{k+q}{q} \right) + 2A_1 k e^{-k\Delta/\epsilon - q\Delta/\epsilon} \right). \quad (\text{C.8b})$$

Hence

$$\begin{aligned} \psi = c_1 \int_0^\infty & \left(-A_1 \left[(k+q) e^{-kx_3 - 2k\Delta/\epsilon} - 2k e^{-qx_3 - (\Delta/\epsilon)(k+q)} \right] \right. \\ & \left. - \frac{A_2}{i\epsilon^2 \gamma^2} \left[\frac{k(k+q) e^{-qx_3 - 2q\Delta/\epsilon}}{q} - 2k e^{-kx_3 - (\Delta/\epsilon)(k+q)} \right] \right) \frac{\sin kx_2}{(k-q)} dk. \end{aligned} \quad (\text{C.9})$$

We now take advantage of the fact that $\Delta/\epsilon \gg 1$ to simplify (C.9). Rescaling the variable of integration $k = (\Delta/\epsilon)^{-1}u$ and defining $p_\tau \equiv \sqrt{u^2 + \tau^2}$

$$\begin{aligned} \psi = (\Delta/\epsilon)^{-1} c_1 \int_0^\infty & \left(-A_1 \left[(u+p_\tau) e^{-ux_3 (\Delta/\epsilon)^{-1}} e^{-2u} - 2u e^{-p_\tau x_3 (\Delta/\epsilon)^{-1}} e^{-(p_\tau+u)} \right] \right. \\ & \left. - \frac{A_2}{i\epsilon^2 \gamma^2} \left[\frac{u(u+p_\tau) e^{-p_\tau x_3 (\Delta/\epsilon)^{-1}} e^{-2p_\tau}}{p_\tau} - 2u e^{-ux_3 (\Delta/\epsilon)^{-1}} e^{-(p_\tau+u)} \right] \right) \frac{\sin((\Delta/\epsilon)^{-1}ux_2)}{(u-p_\tau)} du. \end{aligned} \quad (\text{C.10})$$

So when $x_3 = O(1)$ (i.e. in the vicinity of the cylinder),

$$\begin{aligned} \psi = c_1 (\Delta/\epsilon)^{-2} x_2 & \left(-A_1 \int_0^\infty u \left(\frac{u+p_\tau}{u-p_\tau} \right) e^{-2u} du + 2A_1 \int_0^\infty \frac{u^2 e^{-(u+p_\tau)}}{(u-p_\tau)} du \right. \\ & \left. - A_2 ((i\epsilon\gamma)^{-2} \int_0^\infty \frac{u^2(u+p_\tau)}{p_\tau(u-p_\tau)} e^{-2p_\tau} du + 2A_2 (i\epsilon\gamma)^{-2} \int_0^\infty \frac{u^2 e^{-(u+p_\tau)}}{(u-p_\tau)} du \right) + O((\Delta/\epsilon)^{-3}), \\ & = c_1 x_2 (\Delta/\epsilon)^{-2} I(\tau, \sqrt{i\epsilon\gamma}) + O((\Delta/\epsilon)^{-3}), \end{aligned} \quad (\text{C.11})$$

where

$$I(\tau, \sqrt{i\epsilon\gamma}) = -A_1 I_1(\tau) - A_2 I_2(\tau) + 2 \left(A_1 + \frac{A_2}{i\epsilon^2 \gamma^2} \right) I_3(\tau), \quad (\text{C.12a})$$

$$I_1(\tau) \equiv \int_0^\infty u \left(\frac{u+p_\tau}{u-p_\tau} \right) e^{-2u} du, \quad (\text{C.12b})$$

$$I_2(\tau) \equiv \int_0^\infty \frac{u^2}{p_\tau} \left(\frac{u+p_\tau}{u-p_\tau} \right) e^{-2p_\tau} du, \quad (\text{C.12c})$$

$$I_3(\tau) \equiv \int_0^\infty \left(\frac{u^2}{u-p_\tau} \right) e^{-(u+p_\tau)} du. \quad (\text{C.12d})$$

Hence we have determined the strength of the uniform flow in (C.1)

$$c_2 = c_1(\Delta/\epsilon)^{-2}I(\tau, \sqrt{i\epsilon\gamma}). \quad (\text{C.13})$$

We now have

$$\psi = c_1 \left(-A_1 \frac{1}{r} + A_2 \frac{K_1(\sqrt{i\epsilon\gamma}r)}{\sqrt{i\epsilon\gamma}} + \frac{I(\tau, \sqrt{i\epsilon\gamma})}{(\Delta/\epsilon)^2} r \right) \cos \theta, \quad (\text{C.14})$$

with no-slip on the cylinder demanding that

$$c_1 = \left(1 - (\Delta/\epsilon)^{-2}I(\tau, \sqrt{i\epsilon\gamma}) \right)^{-1} \quad (\text{C.15})$$

where it can be shown that this value of c_1 also enforces no-penetration at the cylinder surface. The strength of the Stokeslet in (C.14) determines the drag, with the contribution from a Stokeslet of unit strength given by Stokes (1851). Hence, in our case

$$D = \left(1 - (\Delta/\epsilon)^{-2}I(\tau, \sqrt{i\epsilon\gamma}) \right)^{-1} \pi i \epsilon^2 \gamma^2 \left(1 + \frac{4K_1(\sqrt{i\epsilon\gamma})}{\sqrt{i\epsilon\gamma}K_0(\sqrt{i\epsilon\gamma})} \right). \quad (\text{C.16})$$

C.2 Quasi-steady limit

We now examine the limit $\tau \ll 1$ of (C.16), which corresponds to the case where vorticity diffuses distances much greater than the wall–cylinder separation. In this limit we asymptotically expand the integrals C.12(b–d) by splitting the integral at $u = u_0$, where $(\delta/\epsilon) = \tau/u_0 \ll 1$ and rescale the integration variable close to zero

$$I_1 \equiv I_{11} + I_{12} = \tau^2 \int_0^\delta v \left(\frac{v+p_1}{v-p_1} \right) e^{-2\tau v} dv + \int_{u_0}^\infty u \left(\frac{u+p_\tau}{u-p_\tau} \right) e^{-2u} du, \quad (\text{C.17a})$$

$$I_2 \equiv I_{21} + I_{22} = \tau^2 \int_0^\delta \frac{v^2}{p_1} \left(\frac{v+p_1}{v-p_1} \right) e^{-2\tau p_1} dv + \int_{u_0}^\infty \frac{u^2}{p_\tau} \left(\frac{u+p_\tau}{u-p_\tau} \right) e^{-2p_\tau} du, \quad (\text{C.17b})$$

$$I_3 \equiv I_{31} + I_{32} = \tau^2 \int_0^\delta \left(\frac{v^2}{v-p_1} \right) e^{-\tau(v+p_1)} dv + \int_{u_0}^\infty \left(\frac{u^2}{u-p_\tau} \right) e^{-(u+p_\tau)} du, \quad (\text{C.17c})$$

where $p_1 = \sqrt{v^2 + 1}$ and $u = \tau v$. We can now expand both integrands in τ

$$I_{11} = \int_0^\delta (\tau^2 v - 2\tau^3 v^2 + 2\tau^4 v^3) \left(\frac{v + p_1}{v - p_1} \right) dv + O(\tau^5), \quad (\text{C.18a})$$

$$I_{12} = \int_{u_0}^\infty \left(-\frac{4u^3}{\tau^2} - 2u + \frac{\tau^2}{4u} - \frac{\tau^4}{8u^3} \right) e^{-2u} du + O(\tau^5), \quad (\text{C.18b})$$

$$I_{21} = \tau^2 \int_0^\delta \frac{v^2}{p_1} \left(\frac{v + p_1}{v - p_1} \right) e^{-2\tau\sqrt{v^2 + \tau^2}} dv + O(\tau^5), \quad (\text{C.18c})$$

$$I_{22} = \int_{u_0}^\infty \frac{u^2}{p_\tau} \left(\frac{u + p_\tau}{u - p_\tau} \right) e^{-2p_\tau} du + O(\tau^5), \quad (\text{C.18d})$$

$$I_{31} = \tau^2 \int_0^\delta \frac{v^2}{v - p_1} e^{-\tau(v + \sqrt{v^2 + 1})} dv + O(\tau^5), \quad (\text{C.18e})$$

$$I_{32} = \int_{u_0}^\infty \left(-2u^3 \tau^{-2} + \left(u^2 - \frac{1}{2}u \right) - \frac{1}{8} \frac{(2u^2 - 1)}{u} \tau^2 \right) e^{-2u} du + O(\tau^5) \quad (\text{C.18f})$$

all subject to $O(\delta^2 \tau^2, \tau^5)$ errors. Evaluating these integrals up to $O(\delta^2)$ terms gives

$$I_1 = -\frac{3}{2}\tau^{-2} - \frac{1}{2} - \frac{1}{4}\tau^2 \left(\epsilon_0 + \ln \tau + \frac{1}{4} \right) + \frac{8}{15}\tau^3 + \frac{1}{4}\tau^4 \left(\epsilon_0 + \ln \tau - \frac{13}{12} \right), \quad (\text{C.19a})$$

$$I_2 = -\frac{3}{2}\tau^{-2} + 1 + \frac{1}{4}\tau^2 \left(-\frac{13}{4} + \epsilon_0 + \ln \tau \right) + \frac{8}{15}\tau^3 - \frac{3}{8}\tau^4, \quad (\text{C.19b})$$

$$I_3 = -\frac{3}{4}\tau^{-2} + \frac{1}{8} - \frac{1}{8}\tau^2 \left(\frac{3}{4} + \epsilon_0 + \ln \tau \right) + \frac{4}{15}\tau^3 + \frac{1}{16}\tau^4 \left(\epsilon_0 + \ln \tau - \frac{25}{12} \right), \quad (\text{C.19c})$$

again subject to $O(\delta^2 \tau^2, \tau^5)$ errors and where $\epsilon_0 \sim 0.5772$ is Euler's constant. Substitution of C.19(a–c) into C.12(a) then yields

$$I(\tau, \gamma) = \frac{\tau^2}{i\epsilon^2 \gamma^2} \frac{(1 - \epsilon_0 - \ln \tau)}{(\ln 2 - \ln \sqrt{i\epsilon\gamma} - \epsilon_0)} - \frac{3}{8(\ln 2 - \ln \sqrt{i\epsilon\gamma} - \epsilon_0)} + \frac{\tau^4}{4i\epsilon^2 \gamma^2}, \quad (\text{C.20})$$

subject to $O(\tau^2 / \ln \sqrt{i\epsilon\gamma}, \tau^5 / i\epsilon^2 \gamma^2)$ errors. From (C.16) we obtain the drag

$$D = \frac{4\pi}{(\ln(\Delta/\epsilon) + \ln 2 - 1 - \tau^2/4)}, \quad (\text{C.21})$$

plus $O(i\epsilon^2 \gamma^2 / \ln(\Delta/\epsilon), ((\Delta/\epsilon)^2 \ln \sqrt{i\epsilon\gamma})^{-1}, \tau^4)$ errors.

Appendix D

Two-dimensional inviscid flow for a cylinder touching a wall

In § 2.2.3 we consider high-frequency oscillations ($\epsilon\gamma \gg 1$) where separation distance is comparable with the boundary-layer thickness ($\Delta/\epsilon \lesssim (\epsilon\gamma)^{-1}$). The geometry of the inviscid outer flow, where the cylinder touches the wall, can be mapped to a rectilinear

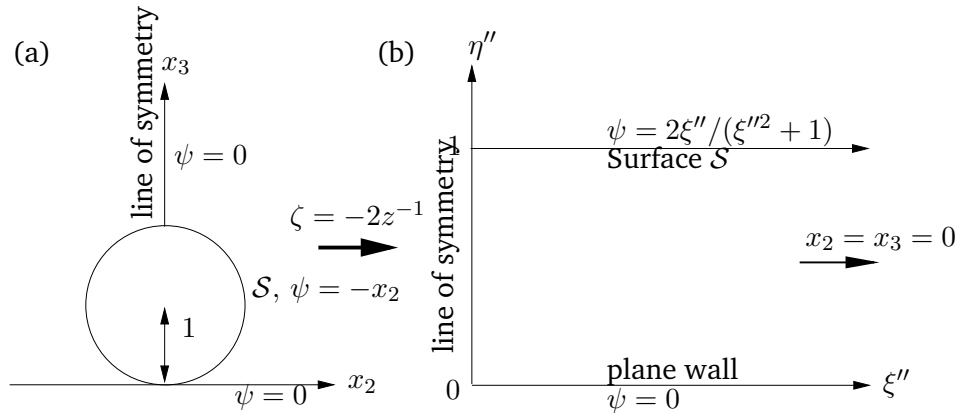


FIGURE D.1: Conformal map $\zeta = -2z^{-1}$, $z = x_2 + ix_3$, $\zeta = \xi'' + i\eta''$ takes the flow domain for a circular cylinder, whose surface S touches a plane wall, into an infinite strip.

coordinate system using the conformal mapping

$$\xi'' = -2x_2/(x_2^2 + x_3^2), \quad \eta'' = 2x_3/(x_2^2 + x_3^2), \quad (\text{D.1})$$

which leaves us needing to solve Laplace's equation $\psi_{\xi''\xi''}^{(0)} + \psi_{\eta''\eta''}^{(0)} = 0$ in the infinite strip $0 \leq \eta'' \leq 1$. In this new flow domain $\eta'' = 0$ and $\eta'' = 1$ represent the wall and cylinder surface \mathcal{S} , respectively, and $\xi'' = 0$ represents the vertical line of symmetry (see figure D.1), hence giving the boundary conditions

$$\psi^{(0)}(\xi'', 0) = \psi^{(0)}(0, 0 \leq \eta'' \leq 1) = 0, \quad \psi^{(0)}(\xi'', 1) = -x_2 = 2\xi''/(\xi''^2 + 1). \quad (\text{D.2})$$

We express the streamfunction in the form

$$\psi^{(0)}(\xi'', \eta'') = 2 \int_0^\infty A(k) \sinh 2\pi k \eta'' \sin 2\pi k \xi'' \, dk, \quad (\text{D.3})$$

which satisfies the condition $\psi = 0$ on the wall and on the line of symmetry, and determine $A(k)$ by imposing the condition on the cylinder surface that

$$\begin{aligned} 2\xi''/(\xi''^2 + 1) &= 2 \int_0^\infty 2\pi e^{-2\pi k} \sin(2\pi k \xi'') \, dk \\ &= \psi^{(0)}(\xi'', 1) = 2 \int_0^\infty A(k) \sinh(2\pi k) \sin(2\pi k \xi'') \, dk, \end{aligned} \quad (\text{D.4})$$

which yields

$$A(k) = 2\pi e^{-2\pi k} \sinh(2\pi k)^{-1}. \quad (\text{D.5})$$

Appendix E

Unsteady slender-body-theory integrals

We now derive the integral approximations which are central to modified resistive-force theory presented in § 3.2.

E.1 Distribution-independent integrals

In what follows we work in a frame of reference parallel to the cylinder's axis (i.e. the unit tangent to the cylinder is $\mathbf{t} = \hat{\mathbf{x}}_1$, assuming $\alpha = 0$), using the cylindrical polar coordinates described in (3.11). The coefficient of the local velocity–force relationship (3.12*b*) satisfies $I_{ij} = I_{ji}$ from (3.4, 3.8). This integral can be approximated by splitting the domain of integration (for $\epsilon \ll \delta \ll 1$)

$$I_{ij}(\xi; \gamma) = \left(\int_{\xi-\delta}^{\xi+\delta} + \int_{-1}^{\xi-\delta} + \int_{\xi+\delta}^1 \right) [S_{ij}(\hat{\mathbf{x}}; \gamma) + a_{kj} Q_{ik}(\hat{\mathbf{x}})] \, ds, \quad (\text{E.1})$$

so that $I_{ij} \equiv I_{ij}^{(1)} + I_{ij}^{(2)} + I_{ij}^{(3)}$ respectively. In $I_{ij}^{(1)}$, $\hat{r} \leq \delta \ll 1$ and we can expand the Stokeslet's exponential terms (3.4*c,d*) about $\hat{r} = 0$. In $I_{ij}^{(3)}$ we can expand about

$\hat{r} = (s - \xi)$. Therefore $I_{ij}^{(1)}$ and $I_{ij}^{(3)}$ have terms with the general form

$$\epsilon^{l+n} \cos^l \theta \sin^n \theta \int_{\xi-\delta}^{\xi+\delta} \frac{(s-\xi)^p}{((s-\xi)^2 + \epsilon^2)^{m/2}} ds, \quad \epsilon^{l+n} \cos^l \theta \sin^n \theta \int_{\xi+\delta}^1 \frac{e^{-\kappa\sqrt{i}\gamma(s-\xi)}}{(s-\xi)^{m-p}} ds, \quad (\text{E.2})$$

($l, n = 0, 1, p = 0, 1, 2$ and $m = 1, \dots, 5, \kappa = 0, 1$), respectively (and similarly for $I_{ij}^{(2)}$). Expressions of the form (E.2) can be integrated directly and then expanded in ϵ . Substituting these expansions into (E.1) and noting that for zero tilt the dipole coefficients are $a_{k1} = 0, a_{k2} = -(\epsilon^2/2)\delta_{k2}, a_{k3} = -(\epsilon^2/2)\delta_{k3}$ leads to the following approximations for the I_{ij} via lengthy but straightforward calculation:

$$\begin{aligned} I_{11}(\xi; \gamma) &= -\frac{2e^{\sqrt{i}\gamma(\xi-1)}}{\sqrt{i}\gamma(\xi-1)} + \frac{2e^{-\sqrt{i}\gamma(\xi+1)}}{\sqrt{i}\gamma(\xi+1)} - \frac{2ie^{\sqrt{i}\gamma(\xi-1)}}{\gamma^2(\xi-1)^2} - \frac{2ie^{-\sqrt{i}\gamma(\xi+1)}}{\gamma^2(\xi+1)^2} \\ &\quad + \frac{2i}{\gamma^2(\xi-1)^2} + \frac{2i}{\gamma^2(\xi+1)^2} - 2\text{Ei}(-\sqrt{i}\gamma(\xi-1)) - 2\text{Ei}(\sqrt{i}\gamma(\xi+1)) \\ &\quad - 4\epsilon_0 - 4\ln\sqrt{i}\gamma + 2\ln 4 - 4\ln\epsilon, \end{aligned} \quad (\text{E.3a})$$

$$\begin{aligned} I_{22}(\xi; \gamma) &= \frac{e^{\sqrt{i}\gamma(\xi-1)}}{\sqrt{i}\gamma(\xi-1)} - \frac{e^{-\sqrt{i}\gamma(\xi+1)}}{\sqrt{i}\gamma(\xi+1)} + \frac{ie^{\sqrt{i}\gamma(\xi-1)}}{\gamma^2(\xi-1)^2} + \frac{ie^{-\sqrt{i}\gamma(\xi+1)}}{\gamma^2(\xi+1)^2} \\ &\quad - \text{Ei}(-\sqrt{i}\gamma(\xi-1)) - \text{Ei}(\sqrt{i}\gamma(\xi+1)) - \frac{i}{\gamma^2(\xi-1)^2} - \frac{i}{\gamma^2(\xi+1)^2} \\ &\quad - 2\epsilon_0 - 2\ln\sqrt{i}\gamma + \ln 4 - 2\ln\epsilon, \end{aligned} \quad (\text{E.3b})$$

$$I_{33}(\xi; \gamma) = I_{22}(\xi; \gamma), \quad I_{12}(\xi; \gamma) = I_{13}(\xi; \gamma) = I_{23}(\xi; \gamma) = 0, \quad (\text{E.3c})$$

subject to at most $O(\epsilon \ln \epsilon)$ errors, due to neglected terms in the evaluation of expressions with the form given by (E.2). $\text{Ei}(z) \equiv \int_1^\infty t^{-1} e^{-tz} dt$ is the exponential integral and $\epsilon_0 \approx 0.5772$ is Euler's constant. The choice of dipole coefficient a_{kj} has eliminated any θ -dependence in the I_{ij} .

E.2 Distribution-dependent integrals

The non-local velocity–force relationship in (3.12) comes from terms of the form (3.12c). Evaluation of these integrals is achieved by once again splitting the domain of integration as in (E.1) to give $T_i(\xi, \mathbf{f}; \gamma) = T_i^{(1)} + T_i^{(2)} + T_i^{(3)}$. In $T_i^{(1)}$, we expand $f_j(s)$ about ξ and the exponential terms in S_{ij} (3.4b) about $\hat{r} = 0$, yielding terms with the general

form

$$\epsilon^{l+n} f_j^{(\varsigma)}(\xi) \cos^l \theta \sin^n \theta \int_{\xi-\delta}^{\xi+\delta} \frac{(s-\xi)^{p+\varsigma}}{((s-\xi)^2 + \epsilon^2)^{m/2}} ds, \quad (\text{E.4})$$

for $m = 1 \dots 5$, $l, n = 0, 1$, $p = 0, \dots, 2$ and $\varsigma = 1 \dots m - p$. The superscript on f_j denotes its ς th derivative. It can be shown that these integrals produce expressions which are algebraically small in ϵ and hence make no contribution to T_i . In $T_i^{(3)}$, $\hat{r} = (s - \xi) + O(\epsilon^2/\delta)$ and we can expand the integrand about $\hat{r} = (s - \xi)$. This results in Stokeslet contributions to $T_i^{(3)}$ of the form

$$\int_{\xi+\delta}^1 \frac{(f_j(s; \gamma, \Delta) - f_j(\xi; \gamma, \Delta)) e^{-\sqrt{i}\gamma(s-\xi)}}{(s-\xi)^M} ds \quad (M \leq 2), \quad (\text{E.5a})$$

$$\int_{\xi+\delta}^1 \frac{(f_j(s; \gamma, \Delta) - f_j(\xi; \gamma, \Delta)) (e^{-\sqrt{i}\gamma(s-\xi)} - 1)}{(s-\xi)^M} ds \quad (M = 3), \quad (\text{E.5b})$$

$$\epsilon^{l+n} \cos^l \theta \sin^n \theta \int_{\xi+\delta}^1 \frac{(f_j(s; \gamma, \Delta) - f_j(\xi; \gamma, \Delta)) e^{-\sqrt{i}\gamma(s-\xi)}}{(s-\xi)^{m-2+l+n}} ds \quad (m \leq 4), \quad (\text{E.5c})$$

$$\epsilon^{l+n} \cos^l \theta \sin^n \theta \int_{\xi+\delta}^1 \frac{(f_j(s; \gamma, \Delta) - f_j(\xi; \gamma, \Delta)) (e^{-\sqrt{i}\gamma(s-\xi)} - 1)}{(s-\xi)^{m-2+l+n}} ds \quad (m = 5) \quad (\text{E.5d})$$

and similarly for $T_i^{(2)}$. Provided that f_j is not algebraically singular in s over the interval of integration, (E.5c,d) are $O(\epsilon^{l+n}/\delta^{m-2+l+n})$ and so for non-zero l or n we are able to choose δ such that these integrals are algebraically small in ϵ . Since $a_{kj} = O(\epsilon^2)$, the same reasoning leads us to deduce that the dipoles make no leading-order contribution to $T_i^{(3)}$ or $T_i^{(2)}$.

Therefore the only non-zero contributions to T_i from (E.5c,d) come from S_{ij} terms with l and n both zero. Under these circumstances the integrals (E.5c,d) assume the form of (E.5a,b). The δ -dependence in the integration limits can be removed by considering these integrals in the interval $(\xi - \delta, \xi + \delta)$, where we can expand the exponential

terms about $|s - \xi|$ and $f_j(s; \gamma, \Delta)$ about ξ :

$$\begin{aligned}
& \int_{\xi-\delta}^{\xi+\delta} \frac{(f_j(s; \gamma, \Delta) - f_j(\xi; \gamma, \Delta)) e^{-\sqrt{i}\gamma|s-\xi|}}{|s - \xi|^M} ds \\
&= O \left(\int_{\xi-\delta}^{\xi+\delta} \frac{(f_j(s; \gamma, \Delta) - f_j(\xi; \gamma, \Delta)) (e^{-\sqrt{i}\gamma|s-\xi|} - 1)}{|s - \xi|^3} ds \right) \\
&= O \left(\int_{\xi-\delta}^{\xi+\delta} \frac{(s - \xi)}{|s - \xi|^M} ds \right) = 0 \quad (M \leq 2) \quad (\text{E.6a})
\end{aligned}$$

(subject to only algebraically small errors in ϵ), where integration is defined in the Cauchy-principal-value sense. Therefore terms in $T_i^{(2)} + T_i^{(3)}$ can be expressed as Cauchy-principal-value integrals between -1 and 1 . This combined with the fact that the integrals given by (E.4) make no $O(1)$ contribution, means (for $m \leq 3$)

$$\begin{aligned}
& \int_{-1}^1 \frac{(f_j(s; \gamma, \Delta) - f_j(\xi; \gamma, \Delta)) (e^{-\sqrt{i}\gamma\sqrt{(s-\xi)^2 + \epsilon^2}} - \delta_{3m})}{((s - \xi)^2 + \epsilon^2)^{m/2}} ds \\
&\approx \int_{-1}^1 \frac{(f_j(s; \gamma, \Delta) - f_j(\xi; \gamma, \Delta)) (e^{-\sqrt{i}\gamma|s-\xi|} - \delta_{3m})}{|s - \xi|^m} ds \quad (\text{E.7})
\end{aligned}$$

to leading order in ϵ . Substituting (E.7) into (3.12c), T_i reduces (up to algebraically small error in ϵ) the simpler quantity \mathcal{T}_i given in (3.16), which is diagonal in f_i .

Bibliography

- R. K. Agarwal, K. Y. Yun, and R. Balakrishnan. Beyond Navier–Stokes: Burnett equations for flows in the continuum-transition region. *Phys. Fluids*, 13:3061–3085, 2001.
- T. R. Albrecht, S. Akamine, T. E. Carver, and C. F. Quate. Microfabrication of cantilever styli for the atomic force microscope. *J. Vac. Sci. Technol. A*, 8:3386–3396, 1990.
- J. Alcaraz, L. Buscemi, M. Puig-de Morales, J. Colchero, A. Baro, and D. Navajas. Correction of microrheological measurements of soft samples with atomic force microscopy for the hydrodynamic drag on the cantilever. *Langmuir*, 18:716–721, 2002.
- A. Avudainayagam and J. Geetha. Oscillatory line singularities of Stokes’ flows. *Int. J. Engng Sci.*, 31:1295–1299, 1993.
- A. Avudainayagam and J. Geetha. Unsteady singularities of Stokes’ flows in two dimensions. *Int. J. Engng. Sci.*, 33:1713–1724, 1995.
- A. Avudainayagam and J. Geetha. A boundary-integral equation for two-dimensional oscillatory Stokes flow past an arbitrary body. *J. Eng. Math.*, 33:251–258, 1998.
- A. J. Bard, F. R. F. Fan, and D. T. Pierce. Chemical imaging of surfaces with the scanning electron microscope. *Science*, 254:68–74, 1991.
- J. L. Barrat and L. Bocquet. Large slip effect at a nonwetting fluid–solid interface. *Phys. Rev. Lett.*, 82:4671–4674, 1999.
- A. B. Basset. *A Treatise on Hydrodynamics*, vol. 2. Cambridge: Deighton Bell, 1888.

- G. K. Batchelor. Slender-body theory for particles of arbitrary cross-section in Stokes flow. *J. Fluid Mech.*, 44:419–440, 1970.
- J. Baudry, E. Charlaix, A. Tonck, and D. Mazuyer. Experimental evidence for a large slip effect at a nonwetting fluid–solid interface. *Langmuir*, 17:5232–5236, 2001.
- G. Binnig, C. F. Quate, and C. Gerber. Atomic force microscope. *Phys. Rev. Lett.*, 56:930–933, 1986.
- G. Binnig, H. Rohrer, Ch. Gerber, and E. Weibel. Tunneling through a controllable vacuum gap. *Appl. Phys. Lett.*, 40:178–180, 1982.
- J. R. Blake. A note on the image system for a Stokeslet in a no-slip boundary. *Proc. Camb. Phil. Soc.*, 70:303–310, 1971.
- J. R. Blake. A model for the micro-structure in ciliated organisms. *J. Fluid Mech.*, 55:1–23, 1972.
- J. R. Blake. Singularities of viscous flow. Part II: Applications to slender body theory. *J. Eng. Math.*, 8:113–124, 1974.
- J. R. Blake. On the generation of viscous toroidal eddies in a cylinder. *J. Fluid Mech.*, 95:209–222, 1979.
- J. R. Blake. Mechanics of muco-ciliary transport. *IMA J. Appl. Math.*, 32:69–87, 1984.
- J. R. Blake and A. T. Chwang. Fundamental singularities of viscous flow. Part I: The image systems in the vicinity of a stationary no-slip boundary. *J. Eng. Math.*, 8:23–29, 1974.
- L. Bocquet and J. L. Barrat. Hydrodynamic boundary conditions, correlation functions, and Kubo relations for confined fluids. *Phys. Rev. E*, 49:3079–3092, 1994.
- E. Bonaccorso, S. Butt, and V. S. J. Craig. Surface roughness and hydrodynamic boundary slip of a Newtonian fluid in a completely wetting system. *Phys. Rev. Lett.*, 90:144501, 2003.

- E. Bonaccorso, M. Kappl, and H. S. Butt. Hydrodynamic force measurements: Boundary slip of water on hydrophilic surfaces and electrokinetic effects. *Phys. Rev. Lett.*, 88: 076103, 2002.
- C. Brennen and H. Winet. Fluid mechanics of propulsion by cilia and flagella. *Ann. Rev. Fluid Mech.*, 9:339–398, 1977.
- H. Brenner. The slow motion of a sphere through a viscous fluid towards a plane surface. *Chem. Eng. Sci.*, 16:242–251, 1961.
- H. Brenner. Effect of finite boundaries on the Stokes resistance of an arbitrary particle. *J. Fluid Mech.*, 12:35–48, 1962.
- H. Brenner. The Stokes resistance of an arbitrary particle: IV. arbitrary fields of flow. *Chem. Eng. Sci.*, 19:703, 1964.
- M. M. Britton and P. T. Callaghan. Two-phase shear band structures at uniform stress. *Phys. Rev. Lett.*, 78:4930–4933, 1997.
- M. Broday. Motion of nanobeads proximate to plasma membranes during single particle tracking. *B. Math. Biol.*, 64:531–563, 2002.
- C.J. Brokaw. Non-sinusoidal bending waves of sperm flagella. *J. Exp. Biol.*, 43:155–169, 1965.
- N. A. Burnham, D. D. Dominguez, R. L. Mowery, and R. J. Colton. Probing the surface forces of monolayer films with an atomic-force microscope. *Phys. Rev. Lett.*, 64:1931–1934, 1990.
- C. Bustamante, J. Vesenka, C. L. Tang, W. Rees, M. Guthod, and R. Keller. Circular DNA imaged in air by scanning force microscopy. *Biochemistry*, 31:22–26, 1992.
- H.-J. Butt and M. Jaschke. Calculation of thermal noise in atomic force microscopy. *Nanotechnology*, 6:1995, 1995.

- H.-J. Butt, P. Siedle, K. Seifert, K. Fendler, T. Seeger, E. Bamberg, A. L. Weisenhorn, K. Goldie, and A. Engel. Scan speed limit in atomic force microscopy. *J. Microsc.*, 169:75–84, 1993.
- P. W. Carpenter. The hydrodynamic stability of flow of Kramer-type compliant surfaces. Part 2. Flow-induced surface instabilities. *J. Fluid Mech.*, 170:199–232, 1986.
- P. W. Carpenter and A. D. Garrad. The hydrodynamic stability of flow over Kramer-type compliant surfaces. Part 1. Tollmien-Schlichting instabilities. *J. Fluid Mech.*, 155:465–510, 1985.
- E. Chadwick. A slender-body theory in Oseen flow. *Proc. Roy. Soc. London A*, 458:2007–2016, 2002.
- D. Chandler. *Introduction to modern statistical physics*. Oxford University Press, 1987.
- G. Y. Chen, R. J. Warmack, T. Thundat, and D. P. Allison. Resonance response of scanning force microscopy cantilevers. *Rev. Sci. Instrum.*, 65:2532–2537, 1994.
- J. H. J. Cho, B. M. Law, and F. Rieutord. Dipole-dependent slip of Newtonian fluids at smooth solid hydrophobic surfaces. *Phys. Rev. Lett.*, 92:166102, 2004.
- C. H. Choi, K. Johan, A. Westin, and K. S. Breuer. Apparent slip flows in hydrophilic and hydrophobic microchannels. *Phys. Fluids*, 15:2897–2902, 2003.
- J. W. M. Chon, P. Mulvaney, and J. E. Sader. Experimental validation of theoretical models for the frequency response of atomic force microscope cantilever beams immersed in fluids. *J. Appl. Phys.*, 87:3978–3988, 2000.
- J. Chu and M-U. Kim. Two-dimensional oscillatory Stokes flows between two parallel planes. *Fluid Dyn. Res.*, 29:7–24, 2001.
- J. Chu and M-U. Kim. Two-dimensional oscillatory Stokes flow in the region with a semi-infinite plate parallel to an infinite plane wall. *Fluid Dyn. Res.*, 31:229–251, 2002.

- J. Chu and M-U. Kim. Oscillatory Stokes flow due to motions of a circular disk parallel to an infinite plane wall. *Fluid Dyn. Res.*, 34:77–97, 2004.
- A. T. Chwang and T. Yao-Tsu Wu. Hydromechanics of low-Reynolds number flow. Part 1. Rotation of axisymmetric prolate bodies. *J. Fluid Mech.*, 63:607–622, 1974.
- A.T. Chwang and T.Y. Wu. A note on the helical movement of micro-organisms. *Proc. Roy. Soc. B*, 178:327–346, 1971.
- R. J. Clarke, S. M. Cox, P. M. Williams, and O. E. Jensen. The drag on a microcantilever oscillating near a wall. *J. Fluid Mech. (to appear)*, 2005a.
- R. J. Clarke, O. E. Jensen, J. Billingham, and P. M. Williams. Three-dimensional flow due to a microcantilever oscillating near a wall: an unsteady slender-body analysis. *Proc. Roy. Soc. London A (submitted)*, 2005b.
- J.P. Cleveland, S. Manne, D. Bocek, and P. K. Hansma. A nondestructive method for determining the spring constant of cantilevers for scanning force microscopy. *Rev. Sci. Instrum.*, 64:403–405, 1993.
- C. Cottin-Bizonne, C. Barentin, E. Charlaix, L. Bocquet, and J. L. Barrat. Dynamics of simple liquids at heterogeneous surfaces: Molecular dynamics simulations and hydrodynamic description. *Eur. Phys. J. E.*, 15:427–438, 2004.
- C. Cottin-Bizonne, J. L. Barrat, L. Bocquet, and E. Charlaix. Low-friction flows of liquid at nanopatterned interfaces. *Nature Mat.*, 2:237–240, 2003.
- C. Cottin-Bizonne, B. Cross, A. Steinberger, and E. Charlaix. Boundary slip on smooth hydrophobic surfaces: intrinsic effects and possible artifacts. *Phys. Rev. Lett.*, 94:056102, 2005.
- R. G. Cox. The motion of long slender bodies in a viscous fluid. Part I: General theory. *J. Fluid Mech.*, 44:791–810, 1970.
- R. G. Cox. The motion of long slender bodies in a viscous fluid. Part 2: Shear flow. *J. Fluid Mech.*, 45:625–657, 1971.

- V. Craig and C. Neto. In situ calibration of colloid probe cantilevers in force microscopy: hydrodynamic drag on a sphere approaching a wall. *Langmuir*, 17:6018–6022, 2001.
- V. S. J. Craig, C. Neto, and D. R. M. Williams. Shear-dependent boundary slip in aqueous Newtonian liquid. *Phys. Rev. Lett.*, 87:054504, 2001.
- D. M. Czajkowsky, M. J. Allen, V. Elings, and Z. F. Shao. Direct visualization of surface-charge in aqueous-solution. *Ultramicroscopy*, 74:1–5, 1998.
- A. M. J. Davis. A hydrodynamic model of the oscillating screen viscometer. *Phys. Fluids A*, 5:2095–2103, 1993a.
- A. M. J. Davis. Some asymmetric Stokes flows that are structurally similar. *Phys. Fluids A*, 5:2086–2094, 1993b.
- N. J. De Mestre. Low-Reynolds-number fall of slender cylinders near boundaries. *J. Fluid Mech.*, 58:641–656, 1973.
- N. J. De Mestre and W. B. Russel. Low-Reynolds-number translation of a slender cylinder near a plane wall. *J. Eng. Math.*, 9:81–91, 1975.
- W. R. Dean and P. E. Montagnon. On the steady motion of viscous liquid in a corner. *Proc. Camb. Phil. Soc.*, pages 389–394, 1949.
- J. Ding and Y. Wenjiig. A fast integral approach for drag force calculations due to oscillatory slip Stokes flow. *Int. J. Numer. Meth. Eng.*, 60:1535–1567, 2004.
- J. M. Dorrepaal, M. E. O’Neill, and K. B. Ranger. Two-dimensional Stokes flow with cylinders and line singularities. *Mathematika*, 31:65–75, 1984.
- U. Durig, F. Pohl, and F. Rohrer. Near field optical scanning microscopy. *J. Appl. Phys.*, 59:3318–3327, 1986.
- L. Durlofsky and J. F. Brady. Analysis of the Brinkman equations as a model for flow in porous media. *Phys. Fluids*, 30:3329–3341, 1987.
- F. Elmer and M. Dreier. Eigenfrequencies of a rectangular atomic force microscope cantilever in a medium. *J. Appl. Phys.*, 81:7709–7714, 1997.

- E. Evans. Probing the relation between force–lifetime–and chemistry in single molecular bonds. *Annu. Rev. Biophys. Biomol. Struct.*, 30:105–128, 2001.
- M. Faraday. On a peculiar class of acoustical figures, and on certain forms assumed by groups of particles on vibrating elastic surfaces. *Trans. Roy. Soc. (London)*, 121: 229–340, 1831.
- O. H. Faxen. Die Bewegung einer starren Kugel Längs der Achse eines mit zäher Flüssigkeit gefüllten Rohres. *Arkiv. Mat. Astr. Fys.*, 17:27, 1923.
- O. H. Faxen. Der Widerstand gegen die Bewegung einer starren Kugel in einer zähen Flüssigkeit, die zwischen zwei parallelen, ebenen Wänden eingeschlossen ist. *Ark. Mat. Astr. Fys.*, 18:29, 1924.
- J. Feng, P. Ganatos, and S. Weinbaum. The general motion of a circular disk in a Brinkman medium. *Phys. Fluids*, 10:2137–2146, 1998a.
- J. Feng, P. Ganatos, and S. Weinbaum. Motion of a sphere near planar confining boundaries in a Brinkman medium. *J. Fluid Mech.*, 375:265–296, 1998b.
- J. Feng and D. D. Joseph. The unsteady motion of solid bodies in creeping flows. *J. Fluid Mech.*, 303, 1995.
- F. Feuillebois and A. Lasek. On the rotational historic term in non-stationary Stokes flow. *Q. Jl. Mech. Appl. Math.*, 31:435–443, 1977.
- M. D. Finn and S. M. Cox. Stokes flow in a mixer with changing geometry. *J. Eng. Math.*, 41:75–99, 2001.
- E.-L. Florin, V. T. Moy, and H. E. Gaub. Adhesion forces between individual ligand-receptor pairs. *Science*, 264:415–417, 1994.
- J. Foss, C. Tropea, and A. Yarin. *Handbook of experimental fluid dynamics*. Springer, New-York, 2005.
- C. D. Frisbie, L. F. Rozsnyai, A. Noy, M. S. Wrighton, and C. M. Lieber. Functional-group imaging by chemical force microscopy. *Science*, 265:2071–2074, 1994.

- P. D. Frymier, R. M. Ford, and H. C. Berg. 3-dimensional tracking of motile bacteria near a solid planar surface. *P. Natl. Acad. Sci. USA*, 92:6195–6199, 1995.
- M Gad-El-Hak. Flow physics in MEMS. *Mec. Ind.*, 2:313–341, 2001.
- M.A. Gallis and J.R. Torczynski. An improved reynolds-equation model for gas damping of microbeam motion. *J. Microelectromech. Sys.*, 13:653–659, 2004.
- E. Gavze. The accelerated motion of rigid bodies in non-steady Stokes flow. *Int. J. Multiphase Flow*, 16:153–166, 1990.
- J. Geer. Stokes flow past a slender body of revolution. *J. Fluid Mech.*, 78:577–600, 1976.
- A. J. Gil, J. Colchero, M. Luna, J. Gomez-Herrero, and A. M. Baro. Adsorption of water on solid surfaces studied by scanning force microscopy. *Langmuir*, 16:5086–5092, 2000.
- M. Grandbois, W. Dettmann, M. Benoit, and H. E. Gaub. Affinity imaging of red blood cells using an atomic force microscope. *J. Histochem. Cytochem.*, 48:719–724, 2000.
- S. Granick, X. Y. Zhu, and H. Lee. Slippery questions about complex fluids flowing past solids. *Nature Mat.*, 2:221–227, 2003.
- J Gray and G.J. Hancock. The propulsion of sea-urchin spermatozoa. *Proc. Roy. Soc.*, 32:96–121, 1955.
- C. P. Green and J. E. Sader. Torsional frequency response of cantilever beams immersed in viscous fluids with applications to the atomic force microscope. *J. Appl. Phys.*, 92: 6262–6274, 2002.
- C. P. Green and J. E. Sader. Small amplitude oscillations of a thin beam immersed in a viscous fluid near a solid surface. *Phys. Fluids*, 17:073102, 2005.
- N. H. Green, S. Allen, M. C. Davies, C. J. Roberts, S. J. B. Tandler, and P. M. Williams. Force sensing and mapping by atomic force microscopy. *Trends in Analytical Chemistry*, 21:64–72, 2002.

- W. W. Hackborn. Asymmetric Stokes' flow between parallel planes due to a rotlet. *J. Fluid Mech.*, 218:531–546, 1980.
- P. Hall and D. T. Papegeorgiou. The onset of chaos in a class of Navier-Stokes solutions. *J. Fluid Mech.*, 393:59–87, 1999.
- P. Hallet, G. Offer, and M. J. Miles. Atomic force microscopy of the myosin molecule. *Biophys. J.*, 68:1604–1606, 1995.
- G. J. Hancock. The self propulsion of microscopic organisms through liquids. *Proc. Roy. Soc.*, A214:96–121, 1953.
- P. K. Hansma, J. P. Cleveland, M. Radmacher, D. A. Walters, P. E. Hillner, M. Benzanilla, M. Fritz, D. Vie, H. G. Hansma, C. B. Prater, J. Massie, L. Fukunaga, J. Gurley, and V. Elings. Tapping mode atomic-force microscopy in liquids. *Appl. Phys. Lett.*, 64:1738–1740, 1994.
- P. K. Hansma, B. Drake, O. Marti, S. A. Gould, and C. B. Prater. The scanning ion-conductance microscope. *Science*, 243:641–643, 1989.
- H. Hasimoto and O. Sano. Stokeslets and eddies in creeping flow. *Ann. Rev. Fluid Mech.*, 12:335–363, 1980.
- E. H. Hauge and Martin-Löf. Fluctuating-hydrodynamics and Brownian motion. *J. Stat. Phys.*, 7:259–281, 1973.
- C. L. Henry, C. Neto, D. R. Evans, S. Biggs, and V. S. J. Craig. The effect of surfactant adsorption on liquid boundary slippage. *Physica A*, 339:60–65, 2004.
- J. B. Heymann, D. J. Müller, K. Mitsuoka, and A. Engel. Electron and atomic force microscopy of membrane proteins. *Curr. Opin. Struct. Biol.*, 7:543–549, 1997.
- J. J. L. Higdon. The generation of feeding currents by flagellar motions. *J. Fluid Mech.*, 94:305–330, 1979a.
- J. J. L. Higdon. A hydrodynamic analysis of flagellar propulsion. *J. Fluid Mech.*, 90:685–711, 1979b.

- J. J. L. Higdon. The hydrodynamics of flagellar propulsion: helical waves. *J. Fluid Mech.*, 94:331–351, 1979c.
- E. J. Hinch. Application of the Langevin equation to fluid suspensions. *J. Fluid Mech.*, 72:499–511, 1975.
- R. Hocquart. Regime instante d'un liquide dans lequel un ellipsoïde de révolution tourne autour de son axe. *C. R. Acad. Sci. Paris*, 283A:1119–1122, 1976.
- R. Hocquart and E. J. Hinch. The long-time tail of the angular velocity autocorrelation function for a rigid-Brownian particle of arbitrary centrally symmetric shape. *J. Fluid Mech.*, 137:217–220, 1983.
- C. Huh and L. E. Scriven. Hydrodynamic model of steady movement of a solid/liquid/fluid contact line. *J. Colloid Int. Sci.*, 35:85–101, 1971.
- S. W. Hui, R. Viswanathan, J. A. Zasadzinski, and J. N. Israelachvili. The structure and stability of phospholipid bilayers by atomic force microscopy. *Biophys. J.*, 68:171–178, 1995.
- J.L. Hutter and J. Bechhoefer. Calibration of atomic-force microscope tips. *Rev. Sci. Instrum.*, 64:1868–1873, 1993.
- N. Ishida, T. Inoue, M. Miyahara, and K. Higashitani. Nanobubbles on a hydrophobic surface in water observed by tapping-mode atomic force microscopy. *Langmuir*, 16:6377–6380, 2000.
- J. N. Israelachvili. Measurement of the viscosity of liquids in very thin films. *J. Colloid Interf. Sci.*, 110:263–271, 1986a.
- J. N. Israelachvili. Measurement of the viscosity of liquids in very thin films. *J. Colloid Int. Sci.*, 110:263–271, 1986b.
- H. Janovjak, J. Struckmeier, and D. J. Müller. Hydrodynamic effects in fast AFM single-molecule force measurements. *Eur. Biophys. J. Biophys. Lett.*, pages 1–12, 2004.

- G. B. Jeffery. Plane stress and plane strain in bipolar coordinates. *Phil. Trans. Roy. Soc.*, 221:265–293, 1921.
- D. J. Jeffrey and Y. Onishi. The slow motion of a cylinder next to a plane wall. *Q. J. Mech. Appl. Math.*, 34:129–137, 1981.
- R. E. Johnson. An improved slender body theory for Stokes flow. *J. Fluid Mech.*, 99: 411–431, 1980.
- P. Joseph and P. Tabeling. Direct measurement of the apparent slip length. *Phys. Rev. E*, 71:035303, 2005.
- R. P. Kanwal. Rotatory and longitudinal oscillations of axi-symmetric bodies in a viscous fluid. *Q. J. Mech. Appl. Math.*, 8:146, 1955a.
- R. P. Kanwal. Vibrations of elliptic cylinders and a flat plate in a viscous fluids. *Z. Angew. Math. Mech.*, 35:17–22, 1955b.
- R. P. Kanwal. Drag on an axially symmetric body vibrating slowly along its axis in a viscous fluid. *J. Fluid Mech.*, 19:631, 1964.
- R. P. Kanwal. Note on slow rotation or rotary oscillation of axisymmetric bodies in hydrodynamics and magnetohydrodynamics. *J. Fluid Mech.*, 41:721–726, 1970.
- S.J. Karrila. *Linear operator theory applied to fast computation strategies for particle interactions in viscous flows*. PhD thesis, University of Wisconsin–Madison, 1988.
- D. F. Katz, J. R. Blake, and S. L. Paveri-Fontana. On the movement of slender bodies near plane boundaries at low Reynolds number. *J. Fluid Mech.*, 72:529–540, 1975.
- J. Keller and I. R. Sol. Slender-body theory for slow viscous flow. *J. Fluid Mech.*, 75: 705–714, 1976.
- S. G. Kelly. *Fundamentals of mechanical vibrations*. McGraw-Hill, 1993.
- R. E. Khayat and R. G. Cox. Inertia effects on the motion of long slender bodies. *J. Fluid Mech.*, 209:435–462, 1989.

- M-U. Kim, K. W. Kim, Y.-H. Cho, and B. M. Kwak. Hydrodynamic force on a plate near the plane wall. Part I: plate in sliding motion. *Fluid Dyn. Res.*, 29:137–170, 2001a.
- M-U. Kim, K. W. Kim, Y.-H. Cho, and B. M. Kwak. Hydrodynamic force on a plate near the plane wall. Part II: plate in squeezing motion. *Fluid Dyn. Res.*, 29:171–198, 2001b.
- S. Kim and W. B. Russel. The hydrodynamic interactions between two spheres in a Brinkman medium. *J. Fluid Mech.*, 154:253–268, 1985.
- S. Kirstein, M. Mertesdorf, and M. Schonhoff. The influence of a viscous fluid on the vibration dynamics of scanning near-field optical microscopy fiber probes and atomic force microscopy cantilevers. *J. Appl. Phys.*, 1998.
- J. Koplik, J. R. Banavar, and J. F. Willemsen. Molecular dynamics of fluid flow at solid-surfaces. *Phys. Fluids*, 1:781–794, 1989.
- H. Lamb. *Hydrodynamics*. Cambridge University Press, 1932.
- L. D. Landau and E. M. Lifshitz. *Fluid Mechanics*. Pergamon, Oxford, 1959.
- E. Lauga and H. Stone. Effective slip in pressure-driven Stokes flow. *J. Fluid Mech.*, 489:55–77, 2003.
- C. J. Lawrence and S. Weinbaum. The force on an axisymmetric body in linearized time-dependent motion: a new memory term. *J. Fluid Mech.*, 171:209–218, 1986.
- C. J. Lawrence and S. Weinbaum. The unsteady force on a body at low Reynolds number; the axisymmetric motion of a spheroid. *J. Fluid Mech.*, 189:463–489, 1988.
- G. U. Lee, L. A. Chrisey, and R. J. Colten. Direct measurement of the forces between complementary strands of DNA. *Science*, 266:771–773, 1994.
- M. J. Lighthill. *Mathematical biofluidynamics*. Philadelphia: SIAM, 1975.
- N. Liron and J. R. Blake. Existence of viscous eddies near boundaries. *J. Fluid Mech.*, 107:109–129, 1981.

- N. Liron and S. Mochon. Stokes flow for a Stokeslet between parallel flat plates. *J. Eng. Math.*, 10:287–303, 1976.
- M. Loewenberg. The unsteady Stokes resistance of arbitrarily oriented, finite-length cylinders. *Phys. Fluids*, 5:3004–3006, 1993.
- M. Loewenberg. Asymmetric, oscillatory motion of a finite-length cylinder: The macroscopic effect of particle edges. *Phys. Fluids*, 6:1095–1107, 1994a.
- M. Loewenberg. Axisymmetric unsteady Stokes flow past an oscillating finite-length cylinder. *J. Fluid Mech.*, 265:265–288, 1994b.
- H. A. Lorentz. A general theorem on the motion of a fluid with friction and a few results derived from it (translated into english by H.K.Kuiken). *J. Eng. Math.*, 30:19–24, 1896.
- H. A. Lorentz. Ein allgemeiner Satz, die Bewegung einer reibenden Flüssigkeit betreffend, nebst einigen Anwendungen desselben. *Abhand. Theor. Phys.*, 1:23–42, 1907.
- M. Ludwig, W. Dettmann, and H. E. Gaub. Atomic force microscope imaging contrast based on molecular recognition. *Biophys. J.*, 72:445–448, 1997.
- Y. L. Lyubchenko, L. S. Shlyakhtenko, R. E. Harrington, P. I. Oden, and S. M. Lindsay. Atomic force microscopy of long DNA: imaging in air and under water. *Proc. Natl. Acad. Sci. USA*, 90:2137–2140, 1993.
- H. Ma, J. Jimenez, and R. Rajagopalan. Brownian fluctuation spectroscopy using atomic force microscopes. *Langmuir*, 16:2254–2261, 2000.
- A. Maali, C. Hurth, R. Boisgard, C. Jai, T. Cohen-Bouhacina, and J. P. Aime. Hydrodynamics of oscillating atomic force microscopy cantilevers in viscous fluids. *J. Appl. Phys.*, 97:97–102, 2005.
- N. Maeda and T. Senden. A method for the calibration of force microscopy cantilevers via hydrodynamic drag. *Langmuir*, 16:9282–9286, 2000.

- Y. Magariyama, M. Ichibu, K. Nakata, K. Baba, T. Ohtani, S. Kudo, and T. Goto. Difference in bacterial motion between forward and backward swimming caused by the wall effect. *Biophys. J.*, 88:3648–3658, 2005.
- L. T. Mazzola, C. W. Frank, S. P. A. Fodor, C. Mosher, R. Lartius, and E. Henderson. Discrimination of DNA hybridization using chemical force microscopy. *Biophys. J.*, 76:2922–2933, 1999.
- C. Neto, V. S. J. Craig, and D. R. M. Williams. Evidence of shear-dependent boundary slip in Newtonian liquids. *Eur. Phys. J.*, 12:S71–S74, 2003.
- S.M. Notley, S. Biggs, and V.S.J Craig. Calibration of colloid probe cantilevers using the dynamic viscous response of a confined liquid. *Rev. Sci. Instrum.*, 74:4026–4032, 2003.
- L. Onsager. Reciprocal relations in irreversible processes I. *Phys. Rev.*, 37:405–426, 1931.
- B. A. A. Orme, J. R. Blake, and S. R. Otto. Modelling the motion of particles around choanoflagellates. *J. Fluid Mech.*, 475:333–355, 2003.
- C. W. Oseen. Über die Stokessche Formel und über eine verwandte Aufgabe in der Hydrodynamik. *Ark. Math. Astr. Fys.*, 6, 1910.
- C. W. Oseen. *Neuere Methoden und Ergebnisse in der Hydrodynamik*. Leipzig: Akad.-Verlag., 1927.
- M. R. Paul and M. C. Cross. Stochastic dynamics of nanoscale mechanical oscillators immersed in a viscous fluid. *Phys. Rev. Lett.*, 92:235501, 2004.
- M. Pettitt. *Prey capture and ingestion in choanoflagellates*. PhD thesis, Birmingham University, 2001.
- N. Phan-Thien, T. Tran-Cong, and M. Ramia. A boundary-element analysis of flagellar propulsion. *J. Fluid Mech.*, 184:533–549, 1987.

- R. Pit, H. Hervert, and L. Leger. Direct experimental evidence of slip in hexadecane: solid interfaces. *Phys. Rev. Lett.*, 85:980–983, 2000.
- C. Pozrikidis. A singularity method for unsteady linearized flow. *Phys. Fluids*, 9:1508–1520, 1989a.
- C. Pozrikidis. A study of linearized oscillatory flow past particles by the boundary-integral method. *J. Fluid Mech.*, 202:17–41, 1989b.
- C. Pozrikidis. *Introduction of Theoretical and Computation Fluids Dynamics*. Oxford, 1996.
- I. Proudman and J. R. A. Pearson. Expansions at small Reynolds numbers for the flow past a sphere and a circular cylinder. *J. Fluid Mech.*, 2:237–262, 1957.
- M. Radmacher, J. P. Cleveland, M. Fritz, H. G. Hansma, and P. K. Hansma. Mapping interaction forces with the atomic force microscope. *Biophys. J.*, 66:2159–2165, 1994.
- A. Rahman. Liquid structure and self-diffusion. *J. Chem. Phys.*, 45:2585, 1964.
- R. Rajagopalan. Atomic force and optical force microscopy: applications to interfacial microhydrodynamics. *Colloids and Surfaces*, 174:253–267, 2000.
- K. B. Ranger. Eddies in two-dimensional Stokes' flow. *Int. J. Engng Sci.*, 18:181–190, 1980.
- Lord Rayleigh. On the circulation of air observed in Kundt's tubes, and on some allied acoustical problems. *Phil. Trans. (A)*, 175:1–21, 1884.
- L. E. Reichl. *A modern course in statistical physics*. University of Texas Press, 1987.
- S. Richardson. On the no-slip boundary condition. *J. Fluid Mech.*, 59:707–719, 1973.
- M. Rief, M. Gautel, F. Oesterhelt, J. M. Fernandez, and H. E. Gaub. Reversible unfolding of individual titin immunoglobulin domains by AFM. *Science*, 276:1109–1112, 1997.
- N. Riley. Oscillatory viscous flows. Review and extension. *J. Inst. Maths. Applics.*, 3:419–434, 1967.

- N. Riley. Steady streaming. *Ann. Rev. Fluid Mech.*, 33:43–65, 2001.
- L. Rosenhead. *Laminar Boundary Layers*. Clarendon, Oxford, 1963.
- A. Roters and D. Johannsmann. Distance-dependent noise measurements in scanning force microscopy. *J. Phys. Condens. Matter*, 8:7561–7577, 1996.
- S. Roy, R. Raju, H. F. Chuang, B. A. Cruden, and M. Meyyappan. Modeling gas flow through microchannels and nanopores. *J. Appl. Phys.*, 93:4870–4879, 2003.
- W. B. Russel, E. J. Hinch, L. G. Leal, and G. Tieffenbruck. Rods falling near a vertical wall. *J. Fluid Mech.*, 83:273–287, 1977.
- J. E. Sader. Frequency response of cantilever beams immersed in viscous fluids with applications to the atomic force microscope. *J. Appl. Phys.*, 84:64–76, 1998.
- J. E. Sader. Calibration of rectangular atomic force microscope cantilevers. *Rev. Sci. Instrum.*, 70:3967–3969, 1999.
- J. E. Sader. Susceptibility of atomic force microscope cantilevers to lateral forces. *Rev. Sci. Instrum.*, 74:2438–2443, 2003.
- J. E. Sader and C. P. Green. Torsional frequency response of cantilever beams immersed in viscous fluids with applications to the atomic force microscope. *J. Appl. Phys.*, 92:6262–6274, 2002.
- J. E. Sader, I Larson, P. Mulvaney, and L. R. White. Method for the calibration of atomic force microscope cantilevers. *Rev. Sci. Instrum.*, 66:3789–3798, 1995.
- J. E. Sader and L. R. White. Theoretical analysis of the static deflection of plates for atomic force microscope applications. *J. Appl. Phys.*, 74:1–9, 1993.
- J. J. Saenz, N. Garcia, P. Grutter, E. Meyer, R. Heinzelmann, R. Wiesendanger, L. Rosenthaler, H. R. Hidber, and H. J. Gunterodt. Observation of magnetic forces by the atomic force microscope. *J. Appl. Phys.*, 63:4293–4295, 1987.
- N. C. Santos and M. A. R. B. Castanho. An overview of the biophysical applications of atomic force microscopy. *Biophys. Chem.*, 107:133–149, 2004.

- H. Schlichting. Berechnung ebener periodischer Grenzschichtströmungen. *Phys. Z.*, 33: 327–335, 1932.
- W. R. Schowalter. The behaviour of complex fluids at solid boundaries. *J. Non-Newtonian Fluid Mech.*, 29:25–36, 1988.
- T. W. Secomb. Flow in a channel with pulsating walls. *J. Fluid Mech.*, 88:273–288, 1978.
- L. Shatz. Singularity method for oblate and prolate spheroids in Stokes and linearized oscillatory flow. *Phys. Fluids*, 16:664–677, 2004.
- N.R. Silvestre and M.E.J. Holwill. Analysis of hypothetical flagellar waveforms. *J. Theor. Biol.*, 35:505, 1972.
- S. H. Smith. Unsteady Stokes' flow in two dimensions. *J. Eng. Math.*, 21:281–285, 1987.
- S. H. Smith. The time-dependent Stokes paradox. *Q. J. Appl. Math.*, 3:427–435, 1991.
- S. H. Smith. Unsteady separation for Stokes flow in two dimensions. *Phys. Fluids A*, 5: 1095–1104, 1993.
- S. H. Smith. Structural changes in transient Stokes flow. *Q. Jl. Mech. Appl. Math.*, 48: 285–309, 1995.
- S. H. Smith. Slow oscillatory Stokes flow. *Q. Appl. Math.*, 55:1–22, 1997.
- R. W. Stark, T. Drobek, and W. M. Heckl. Thermomechanical noise of a free v-shaped cantilever for atomic-force microscopy. *Ultramicroscopy*, 86:207–215, 2001.
- G. G. Stokes. On the effect of the internal friction of fluids on the motion of pendulums. *Trans. Camb. Phil. Soc.*, 9:182–187, 1851.
- T. Strunz, K. Oroszlan, R. Schafer, and H. J. Guntherodt. Dynamic force spectroscopy of single DNA molecules. *Proc. Natl. Acad. Sci. USA*, 96:11277–12782, 1999.

- J. T. Stuart. Double boundary layers in oscillatory viscous flow. *J. Fluid Mech.*, 24: 673–687, 1966.
- J. T. Stuart, R. C. DiPrima, P. M. Eagles, and A. Davey. On the instability of the flow in a squeeze lubrication film. *Proc. Roy. Soc. Lond. A*, 430:347–375, 1990.
- M. Sugihara-Seki. Motion of a sphere in a cylindrical tube filled with Brinkman medium. *Fluid Dyn. Res.*, 34:59–76, 2004.
- G. Sun, E. Bonaccorso, V. Franz, and H. S. Butt. Confined liquid: Simultaneous observation of a molecularly layered structure and hydrodynamic slip. *J. Chem. Phys.*, 117: 10311–10314, 2002.
- G. I. Taylor. *Problems of hydrodynamics and continuum mechanics*. SIAM Publ., 1969.
- P. Tekasakul, R. V. Tompson, and S. K. Loyalka. Rotary oscillations of arbitrary axisymmetry bodies in an axisymmetric viscous flow: numerical solutions. *Phys. Fluids*, 10, 1998.
- P. A. Thompson and S. M. Troian. A general boundary condition for liquid flow at solid surfaces. *Phys. Rev. Lett.*, 63:766–769, 1997.
- J. P. K. Tillett. Axial and transverse Stokes flow past slender axisymmetric bodies. *J. Fluid Mech.*, 44:401–417, 1970.
- S. Timoshenko and S. Woinowsky-Krieger. *Theory of Shells and Plates*. McGraw-Hill, 1959.
- D. M. Tolstoi. Molecular theory for slippage of liquids over solid surfaces. *Doklady Akad. Nauk. SSSR*, 85:1089, 1952.
- J. F. Trahan and R. G. Hussey. The Stokes drag on a horizontal cylinder falling towards a horizontal plane. *Phys. Fluids*, 28:2961–2967, 1985.
- E. O. Tuck. Some methods for flows past blunt slender bodies. *J. Fluid Mech.*, 18: 619–635, 1964.

- E. O. Tuck. Calculation of unsteady flow due to small motions of cylinders in a viscous fluid. *J. Eng. Math.*, 3:29–44, 1969.
- M. Van Dyke. *Album of fluid motion*. Parabolic Press, 1982.
- J. Vesenka, C. Mosher, S. Schaus, L. Ambrosio, and E. Henderson. Combining optical and atomic force microscopy for life science research. *Biotechniques*, 19:240–253, 1995.
- M. B. Viani, T. E. Schäffer, A. Chand, M. Rief, H. E. Gaub, and P. K. Hansma. Small cantilevers for force spectroscopy of single molecules. *J. Appl. Phys.*, 86:2258–2262, 1999.
- O. I. Vinogradova. Slippage of water over hydrophobic surfaces. *Int. J. Mineral Process*, 56:31–60, 1999.
- O. L. Vinogradova, H. Butt, G. E. Yakubov, and F. Feuillebois. Dynamics effects on force measurements I. Viscous drag on the atomic force microscope cantilever. *Rev. Sci. Instrum.*, 72:2330–2339, 2001.
- O. L. Vinogradova and G. E. Yakubov. Dynamic effects on force measurements. 2. lubrication and the atomic force microscope. *Langmuir*, 19:1227–1234, 2003.
- D. A. Walters, J. P. Cleveland, N. H. Thomson, P. K. Hansma, M. A. Wendman, G. Gurley, and V. Elings. Short cantilevers for atomic force microscopy. *Rev. Sci. Instrum.*, 67:3583–3590, 1996.
- G. H. Wannier. A contribution to the hydrodynamics of lubrication. *Q. Appl. Math.*, 8:1–32, 1950.
- E. B. B. Watson, W. H. H. Banks, M. B. Zaturka, and P. G. Drazin. On transition to chaos in two-dimensional channel flow symmetrically driven by accelerating walls. *J. Fluid Mech.*, 212:451–485, 1990.
- A. L. Weisenhorn, B. Drake, C. B. Prater, S. A. C. Gould, P. K. Hansma, F. Ohnesorge, M. Egger, S. P. Heyn, and H. E. Gaub. Immobilized proteins in buffer imaged at molecular resolution by atomic force microscopy. *Biophys. J.*, 58:1251–1258, 1990.

- M. P. L. Werts, E. W. van der Vegte, and G. Hadziioannou. Surface chemical reactions probed with scanning force microscopy. *Langmuir*, 13:4939–4942, 1997.
- C. H. Wiggins, D. Riveline, and R. E. Goldstein. Trapping and wiggling: elastohydrodynamics of driven microfilaments. *Biophys. J.*, 74:1043–1060, 1998.
- W. E. Williams. Boundary effects in Stokes flow. *J. Fluid Mech.*, 24:285, 1966a.
- W. E. Williams. A note on slow vibrations in a viscous fluid. *J. Fluid Mech.*, 25:589–590, 1966b.
- R. G. Winkler, J. P. Spatz, S. Sheiko, M. Moller, P. Reineker, and O. Marti. Imaging material properties by resonant tapping-force microscopy: a model investigation. *Phys. Rev. B.*, 54:8908–8912, 1996.
- C. W. Wolgemuth, T. R. Powers, and R. E. Goldstein. Twirling and whirling: viscous dynamics of rotating elastic filaments. *Phys. Rev. Lett.*, 84:1623–1626, 2000.
- D. L. Worcester, R. G. Miller, and P. J. Bryant. Atomic force microscopy of purple membranes. *J. Microsc.*, 152:817–821, 1988.
- G. K. Youngren and A. Acrivos. Stokes flow past a particle of arbitrary shape: a numerical method of solution. *J. Fluid Mech.*, 69, 1975.
- W. Zhang and H. A. Stone. Oscillatory motions of circular disks and nearly spherical particles in viscous flows. *J. Fluid Mech.*, 367:329–358, 1998.
- Y. Zhu and S. Granick. Rate-dependent slip of newtonian liquid at smooth surfaces. *Phys. Rev. Lett.*, 87:096105, 2001.
- Y. Zhu and S. Granick. Limits of the hydrodynamic no-slip boundary conditions. *Phys. Rev. Lett.*, 88:106102, 2002.
- R. Zwanzig and M. Bixon. Hydrodynamic theory of velocity correlation function. *Phys. Rev. A* 2, 2:2005, 1970.